

CRANFIELD UNIVERSITY

Joshua Marius Sebastiampillai

PERFORMANCE AND PRELIMINARY DESIGN OF NUTATING
DISC ENGINE TOPPING CYCLES FOR CIVIL AERO-ENGINE
APPLICATIONS

SCHOOL OF AEROSPACE, TRANSPORT AND
MANUFACTURING
Phd In Aerospace

Academic Year: 2015 - 2018

Supervisor: Dr. D. Nalianda Karumbaiah
Associate Supervisor: Dr. Vishal Sethi
September 2018

CRANFIELD UNIVERSITY

SCHOOL OF AEROSPACE, TRANSPORT AND
MANUFACTURING

PhD in Aerospace

Academic Year 2015 - 2018

JOSHUA MARIUS SEBASTIAMPILLAI

PERFORMANCE AND PRELIMINARY DESIGN OF NUTATING
DISC ENGINE TOPPING CYCLES FOR CIVIL AERO-ENGINE
APPLICATIONS

Supervisor: Dr. D. Nalianda Karumbaiah

Associate Supervisor: Dr. Vishal Sethi

September 2018

This thesis is submitted in partial fulfilment of the requirements for
the degree of PhD in Aerospace

***(NB. This section can be removed if the award of the degree is
based solely on examination of the thesis)***

© Cranfield University 2018. All rights reserved. No part of this
publication may be reproduced without the written permission of the
copyright owner.

ABSTRACT

Within the next thirty years evolutionary approaches to aero engine development will struggle to keep abreast with ever stringent environmental targets. A key component of the environmental targets stipulated by the SRIA is to reduce mission fuel burn by 75% by the year 2050, when compared to a year 2000 baseline. If the mission fuel burn benefits attributed to flight path optimization are excluded, a fuel burn target of 68% is postulated. Therefore, radical approaches to aero-engine development in terms of thermal and propulsive efficiency improvements need to be considered. One particular concept involves the inclusion of an un-ducted contra rotating propeller array to increase the propulsive efficiency of an aero-engine, for a short range aircraft, by the 2050 time frame. Concurrently a pressure-rise combustion system, called the nutating disc engine system, can increase the thermal efficiency of the year 2050 short-haul engine.

The nutating disc engine system concept is a strong contender due to its power density. The feasibility of the nutating disc engine system has been previously investigated for unmanned vehicle applications. However, this work investigates the performance benefits of incorporating a nutating disc engine system in a geared open rotor engine for the year 2050. According to the investigated literature, a methodology to size the nutating disc engine system and predict its potential fuel burn performance benefit in a geared open rotor configuration is lacking.

In addition, there is a lack of knowledge regarding the impact synergetic technologies such as intercooling and secondary combustion affect the performance of a nutating disc engine system coupled to an un-ducted contra rotating propeller array.

Hence, the primary contribution of this work is to determine a methodology to predict the size and turbo-charged performance of a nutating disc engine system. An outcome of this contribution determines whether a geared open rotor engine with a nutating disc engine system can meet the fuel burn target of 68%, when compared to a year 2000 baseline engine. This investigation is furthered with an uncertainty analysis, to show the variability of potential 2050 fuel burn estimates. The derived nutating disc engine system sizing methodology shows confluence with known prototype dimensions and CAD based sizing approaches. The used thermodynamic model also shows reasonable levels of confluence with published literature.

Another outcome of the primary contribution to knowledge, is to determine whether synergetic technologies such as intercooling and secondary combustion can meet the 68% fuel burn target in conjunction with a nutating disc engine system in a geared open rotor engine architecture. These investigations are furthered by an uncertainty analysis. The secondary contribution of this work is to provide preliminary performance and mass estimates of Y2050 engine configurations that can meet the 68% fuel burn target.

An engine specification for a year 2000 baseline engine and a reference year 2050 geared open rotor engine are proposed to benchmark the relative fuel burn benefit achieved by a perceived year 2050 nutating disc engine system engine configurations. The reference 2050 geared open rotor engine, on a short range aircraft, determines engine technology levels for further radical engine configurations in this work. The reference year 2050 engine, geared open rotor, produces a fuel-burn benefit of 58.9% relative to a comparable year 2000 baseline.

Since it falls short of the 68% target fuel-burn benefit, the viability of a nutating disc engine system is considered. A geared open rotor with a nutating disc engine system can provide fuel burn benefits of 63% relative to a year 2000 baseline. An uncertainty study indicates, that the proposed engine configuration can provide relative fuel burn benefits from 37% to 71%, when compared to a year 2000 baseline.

The inclusion of intercooling, secondary combustion and a combination of the two with a nutating disc engine system produced fuel burn benefits of 64%, 71% and 65% respectively relative to year 2000 baseline, as a consequence of a targeted search optimization. The design variables

that influence the uncertainty the most in all the investigated nutating disc engine variants are the heat flux through the casing and the ratio of constant volume combustion to constant pressure combustion.

A like for like analysis, for the four investigated engine configurations indicate that a geared open rotor with only a nutating disc engine system provides the highest potential fuel burn benefit. However, when aspects such as NO_x and noise emissions are considered qualitatively it is postulated that a nutating disc engine system with intercooling and secondary combustion technologies is desirable.

Due to the high degree of uncertainty in the perceived fuel burn values, for the proposed engine configurations, a roadmap to progress the nutating disc engine system technology to higher TRL are further detailed.

Keywords:

Nutating Disc Engine, Geared open rotor, SRIA, Intercooler, Secondary combustor

“Do not forsake wisdom, and she will protect you; love her, and she will watch over you. The beginning of wisdom is this: Get wisdom. Though it cost all you have, get understanding.”

Proverbs 4:6-7(NIV)

ACKNOWLEDGEMENTS

I would whole heartedly like to thank Professor Pillidis, Dr. Nalianda and Dr. Sethi in providing me with this opportunity to carry out this research. Dr. Nalianda's and Dr. Sethi's mentorship and guidance has truly been invaluable, throughout this arduous process. In addition, countless thanks to my colleagues Andrew Rolt, Florian Jacob, Diana Guiomar, Francesco Mastropierro, Parash Agrawal and Marvin Elter.

This road of research is long, lonely and arduous and without the support of loved ones it can be like being stuck in a flaming cage in Dante's seventh circle of hell. Words can't describe the immense gratitude that should be placed as a wreath at the feet of my parents Gerard and Ramona; who have taught me to fasten the saddle, steady the stirrups and grab the reins on this bucking beast called life. My dearest siblings Sam, Dave and Andy have been nothing short of a blessing in every sense of the word. The apple of my eye and love of my life; Gosia, words of gratitude do not do justice for being my bastion of support, love and encouragement during this process and forevermore. Payman and his dear family, for their fastidious help and support. A massive Thank you to Gillian Hargreaves for all her support, one of the most helpful people I've ever met.

It would be an injustice not to thank the countless friends who have made this journey possible, namely : Jose Barros, a true friend and confidant. Surya Narranyaran, for the brilliant physics debates. Andrew Rolt, for inspirational discussions about gas turbines. Florian Jacob, for the brainstorming sessions when there was no end in sight. Dr. Alexis Alexiou, for the detailed discussions about gas turbine design principles and immense help with PROOSIS. Professor Tomas Gronstedt, for invaluable advice, engaging discussion and good banter. Nicolas Tantot, for the truly invaluable advice on the design principles of the geared open rotor. Mathieu Belmonte, for his brilliant crash course in PROOIS and invaluable friendship. Dr. Ioannis Roumeliotis, for his brilliant advice throughout.

Kasia T, Asia T., Dorota and Stanislaw T., Marvin E., Gerard T., Francesco M., Parash A, Diana G., Tala S., Alex B., Dawid B., Marco M., Luis C., Yize, Xiaxiou, Dr. Pierre G., Dr. Carlos X, Dr. Anders L., Ahmad L., Kristina S., Sotonte B., Eleanor, Anish V., Arun P., Prafull S., Mehrdad S. Alex N., Abijith C., Nikilesh, Dr. Christos M., CSA Bar team, Corrosion Radar team, Nina S., Tharka P., Alvise P. and to all those I have not mentioned a very big thank you!

This project has received partial funding from the European Union's Horizon 2020 research and innovation programme under Grant Agreement No. 633436 (ULTIMATE). This project has received partial funding from the European Union's Horizon 2020 research and innovation programme under Grant Agreement No. 686340 (DEMOS).

TABLE OF CONTENTS

ABSTRACT	3
ACKNOWLEDGEMENTS.....	6
LIST OF FIGURES.....	10
LIST OF TABLES	15
LIST OF ABBREVIATIONS.....	17
Nomenclature.....	23
1 Introduction.....	30
1.1 Research context.....	33
1.2 Research Aims and Objectives.....	45
1.3 Thesis structure	47
2 Literature Review	49
2.1 Year 2000 baseline short-range engine	49
2.2 Geared open rotor literature review	52
2.3 Nutating Disc system literature review.....	57
2.4 Intercooler literature review.....	69
2.5 Re-heat/ Secondary combustor literature review	71
3 Contribution to knowledge	74
4 Methodology.....	76
4.1 Year 2000 short range engine performance model.....	77
4.1.1 Performance model.....	78
4.2 Year 2050 geared open rotor performance model	82
4.2.1 CRP performance estimation model.....	83
4.2.2 Differential planetary gearbox (DPGB) model	95
4.2.3 DPGB cooling model.....	97
4.2.4 Nozzle duct pressure loss model	98
4.3 Nutating Disc Engine Model.....	99
4.3.1 Nutating disc performance model.....	99
4.3.2 Swept volume estimation of the dual nutating disc engine system configuration.....	107
4.3.3 Volumetric compression ratio estimation.....	112
4.3.4 Combustion and expansion process estimation	115
4.3.5 Auxiliary Components	118
4.4 Intercooler and secondary combustor performance model.....	120
4.4.1 Intercooler performance model	121
4.4.2 Secondary Combustor performance	123
4.5 Component mass estimation methods.....	125
4.5.1 Axial Compressor Mass	126
4.5.2 Centrifugal compressor size and mass model.....	127

4.5.3 Annular Combustor or Secondary combustor	128
4.5.4 Annular Turbine mass	128
4.5.5 Supporting structures, controls and accessory mass	128
4.5.6 Planetary and Bevel Gearbox mass estimation.....	128
4.5.7 Contra rotating propeller system mass and Nacelle mass	129
4.5.8 Nutating disc engine system mass	129
4.5.9 Intercooler mass.....	131
4.6 Relative Fuel burn estimation	131
5 Results and Discussion	134
5.1 Year 2000 short range engine	135
5.2 Year 2050 reference GOR engine	143
5.2.1 Performance overview of the M-GOR2050 engine configuration ...	145
5.2.2 Performance overview of the S-GOR2050-XX engine configurations.....	157
5.2.3 Performance overview of the reference Y2050 GOR	164
5.2.4 Design Sensitivity of the LP- system of the reference GOR2050 engine	169
5.3 Quasi 1-D nutating disc engine system performance and sizing model	180
5.3.1 Parametric analysis for ND sizing methodology	183
5.4 Y2050 GOR-ND IP-drive and Y2050 GOR-ND LP-drive configurations	189
5.4.1 Determining the performance of Y2050 GOR-ND IP-drive and Y2050 GOR-ND LP-drive engines	190
5.5 Performance and mass sensitivities of the Y2050 GOR-ND IP-drive engine configuration	196
5.6 Performance and mass sensitivities of the Y2050 GOR-ND IP-IC-drive engine configuration	207
5.7 Performance and mass sensitivities of the Y2050 GOR-ND IP-SC-drive engine configuration	220
5.8 Performance and mass sensitivities of the Y2050 GOR-ND IP-IC-SC-drive engine configuration.....	227
5.9 Y2050 GOR-ND configuration overview and quasi-qualitative configuration assessment	232
6 Conclusions.....	245
7 Future Work.....	252
7.1 Further work regarding the nutating disc core.....	252
7.1.1 Compressor module	253
7.1.2 Accumulator Module.....	257
7.1.3 Pre-combustor module	261
Combustor-expander module.....	264
7.1.4 Auxiliary system module.....	270
7.2 Further work for the design assessment platform	272

7.2.1 Engine performance, Mass and life module	273
7.2.2 Aircraft performance, Emissions, Noise and Financial modules.....	278
REFERENCES.....	280
APPENDIX-A.....	291
APPENDIX-B.....	305
APPENDIX-C	306
APPENDIX-D	308
APPENDIX-E.....	310
APPENDIX-F.....	314

LIST OF FIGURES

Figure 1- 1: components of a single disc ND engine configuration.	30
Figure 1- 2: Top-down view of a ND engine showing the inlet ‘elbow’ duct	31
Figure 1- 3: Butterflied view and components of a single and dual disc ND engine[2]	32
Figure 1- 4: Projected increase in CO ₂ emissions by year 2050[7]	34
Figure 1- 5: Evolution of engine configurations as a function of the fan pressure ratio and bypass ratio[13,14]	36
Figure 1- 6: Overview of potential Brayton-cycle variants	38
Figure 1- 7: T-s diagram for intercooled and Brayton cycle at similar T ₃ and T ₄ levels	39
Figure 1- 8: T-s diagram for re-heated and Brayton cycle at similar T ₃ and T ₄ levels	40
Figure 1- 9: T-s diagram for recuperated cycle and Brayton cycle at similar T ₄ levels.....	41
Figure 1- 10: Comparative T-s diagram for a bottoming cycle and Brayton cycle.....	42
Figure 1- 11: Comparative T-s diagram for an Otto cycle and Brayton cycle.....	43
Figure 1- 12: Real processes in a Brayton cycle	44
Figure 2- 1: Meridional view of the reference GOR2050 configuration[61]	55
Figure 2- 2: Possible ND- system arrangement in the core of an engine.....	62
Figure 2- 3: Static and dynamic frames of reference indicating the motion of nutating gears[72].....	63
Figure 2- 4 : proposed seal arrangement of a single ND engine system [78]	65
Figure 2- 5 : proposed arrangement of a dual disc nutating disc engine system [78].....	65
Figure 2- 6: P-V diagram of a nutating disc engine system cycle.....	66
Figure 2- 7: Lancette design as proposed by Kormann et al. [85].....	69
Figure 2- 8: Circumferential view of Lancette heat exchanger arrangement.....	70
Figure 2- 9: Involute spiral heat exchanger design[86].....	70
Figure 4- 1: Overview of methodologies employed to estimate the performance of Y2050 nutating disc engine core configurations.....	77
Figure 4- 2: PROOSIS schematic of the Y2000 CFM56-5B engine model	78
Figure 4- 3: Non-dimensional Velocity triangle at 75% blade span[16].....	85
Figure 4- 4: <i>net propeller efficiency correction as a function of helical Mach number</i> [16] ..	86

Figure 4- 5: representative single propeller map [16]	87
Figure 4- 6: Propeller efficiency as a function of the number of propeller blades and propeller loading	88
Figure 4- 7: Propeller efficiency estimation as a function of the number of propeller blades and propeller loading	88
Figure 4- 8: General arrangement of an experimental trailing edge Pylon blower[112].....	89
Figure 4- 9: Coefficient of thrust correction as a function of imaginary advance ratio.	90
Figure 4- 10: Schematic overview of iterative process to determine CRP performance.....	93
Figure 4- 11: Forward propeller map at three operating conditions.....	94
Figure 4- 12: Rear Propeller map at three operating conditions.....	95
Figure 4- 13: Non-dimensional planetary gearbox map.....	96
Figure 4- 14: PROOSIS schematic of DPGB cooling system.....	97
Figure 4- 15: Cross-section of the component under consideration[61].....	98
Figure 4- 16: Mapping thermodynamic stations to geometry of a naturally aspirated ND engine	101
Figure 4- 17: Schematic overview of iterative process to determine ND engine performance.	106
Figure 4- 18: Definition of the variables that determine the size of a single disc in Cartesian co-ordinate system	108
Figure 4- 19: Nutating disc casing definition in Cartesian co-ordinate system.....	109
Figure 4- 20: Definition of wedge parameters.....	110
Figure 4- 21: Definition of the nutating disc areas that are revolved around the y' axis....	111
Figure 4- 22: Projection of the dynamic frame of reference on the static frame of reference	113
Figure 4- 23: Crank angles at which the displaced volumes are to be calculated.....	114
Figure 4- 24: Flow chart that schematically shows the volumetric compression ratio.....	115
Figure 4- 25: y'-x' view of pre-combustor	116
Figure 4- 26: top-down view of the proposed pre-combustion chamber	116
Figure 4- 27: Crank angle limits that define the volumetric expansion ratio.....	117
Figure 4- 28: Overview of methodology to estimate the volumetric expansion ratio.....	118
Figure 4- 29: Possible meridional view of the nutating disc engine systems in the core of a gas turbine	120
Figure 4- 30: Circumferential arrangement of the nutating disc engine systems corresponding to the centre line of the engine.	120

Figure 4- 31: Layout and flow path depiction of two-pass cross-flow intercooler	122
Figure 4- 32: Circumferential arrangement of the intercooler modules	122
Figure 4- 33: Overview of the iterative process to determine the intercooler module performance.....	123
Figure 4- 34: Positioning of the secondary combustor within the gas turbine core	124
Figure 4- 35: Flow path definition within the secondary combustor[93].....	124
Figure 4- 36: Schematic representation of procedure to estimate relative fuel burn benefits for Y2050 GOR-ND engine system configurations	132
Figure 5- 1: schematic of optimizer flow path in the Isight environment.....	136
Figure 5- 2: Radar plot indicating the closeness of fit between the SRTF2000 model and the NEWAC dataset.....	141
Figure 5- 3: SRTF2000 meridional view [61]	143
Figure 5- 4: Schematic of global overview of modelling procedure to produce the GOR2050 configuration	145
Figure 5- 5: Visualization of the potential industry GOR2050 general arrangement by Safran Aircraft Engines [60]	146
Figure 5- 6: Visualization of the mounting location on an Y2050 SR aircraft[106]	146
Figure 5- 7: Radar plot that indicates the closeness of fit between M-GOR2050 configuration and industry reference GOR2050 configuration.....	148
Figure 5- 8: Scaled forward propeller performance map of the M-GOR2050 at three operating conditions.....	151
Figure 5- 9: Scaled rear propeller performance map of the M-GOR2050 at three operating conditions.....	151
Figure 5- 10: HPT exit AN^2 variation as a function of axial exit Mach number.....	153
Figure 5- 11: HPT rotor blade speed variation as a function of the exit hub:tip ratio	154
Figure 5- 12: Representative operating points on the LPT component map.....	156
Figure 5- 13: LPT exit AN^2 variation as a function of exit Mach number	156
Figure 5- 14: LPT exit hub speed variation as a function of the exit hub:tip ratio	157
Figure 5- 15: HPC polytropic efficiency correction as a function of last stage blade height[19]	159
Figure 5- 16: Re-datum (as per the last stage blade height of the M-GOR2050 engine model) HPC polytropic efficiency correction as a function of last stage blade height.	159
Figure 5- 17: Radar plot indicating the quality of fit of the GOR2050 engine	167
Figure 5- 18: Engine cross-section of the reference GOR2050 engine configuration[61]	168

Figure 5- 19: Relative mass breakdown of the reference GOR2050 components[61].....	168
Figure 5- 20: Overview of LP-system design parameters.....	169
Figure 5- 21: Relative change in TOC TSFC as a function of the LPT PR and propeller speed.	171
Figure 5- 22: Relative change in engine mass as a function of the LPT PR and propeller speed.....	172
Figure 5- 23: Relative change in TOC TSFC as a function of the relative propeller spacing and propeller speed.....	173
Figure 5- 24: Relative change in TOC TSFC as a function of relative propeller spacing at a rotational speed of 700 rpm.....	173
Figure 5- 25: Relative TSFC effect as a function of Torque ratio at propeller speed of 700 rpm.....	174
Figure 5- 26: Relative change in TOC TSFC as a function of the rear propeller clipping and propeller speed.....	175
Figure 5- 27: Relative change in engine mass as a function of the rear propeller clipping and propeller speed.....	176
Figure 5- 28: Relative change in TSFC as a function of the front propeller diameter and speed.....	176
Figure 5- 29: Relative change in engine mass as a function of propeller speed and front propeller diameter.....	177
Figure 5- 30: Relative change in Fuel burn by variation of operational speed at CR and EOR	178
Figure 5- 31: PROOSIS model fit compared to the parametric study in [1].....	181
Figure 5- 32: Component mass distribution of the naturally aspirated, and calibrated, dual disc nutating disc engine configuration	183
Figure 5- 33: Variation of swept volume as a function of the ND compressor tip radius and angle of nutation	184
Figure 5- 34: Variation of swept volume as a function of the ND compressor tip radius and hub to tip ratio	185
Figure 5- 35: Relative change in the compressor disc volumetric compression ratio as a function of the angle of nutation and the hub to tip ratio.....	186
Figure 5- 36: Top-down view of nutating disc compressor, with theoretical and potential practical compressor off-take.	187
Figure 5- 37: Variables used in parametric analysis.....	187
Figure 5- 38: Relative change in combustion crank angle as a function of the combustion chamber exit aperture height and the ratio of the expander hub radius and the burner radius	188
Figure 5- 39: Scaled meridional view of the Y2050 GOR-ND IP-drive.....	189

Figure 5- 40: Scaled meridional view of the Y2050 GOR-ND LP-drive	190
Figure 5- 41: Overview of first order optimization employed to derive fuel burn estimates of the IP-drive configuration.....	191
Figure 5- 42: Comparison between the relative mass distribution predicted by Weico 9.6 and methods outlined in Section 5.5 for the reference GOR2050.	192
Figure 5- 43: Sensitivity study of the TOC TSFC dependent nutating disc system design variables.....	198
Figure 5- 44: sensitivity of the engine mass dependent ND system design variables	198
Figure 5- 45: Fuel burn targets and estimates relative to an Y2000 reference	202
Figure 5- 46: relative uncertainty of ND engine system design variables in the nominal 2050 GORIP-drive design	203
Figure 5- 47: Relative change in TOC TSFC as a function of the IPC pressure ratio and inlet mass flow.....	204
Figure 5- 48: Relative change in TOC TSFC as a function of the IPC pressure ratio and inlet mass flow.....	205
Figure 5- 49: Scaled meridional view of the Y2050 GOR-ND IP-IC-drive engine configuration	208
Figure 5- 50: Relative breakdown of key intercooler design variables	210
Figure 5- 51: Relative change in TSFC as a function of axi-centrifugal PR and inlet mass flow.....	211
Figure 5- 52: Relative change in the IP-IC-drive engine mass as a function of the inlet mass flow and axi-centrifugal pressure ratio.....	212
Figure 5- 53: Relative change in TSFC as a function of axi-centrifugal PR and booster PR.	213
Figure 5- 54: relative change in engine mass as a function of booster and axi-centrifugal pressure ratios.....	213
Figure 5- 55: Relative change in TSFC as a function of axi-centrifugal PR and BPR.....	214
Figure 5- 56: Relative change in engine mass as a function of axi-centrifugal PR and BPR	215
Figure 5- 57: Relative change is TSFC as a function of BPR and mass flow.	216
Figure 5- 58: Relative change is mass as a function of BPR and mass flow.	216
Figure 5- 59: relative change of TOC TSFC as a function of cold side total pressure loss and intercooler effectiveness.....	217
Figure 5- 60: Relative change in the mid-CR and EOR TSFC as a function of the total pressure loss and effectiveness of the IC.	218
Figure 5- 61: Scaled meridional view of the Y2050 GOR-ND IP-SC-drive engine configuration	220

Figure 5- 62: Relative uncertainty of key secondary combustor design variables	221
Figure 5- 63: relative change in TOC TSFC as a function of the SC dPqP and inlet mass flow.	224
Figure 5- 64: Relative TOC TSFC variation as a function of the SC fuel flow and the inlet mass flow.....	225
Figure 5- 65: Relative change in engine mass as a function of the inlet mass flow and SC fuel flow.....	225
Figure 5- 66: Relative change in TSFC as a function of the SC fuel flow	226
Figure 5- 67: Scaled meridional view of the Y2050 GOR-ND IP-IC-SC-drive engine configuration	227
Figure 5- 68: Relative change in TOC TSFC as a function of the SC fuel flow rate and the BPR.....	231
Figure 5- 69: Relative change in engine mass as a function of BPR and secondary fuel flow	231
Figure 5- 70: Overview of the relative fuel burn of all Y2050 GOR-ND IP configurations relative to a year 2000 short range mission	236
Figure 5- 71: Quasi-qualitative rank for all configurations	243

LIST OF TABLES

Table 2- 1: Overview of gas turbine performance prediction software	50
Table 2- 2: overview of gas turbine mass estimation tools	51
Table 2- 3: Chronological overview of the development of the open rotor to date	52
Table 2- 4: Overview of open rotor engine configurations.....	54
Table 2- 5: Overview of potential constant-volume combustion enablers.....	57
Table 2- 6: Nutating Disc Engine patent comparison	63
Table 2- 7: Chronological overview of work performed at Cranfield University.....	67
Table 4- 1: NEWAC CFM56-5b type model data specifications.....	78
Table 5- 1: Optimizer global variables.....	136
Table 5- 2: Design Variable bounds used for Isight matching	137
Table 5- 3: Constraints imposed on optimizer	138
Table 5- 4: Scale and Mass factors used in optimization	138

Table 5- 5: SRTF2000 engine specification	139
Table 5- 6: SRTF2000 comparison versus NEWAC data specification.....	141
Table 5- 7: Absolute rotational speeds of SRTF2000 and component parameters at EOR	142
Table 5- 8: industry based reference GOR2050 design parameters at mid-cruise[60].....	146
Table 5- 9: Operational envelope as specified by Safran Aircraft Engines	147
Table 5- 10: M-GOR2050 general performance figures compared to industry GOR2050 performance figures.....	147
Table 5- 11: Effect of varying CRP speeds on the pitch setting throughout the flight envelope	149
Table 5- 12: S-GOR2050-XX design point thrust ratings and flight conditions	158
Table 5- 13: Upper and lower bounds imposed on design variables within the optimization	161
Table 5- 14: Overview of S-GOR2050-XX series engine models at TOC.....	162
Table 5- 15: Overview of S-GOR2050-XX series engine models at EOR.....	163
Table 5- 16: Frozen global engine specification demanded by Y2050 SR aircraft.....	164
Table 5- 17: Design variable ranges, constraints and optimizer objectives set within the I- sight environment	165
Table 5- 18: Reference GOR2050 performance overview at TOC, CR and EOR	166
Table 5- 19: Overview of the variables used in the GOR2050 LP-system parametric study	170
Table 5- 20: Input variables for the reference case in [1]	181
Table 5- 21: Calibration of proposed sizing methodology.....	182
Table 5- 22: Coefficients to estimate the swept volume of a single disc at varying hub to tip ratios.	185
Table 5- 23: Design parameter bounds, constraints and objective for the IP-drive variant at TOC conditions	193
Table 5- 24: Overview of the performance of the Y2050 GOR-ND IP-drive and LP-drive configurations	194
Table 5- 25: relative fuel burn benefits of Y2050 GOR-ND IP-drive design variants	199
Table 5- 26: Noise dependent and NO _x emission dependent parameters	206
Table 5- 27: Ranges of the TOC design variables for the targeted optimization for the Y2050 GOR-IP-IC-drive configuration	208
Table 5- 28: Performance overview of Y2050 GOR-ND IP-IC-drive engine performance	209
Table 5- 29: Parameter comparison of three engines at EOR conditions	219

Table 5- 30: Y2050 GOR-ND-IP-SC design point parameters for targeted optimization..	221
Table 5- 31: Performance overview of the Y2050 GOR-ND IP-SC- drive configuration...	222
Table 5- 32: Comparative overview of three engine configurations at EOR conditions....	226
Table 5- 33: Overview of the performance of the Y2050 GOR-ND IP-IC-SC-drive engine configuration	228
Table 5- 34: Parameter comparison of four engines at EOR conditions	232
Table 5- 35: Parameters used in comparative study for Y2050 GOR-ND IP-drive variants	233
Table 5- 36: Performance overview of Y2050 IP-drive derivative configurations.....	235
Table 5- 37: Y2050 GOR-ND IP-drive variants TRL-1 quasi-qualitative rank overview....	238
Table 5- 38: Y2050 GOR-ND IP-drive variants TRL 3-4 quasi-qualitative rank overview.	240
Table 5- 39: Y2050 GOR-ND IP-drive variants TRL 4-production quasi-qualitative rank overview.....	241
Table 7- 1: Preliminary bill of materials for the accumulator rig.....	259

LIST OF ABBREVIATIONS

ACARE	Advisory council for aviation research in Europe
AGARD	Advisory Group for Aerospace Research and Development
AHEAD	Advanced hybrid engines for aircraft development
ATLAS	Cranfield Preliminary engine mass estimation tool
ATW	advanced tube and wing
B777	Boeing 777 widebodyaircraft
BMT	blade metal temperatures
BPR	bypass ratio
Cac	cooling air coefficient
CAD	computer aided design
CCA	cooled cooling air
CCGT	combined cycle gas turbine

CDP	compressor delivery pressure
CDT	compressor delivery temperature
CeRAS	central reference aircraft data system
CFD	computational fluid dynamics
CFM	designation to the joint venture between General Electric and Safran
CO	Carbon Monoxide
CR	cruise
CROR	contra-rotating open rotor
CRP	contra rotating propeller
DAQ	data acquisition system
DDOR	direct drive open rotor
DNS	direct numerical simulation
DPGB	differential planetary gearbox
EASA	European aviation safety agency
ECS	environmental cabin system
EGT	exhaust gas temperature
EGT	exhaust gas temperature
EIS	Entry in to service
EOR	end of runway
EP	polytropic efficiency
EqSS	equivalent single stage
ERJ	Embraer regional jet
FAA	Federal Aviation authority
FAR	fuel to air ratio

FB	fuel burn
FEA	Finite element analysis
FHV	fuel heating value
FS	factor of safety
GE	General electric
GOR	geared open rotor
GOR2050	gererd open rotor configuration for year 2050
GT	gas turbine
HP	high pressure
HPC	high pressure compressor
HPT	high pressure turbine
HT	hub to tip ratio
IAE	international aero engines
IGV	inlet guide vane
IP	intermediate pressure
IPC	intermediate pressure compressor
IPT	intermediate pressure turbine
JSF	joint strike fighter
LEMCOTEC	Low emission core engine technologies
LES	large eddy simulation
LP	Low pressure
LPT	low pressure turbine
LQR	Linear quadratic regulator
LTO	landing and take-off

MD	mc donnel douglas
MFT	map fitting tool
M-GOR2050	matched engine configuration for Safran's stipulated EIS2050 GOR
MN	mach number
MTBF	mean time before failure
NACA	National advisory committee for aeronautics
NASA	National aeronautics and space administration
ND	nutating disc
NEWAC	new aero engine concepts
NGV	nozzle guide vane
NK	Kuznetsov design bureau designation of contra-rotating proepller engine
NLTF	non linear fuel trade factors
Nox	nitrous oxide
NPSS	numerical propulsion system simulation
OEM	orginal equipment manufacurer
OGV	outlet guide vane
ONERA	Office National d'Etudes et de Recherches Aérospatiales
OPR	overall pressure ratio
P&W	Pratt and Whitney
PCM	pitch control mechanism
PDE	pulse detonation engine
PF	NASA designation to highly swept propeller blades
PID	Proportional-integral-derivative controller
PIV	particle image velocimetry

PMU	power management unit
PR	pressure ratio
PROOSIS	Propulsion object oriented Simulation software
PWT	power turbine
RNI	Reynolds number index
RWTH	Rheinisch-Westfälische Technische Hochschule Aachen
S-GOR2050-18	scaled year 2050 geared open rotor with top of climb net thrust of 18kN
S-GOR2050-22	scaled year 2050 geared open rotor with top of climb net thrust of 22kN
S-GOR2050-25	scaled year 2050 geared open rotor with top of climb net thrust of 25kN
SR	NASA designation of highly swept propeller blades on their demonstrator
SR	short range
SRIA	Strategic research and innovation agenda
SROR	single rotating open rotor
SRP	single rotating propeller
SRTF2000	short range turbofan
TBC	thermal barrier coating
TERA	techno economic risk assesment
TET	turbine entry temperature
TF	technology factor
TM	technical memorandum
TOC	Top of climb
TR	torque ratio
TRL	technology readiness level
TRL	technology readiness level

TU	Tupolev
UDF	unducted direct drive fan
UHC	unburned hydro carbons
ULTIMATE	Ultra low emission technology innovations for mid-century aircraft turbine engines
URANS	Unsteady Reynold averaged numerical solutions
VF	void fraction
VIGV	variable inlet guide vane
VITAL	Environmentally firendly aero engine
VSV	variable stator vanes
VTOL	vertical take-off and landing
VVT	variable valve timing
WATE	mass analysis software of gas turbine engines
WeiCo	mass and cost software from Chalmers University
WR	wave rotor
XF	designation of US army aircraft with contra rotating propellers
Y2000	year 2000
Y2050	year 2050
Y2050 GOR-ND IP-drive	Geared open rotor engine with a nutating disc core powering the intermediate pressure shaft
Y2050 GOR-ND IP-IC-drive	Geared open rotor engine with an intercooled-nutating disc core powering the intermediate pressure shaft
Y2050 GOR-ND IP-IC-SC-drive	Geared open rotor engine with an intercooled-reheated-nutating disc core powering the intermediate pressure shaft
Y2050 GOR-ND IP-SC-drive	Geared open rotor engine with a reheated-nutating disc core powering the intermediate pressure shaft

Y2050 GOR-ND LP-drive	Geared open rotor engine with a nutating disc core powering the low pressure shaft
Y2050 ND-GOR	year 2050 nutating disc engine geared open rotor

Nomenclature

# NDs (-)	number of nutating disc cores
a (-)	coefficient to determine the swept volume of the nutating disc
a (-)	exponent of the mass estimation for the burner
a (-)	calibration constant for the wiebe function
a (m/s)	speed of sound
A (m ²)	area
A (m ²)	cross-sectional area of plenum
A (m ²)	wetted area during the combustion process using Wochisni's equation
A _n (m ²)	triangular area of internal nutating disc structure to be swept
AN ² (rpm ² m ²)	preliminary turbine mechanical limitation metric circular-rectangular area of internal nutating disc structure to be swept to
A _o (m ²)	determine the swept volume
b (-)	coefficient to determine the swept volume of the nutating disc
B (deg.)	flow deflection
b (m)	blade chord
B (m)	equivalent bore diameter
Bi (-)	Biot number
BnBF (-)	number of propellers in the first propeller array
BnBR (-)	number of propellers in the rear propeller array
BPR (-)	bypass pressure ratio
c (-)	coefficient to determine the swept volume of the nutating disc crank angle per shaft revolution during the entire combustion process of the
CA (deg.)	nutating disc engine
C _{ac} (-)	cooling air coefficient
COT (K)	combustor outlet temperature
C _p (J/kg.K)	isobaric heat capacity
C _{pwr} (-)	coefficient of power
C _t (-)	coefficient of thrust
C _v (J/kg.K)	isochoric heat capacity
C _x (-)	nozzle discharge coefficient
D (m)	diameter
DE (m)	height of aperture of nutating disc pre-combustor
dp _{qp} (-)	total pressure loss
dr (m)	change in radius
dT (K)	change in temperature

eff (-)	cooling effectiveness for the HPT rotors
EGT (K)	exhaust gas temperature of the LPT
EP23 (-)	polytropic efficiency of the IPC
EP27 (-)	polytropic efficiency of the HPC
ETP (-)	polytropic efficiency
FAR (-)	fuel to air ratio
FB (%)	fuel burn benefit/penalty
FHV (MJ/kg)	fuel heating value
Fn(N)	Net Thrust
f_p (-)	total pressure loss
f_{ql} (-)	total heat loss factor
h (J/kg)	specific enthalpy
H (m)	blade height
H (m)	height of nutating disc core
Heat (kW)	heat lost from the air-oil heat exchanger
HT (-)	hub to tip ratio
J (-)	advance ratio
k (-)	radii ratio between carrier and sun gears
k (-)	number of power cycles per shaft revolutions
K_1 (-)	proportional constant to estimate the mass of the centrifugal compressor
K_2 (-)	proportional constant to estimate the mass of the centrifugal compressor
K_b (-)	proportional constant to determine the mass of the burner
K_b (-)	proportional constant to determine the mass of the supporting mass contribution of the engine
K_c (-)	proportional constant to determine the mass of the axial compressor
K_c (-)	work loading characteristic for multi-stage turbines
K_{comb} (-)	combustion pattern factor
K_{cool} (-)	cooling flow factor
K_{inp} (-)	Calibration constant for polytropic efficiency estimation
K_t (-)	proportional constant to determine the mass of the axial turbine
K_w (-)	gearbox mass prediction constant
l (m)	axial length of plenum inlet duct
L (m)	length of plenum exit duct
L (m)	length of turbomachinery component
l_f (-)	wedge to disc radius ratio
LHV (MJ/kg)	lower heating value
M (-)	Mach number
m (-)	calibration constant for the wiebe function
\dot{m} (kg/s)	mass flow
m(-)	mass flow fraction
M^* (-)	Critical helical Mach number
Mach (-)	Mach number
MF(-)	mass factor

N (-)	number of stages
n (rpm)	rotational speed
N (rpm)	rotational speeds of the propellers
NcRdes (-)	map scaling factor
NcRdesMap (-)	map scaling factor
NL (rpm)	rotational speed of the low pressure spool
Nmech (rpm)	rotational speed of the shaft
OPR (-)	overall pressure ratio
OPR (-)	overall pressure ratio
P (Pa)	total pressure
PR (-)	pressure ratio
Pw (kW)	power
Pwr (kW)	power of flows in the intercooler
Q (Nm)	Torque
Q (W)	Absolute heat transferred
R (J/kg.K)	gas constant
r (m)	propeller radius
r (m)	radius
R (m)	outer radius of the toroidal structure
r (m)	inner radius of the toroidal structure
r(-)	volumetric expansion or compression ratio
r71 (-)	overall volumetric expansion ratio
SF (-)	scale factor
SFC (g/kN.s)	Specific fuel consumption
T (K)	total temperature
t (m)	thickness
t (sec)	time
T06 (K)	average cycle temperature at the end of the constant pressure combustion proces in the nutsting disc engine
Tblade (K)	blade metal temperature
TET (K)	Turbine entry temperature
TF (-)	technology factor
Tm41 (K)	Blade metal temperature of HPT rotor
TR (-)	Torque ratio between the fore and aft propellers
TR (-)	Torque ratio between the fore and aft propellers
TSFC (g/kN.s)	thrust specific fuel consumption
T _w (K)	wall temperature
U (m/s)	tip speed
V (m/s)	velocity
V (m ³)	volume
VF (-)	void fraction
Vind (m/s)	induced velocity

W (kg)	mass of the engine
\dot{W} (kg/s)	mass flow
W (kg/s)	mass flow
\dot{w} (kW)	power
\dot{w}' (kW/kg)	specific power
w (m/s)	average flow speed during constant volume combustion
W_b (kg)	burner mass
W_{bld} (-)	percentage of compressor bleed
W_F (kg/s)	fuel flow rate
WF (-)	Weight factor
W_s (kg)	mass of supporting structure
W_t (kg)	mass of the turbine
XR (-)	ratio of burner radius to the radius of the
z (-)	relative spacing between propellers
Subscripts	
0	free-stream velocity
1	station 1 in ARP755 engine station nomenclature
1	station numbering corresponding to the forward propeller
2	station number corresponding to the rear propeller
2	station 2 in ARP755 engine station nomenclature
11	induced velocity impact by the fore propeller on the fore propeller
12	induced velocity of the fore propeller on the aft propeller
12	volumetric compression ratio from station 1 to 2 in the nutating disc core
18	station 18 according to ARP755A
20	station 20 according to ARP755A
21	induced velocity of the aft propeller on the fore propeller
22	induced velocity of the rear propeller on the rear propeller
23	the volumetric compression/expansion ratio in the nutating disc from station 3 to 4
34	the volumetric compression/expansion ratio in the nutating disc from station 2 to 4
01 to 07	station numbering of the nutating disc engine
12A	axial component of the induced velocity of the fore propeller on the rear propeller
12T	tangential component of velocity of the fore propeller on the rear propeller
1shr,rel	relative shroud Mach number
a	inlet mass flow
a	axial
allow	allowable efficiency
amb	ambient
at	atmosphere
aw	wall temperature
b	burner radii of the nutating disc core
b	burner

bu	burner
c	volumetric compression ratio
c	cooled
c	cooling mass flow or temperature
c, int	internal convective effectiveness
carrier	carrier gears of epicyclic gearbox
casing	nutating disc casing volume
centri	centrifugal compressor
centri _{casing}	centrifugal compressor casing
centri _{total}	total centrifugal compressor mass
climb	climb phase of flight
cold or hot	hot or cold side total pressure loss/ enthalpy
combustion	combustion crank angle per shaft revolution
cool	related to cooling mass flows in the HPT rotors
cooling	effectiveness for the heat-exchanger
corr	corrected
corrM	slope of efficiency correction for high helical Mach numbers
Cp	map scale factor corresponding to coefficient of power
cruise	cruise phase of flight
Ct	correction factor imposed on pylon blowing
cy	heat loss factor through the nutating disc casing
disc	disc area
disc	weight or volume of the nutating disc
disc1	compressor disc of dual-disk nutating disc engine core
disc2	expander disc of dual-disk nutating disc engine core
disp	displaced volume
DPGB	corresponds to the heat lost from the air-oil heat exchanger
e	expander
e	exit
e plenum	exit of the plenum
EIS	entry in to service
ext	external
f	fuel flow
f	fuel flow
F	forward propeller
f	film cooling effectiveness
fuel	fuel flow
g	gas path temperature or mass flow
gb	gearbox
h	hub diameter
h	hub
h	hoop
H0.75	helical Mach number at 75% blade span
hub	hub
i	inlet

i	inner radius
I, optimum	stage wise optimum work loading and flow coefficient
i plenum	inlet to the plenum
ii	representation of the propeller designation
il	inlet total pressure loss
im	imaginary component of velocity
intercooler	intercooler mass
isen	isentropic efficiency
J	advance ratio
m	mean position
m, in	mean diameter at the beginning of a turbomachinery component
m, out	mean diameter at the end of a turbomachinery component
map	map values
material	density of the material
max	maximum length of the plenum ducts
me	mechanical
mech	mechanical power off-take
met	metal
mx	maximum value
N	nacelle
ND	nutating disc
ND,max	maximum pressure in ND engine
net	net propeller efficiency
o	outer radius
p	profile losses
pol	polytropic
poly, HPT	polytropic efficiency correction based on HPC last stage blade height
poly,HPC	polytropic efficiency correction based on blade height
propeller	propeller mass
R	rear propeller
r	radial
r	rotor
Re	Reynolds number
ref	reference
rel	relative value of total temperature
ring	ring gear of epicyclic gearbox
rotor,in	mass flow going in to the rotor of the HPT
s	rotational speed in rotations per second
s	real process
s	stator
sc	secondary combustor
scoop	mass flow going in to the scoop
shaft	shaft torque
shr	shroud
st	crank angle corresponding to the start of the combustion process

sun	sun gear of epicyclic gearbox
sw	swept volume
t	tip diameter
t	tip
t	turbine
t,rel	total relative temperature for the turbine rotor
take-off	enf of runwat phase of flight
TBC	thermal barrier coating
th	thermal efficiency
total	total pressure loss
uc	uncooled
Wc	corrected mass flow
wedge	volume of the wedge
X4	station 5 in the air-oil gearbox cooler
X5	station 4 in the air-oil gearbox cooler
Greeks	
Ω (m/s)	blade rotational speed
η (-)	efficiency
ρ (kg/m ³)	density
δ (-)	correction factor or penalty factor
ϵ (-)	convection cooling effectiveness or film cooling effectiveness
Θ_1 (-)	temperature ratio in the nutating disc engine that determines the maximum cycle temperature due to constant volume combustion
Θ_2 (-)	temperature ratio in the nutating disc engine that determines the average cycle temperature after constant pressure combustion
ϕ (deg.)	crank angle per shaft revolution
ψ (deg.)	semi-wedge angle
ω (rad/sec)	rotational speed or frequency
ζ (-)	intercooler effectiveness
σ (Pa)	Stress
α (deg.)	angle of nutation
Θ_i (deg.)	absolute crank angle
$\Delta\theta$ (deg.)	absolute combustion crank angle
Δ (-)	change in variable/ parameter
Ψ (-)	average stage loading/ work coefficient
ϕ (-)	flow coefficient

1 Introduction

The nutating disc (ND) engine (Figure 1-1) is a unique machine since it uses separate chambers for compression, combustion and expansion processes when compared to piston engines, where all the processes take place within the same chamber. Its operation is comparable to that of a gas turbine since the thermodynamic processes are carried out in separate chambers [1]. Another unique feature of the ND engine is its ability to use all the enclosed chambers, to produce work, during a shaft revolution. This design feature lends itself to its power dense nature. Figure 1-1 illustrates the components of a naturally aspirated single disc nutating disc engine. The layout consists of an inlet, compression chamber, accumulator, combustion chamber, expansion chamber and an exhaust manifold [1]. Figure 1-2 shows that air enters the compression chamber through an “elbow-duct”. It is subsequently compressed, by the nutation motion of the disc, and stored in an accumulation chamber after passing through a non-return or solenoid controlled valve. After the air is retained in the accumulation chamber it is accepted in to the combustion chamber through a valve, where it is mixed with fuel and ignited by a spark plug. Constant volume combustion occurs in the combustion chamber followed by constant pressure combustion through a portion of the expansion chamber – primarily due to inadequate residence time in the combustion chamber. Finally, the combusted gases expand through the rest of the expansion chamber and exit through exhaust valves housed in the exhaust manifold. Alternatively, the combusted gases can be exhausted via a port located adjacent to the inlet port. The subsequent excess power is transmitted by a z-shaft, which converts the nutating motion of the disc in to a rotating motion when the z-shaft is coupled to a concentric shaft.

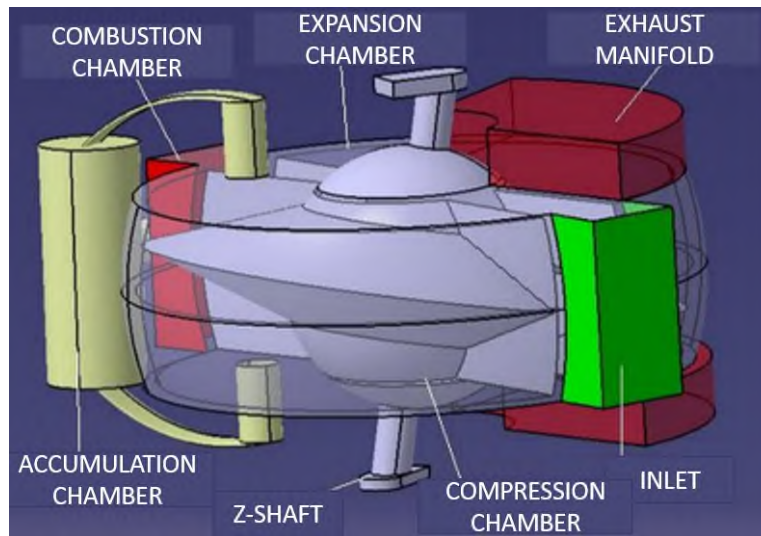


Figure 1- 1: components of a single disc ND engine configuration.

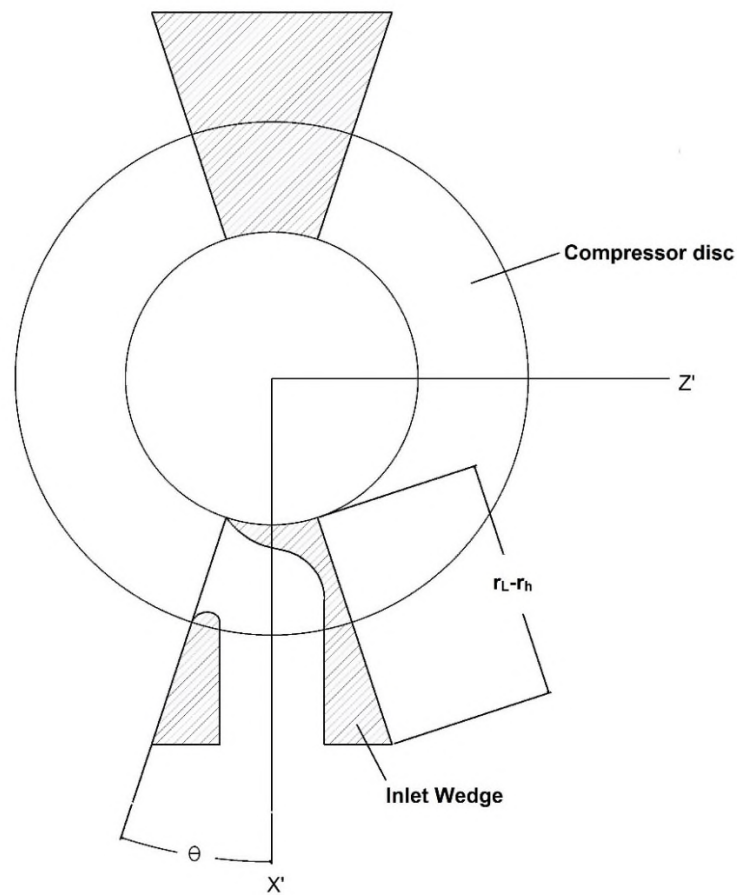


Figure 1-2: Top-down view of a ND engine showing the inlet 'elbow' duct

The aforementioned processes are applicable to both a single-disc nutating engine configuration and a multi-disc nutating engine configuration. Figure 1-3 [2] indicates that both the compression and expansion processes can take place in a single-disc arrangement, where it is assumed that the single nutating disc engines are split about the red axis. The main issue that arises with this configuration is that the nutating disc structure is subject to uneven thermal loading during operation – which is likely to reduce life when considered in conjunction with high load operation. To alleviate the inherent issue a two-disc arrangement can be considered, as shown in Figure 1-3. In this case separate discs are dedicated to compression and expansion processes, and the discs consequently have more symmetrical thermal loading. Details with regards to its operation are highlighted in the methodology chapter. It must be re-iterated that the intake and expansion processes can be either governed through a port or a valve mechanism. Figure 1-1 shows a single ND engine with a ported inlet and a valved exhaust. For the ND engine considered within the context of this work, both the inlet and exhaust are assumed to be ported. This is done primarily because the inclusion of further valves increases the part count and hence can potentially reduce the

potential availability. Therefore, in terms of the defining features of the ND engine considered, the ND-engine shall have 2-discs with ported intakes and exhausts as shown in Figure 1-3.

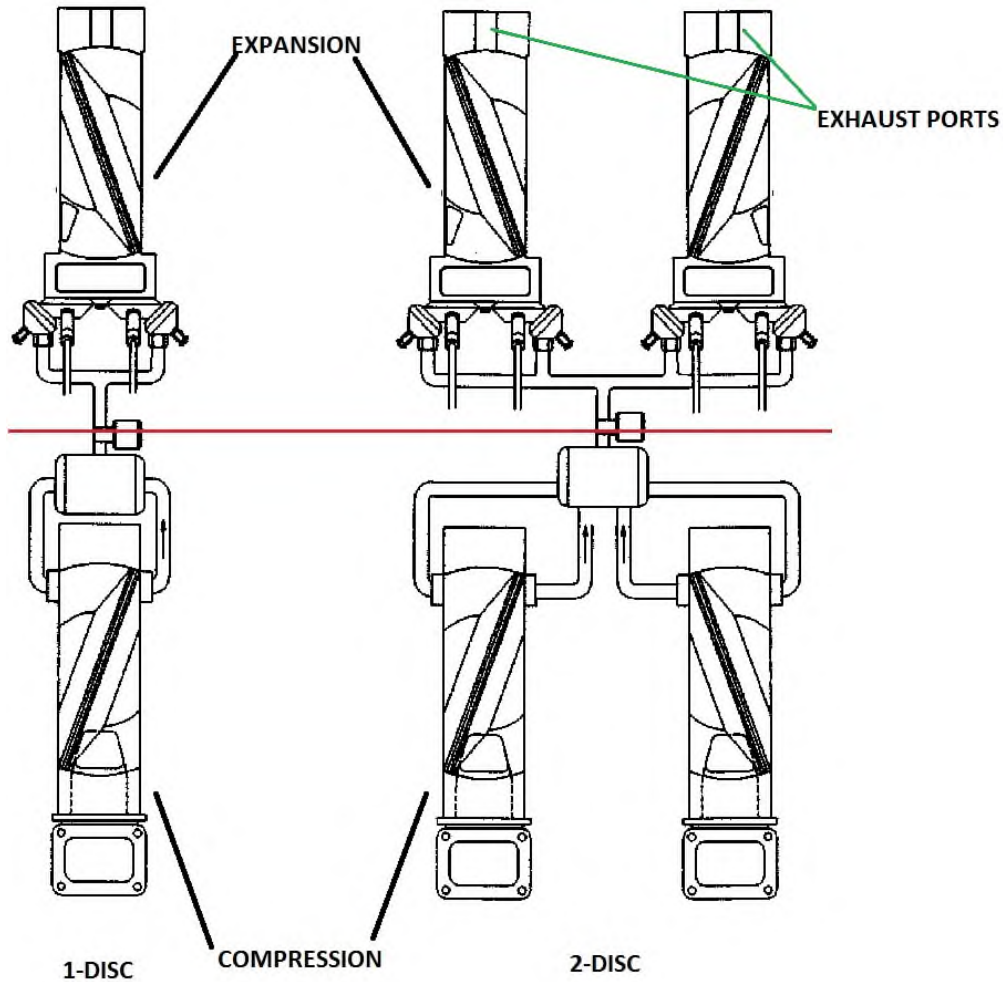


Figure 1- 3: Butterflied view and components of a single and dual disc ND engine[2]

One of the aims of this thesis is to determine the performance benefits derived from integrating the nutating disc within the architecture of an aero-gas turbine. In order to do so, improvements to the state of the art performance and sizing methodologies of the nutating disc engine need to be developed. The following sub-section provides a narrative as to what the necessity is for incorporating a nutating disc engine within the architecture of an aero gas turbine. Henceforth, the nutating disc engine in either a naturally aspirated or turbo-compounded configuration will either be referred to as nutating disc system (ND system) or a nutating disc engine system (ND engine system).

1.1 Research context

Demand in the aviation sector is projected to grow at an annual rate of 4.1% within the next 20 years [3]. These projections coupled with ever sensitive emission legislations call for action within the civil aviation sector for severely reducing green-house gases by 2050 [4]. The time intensive nature of innovation within the sector, primarily due to tight certification legislation and the inherent capital intensive nature, a concept can take roughly 15 years from the design phase to entry in to service [5]. In order to address these issues, the Advisory council for aviation research in Europe (ACARE) have issued a strategic research and innovation agenda (SRIA) and their goals can be summarized by the following challenges [5]:

- SRIA Challenge 1: Meeting market and societal needs.
- SRIA Challenge 2: Maintaining and extending industrial leadership
- SRIA Challenge 3: Protecting the environment and energy supply
- SRIA Challenge 4: Ensuring safety and security
- SRIA Challenge 5: Prioritizing research, testing capabilities and education

Out of the aforementioned SRIA challenges, the third challenge includes the necessity of reducing energy consumption by 75% by the year 2050 from year 2000 baseline energy consumption levels, in the civil aviation sector. In addition, the third SRIA target calls for significant reduction in NO_x and noise production levels by the year 2050 when compared to a year 2000 baseline [5].

In order to reach these high targets, it is necessary for all the key stakeholders within the aviation industry to strive for minimizing fuel consumption (which coincides with energy consumption) in the operation of civil aircraft. The reduction of fuel burn can be brought about by developing more efficient propulsion units, low-drag fuselage structures and optimizing flightpaths and ground operations by using efficient flight planning techniques. Historically, within the aero-gas turbine industry, energy consumption reduction has been implemented by increasing operating pressure ratios (OPRs), turbine entry temperatures (TETs), turbomachinery component efficiencies and material improvements. Similarly, it is postulated that aircraft manufacturers aim to reduce the drag count of standard tube-wing aircrafts by improvements in aerodynamics and a reduction in empty structural mass of the fuselage via the implementation of composite structures [6,7]. Fuel burn reductions have also been addressed by strategic flight planning, which is achieved by minimizing the difference

between the distance proposed in flight plans and the actual flown trajectories of the aircraft [8].

Based on projections of historic rates of fuel burn reduction, which coincides with reduced energy consumption, it can be postulated that the aviation sector would not be able to meet the 75% energy consumption reduction by the year 2050[7]. Hence, a step decrease in fuel burn is required to meet the stringent year 2050 targets. Figure 1-4 provides an initial outlook in to the projected increase in air traffic demand growth and the subsequent relative impact that would have on potential energy consumption and CO₂ emissions by year 2050 (highlighted by dashed line) [7]. Consequently it is surmised that a significant reduction of energy consumption is required to reach the benchmark set by the third SRIA challenge [9]. Prior to determining why the nutating disc engine was chosen to address the SRIA 2050 fuel burn target, an overall perspective should be provided for the potential magnitude of fuel burn savings stemming from flight path optimization, aircraft improvements and engine improvements respectively. According to Jensen et al., optimization of flight paths and speeds lead to potential fuel burn reductions of 1.75% to 1.96% for short haul missions [10]. The work conducted by Nickol et al. indicates that the potential fuel burn benefits for advanced tube and wing aircraft concepts, by introducing technologies that reduce drag and mass, amounts to roughly 20% for short haul missions [11]. From the work conducted by Nickol et al., it can be seen that the advances in engine technology could potentially amount to roughly 19% in fuel burn savings [11]. It can be inferred that the relative magnitude of fuel burn savings imparted by the engine alone is significant when compared to the potential fuel burn benefits that stem from flight path optimization and aircraft technology improvements [11].

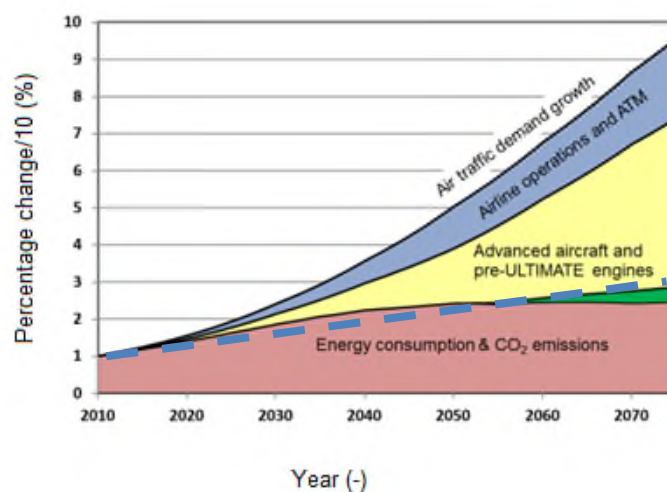


Figure 1- 4: Projected increase in CO₂ emissions by year 2050[7]

This primary aspect of the third SRIA target that this work will address is the potential of reducing energy consumption by 75% by the year 2050, compared to a year 2000 baseline. As mentioned previously, the reduction of energy consumption for the commercial aviation sector can be brought about by improvements in flight path planning, improvements in airframe design and propulsion unit design. Improvements of flight path planning is considered out of the scope of this work. If one excludes the contribution of potential flight planning optimisation in relation to the 75% fuel burn reduction target, the fuel burn reduction target can be reduced to 68% by the year 2050 [7]. Therefore, improvements to the architecture of a standard civil high bypass ratio engine, when installed on a year 2050 tube and wing airframe, in meeting the 68% fuel burn target is the goal of this work. Improvements in the architecture of an aero-gas turbine can involve the following:

- The usage of new high temperature materials that facilitate higher OPR's and TET's in an aero-engine that combust Jet-A fuel. The limitations of the standard Brayton cycle can be further improved by combining cycles, as shown in Figure 1-6.
- The usage of new materials in conjunction with different fuels such as Hydrogen and Methane. In theory, due to their higher lower heating value more efficient aero-engines can be conceived.
- Usage of turbo-distributed electric propulsion systems to reduce potential energy consumption.

This work aims to address the fuel burn reduction target of 68% by considering how a combined aero-cycle combusting Jet-A fuel would perform in doing so.

The overall efficiency of a gas turbine efficiency is the product of its propulsive efficiency and thermal efficiency. The large civil aero-gas turbine industry have historically improved the propulsive efficiency by increasing the bypass ratio and reducing the fan pressure ratios of high bypass ratio turbofans. This in turn, leads to low specific thrust engines, bypass exhaust jet velocities and specific fuel consumption.

However, the increase in bypass ratios lead to increased nacelle mass, increased low pressure turbine (LPT) component mass and increased drag due to an increase in frontal area. These effects eventually undermine the fuel burn benefits derived from propulsive efficiency gains. In order to circumvent an increase in LPT mass, when the bypass-ratio increases, an epicyclic gear train is introduced between the LPT and the fan [12].

This ensures that the LPT and fan can operate at its optimal rotational speed and the stage count of the LPT does not become unrealistically high. The purported fuel burn benefits, by

introducing an epicyclic gearbox between the LPT and fan, are in the order of double digit fuel burn benefits for short range missions[12,13].

In order to further capitalize on the propulsive efficiency benefits of increasing the bypass ratio and decreasing fan pressure ratios, without being subject to the associated mass and drag penalties, it is beneficial to eliminate the nacelle altogether. Figure 1-5 shows how a possible engine architecture can vary as function of the fan pressure ratio and the bypass ratio.

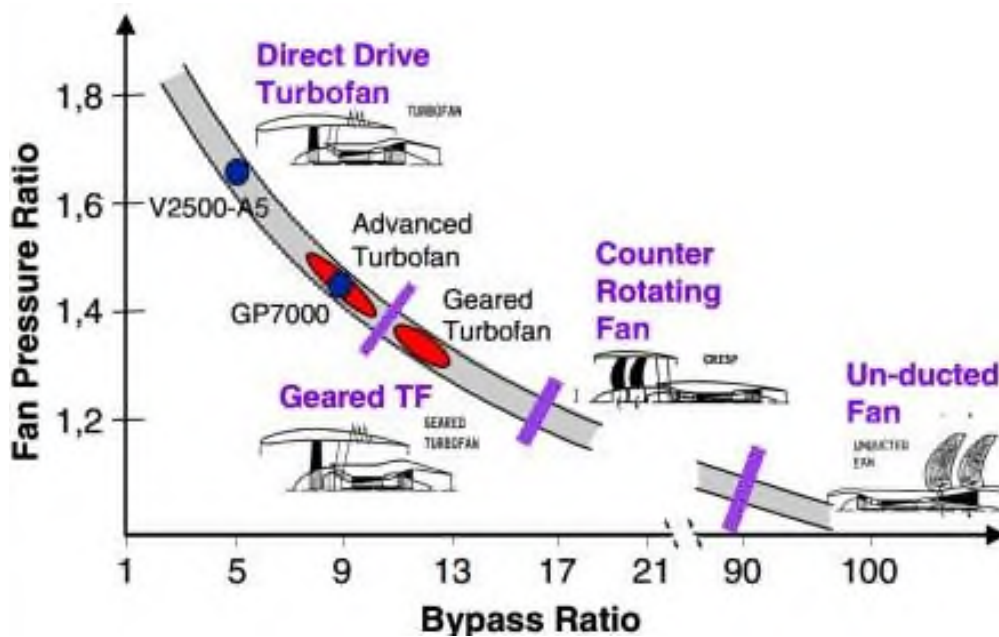


Figure 1- 5: Evolution of engine configurations as a function of the fan pressure ratio and bypass ratio[13,14]

Based on the projections seen in Figure 1-5, it seems that an un-ducted low pressure propulsor seems ideal in terms of achieving ultra-high bypass ratios. The un-ducted turbo fan has two versions a contra rotating open rotor (CROR) and a single rotating open rotor (SROR).

Although the CROR indicates a relatively decreased propulsive efficiency than the SROR [15], the CROR is the preferred configuration as it is able to produce relatively the same levels of propulsive efficiencies of a SROR at reduced propeller diameters. The CROR manages to do so because of its ability to recover the swirl produced by the forward propeller. Due to the relative propulsive efficiency to propeller span benefits of the CROR compared to SROR, the CROR is the preferred engine configuration for un-ducted turbofans.

Contra rotating open rotor engines occur in either a 'puller' or 'pusher' configuration. In the architecture of a 'puller' engine configuration the contra rotating propeller array is located fore of the engine. In the architecture of a 'pusher' engine configuration, the contra rotating propeller array is located at the aft of the engine. Generally, a pusher configuration is preferred based on engine mass and potential cabin noise considerations [16,17]. The 'pusher' configuration can be further divided in to a geared open rotor (GOR) engine concept and a direct drive open rotor (DDOR) concept. The architecture of the LP-system of a DDOR engine concept, involves having a contra rotating turbine powering a contra rotating propeller array. Conversely, in a GOR engine configuration a power turbine powers a contra rotating propeller array via an epicyclical gearbox.

The GOR configuration is preferred over the DDOR because of the relatively more stable operation of the power turbine components and relatively lower levels of complexity [16,17]. The geared open rotor, according to Larsson et al., has apparent fuel burn benefits of 15% compared to a geared turbofan for a comparable short range mission[18]. Hence, it seems that most likely engine configuration, to increase propulsive efficiency, to enter service in the year 2050 is the geared open rotor (GOR). Therefore, this technology enabler is earmarked to be used in the architecture of the final proposed engine that addresses the 68% fuel burn reduction target.

In order to improve the overall efficiency of a gas turbine, besides investigating technologies that improve propulsive efficiency, it is necessary to investigate technologies that improve the thermal efficiency of an aero gas-turbine. In order to increase the thermal efficiency of the gas turbine, manufacturers have historically increased the turbine entry temperatures (TET), overall pressure ratios (OPR) and component efficiencies of high bypass ratio turbofans. Theoretically, the thermal efficiency increase brought about by increasing the component efficiencies, OPR and TET allows the cycle to operate in a region where the overall specific enthalpy to specific entropy generation ratio is relatively high.

However, attaining higher thermal efficiencies by increasing the TETs are reaching their limit as they are limited by material operational temperatures of the high pressure turbine and the adiabatic flame temperature of kerosene – the flame temperature is further curtailed by NO_x legislation. Similarly, increasing OPRs lead to smaller blade spans within the last stages of the HPC-this eventually leads to a reduced high pressure compressor component efficiency due to over tip leakage effects.

Therefore a step change from the current trend of increasing TETs and OPRs is required in order to surpass the inherent plateau of thermal efficiency. This means that it is necessary

to re-assess the fundamentals of the Brayton cycle and investigate technologies that can substantiate potential variants of the Brayton cycle. Figure 1-6, highlights five possible variants of the Brayton cycle, which are:

- Intercooled cycle
- Reheated cycle
- Recuperated cycle
- Bottoming cycle
- Otto cycle

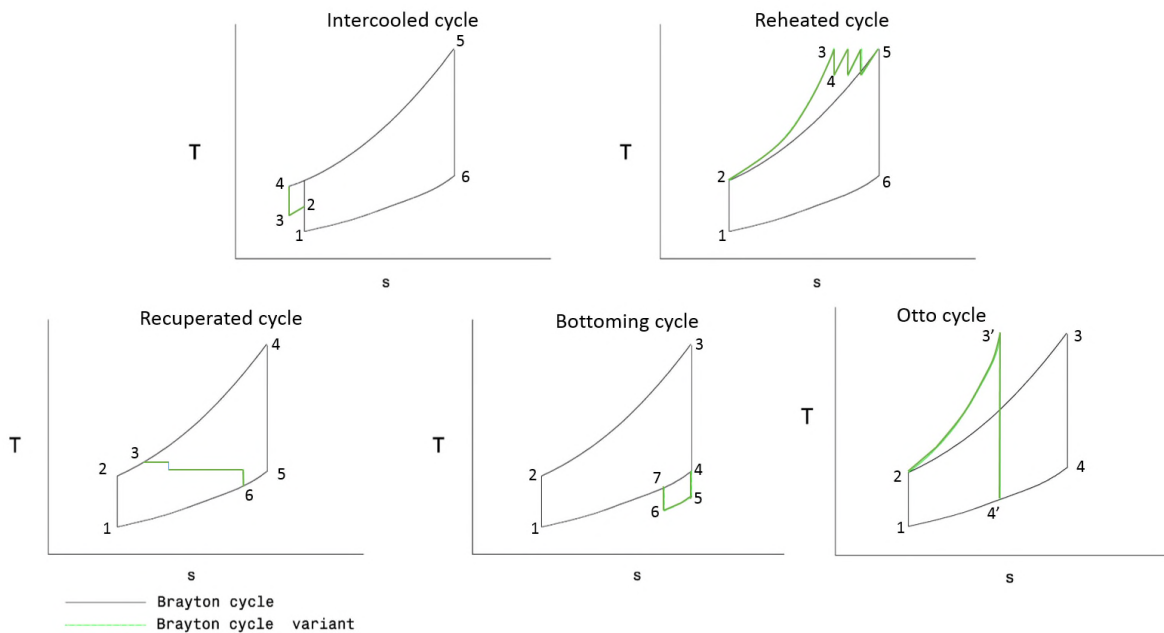


Figure 1- 6: Overview of potential Brayton-cycle variants

Intercooled cycles are advantageous because they lower compressor delivery temperature , before combustion. Thus, this can allow the cycle to increase OPRs and consequently increase the thermal efficiency of the cycle. A second order effect on performance is that lower compressor delivery temperatures lead to relatively lesser amount of core mass flow that needs to be bled-off to cool the HPT components. Practically, on turbofans intercooling can be achieved by using the bypass flow to cool pre-compressed air via a tubular heat exchanger stack[19,20].

Thermodynamically, the intercooled cycle is relatively more efficient than a standard Brayton cycle. If an intercooled cycle and Brayton cycle are considered with similar compressor delivery and combustor outlet temperatures (Figure 1-7) it can be seen that combustor outlet temperature in the intercooled cycle can be achieved at a relatively higher pressure and with

relatively less specific entropy generation. In addition, for a fixed turbine exit pressure it is seen that the exhaust gas temperature would be relatively reduced.

The larger area enclosed by the intercooled cycle relative to the Brayton cycle, in the T-s diagram, is indicative of more useful work derived from the cycle at relatively lower levels of specific entropy generation.

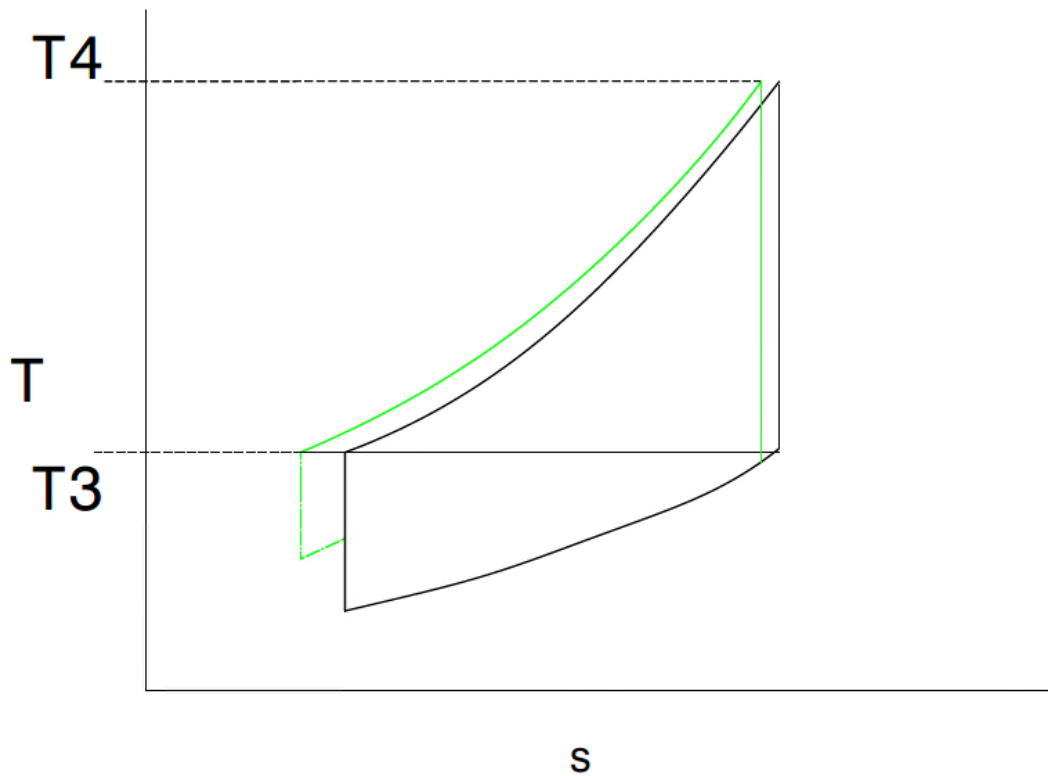


Figure 1- 7: T-s diagram for intercooled and Brayton cycle at similar T3 and T4 levels

Reheated-Brayton cycles also bear potential to overcome the thermal efficiency plateau of the Brayton cycle within a gas turbine engine. One of the primary benefits of re-heated cycles is the possibility to increase the specific power of a turbofan core. A secondary effect entails being able to reduce the peak cycle temperature, and hence reduced flame temperatures and potential reductions in NO_x emissions at end of runway conditions.

Practically, reheat can be achieved by introducing an additional combustion chamber between turbine components or in between turbine stages, similar to the arrangement of the GT-24/26 stationary gas-turbine[21]. The area encompassed by the reheated cycle is greater

than that of a comparable Brayton cycle, therefore more useful work can be derived from the cycle.

Figure 1-8, shows the characteristics of a reheated cycle in comparison to a standard Brayton cycle at similar compressor discharge temperatures and primary combustor discharge temperatures. It is seen that the introduction of reheat technologies allow for more area encompassed by the re-heat cycle, however at relatively higher specific entropy generation than a comparable Brayton cycle. One disadvantage of the reheat configuration is that potential exhaust gas temperature at a fixed exhaust pressure would be higher than that of a standard Brayton cycle.

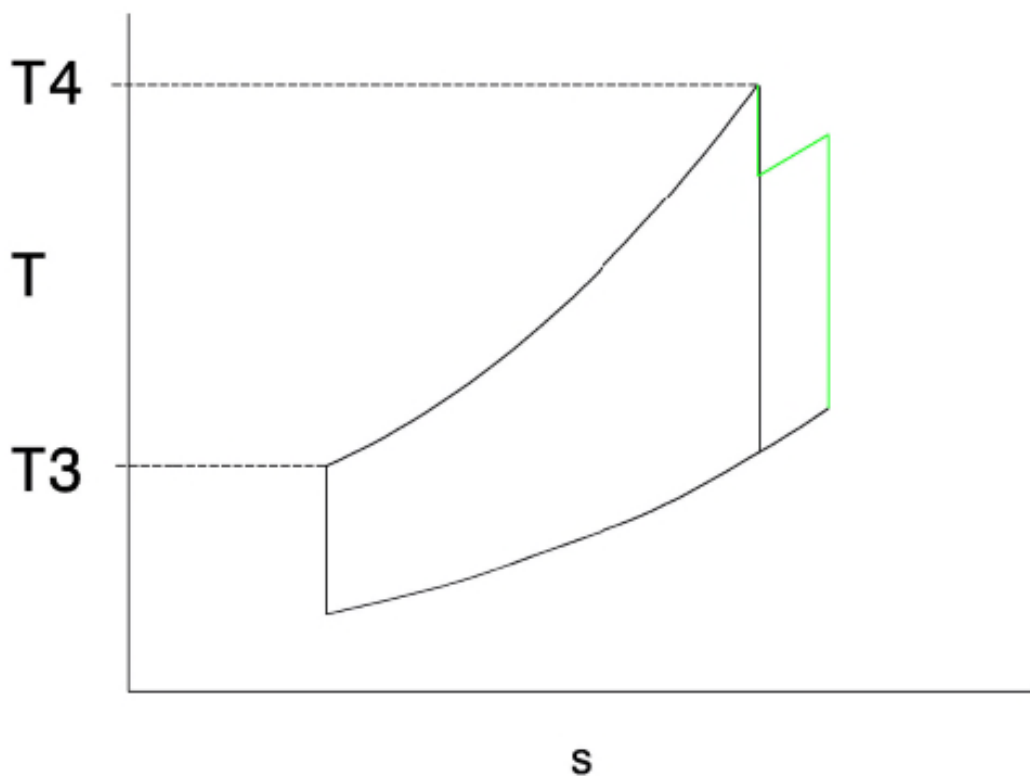


Figure 1- 8: T-s diagram for re-heated and Brayton cycle at similar T3 and T4 levels

Similar to intercooled and reheated cycles, a recuperated cycle also offers thermal efficiency benefits relative to a standard Brayton cycle. The primary benefit is decreased TSFC due to the increment in compressor delivery temperature and the secondary benefit is a decreased exhaust gas temperature.

In practice, heat from the core exhaust gas is rejected to the compressor delivery flow via air-air heat exchanger tube-stacks [22]. As a result of raising the compressor delivery

temperature, the amount of work that has to be added to the cycle to raise the temperature to a similar combustor discharge temperature is lesser, hence it is relatively more efficient than the standard Brayton cycle. Figure 1-9, depicts the benefit of recuperation relative to standard Brayton cycle.

Although recuperated cycles seem like an attractive technology, it does not seem suitable for a 2050 timeframe. Primarily, as OPRs continue to increase the driving temperature difference between the compressor delivery temperatures and exhaust gas temperature will reduce, hence the thermal efficiency benefits offered by recuperation diminishes [23]. In addition, as the combustor delivery temperature increases the relative NO_x emissions produced by the recuperated cycle relative to a standard Brayton cycle should be higher[24]. Thus, recuperated cycles are considered to be less practical feasible in the 2050 time frame, in terms of achieving the 68% fuel burn target.

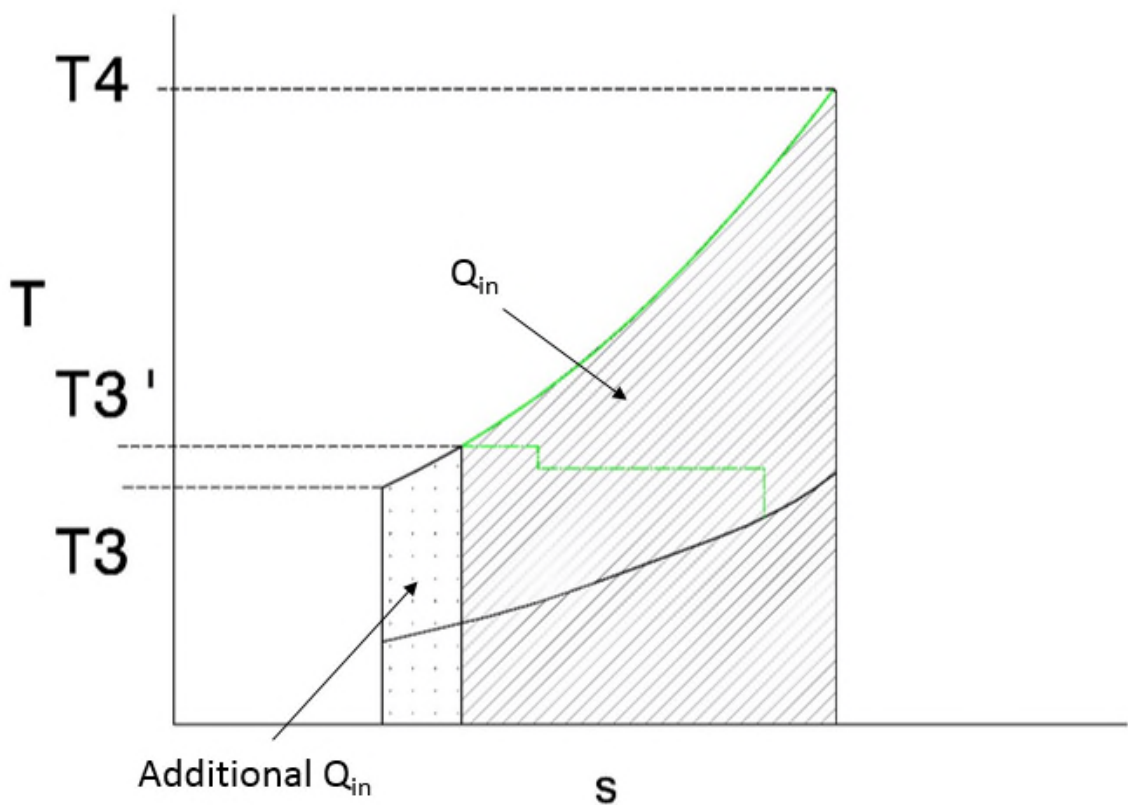


Figure 1- 9: T-s diagram for recuperated cycle and Brayton cycle at similar T4 levels

Bottoming cycles provide an attractive alternative to the standard Brayton cycle, as it utilizes the exhaust heat to produce additional useful power to the cycle. Hypothetically, this can be

achieved by placing a stack of tubular heat-exchangers in the core exhaust stream of a high bypass civil turbofan, where the core exhaust heat is rejected to either super-critical CO₂ or an organic fluid. Consequently, the working fluid in the bottoming cycle is expanded through to a turbine stage which powers a compressor to pump the working fluid through other components in a closed circuit cycle and produce shaft work [25].

This shaft work can then be mechanically or electrically re-introduced in to the cycle. Thermodynamically, the area enclosed by the bottoming-cycle, in Figure 1-10, is higher than a comparable Brayton cycle. Thus, more useful work can be obtained from the combined cycle at comparable levels of entropy generation.

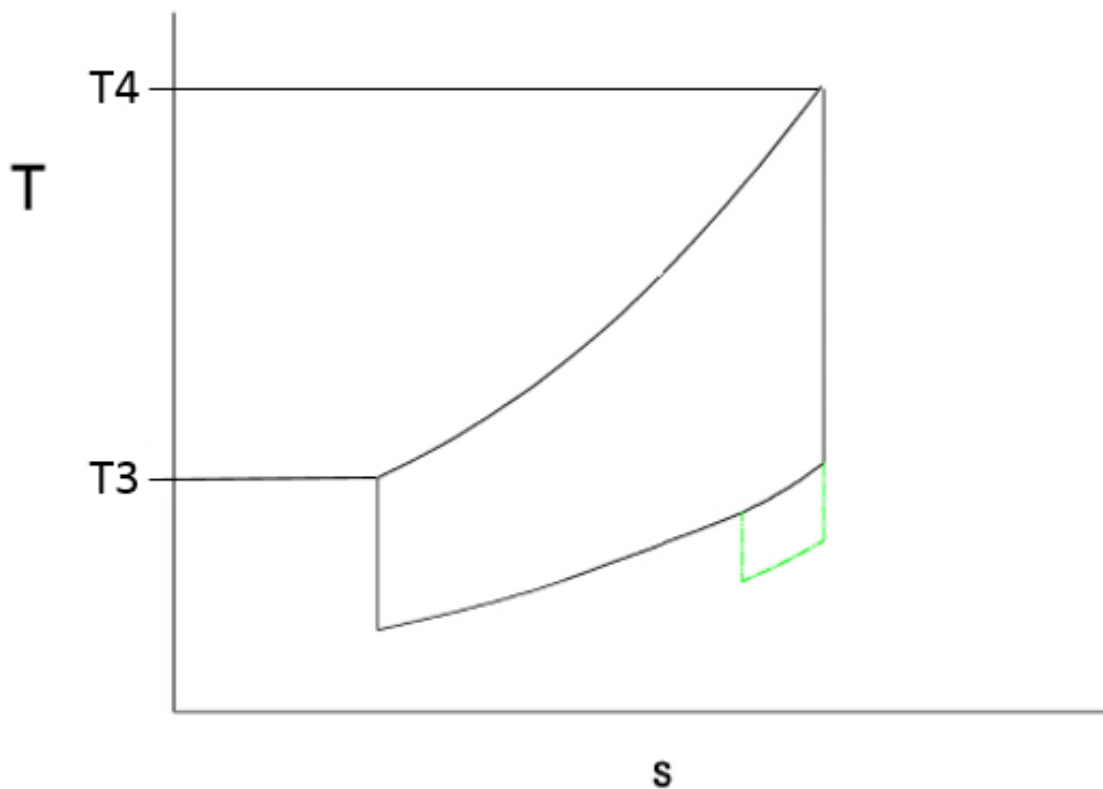


Figure 1- 10: Comparative T-s diagram for a bottoming cycle and Brayton cycle

Currently, the combustion process across a standard annular combustion chamber, in aero-engines, includes a total pressure drop- this characteristic partially attributes to 'combustor' losses and hence the loss of thermal efficiency percentage points. Since, thermodynamically, current combustion processes have been described as constant pressure (isobaric) processes it would seem beneficial to move towards a constant volume combustion process (isochoric).

Figure 1-11 shows the thermodynamic benefit derived from an isochoric combustion process, when compared to an isobaric combustion process, in terms of the specific entropy generated for a fixed combustion temperature[26]. The benefit of an ideal adiabatic isochoric process stems from the 1st law of thermodynamics, where the heat added to a control volume is purely used to increase the system's internal energy. Whereas, in an adiabatic isobaric combustion process the heat added is used to increase the system's internal energy as well as expand the flow-such that the isobaric nature of the process is maintained. Practically, the benefits of the isochoric combustion process can be seen when comparing the overall efficiency of an internal combustion engine (+45%) versus a standard heavy duty land based gas turbine (37-40%) [27]. However, in practice the high overall efficiency benefit is offset (in terms of fuel burn) at higher power outputs due to the quadratic scaling of the mass of conventional internal combustion engine architectures.

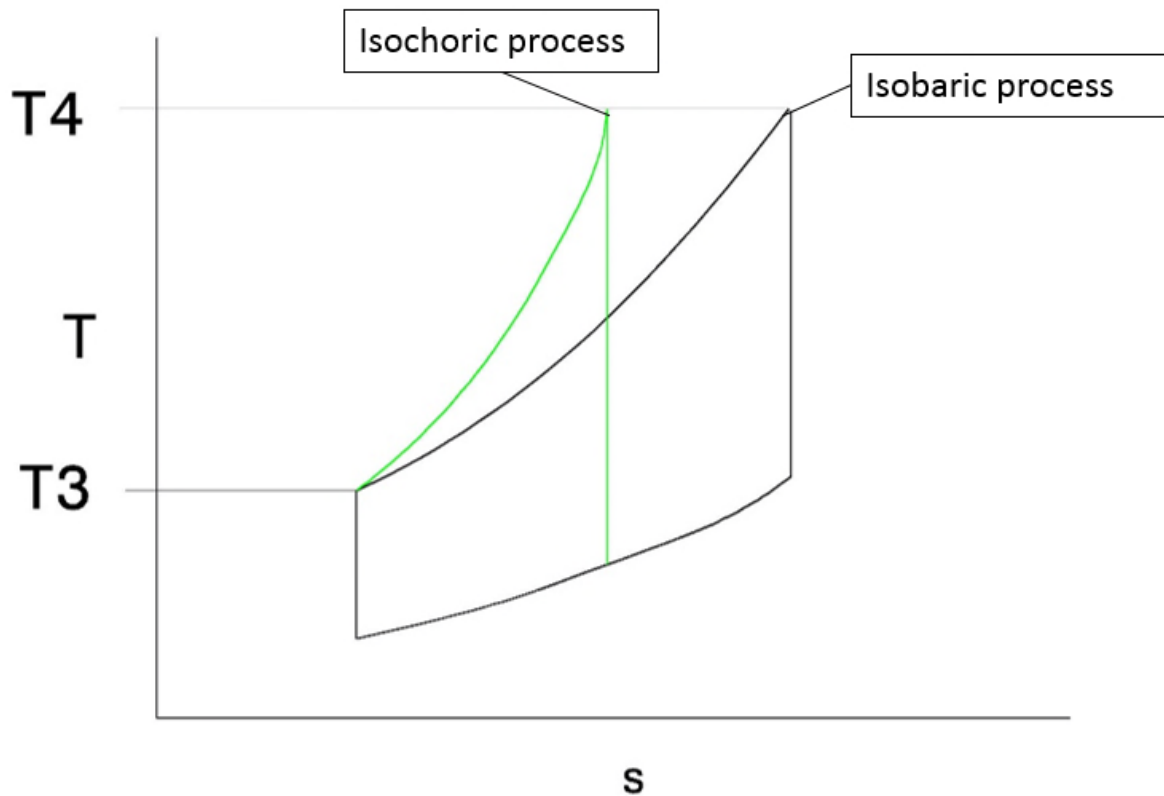


Figure 1- 11: Comparative T-s diagram for an Otto cycle and Brayton cycle

Thus far the potential benefits of the cycle variants were qualitatively investigated considering isentropic processes. If the real processes of a Brayton cycle are considered, as shown in Figure 1-12, it is possible to garner an understanding of the relative scale of heat transferred to a control volume, for the primary processes in a gas-turbine.

The scale of heat transferred to a control volume for the combustion process, represented by the area under the curve, shows the relative scale of the process in comparison to the other processes in a standard Brayton cycle.

Therefore, in order to significantly improve the thermal efficiency of the core of the gas turbine it is essential to improve the efficiency of the combustion process first, prior to addressing improvements in the compressor, turbine and reduction of exhaust gas temperature.

In order to distinguish between the Brayton cycle variants, suggested in Figure 1-6, that affect the combustor work one must consider qualitatively ranking the cycles with regards to their heat generation to specific entropy generation ratio.

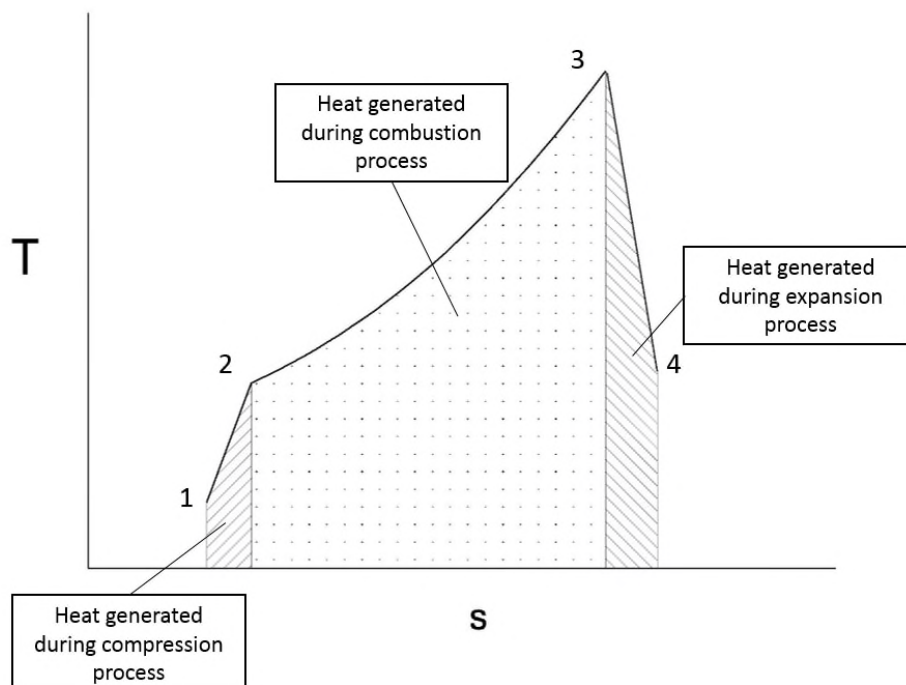


Figure 1- 12: Real processes in a Brayton cycle

Using the relative work to specific entropy generation metric criterion qualitatively, the cycle with a relatively more positive impact on the combustor work would be an Otto-cycle followed closely by the reheat cycle and the intercooled cycle. A recuperated cycle will also directly impact the combustor work, however in the 2050 timeframe they are deemed to be infeasible due to its reduced driving temperature difference as a result of perceived increased OPRs. The bottoming cycle does not directly contribute to the combustor work therefore the thermodynamic benefits of the bottoming cycle have not been investigated within the scope of this work.

One of the objectives of this research is addressing the 68% fuel burn reduction target by considering the incorporation a technology enabler, based on the Otto-cycle, within the architecture of the core turbomachinery of an ultra-high bypass engine. In order, to increase the thermal efficiency of year 2050 engine cores. The incorporation of Brayton cycle additions are complemented by the inclusion of propulsive efficiency technology enablers, in meeting the 68% fuel burn reduction target.

The primary technology enabler that is chosen to bolster thermal efficiency is the nutating disc engine, as mentioned in the beginning of the chapter. The primary technology enabler to bolster the propulsive efficiency of an aero-engine is the geared open rotor (GOR) low pressure propulsive system. The potential performance and feasibility of a turbo-compounded ND core with a GOR is assessed both quantitatively and qualitatively, with regards to the third SRIA challenge and 68% fuel burn target.

The feasibility of the inclusion of a nutating disc engine within the architecture of an aero-engine, having a GOR low pressure propulsive system, is augmented by investigations that quantify and qualify the additional benefits derived from incorporating complementing technology enablers that utilize intercooled cycles and re-heat cycles respectively.

This is considered a necessary addition, to the primary research aim, in order to quantify and qualify which combination(s) of the top three Brayton-cycle variants would meet the third SRIA objective. Therefore, the fundamental aims and objectives of this research is highlighted in the following sub-section.

1.2 Research Aims and Objectives

The aims and objectives of this research are:

- Assess the feasibility of a geared open rotor engine in achieving the 68% fuel burn reduction target. Achieving this objective involves:
 - Establishing a comparable year 2000 engine model, in order to derive baseline engine technology levels and baseline fuel burn values for a fixed mission range.
 - Establishing a comparable year 2050 GOR engine model, in order to derive reference 2050 engine technology levels and fuel burn values for a fixed mission range and trajectory. This will enable a comparison of the fuel burn reduction stemming from the incorporation of the inclusion of GOR propulsive system.

- Assess the feasibility of a geared open rotor engine with a nutating –disc engine core in achieving the 68% fuel burn reduction target. Achieving this objective involves:
 - Synthesizing a potential general arrangement layout, for the incorporation of a nutating disc engine core within a geared open rotor engine
 - Development of a performance and sizing model of the nutating disc engine. A sizing model will dictate the performance of the nutating disc core as well as provide an estimate for the compounded engine mass.
 - Development of a model that sizes the manifolds/ducts that couple discontinuous flow devices to continuous flow devices.
 - Perform a sensitivity study to highlight the potential uncertainty involved in quantifying the relative fuel burn benefits.

- Assess the feasibility of a geared open rotor engine with an intercooled-reheated nutating disc engine core in achieving a 68% fuel burn reduction target. Achieving this target involves:
 - Synthesizing a potential general arrangement layout for the incorporation of an intercooled nutating disc engine core within a geared open rotor engine, a re-heated nutating disc engine core and an intercooled-reheated-nutating disc engine core.
 - Incorporation of performance and sizing methodologies for intercooling and secondary combustion technologies, in defining the models of the proposed engine configurations.
 - Perform a sensitivity study to highlight the potential uncertainty involved in quantifying the relative fuel burn benefits.

- Quantitatively and qualitatively compare and down-select the most feasible of proposed engine configurations, in terms of meeting the entirety of the Third SRIA challenge, from an engine development perspective. This involves:
 - Performing a like for like comparison between the four engine configurations in terms of relative fuel burn, compressor delivery temperature and peak cycle temperature.
 - Qualitatively assess which engine configuration, would be most likely in terms of escalating it from a low TRL level to a production level.

- Provision of a roadmap to escalate the development of the primary technology enabler of the most feasible down-selected engine configuration, past state of the art. This involves:

- Providing potential theoretical experimental and computational methods/setup, in order to further knowledge in the field.

1.3 Thesis structure

The thesis is separated in to seven distinct chapters. The introduction chapter, as the name implies, introduces the concept of the nutating disc engine, what is the significance of this research, what potential variations to the Brayton cycle best suit meeting the 68% fuel burn target by the year 2050 and the aims and objectives of this research.

The second chapter, literature review, highlights the chronological work done to date with regards to maturing of the geared open rotor, nutating disc engine, intercooling and reheat technologies. In addition, a brief overview of the modelling methods available in literature are provided with regards to the performance and mass estimation of the aforementioned technology enablers. Finally, relevant gaps in literature are presented with regards to each technology enabler.

The third chapter, amalgamates the research outline presented in the introduction section with the discovered gaps in literature and presents the stated contributions to knowledge.

The fourth chapter details the methodologies used to model the geared open rotor, ND-engine, intercooler, secondary combustion unit and the fuel burn assessment module.

The fifth chapter, portrays the performance of the baseline year 2000 engine and reference 2050 engine configurations in the first instance. Subsequently, the verification and application of the ND-engine sizing model is presented. After which an overview of the investigated engine configurations are presented, which outperform the reference engine configuration, as well as their associated design sensitivities. Finally, a comparative overview of the engine configurations are then presented.

The sixth chapter, draws conclusions on the performed analyses in accordance with the stated research objectives.

Chapter seven, details what future work has to be done in order to progress past state of the art. Primarily, a detailed roadmap is provided to further research with regards to the ND-engine. Finally, a detailed road map is provided to address the development of research with regards to the additional technology enablers as well as potential future assessment platforms.

2 Literature Review

The chapter initially provides an overview of the engine configurations that are representative of an engine for a short range aircraft by the year 2000. In addition, an overview of the methods used to model the performance and mass of the year 2000 engine configuration are provided. Henceforth, this configuration is referred to as the 'baseline year 2000 engine'.

A brief chronological overview of the development of the potential engine configuration for a 2050 reference geared open rotor are provided, which is henceforth referred to as the 'reference 2050 short range engine'. An overview of the performance and mass estimation methodologies for low pressure turbine, differential planetary gearbox and the contra rotating propeller array of the reference 2050 short range engine are then provided, coupled with highlighting gaps in literature.

Then a chronological overview of the development of the primary technology enabler that will improve thermal efficiency, the ND system, is provided. Methods to predict the performance of the ND system are subsequently provided as well as the observed gaps in literature. Subsequently, a similar approach is used to encapsulate the work to date with regards to intercooling and reheat technologies.

The reasons why an engine configuration for short haul aircrafts are chosen, as opposed to a long-haul aircrafts, to investigate rotating disc systems and geared open rotor propulsion engine configurations are highlighted in section 2.3.

2.1 Year 2000 baseline short-range engine

The thrust class of the baseline year 2000 short-range engine is determined by the thrust demands of the aircraft it is installed on. The baseline aircraft, for short-range missions, was based on an A320 type aircraft. The baseline aircraft specification and performance was provided by the ULTIMATE project[7]. The short range baseline aircraft was designed in the Pacelab aircraft preliminary design environment, which incorporates the semi-empirical preliminary sizing methodologies outline by Raymer and Torenbeek [7]. The specifications of the baseline short-range aircraft were modelled based on the freely available CeRAS A320 models, published by RWTH Aachen [7].

In terms of the baseline short-range powerplants, two of the most prevalent engine options available to an A320 aircraft in the Y2000 timeframe was the CFM56-5b engine and the IAE V2500 power-plant [28]. The engine option that is chosen to be modelled is the CFM56-5b engine option, as it has been historically used as a baseline short range engine for engine

concept exploration in projects such as VITAL, NEWAC and LEMCOTEC [29–31]. The general arrangement of the CFM56-5B engine, consists of a single stage fan, three stage booster, nine stage high pressure compressor, single annular combustor, one stage high pressure turbine and a four stage low pressure turbine[28].

When the OD performance modelling of the baseline Y2000 engine is considered, there is good confluence in the methods used to predict the design point performance of the engine[32,33]. The off-design performance, at a OD fidelity of performance modelling, is determined using scaled component maps in either a beta type or MFT format [15,34]. As a result of established modelling practices there are a handful of commercially available software, that allow for robust modelling of the baseline engine performance model and other engine configurations investigated within the scope of this study. Table 2-1, provides a comparative-qualitative overview of the commercially available software used to model the performance of gas turbines, in the authors opinion.

Table 2- 1: Overview of gas turbine performance prediction software

<u>Gas turbine performance modelling software</u>	<u>gas turbine component library depth</u>	<u>Flexibility</u>	<u>Zooming capability</u>
Gasturb	high	low	low
NPSS	high	high	high
Turbomach	medium	medium	low
PROOSIS	high	high	high

Gasturb is a gas turbine performance estimation tool developed by Joachim Kurzke [35] and has a series of pre-set engine cycles to choose from, hence a score of ‘high’ is adjudicated to the software. Despite having a fair amount of pre-set engine cycles to choose from it is not possible to create custom modules (as is needed in this study) therefore it is not flexible when exploring novel cycles and does not provide a platform to carry out zooming studies, as per the authors opinion. NPSS is an object-oriented gas turbine software, developed by NASA, which allows for the development of complex cycles and a high degree of zooming exercises[36]. Turbomach, is a gas turbine performance software developed by Cranfield University and has been historically been used to estimate the performance of a host of engines [37]. However, zooming exercises may prove to be difficult on this platform, as per the author’s opinion. PROOSIS is a gas-turbine performance software developed by

Empresarios Agrupados that has an architecture similar to that of NPSS and consequently allows for development of complex cycles and zooming exercises[15].

Based on the qualitative judgements made in Table 2-1, it would seem that NPSS and PROOSIS are ideal candidates to model the performance of the baseline engine and the subsequent engine configurations, based on the need to add novel components in to the architecture of standard engines. For the performance modelling of all engine configurations within this study, PROOSIS was chosen as the primary analysis platform, due to the availability of the software compared to NPSS.

The installed mass of the baseline engine can be determined by a series of methods available in literature. Software such as NASA’s open source engine mass estimation tool WATE, Chalmers University mass estimation tool WeiCo and Cranfield University’s mass estimation tool ATLAS are based on the detailed mechanical design of all the components on a standard turbofan [38–40].

Within the scope of the EU funded project ULTIMATE, WeiCo was the preferred mass estimation tool for the short-range baseline engine and reference 2050 engine configuration due to its availability and widespread use across the project. Thus it was consequently used for the year 2000 and year 2050 short-range engine configurations. One drawback of using WeiCo, was that due to restricted access to its source code it was not possible to integrate novel engine components within the estimation tool.

Therefore, for the combined cycle engine configurations a calibrated low-order mass estimation method (Sargenser’s method) coupled with mass estimation methods for the novel components in the cycle were used [41].

Mass estimation tools such as WATE and ATLAS were not considered due to lack of availability and compatibility issues respectively. Table 2-2, provides a brief overview of the functional capabilities of the engine mass estimation tools available, in the author’s opinion.

Table 2- 2: overview of gas turbine mass estimation tools

<u>Gas turbine modelling method/software</u>	<u>Fidelity</u>	<u>Flexibility</u>
NASA WATE	high	low
WeiCo	high	low
ATLAS	high	low

<u>Gas turbine modelling method/software</u>	<u>Fidelity</u>	<u>Flexibility</u>
Sargerser mass estimation method	low	high

2.2 Geared open rotor literature review

The Open rotor concept has been investigated over the last seventy years. Table 2-3, provides a brief chronological overview of the development of the open rotor concept to date.

Table 2- 3: Chronological overview of the development of the open rotor to date

<u>Chronological overview</u>	
40's -50's	Development and application of contra rotating propellers (CRPs) for military purposes. Used on the Westland Wyvern and XF-11 prototype [16,42]. However due to poor reliability of the CRPs a single rotating propeller array were preferred at the time[16]. In addition, the development and operation of the XB-42 Mixmaster aircraft is a unique application of contra-rotating propeller technology in the mid-40's.
50's-60's	The former Soviet Union developed the NK-12 puller contra rotating turboprop engine that was installed on the TU-114 aircraft [43].
60's-70's	Research and development during this period, with regards to contra rotating propeller engine configurations, was stalled due to the prominence of turbofans [16].
70's-80-s	Spurred by the oil-crisis, NASA launched the advanced turboprop program, that looked at the feasibility of highly loaded swept propeller blades using PF-1 in the CRP arrangement [44–46].

	<p>A joint venture between Snecma, GE and NASA saw a pusher direct drive CROR engine (coined UDF) demonstrated on a B727, B7J7 and MD80 aircraft. It was deemed operable but was excessively noisy [44,47,48].</p>
	<p>A joint venture between P&W, Allison and NASA saw a pusher-GOR (coined 578-DX) being demonstrated on a B727. Similar to the UDF it was deemed operable, however it did not meet the FAA's noise legislation at the time [49,50].</p>
80's-90's	<p>A confidential French initiative in collaboration with ONERA further investigated the noise characteristics of the CRPs[51,52].</p>
	<p>A similar initiative was undertaken by Rolls Royce and a few other organizations by understanding the performance and noise characteristics of CRP arrays[53]</p>
	<p>A former Soviet Union era engine development engine called the Ivchenko Progress D-236 was demonstrated. This was a 3-shaft engine in a puller arrangement, which later evolved in to the D-27 engine, still used today [54].</p>
90's-To date	<p>NASA conducted a two-year long assessment of the preliminary assessment of modern open rotors, and concluded that noise concerns still prevailed [55,56]. In addition, P&W sponsored a thesis in to the preliminary investigation of the same[57].</p>
	<p>Under the Cleansky program, there have been numerous projects that have investigated the feasibility of the modern</p>

	CROR. Safran aircraft engines have developed a full scale demonstrator as of 2017[16,58]
--	--

As seen in Table 2-3, the open rotor existed or was conceived in a variety of configurations. So prior to defining a reference 2050 open rotor engine configuration, a brief overview of the potential configurations are presented and assessed. Table 2-4, highlights the potential arrangements the open rotor engine can exist in.

Table 2- 4: Overview of open rotor engine configurations

<u>Open Rotor concept</u>		<u>Operation</u>
Puller	Direct drive	A contra rotating turbine could power a contra rotating propeller array located in the fore of the engine. Attia et al. provides a method to potentially do so [59].
	Geared configuration	The LP torque is distributed to the contra rotating propellers, located in the fore of the engine, via an epicyclic gear train.
Pusher	Direct drive	A contra rotating turbine could power a contra rotating propeller array located in line with the LPT. The UDF demonstrator was designed using this concept[47]
	Geared configuration	The LP torque is distributed to the contra rotating propellers, located in the aft of the engine, via an epicyclic gear train[49]

Inherently, the two puller configurations are not as competitive as the pusher variants. The direct drive puller variant, becomes quite complex in addition to the core turbomachinery seeing distorted flow from the CRP array. The geared puller configuration is relatively better, however would be plagued with similar inlet distortion issues in addition to having a relatively heavier engine configuration when compared to a geared pusher version. This relative increase in mass, in the puller geared configuration, is due to the fact that as the LP shaft

runs through the engine it forces the concentric HP and IP shafts outboard- hence increasing the relative engine mass.

When the two pusher configurations are considered, the geared configuration is preferred because of the inherent benefit of its turbine as opposed to the operational instability of contra rotating turbines[17]. When considering the placement of the epicyclic torque splitter, in the geared open rotor, there are two schools of thought. Rolls Royce favour placing the epicyclic gear train in between the fore and aft propellers of the contra rotating array, while Safran aircraft engine prefer to place the epicyclic gear train fore of both the contra rotating propeller arrays [16,60]. The latter configuration is preferred over the former because of the design flexibility of varying the axial spacing of the propellers, which has an impact on the performance and noise, and the additional benefit of having a less tortuous lubrication system[61].

Therefore the final reference GOR 2050 configuration used, is depicted in Figure 2-1. In addition, it is envisaged that the GOR 2050 will be rear fuselage mounted. Similar to the engine mount configuration in an MD-88 type aircraft. The reason for doing so stems from ground clearance limitations if it is mounted on a low wing configuration and noise limitations if it is mounted in a high wing configuration.

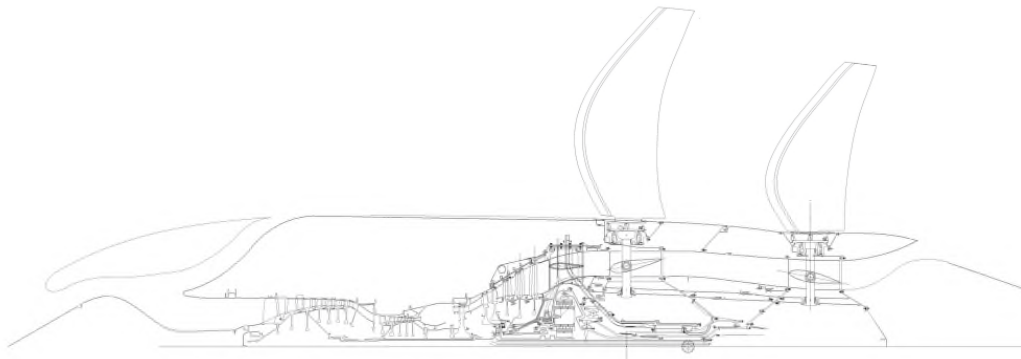


Figure 2- 1: Meridional view of the reference GOR2050 configuration[61]

Since the reference GOR2050 model was developed in PROOSIS, to ensure commonality amongst all concepts, additional performance modules needed to be developed to predict the overall performance of the reference GOR2050 engine. Therefore, in addition to the standard TURBO library used to model turbomachinery components. Models for the contra rotating propeller arrays, differential planetary gearbox, gearbox cooling system and core contra rotating section were modelled for preliminary performance analysis. The performance of the differential planetary gearbox has been defined by Dominy et al[62].

While rudimentary performance models have been suggested for the performance of the gearbox cooling system and core contra rotating system performance have been suggested by Schnork and Bellocq respectively [16,63]. There exists, in the public domain, a significant amount of literature to model the performance of CRP blades through 1D, 2D and 3D methods[16]. The current state of the art 1D CRP modelling methodologies have been covered by [16,64,65], it entails a quasi 1D velocity triangle methodology to estimate the induced axial and tangential velocities by the front on the rear propeller and vice versa. This is then coupled with a stream-tube contraction approximation to account for the effect the axial spacing between the front and rear propeller planes have on the induced axial velocities. In addition, the aforementioned methodologies account for the compressibility effects at relative transonic Mach numbers. Thus, the methods to model the performance of the CRP and the epicyclic gearbox are similar to those specified by Bellocq et al. and Dominy et al., respectively.

Details with regards to the modelling process adjudicated to these engine components are specified in Chapter 4. When the mass estimation of the novel components are considered, Bellocq et al, has provided a rudimentary methodology which has been used for the mass estimation of the novel components.

Based on the literature review conducted for GOR engines, the gaps in literature with regards to the preliminary performance and mass estimates of the constituent LP-system components are:

- The compressibility-effect efficiency correction, due to transonic Mach numbers, is representative of 1980 SR-7 propeller design. This needs to be amended to ascertain the efficiency of state of the art contra rotating propeller blades.
- The impact of pylon blowing on the performance of the CRP array has to be accounted for.
- There is no correlation that estimates the baseline efficiency of the CRP array as a function of its diameter, airfoil profile, airfoil radial stacking, blade twist and sweep. Correlations could potentially be derived using 2D or 3D methods.
- The mass estimates of the propellers are calibrated using 1980's technology limits.
- A mass estimation methodology is needed for the rotating cowl and the pitch-control mechanism. In addition, mechanical and noise constraints needs to be

assessed at a detail level such that they provide adequate constraints on the propeller rotational speeds.

The following sections, details the literature that is available for the primary thermal efficiency technology enabler, the nutating disc system.

2.3 Nutating Disc system literature review

Historically, circa 1950, several attempts have been made to incorporate constant volume combustion technologies within the standard architecture of aero-gas turbines. The most notable entry in to the market is the Napier Nomad-II, which features a turbo-compounded piston topping cycle [66]. It must be mentioned that ‘topping’ in the case of the Napier Nomad-II refers to the excess power produced by the 2-stroke piston banks being used to power the turbomachinery mechanically. Hence from here on in the term ‘topping’ refers to the reintroduction of excess power in to the main cycle, rather than the utilization of the exhaust heat from a prime mover in an industrial combined cycle gas turbine (CCGT) plant, as ‘topping’ is commonly referred to.

Technology enablers that bring about pressure rise combustion that have been considered, historically, are the Pulse detonation engine (PDE), Wankel engine, Piston topping engine and the wave rotor (WR) engine. Although these concepts have their benefits and shortcomings when implemented in a combined Brayton cycle, a relatively new addition of a constant volume combustion machine concept appears to be more competitive with regards to its potential for aerospace applications. The engine concept is referred to as the nutating disc (ND) system. Table 2-5 briefly highlights the benefits and shortcomings (in a qualitative manner) of each of the aforementioned technologies to down-select which technology enabler is most suited for the aero engine combined cycle.

Table 2- 5: Overview of potential constant-volume combustion enablers

<u>Pressure rise combustion enablers</u>					
<u>Feature</u>	<u>ND</u>	<u>PDE</u>	<u>Wankel</u>	<u>Piston topping</u>	<u>WR</u>
Working volume to overall volume ratio	high	high	medium	low	high
Torque curve vs. crank angle 'smoothness'	high	N/A	medium	low	high
Bearing load	low	N/A	high	medium	Very low
Seal speeds	low	N/A	medium	medium	medium
NO _x emissions	low	low	medium	medium	medium

Pressure rise combustion enablers					
Noise	medium	high	medium	medium	high
potential part count	low	low	medium	High	low
ease of coupling	high	low	high	High	high
Technology Readiness Level (TRL)	low	medium	medium	High	medium

The following points describe the rationale for the assessments in Table 2-5, and how each of the technology enablers compares with each other.

- Useful working volume to the overall volume ratio is a critical criterion as it determines the compatibility and compactness of discontinuous flow machines (such as those technologies mentioned in Table 2-5 with the continuous flow machines, like axial or centrifugal turbomachinery). This criterion reflects the relative physical size of the machines and the power to mass ratio for a given volumetric flow. The ND system, PDE and WR concepts indicate the highest potential in this aspect. Smith et al. [67] indicates how the working volume to overall volume ratio of the ND system is an order of magnitude higher than that of the rotary (Wankel) and piston engines (spark ignited or compression ignited internal combustion engines). That being said, PDs and WRs would potentially have a much higher working volume to overall volume ratio [68]. Factors that further influence the qualitative measure of this criterion are the residence time (this variable might have a first order effect on the combustion efficiency), peak pressure and flame temperature during the combustion process. These factors would influence the heat addition, heat rejection and consequently the casing volume of the technology enabler. This assumption will be further investigated.
- The ‘smoothness’ of the torque curve as a function of its crank angle is quintessential to ensure high mechanical transmission efficiency. The ND system utilizes both of its ‘working’ surfaces during a shaft revolution and it has an overlap of its stated processes by a phase angle of 90° as opposed to the Wankel and piston engines [1], thus the ND system should possess a relatively smoother torque output curve. However, the WR should possess the smoothest (near zero amplitude variance) torque curve; as it has a quasi-continuous flow [69].
- Bearing loads are indicative of operational speed limitations for a given power setting. When the ND system is compared to the other configurations (except the PDE and WR concepts) its relative bearing loads should be significantly lower as its centre of mass is stationary [1].

- Seal leakages can reduce thermal efficiency. Due to the unique motion of the nutating discs, the mean seal speeds are relatively low compared to those on rotating components (in Wankel, WR engines and piston engines) [1]. However, the actual leakage rates will be dependent on their detail design.
- NO_x emissions and noise assessments are indicative of how the technology contributes to the third SRIA goal concerning emissions. The apparent low residence times of combustion for each of these technologies implies relatively lower NO_x emissions, assuming stoichiometric conditions. PDE engines, featuring a detonation combustion process, would have a high source of noise as they produce shockwaves during combustion [70].
- The part count is indicative of the impact these technologies would have on cost of manufacturing and the robustness of an assembly line process. PDE, ND system and WR indicate the lowest part count- as is postulated by the number of moving parts.
- The ease of coupling is indicative of the complexity of mechanical interfacing between the technologies and the gas turbine architecture. Since the PDEs are stationary, it appears that it is relatively easier to integrate them mechanically. However, their aerodynamic integration with continuous flow turbomachinery poses issues, particularly due to the detonation waves impinging on the turbine downstream of the PDE[71].
- The TRL of the aforementioned technology enablers is a useful measure in determining the time needed to bring the product to market. The Piston-topping concept seems to be the most likely to enter in to service as it has already been proven in turbocharged aerospace applications such as the Napier Nomad-II.

Based on this preliminary qualitative assessment, appealing solutions for aero applications are the ND system and PDE concepts. The advantages of the PDE over the ND system technology are:

- PDEs have fewer moving parts as opposed to the ND system, hence tend to facilitate easier mechanical coupling with standard turbomachinery.
- When the specific enthalpy to specific entropy generation ratio of the combustion process is considered in isolation, the PDE engine has a higher slope than the ND system [1,70]. This occurs because the PDE engine combusts with a detonation process as opposed to a deflagration process.

However, the ND system is chosen over the PDE in this work, based on the fact that:

- The relative continuity of the ND system flow is higher than that of the PDE, hence it should be aerodynamically simpler to couple to continuous flow machines.
- Shaft power produced by the ND system can be mechanically re-introduced to the gas turbine spools, but this is not directly possible with a PDE.
- The length of the PDE is sensitive to its dependence on the design parameters; this could then lead to longer shafts- and hence egregious rotor dynamic effects.
- The inherent shockwaves produced by the detonation process can prove detrimental to the performance of the turbines downstream of a PDE.

When the integration of the primary selected technology enablers that enhance propulsive and thermal efficiency are selected, it is necessary to determine whether these technology would be more suitable for aero-engines intended for long haul missions or short-haul missions. At this stage a short-haul mission is deemed the primary choice for the evaluation of the primary technologies. The primary reasons as to why the un-ducted GOR LP-system propulsor and ND engine core are investigated for short range engine variants are:

- The GOR LP-system was chosen for a short-haul mission because, the thrust demanded by short-haul aircraft is markedly lower than a long-haul aircraft. A general rule of thumb is that the contra rotating propeller diameter scales quadratically with the demanded thrust rating[16,61]. Consequently the contra rotating propeller mass scales with a power of two to the propeller diameter. Therefore, the inherent specific fuel consumption benefits of the GOR engine configuration are offset by the increase in engine mass. Second order effects include having larger supporting pylons, assuming a rear fuselage installation. This increases the aircraft mass and adversely affects the longitudinal stability of the aircraft, which can lead to larger lifting surface areas. This in turn will lead to a heavier aircraft, higher lift-induced drag during cruise and thus even higher thrust ratings demanded from the engine. Thus, an engine corresponding to a short-range mission is deemed the suitable for investigation.
- The inherently smaller core flow of a short range engine, compared to a long range (LR) engine, would lend itself to a smaller size of ND system (for a fixed number of ND systems in a combined cycle). Since the mass of the ND system is then roughly proportional to the core flow to the power of 1.5[72], one would expect a relatively heavier integrated ND system configuration for the long range engine as opposed to the short range engine.

- In addition, as core flows decrease in a short range engine configuration the peak cycle temperatures (TETs) would have to rise relative to long range engine configuration. This in turn leads to a more efficient ND system cycle as seen in the parametric study performed for a naturally aspirated ND system cycle by Korakianitis et al [1]. Essentially, the short range engine compared to a comparable long range engine would have a higher specific power core.
- The ND system would be arranged circumferentially in the meridional view (Figure 2-2) in an aero topping cycle arrangement in the first instance. Once the circumferential distribution of nutating disc systems reaches its packaging capacity, another row of radially stacked ND systems needs to be incorporated in to the engine architecture. If the dimensions of a single ND system unit are considered to be the same for a short range and long range engines, by virtue of the core mass flow scale effects it would be more likely that the long range engine configuration would have more axially stacked banks of ND systems. In this scenario, the corresponding shaft length of an integrated array of ND systems in a long range engine configuration would be longer relative to a short range engine configuration. This would consequently lead to a heavier structural frame (for the array of ND systems), increased number of roller bearings and possibly egregious rotor dynamics effects.
- The thermal efficiency benefit gained from raising compressor peak delivery pressures (conventionally P3) in the short range engine variant tends to be curtailed due to the exacerbated compressor efficiency losses. This primarily occurs due to relatively high tip leakage losses at the smaller last stage of the HPC, but by the addition of the ND systems, particularly for a short range engine variant, this efficiency loss can be reduced enabling higher peak cycle pressures.

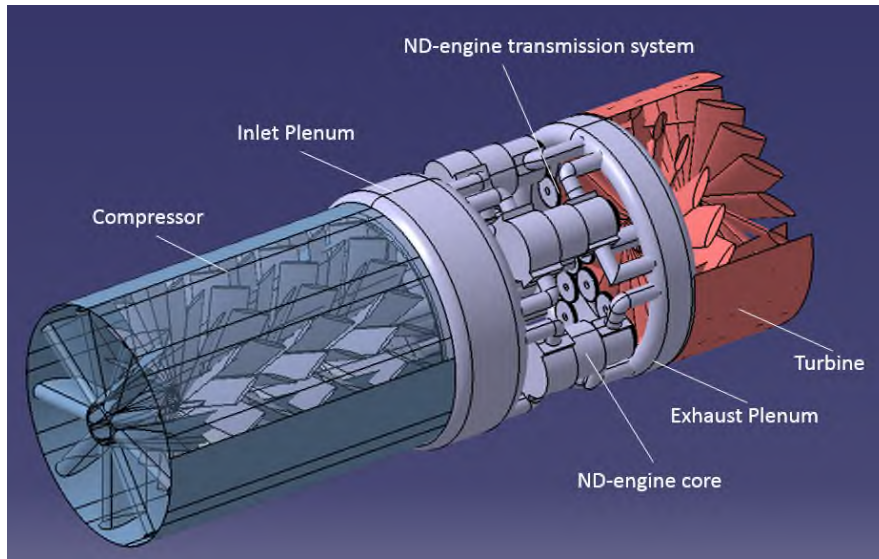


Figure 2- 2: Possible ND- system arrangement in the core of an engine

The nutation motion is most easily visualized by the wobbling of a coin on a table. The dynamics of a body in nutation has been captured in literature by Anderson [73] with regards to a nutating gear system in a Cartesian coordinate system. One of the shortcomings of the derivation is that it holds true for only minute angles of nutation, as the nutating motion is constrained in two planes [$z-x_0$ and the $y-x_0$ plane] (see Figure 2-3) whereas the nutating motion representative of a ND engine should be constrained in just one plane [$y-x_0$ plane].

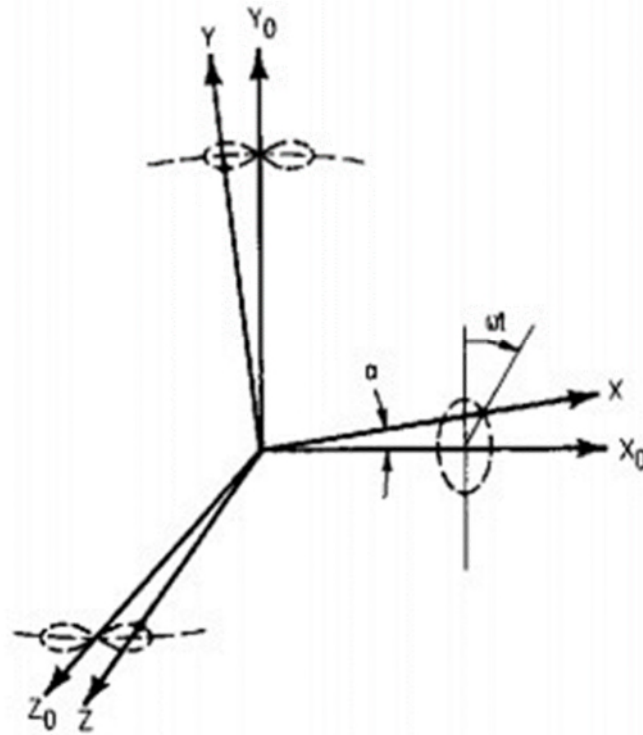


Figure 2- 3: Static and dynamic frames of reference indicating the motion of nutating gears[73]

The nutation motion representative of being constrained in one plane was first exploited by Dakeyne, circa 1830, when he applied for a patent postulating its use as a hydraulic expansion device. Dakeyne’s idea was furthered by Davies, and working prototypes were developed as power utility steam engines [74]. A century later (1961), D. Day postulated the use of the nutation motion in conjunction with an Otto cycle to produce a power dense internal combustion engine (ICE) [75]. State of the art patent filings, to date, suggest two ICE’s that exploit the nutation motion; L. Meyer’s nutating disc engine(1993) [76] and H. McMaster’s wobble plate engine(2002) [77]. Table 2-6 indicates the similarities and differences between the three latest ND engine system concepts.

Table 2- 6: Nutating Disc Engine patent comparison

<u>PATENT</u>	<u>YEAR</u>	<u>SIMILARITIES</u>	<u>DIFFERENCES</u>
			<ul style="list-style-type: none"> Compared Meyer’s nutating internal combustion engine the disc itself is flat as opposed to a convex shape. Furthermore,

PATENT	YEAR	SIMILARITIES	DIFFERENCES
Nutating disc internal combustion engine by Day	1963	All technologies utilize both faces of the nutating disc during its operation, and have separate chambers for compression and expansion. The power cycles for all technologies overlap by a phase angle of 90°.	<p>combustion and expansion processes occur in the same chamber. The exhaust port isn't cam controlled.</p> <ul style="list-style-type: none"> Compared to McMaster's wobble engine the 'upper' and 'lower' ends of the inner casing walls are flat as opposed to the conical nature of the wobble plate engine.
Nutating internal combustion engine by Meyer	1993		<ul style="list-style-type: none"> Compared to Meyers internal combustion engine the disc possesses a convex shape and in addition possesses a pre-combustion chamber. The exhaust ports are cam controlled. Compared to Mc Master's wobble engine the 'upper' and 'lower' ends of the inner casing walls are flat.
Wobble engine by McMaster	2002		<ul style="list-style-type: none"> Compared to Day's nutating disc engine 'upper' and 'lower' ends of the inner casing walls are conical. Compared to Meyer's nutating disc engine expansion and combustion occurs in the same chamber.

Out of the three state of the art concepts the most widely published, in public domain literature, belongs to that of L. Meyer's ND engine. Circa 2004, Korakianitis et al. published a series of papers [1,2,78] describing the OD thermodynamic performance, operation and potential issues facing a naturally aspirated ND engine system. With regards to the arrangement of the ND engine system, it consists of a convex disc mounted on an angled shaft that is connected to another concentric shaft by a 'z- arm' (see Figure 2-4)-in a single disc ND configuration. Just as [79] illustrates it utilizes both faces of the disc and have separate chambers for intake/compression and expansion/exhaust. Claimed operational benefits are:

- Since each thermodynamic process lasts for 270 degree crank angle and that both faces of the ND are utilized per shaft revolution there is a 90 degree overlap between the two faces of the ND-hence a smoother torque curve can be achieved as opposed to a similar piston engine.

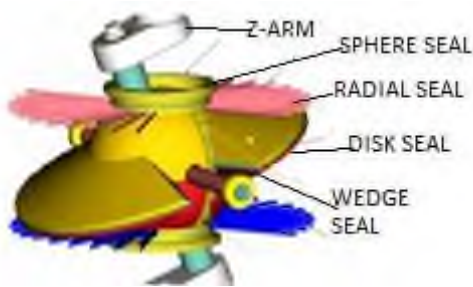


Figure 2- 4 : proposed seal arrangement of a single ND engine system [79]



Figure 2- 5 : proposed arrangement of a dual disc nutating disc engine system [79]

- Since the centre of mass of the disc remains stationary, there is a reduction of bearing loads as opposed to piston engines [1].
- It is further postulated that the compression and expansion volumes can be varied by employing a 2-disc configuration (see Figure 2-5)-this can lead to 'self-supercharged ' cycle and reduced thermal stresses as opposed to a single disc naturally aspirated configuration.

The OD thermodynamic process for a ND engine system, stipulated by Korakianitis [1], is illustrated in Figure 2-6. Process 01-02 indicates adiabatic compression of the working fluid, Process 02-04 indicate the adiabatic expansion of the fluid from the end of the compression process through the accumulator and finally to the pre-combustion chamber. Processes 04-

06 indicate the constant volume combustion and constant pressure combustion (assumed to be spark ignited for the investigations henceforth) that occurs across the pre-combustion chamber and a section of the expansion chamber. Process 06-07 indicates the expansion of the combustion products through to the exhaust ports. Furthermore, the properties of the working fluids applicable to a nutating disc engine system, are given by Korakianitis [80]. The thermodynamic cycle represented by Koriakinitis et al., is similar to a Seliger or Humphrey cycle.

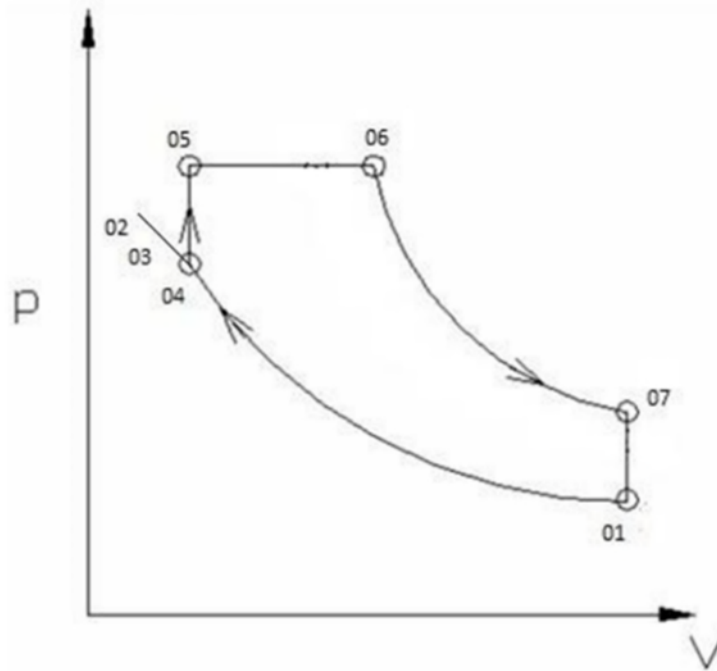


Figure 2- 6: P-V diagram of a nutating disc engine system cycle

In addition to defining the basic thermodynamic cycle, additional features have been added to give the model flexibility with regards to simulating over/under expanded cycles (applicable to a 2-disc configuration), ability to express the ratio of constant volume: constant pressure combustion and the heat loss to the surroundings as a result of having periodic combustion.

Therefore, the current state of the art (at the time of writing this) design point 0D thermodynamic modelling methodology of the ND engine system is described by Korakianitis et al. One of the shortcomings of this methodology is its inability to capture the effects of the geometry of the ND engine configuration with regards to its allowable performance. The current state of the art off- design performance methodology, with regards to the nutating disc system, is one that is also suggested by Korakianitis et al [2]. It involves:

- Performing a parametric study for a particular ND engine system, at a design point rpm, by changing the max cycle temperature and volumetric compression ratio. By

doing so, a map is created where the power output is expressed as a function of thermal efficiency, volumetric compression ratio and maximum cycle temperature.

- Assume a first order approximation that power is directly proportional to rpm.
- Determining the combination of maximum cycle temperature and volumetric compression ratio that yields the highest thermal efficiency.

The shortcoming of this methodology is that the volumetric compression ratio is a quantity that is determined by the geometry and is generally fixed for a particular design. The inclusion of the assumption of variable valve timing (VVT) technology (part load miller cycle control) being used in the compression chamber [81] can potentially account for this 'effective volumetric compression ratio'. However, when the volumetric compression ratio changes it does come at the expense of a varied efficiency of the assumed adiabatic compression process - this will occur as there will be leakage of air from the accumulator back to the compression chamber as a result of advancing/delaying the valve timing between the accumulator and the pre-combustion chamber, therefore the expected turbulence within the compression chamber would increase and the assumption of a fixed compression efficiency would no longer be valid. The degree of how much the volumetric compression ratio can be varied, also depends on its geometry.

Circa 2007, the US Army, NASA and Kinetic BEI created a proof of concept prototype of the ND engine system to a TRL 6 level [79]. This publication ([79]) is the only available literature in the public domain that provides a mass and size estimation of a 2-disc ND engine system as a function of disc diameter, total volume displacement and estimated power.

Since the inception of this work, additional research has been carried out on the nutating disc engine at Cranfield University. Table 2-7, highlights the work done in a chronological order.

Table 2- 7: Chronological overview of work performed at Cranfield University

<u>Author</u>	<u>Aspect investigated</u>
Mohanarangan	Replicated the performance model introduced by Korikanitis and performed preliminary integration exercises [82].

Quintana	Investigated the feasibility of integrating a ND-engine system within the core of a high bypass ratio engine to power the ERJ-145. It was determined that four 15 inch diameter cores were needed to match the flow rates. The ND engine systems were too big and consequently proposed to be stored in the baggage compartment of the ERJ-145. In addition, a 45% increase in the baseline engine TSFC was determined [83].
Nadhira	State of the art CFD studies on the investigation of the volumetric and isentropic efficiency of a ND engine system compressor as a function of operating speed were carried out. The main shortcoming of this work is that the seal leakages were adjusted in order to allow for numerical diffusion, consequently there was a mass and temperature accumulation during the URANS CFD study. Subsequently, this lead to a calculated isentropic efficiency over unity[84].
Liberti	The intended outcome of this study was to determine the ratio of constant volume combustion to constant pressure combustion and the amount of heat lost to the surroundings during combustion, during the operation of the ND engine system via CFD studies. The outcome of this work defined the timing sequence of fuel-air injection, spark ignition, combustion, expansion and exhaust. In addition, the maximum crank angle where the constant volume combustion transitions to constant pressure combustion is determined for a fixed geometry[85].

Based on the work performed to date **the gaps in literature**, with regards to the performance and mass of the nutating disc engine are:

- There is no methodology to parametrically size the nutating disc engine system. The performance of the nutating disc engine system is linked to the geometric sizing of the nutating disc engine system.
- There are a series of assumptions that are used for the preliminary performance model, and the design constraints or associated uncertainties for these assumptions are unknown.

- The potential fuel burn benefit the ND engine system can deliver, when it is integrated in to an engine, has not been explicitly determined.

2.4 Intercooler literature review

The intercoolers, historically investigated in aero-engine concepts are mostly tubular heat exchangers due to their relatively high surface area to volume ratio and low mass. Historically, a variety of heat exchanger types have been proposed. The concept of the Lancette heat exchanger has been explored by MTU in programs such as NEWAC, VITAL and LEMCOTEC [86]. Its intended use was for recuperation applications and considered to be mounted in the exhaust stream of the hot nozzle. It consists of a series of stacked elliptical tubes per module, which is fed and scavenged by cylindrical heads (Figure 2-7). The heat exchanger was designed to bear thermal cycling fatigue limits expected in aero-applications. Based on the study considered by Kormann et al, the Lancette design showed TSFC benefits of 15% relative to a year 2000 baseline [86].

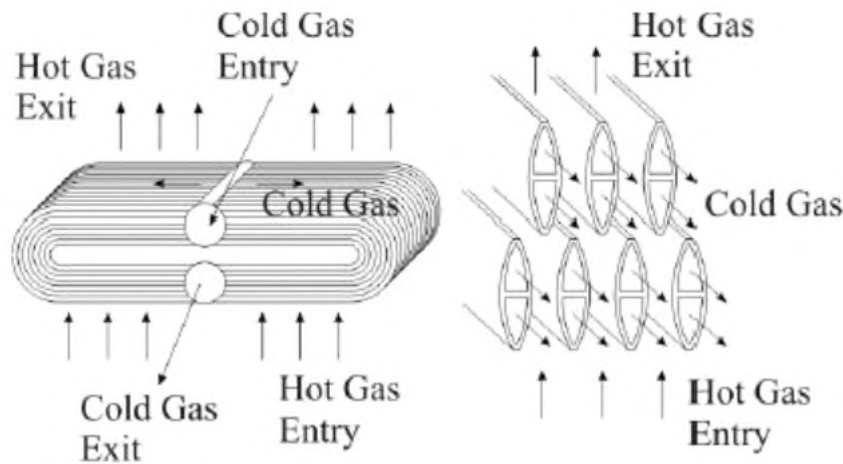


Figure 2- 7: Lancette design as proposed by Kormann et al. [86]

Figure 2-8 indicates the issue with this arrangement when it is considered for intercooling applications in an aero-engine. Figure 2-8, indicates the possible placement of the Lancette intercooler modules circumferentially in a potential intercooled turbofan configuration. It is apparent that the available circumferential area is not being effectively used to acquire the best temperature effectiveness.

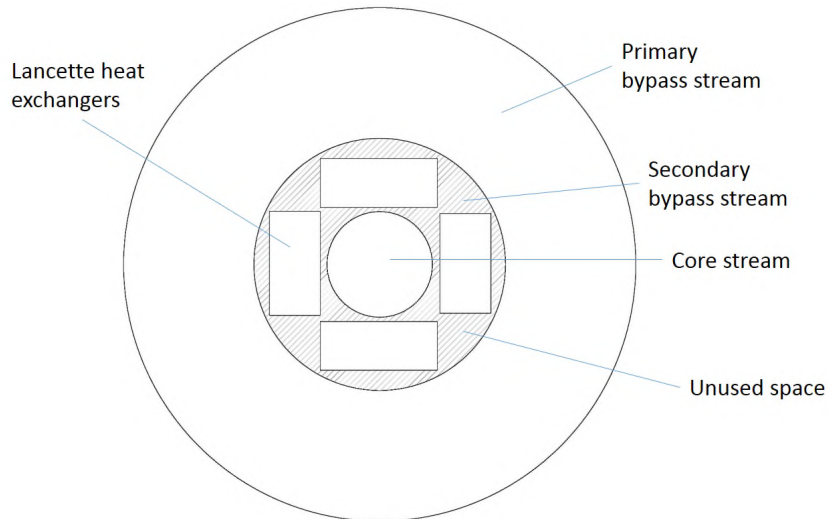


Figure 2- 8: Circumferential view of Lancette heat exchanger arrangement

Therefore in order to achieve good circumferential space utility Zhao et al. at Chalmers University proposed an involute spiral heat exchanger [87], as seen in Figure 2-9. Due to the compact arrangement of the heat exchanger, it boasts fuel burn improvements of 3.9% relative to the Lancette design[88]

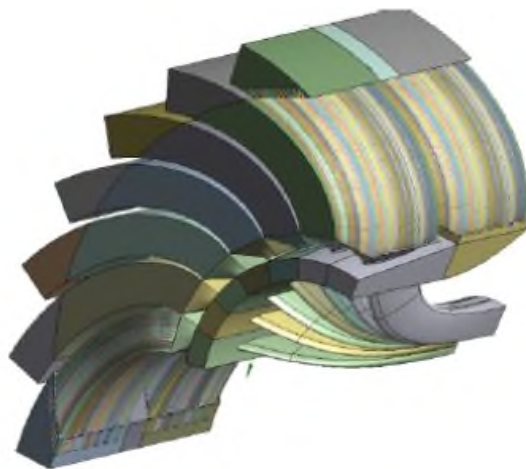


Figure 2- 9: Involute spiral heat exchanger design[87]

Due to the compact arrangement of the involute spiral arrangement, it was considered for future engine concept assessment within this work.

There are primarily two preliminary methods that can be used to determine the performance of the involute spiral arrangement. A higher fidelity method proposed by Zhao et al. predicts the temperature effectiveness and total pressure loss of the heat exchanger as a function of

the tube stack geometry, spacing and operational conditions. A lower fidelity method is proposed by Alexiou et al, within the framework of the TURBO 3.2 library (in PROOSIS) which involves assigning an effectiveness and total pressure loss estimation [89]. The lower fidelity model was preferred over the higher fidelity model because incorporating a higher order model of the intercooler in conjunction with a nutating disc model and a CRP model would violate the number of closure equations allowed to be solved under educational license of PROOSIS available to the author.

Based on the literature review conducted, there is scope to further the understanding of steady-state intercooler performance for an aero-engine. Namely by:

- Assessing the potential fuel burn impact of implementing an involute spiral intercooler in an open rotor engine configuration.
- Assessing of the potential impact of fouling and ice accretion on the involute spiral intercooler performance in a turbofan.

2.5 Re-heat/ Secondary combustor literature review

Historically the re-heat concept has been extensively used for military applications, in the form of afterburners. However, for civil aero purposes it is more beneficial if the secondary combustion occur as soon after the primary combustor as possible to negate excessively high specific fuel consumption. A good representation of this type of engine cycle has been demonstrated by the GT24/26 stationary engine configurations[21]. Conceptual application of reheat combustors within the architecture of a high bypass turbofan engine has been investigated by Vogeler and Kohler [90,91]. Both Vogeler and Kohler estimated that the reheat combustor would be a standard annular combustion chamber, similar to the primary combustor. Kohler discovered that by implementing the reheat technology a TSFC benefit of 1.5% can be achieved relative to Rolls Royce's Ultrafan engine concept [91].

Another combustor design, in context of reheat potential, was studied by Levy et al. [92] within the context of the AHEAD project [93]. The proposed combustion chamber has a re-circulating vortex that entrains the fuel and ensures heat release during combustion at relatively low total pressure losses and potentially lower NO_x emissions in comparison to an annular combustor [92]. This was seen in Bueno's 3D URANS assessment of an oxy-poor flame combustor [94]. Therefore, the re-circulating flow combustor was chosen as the re-heat combustor of choice for the assessment of future engine configurations.

The method to determine the performance of a re-circulating combustor is assumed to be similar to that of a standard annular combustor, and is modelled based on the principles

outlined in [89]. The method assumed to be used to determine the mass of the re-circulating burner is assumed to be the same as that outlined by Sargerser[41].

Based on the conducted literature review, the following un-explored aspects of the re-circulating secondary combustor research, at a preliminary design level, are:

- The fuel burn benefits derived from integrating a reheat combustor within the architecture of a geared open rotor have not been assessed.
- A preliminary mass estimation methodology for the re-circulating combustor has not been derived.
- A correlation to predict the off-design performance of the re-circulating combustor is needed.
- Altitude re-light capability of the combustor design has to be assessed.

3 Contribution to knowledge

One of the main objectives of this work is to investigate the feasibility of a nutating disc engine system, which is integrated in to year 2050 geared open rotor and aircraft, in achieving a 68% mission fuel burn benefit relative to a comparable year 2000 mission. In order to investigate the potential mission fuel burn benefit it is essential to predict the performance of the nutating disc engine system as well as estimate the size of the device. As per the conducted literature review, to date there exists a methodology to predict the performance of a nutating disc engine system. However, there is no available methodology to provide the preliminary size of the nutating disc engine system. Hence, the **primary contribution to knowledge is the introduction of a preliminary methodology to size the nutating disc engine system**. This methodology provides a limit as to the achievable net shaft power available from a nutating disc engine system as well as its component mass. The introduction of this sizing methodology allows for the investigation of the potential mission fuel burn estimates expected, when the nutating disc engine system is integrated within the architecture of a geared open rotor.

An additional research objective, is to investigate whether synergetic technologies to the nutating disc engine system, such as re-heated combustion and intercooling would meet the stipulated 68% fuel burn reduction target, in a geared open rotor engine configuration. Therefore, representative steady state preliminary engine models are created to investigate whether the nutating disc engine system and the aforementioned synergetic technologies would meet the stipulated 68% fuel-burn reduction target. The performance and preliminary design of these engine configurations have not been reported in the available literature. Hence, the secondary contribution to knowledge of this work is **the depiction of the preliminary performance and mass estimates of the following aero-engine configurations**:

- **Nutating disc engine system in a geared open rotor**
- **Intercooled-nutating disc engine system in a geared open rotor**
- **Re-heated- nutating disc engine system in a geared open rotor**
- **Intercooled-re-heated- nutating disc engine system in a geared open rotor**

4 Methodology

This section highlights the methodologies required to estimate the performance of a turbo-charged nutating disc engine system. Prior to investigating the performance of the novel aero-engine configuration, it is necessary to establish the performance of a comparable year 2000 and year 2050 reference engine. This includes the following:

- Including a method to estimate the preliminary performance of a baseline year 2000 turbofan engine that powers a short range year 2000 aircraft.
- Including a method to estimate the preliminary performance of a reference year 2050 geared open rotor engine, which powers a short range year 2050 aircraft.

In order, to estimate the performance and relative fuel burn benefit of a nutating disc engine system based aero-engine configuration, as well as intercooled and re-heated nutating disc engine system variants, the following methods are included:

- A method to estimate the performance and size of a nutating disc engine system
- A method to estimate the performance of an intercooler and secondary combustor within the architecture of a nutating disc engine system based aero-engine.
- A method to estimate the mass of the baseline year 2000, reference year 2050 engine configurations, nutating disc engine system, intercooler and secondary combustion systems.
- A Method to estimate the relative fuel burn of the combined cycle engine configurations when compared to the baseline and reference engine configurations.

The methodologies defined for modelling the baseline year 2000 engine, year 2050 reference engine, nutating disc engine system, intercooler, secondary combustor and the associated combined cycles were conducted in the software called “Propulsion Object Oriented Simulation software” (PROOSIS 3.6.14, Empresarios Agrupados Internacional, Madrid, Spain)[95]. Whereas, the methodology to estimate the relative fuel burn benefit or penalty is derived using non-linear trade burn factors provided by ULTIMATE project [96].

It is necessary, to estimate the performance and mass of the year-2000 baseline engine and the reference year 2050 GOR engine in order to compare the performance of the combined cycle configurations with perceived state of the art year 2050 designs [60]. Within the scope of this work four nutating disc engine core configurations are considered, and are expected to share similar components for all configurations. However, there are components that will be novel to each configuration, such as the nutating disc engine system, intercooler, etc. Therefore a library of the possible engine component models were created so that the performance and mass of all the engine configurations could be explored, by combining the

appropriate component models to create the desired engine configuration. Once the performance and mass of the engine configurations are ascertained, their effects on mission fuel burn are determined by utilising the non-linear fuel burn factors. An overview of this process is presented in Figure 4-1.

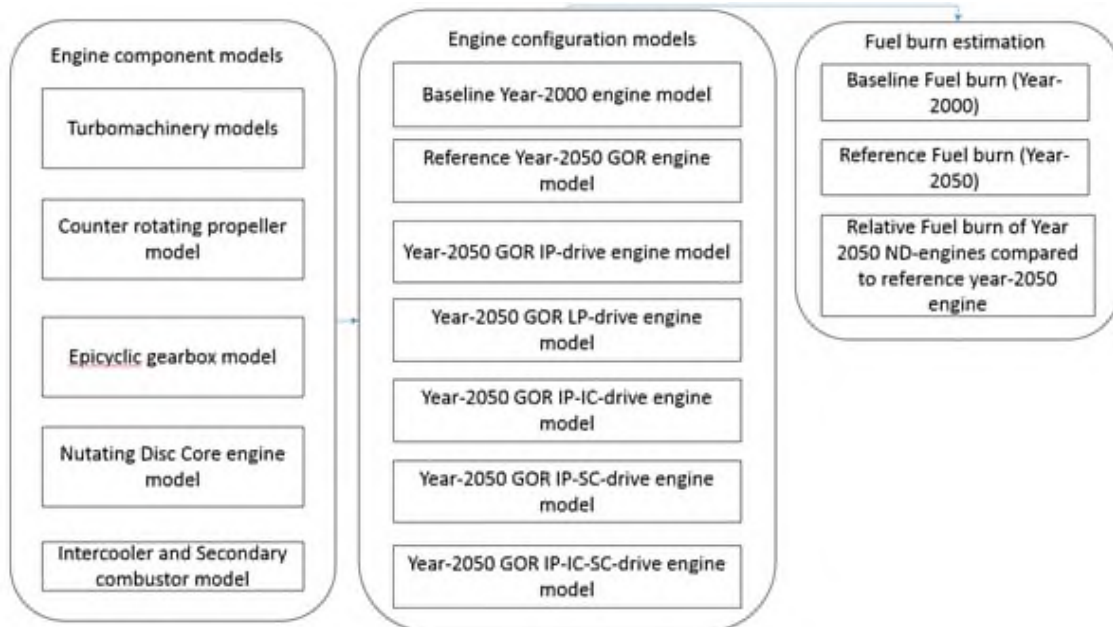


Figure 4- 1: Overview of methodologies employed to estimate the performance of Y2050 nutating disc engine core configurations.

4.1 Year 2000 short range engine performance model

The short-range year 2000 turbofan (SRTF2000) engine performance model, to compare short range-EIS2050 nutating disc topped engines and reference 2050 engine concepts against, is based on the engine performance specifications of the CFM56-5B engine configuration. Since the CFM56-5B engine performance specifications have been the Y2000 baseline engine of previous exploratory engine studies, it has also been chosen as the Y2000 baseline engine for this work. Hence a representative engine performance model should be constructed to match the short range engine specification highlighted in the NEWAC project. Table 4-1 lists the SRTF2000 engine performance model specifications as per NEWAC data [97]. The station numbering in Table 4-1 are consistent with the acceptable practices in ARP 755A[98].

Table 4- 1: NEWAC CFM56-5b type model data specifications

<u>Parameter</u>	<u>Units</u>	<u>TOC</u>	<u>CR</u>	<u>EOR</u>
Mach	-	N/A	N/A	N/A
Altitude	m	10700	10700	0
dT ISA	K	N/A	N/A	N/A
W2	kg/s	150.66	140.87	372.02
BPR	-	4.63	5.11	5.10
W _f	kg/s	0.56	0.37	1.31
OPR	-	35.50	27.85	27.70
TTSFC	g/kNs	18.71	17.11	13.59
Fn	kN	30.14	21.90	96.06

4.1.1 Performance model

The SRTF2000 engine performance model was modelled in PROOSIS as a two-shaft turbofan with separate flow exhaust nozzles, which is representative of the year 2000 state of the art CFM56-5B engines in service. Figure 4-1 shows a schematic of the PROOSIS model, with the associated components.

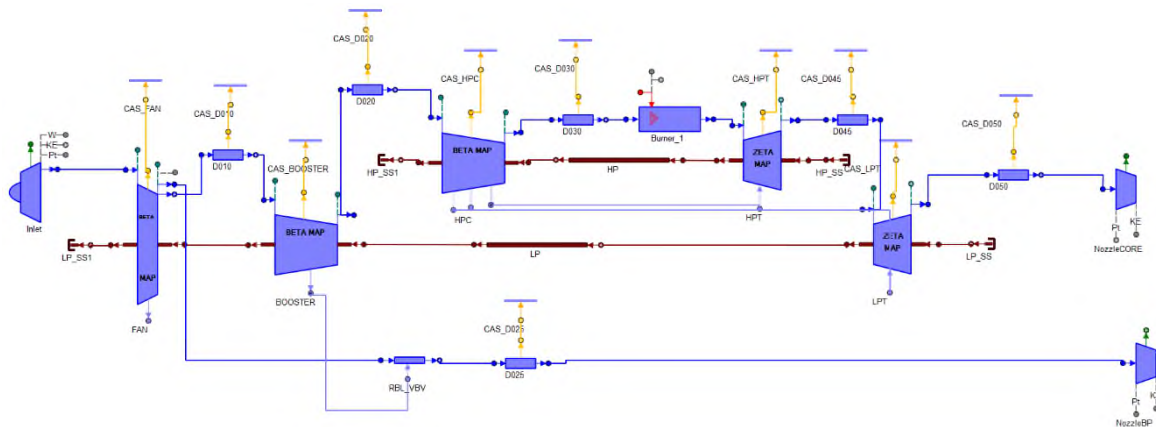


Figure 4- 2: PROOSIS schematic of the Y2000 CFM56-5B engine model

The modelling activities for the short range turbofan (SRTF2000) model has not included any Reynolds number corrections for component efficiency and flow capacity variation.

4.1.1.1 Fan, Bypass duct and cold nozzle

The fan component in PROOSIS separates the operation of the fan into two separate sub-components, namely the core and bypass sections. One reason for this is that the two sections can reach peak efficiencies at different loading conditions. However, the fan performance stipulated by the NEWAC data indicates similar pressure ratios and isentropic efficiencies so the pressure ratios for the bypass and core streams have been kept the same at design conditions (at TOC conditions).

In order to ascertain the off-design performance of the fan for the core and bypass section respectively, a beta type map [99] was used for the bypass section and NASA's beta type map (map B) from the Quiet Engine program was used as the component characteristic of the core section [100]. In order to match the off-design performance in the NEWAC specification, the scaling factors for the map were used as variables in the matching of the NEWAC data performance.

In order to replicate the potential total pressure losses seen in the inlet and the bypass duct, total pressure loss figures of 2.5% were imposed. It was assumed that the pressure losses would not scale with the corrected mass flow at off-design conditions. Finally, when it came to modelling the performance of the cold nozzle, a thrust coefficient of 0.991 was imposed at the design point (TOC). It was also assumed that the cold nozzle thrust coefficient would not vary at off-design conditions.

4.1.1.2 Booster component

The Booster stage of a CFM56-5b type engine performance model uses a scaled BETA type compressor component map that is representative of a NASA-CR-174645 booster map [101] for calculating the off-design performance of the component. In addition, the design point pressure and the isentropic efficiencies are imposed at TOC conditions as per the NEWAC data specifications.

When the off-design performance was considered, the application of variable inlet guide vane (VIGV) schedules and blow-off bleed for surge margin control was not included.

4.1.1.3 High Pressure Compressor

Since the isentropic efficiency and pressure ratio of the HPC component was not provided in the NEWAC data, they were set as variables during the data matching process. The primary goal of the matching process was to achieve the same OPR of the NEWAC specification while imposing total pressure losses in the inter-connecting ducts.

In order to predict the off-design performance of the component, a scaled BETA type NASA TM 101433 example compressor map was used [102]. Similarly to the Booster component, no VIGV and blow-off bleed control measures were adopted for surge margin control. In addition, a 12.4% bleed is assumed to be taken at the compressor discharge pressure seal (CDP) in order to cool an equivalent single stage high pressure turbine (HPT) and this percentage is assumed to be constant across the flight envelope. Within the framework of the component, in PROOSIS, this corresponds to off-taking the bleed at the end of the component. It is also assumed that no active tip clearance control technology is used within this component.

4.1.1.4 Combustor

The combustion chamber component is assumed to mirror the performance of a dual annular combustion chamber, inherent to CFM56-5B combustion chamber design at an EIS of year 2000 [103]. It is assumed that the total pressure drop across the combustion chamber is 4.25%, rather than 4.5%, and the burner efficiency is 99.95%, these values correspond to typical values assumed in gas turbine performance estimation literature [32]. It is also assumed that the total pressure loss and efficiency of the combustion chamber does not scale with the corrected mass flow at off-design conditions. In addition, the combustor outlet temperature (COT) was used as a handle in ascertaining the performance of the CFM56-5B type performance model at design point and at off-design conditions

4.1.1.5 High Pressure Turbine

The high pressure turbine (HPT) component in PROOSIS is designed as an equivalent single stage (EqSS) turbine. Since the isentropic efficiency of the component, at any operating condition, was not specified in the associated NEWAC data it was set as a design variable. In addition, the cooling air coefficient (CAc), the relative total temperature multiplier ($T_{rel,C}$), the percentage bleed used in the nozzle guide vane (NGV) and the rotor were ascertained at TOC conditions such that the average blade metal temperature at EOR conditions did not exceed 1340K [60]. The aforementioned blade metal temperature value coincides with the maximum operational temperature of nickel based alloys that are used to manufacture the HPT NGVs and rotors. In addition, it is assumed that only internal convection cooling is utilised for the rotors and the NGV. The specific cooling assumptions for the SRTF2000 engine performance model are presented as follows:

- The cooling air coefficient (CAc) is chosen as 0.05. Equation 4-1 indicates how the chosen cooling air coefficient relates to the convective cooling effectiveness (eff_{cool}) of the rotor and NGV.

- The relative total temperature multiplier, that dictates the relative total temperature that the rotor sees ($T_{rel,C}$) is chosen as 0.9. Equation 4-2 indicates the relationship between the exit NGV temperature and the relative total temperature of the rotor.
- The percentage CDP bleed that enters the NGV is chosen at 45% and the percentage bleed that is pumped in to the rotor, after being pre-swirled, is set to 55%
- Lastly, it is assumed that 90% of the flow is reintroduced into the gas path and does work

$$CAC = \frac{W_{cool}}{W_{rotor,in}} * \frac{(1 - eff_{cool})}{eff_{cool}} \quad 4-1$$

$$T_{t,rel} = T_{t,NGV_exit} * T_{rel,C} \quad 4-2$$

In order to derive the off-design performance of a representative HPT component, a scaled zeta type high-work low aspect ratio turbine map extracted from NASA TM83655 was used [104]. The type of map used for this particular component was a delta specific enthalpy versus corrected mass flow map, as opposed to a pressure ratio versus corrected mass flow map. It also must be mentioned that active tip clearance control, by means of impingement cooling on the casing has not been considered in this analysis.

4.1.1.6 Low Pressure Turbine

As in the case of the HPT, the low pressure turbine (LPT) was modelled as an EqSS turbine. The LPT design point isentropic efficiency was specified in the NEWAC dataset, and has been imposed as a fixed design parameter from the outset. It is assumed that this component is uncooled. In order to ascertain the off-design performance of the LPT, a scaled ZETA type AGARD two-stage turbine component map has been chosen [105]. Similarly to the HPT component, this used a delta specific enthalpy versus corrected mass flow type map.

4.1.1.7 Hot nozzle

The hot nozzle coefficient of thrust and total pressure loss is selected. It is also assumed that the chosen values are fixed throughout the flight envelope and do not scale with the corrected mass flow at off-design conditions.

4.1.1.8 ECS requirements and mechanical losses

It is assumed that an overboard bleed of 0.5 kg/s is needed at TOC conditions to facilitate environmental cabin system (ECS) requirements. It is assumed that the bleed is taken at

40% of the relative enthalpy rises of the HPC. It is also assumed that a fixed percentage overboard bleed is taken at all flight conditions. In addition, a 67kW power offtake is assumed to be taken from the high spool shaft to meet the power requirements of auxiliary systems such as the fuel pumps, oil pumps and to overcome windage losses [32]. It is also assumed that the power offtake is fixed across the entire flight envelope.

4.1.1.9 Rotational Speeds

Neither the absolute nor the non-dimensional rotational speeds of the turbomachinery were specified in the NEWAC data at any operating point.

Based on the cross-sectional drawing of the matched SRTF2000 engine, the component geometry was determined [61]. The measured geometry and assumed values on corrected rotational speed are used to develop a number of key mechanical parameters. The operational speed of the HP and LP spool are derived from the EASA type certificate data sheet, by scaling the stated operational speeds to replicate 100% absolute rotational speeds [106]. The exit hub to tip ratios of the HPT and LPT are derived from a scaled cutaway of the CFM56-5B engine [106]. A representative exit axial flow Mach number is chosen at EOR conditions to determine the exit area and rim speeds of the HPT and LPT respectively, which must not exceed $5.0e+07 \text{ rpm}^2\text{m}^2$ and 400 m/s respectively [32].

4.2 Year 2050 geared open rotor performance model

The envisaged advanced tube and wing (ATW) aircraft design for short to mid-range intra-missions (SR) in year 2050 is deemed likely to feature a GOR propulsor. Revolutionary concepts in SR aircraft design and manufacturing, that are assumed to be introduced by entry into service of 2050, claim to significantly reduce the drag of the SR aircraft while maintaining similar levels of payload capacities as of year 2000 [107]. Consequently, the design point thrust rating of the GOR engine would be lesser than a comparable Y2000 design.

In order to benchmark the performance of a year 2050 geared open rotor (GOR) configuration a two-pronged approach is adopted. In the first instance, a GOR performance model is constructed to match the stated performance in [60]. Safran Aircraft Engines, who were spearheading the development of a GOR amongst the engine OEMs, have provided performance specifications for an EIS of 2050 under the scope of ULTIMATE[60]. These performance estimates define the engine technology limits, such as the HPT blade metal temperature, HPC last stage blade height, propeller loading, etc. The engine technology limits derived from the 'matched' performance model are then applied to the engine

performance models that align with the reduced thrust requirements of a potential SR advanced tube and wing fuselage in Y2050.

Similar to the modelling approaches carried out for the SRTF2000 engine, all the simulations required to model the GOR engine were carried out in the commercially available software PROOSIS [95]. Due to the bespoke arrangement of the GOR certain novel components had to be assembled to estimate the performance of the GOR, namely:

- Contra rotating propeller (CRP) array component
- Planetary differential gear box component (DPGB)
- DPGB cooling system
- Inter connecting duct between the power turbine (PWT) and the core nozzle

The following sections highlight the methods and modelling assumptions used in assembling a representative GOR model. From the outset, the station numbering of the components in the GOR engine performance model correspond to those in ARP755A [98]

4.2.1 CRP performance estimation model

The contra rotating propeller is envisaged to be a critical component within a year 2050 GOR engine. The un-ducted nature of the contra rotating propeller leads to a unique modelling approach for its steady state operation, as opposed to a conventional fan in a ducted turbofan. There are a series of 2D methodologies that are based on blade element methods coupled with either momentum models, lifting-line models or vortex models to capture the performance of a CRP array[16]. Higher fidelity models include 3D methods to capture the performance of a CRP array [16]. However, due to the computational cost involved with these higher fidelity methods, a 1D methodology, first introduced by Bellocq. et al., is deemed the most suitable to predict the performance of a CRP array. This methodology couples a blade element method approach and a stream-tube contraction approach that is based on momentum models [16]. This segment of the thesis focuses on a bespoke 1D method to predict the performance of the CRP propeller array, which has been introduced previously by Bellocq et al. The following assumptions are employed for the 1D CRP performance methodologies [16]:

- It is assumed that the performance of the CRP array is estimated at 75% span[16]. The performance of the CRP is resolved at 75% span as it coincides with the spanwise location of the mean aerodynamic chord of the propeller.
- The effect of gust loads, acting perpendicular or tangentially to the propeller arrays are not accounted for.
- The effect of blade passing frequency on the performance is not accounted for.

- Blade element methods are utilised to determine the 1D performance of the CRP array [108].
- Each propeller is assumed to work on the flow field generated by the flight speed and the effects of the other propeller. The influence of the rear propeller (subscript 2) on the velocity field of the forward propeller (subscript 1) is called interference velocity of the rear propeller on the forward propeller and is denoted by $V_{ind_{21}}$ (similar definition for $V_{ind_{12}}$). $V_{ind_{21}}$ can be reduced in to axial and tangential vectors as $V_{ind_{21A}}$ and $V_{ind_{21T}}$ (analogous definition for $V_{ind_{12A}}$ and $V_{ind_{12T}}$). Refer to Figure 4-3 for clarification with regards to the component velocities[16].
- It is assumed that radial flows incipient to both propellers have a negligible impact on the performance of the CRP propeller array.
- Each propeller produces its own induced velocity ($V_{ind_{11}}$ and $V_{ind_{22}}$). It corresponds to the change in velocity (both axial and tangential) produced by the operation of each propeller. $V_{ind_{ii}}$ for a propeller operating in a CRP arrangement is assumed to be equal to $V_{ind_{ii}}$ for a single rotating propeller (SRP) operating in isolation in the velocity field produced by the flight speed and the effects of the other propeller[16].
- The velocities induced by each propeller have a periodic characteristic. They are replaced by magnitudes equal to the time average of the induced velocities.
- The tangential interference velocity of the rear propeller on the forward propeller ($V_{ind_{21T}}$) is neglected for being an order of magnitude smaller than other interference velocities [109].
- It is assumed that the nacelle diameter does not change from the forward to the rear propeller[16].
- It is assumed that the density of air does not vary when resolving the flow velocity triangles between the forward and rear propeller.
- In order to determine the off-design performance of the CRP array, the same map is used for the forward and rear propeller[16].
- $V_{ind_{21A}}$ and $V_{ind_{12A}}$ are uniform for every blade element of the propeller[16].
- $V_{ind_{12T}} = \Omega_{ind_{12r}}$ with constant blade rotational speeds between the forward and rear propellers. It is assumed that the tangential induced velocity component of the forward propeller on the rear is equivalent to the induced tangential blade speed, which is assuming that the induced tangential blade speed is constant at design point [16].

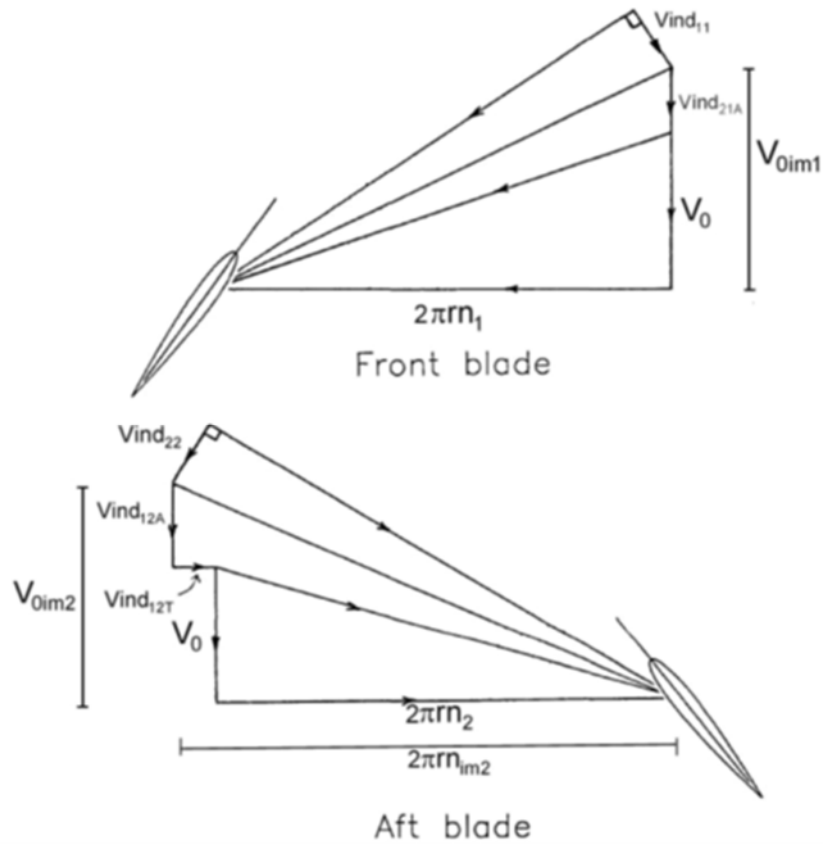


Figure 4- 3: Non-dimensional Velocity triangle at 75% blade span[16]

The performance of the CRP can be estimated via an iterative process, which involves the estimation of the forward propeller and the rear propeller performance respectively. The following sub-sections highlight the calculation procedure employed in estimating the performance of the contra rotating propeller array.

4.2.1.1 Forward Propeller performance estimation

The CRP performance is done iteratively because both propellers influence each other and their equations have to be solved simultaneously. Therefore, for this methodology, $V_{ind_{21A}}$ (axial induced velocity of the rear propeller on the forward propeller) is used as an iteration variable; it is guessed at the beginning of the CRP calculation process and is obtained at the end. The input power to each propeller, the diameters of the propellers (D), the flight speed (V_0), ambient conditions and rotational speeds of the propellers (n) are known (input variables). Since $V_{ind_{21A}}$ is the same for every blade element, an imaginary flight velocity (V_{0im1}) can be calculated as [16]:

$$V_{0im1} = V_0 + V_{ind_{21A}} \quad 4-3$$

Consequently, an imaginary advance ratio (J_{im1}) can be calculated for this imaginary flight condition, and is expressed as:

$$J_{im1} = V_{0im1}/n_1 D_1 \quad 4-4$$

The propeller efficiency is defined as an input (η_{allow}) and is corrected for compressibility losses as defined by Equation 4-5 to Equation 4-7 (The flight Mach number (M_0) is calculated as V_{0im1}/a , where 'a' refers to the speed of sound). These efficiency corrections are based on the fact that SRP efficiency reduces significantly, regardless of the propeller advance ratio, after a helical Mach number (defined as the helical Mach number at 75% of the propeller span, where the helical Mach number is representative of the relative Mach number in compressor theory) of ~ 0.9 ($M_{*H0.75}$) illustrated by Figure 4-4 [110]. The variable $Slope_{corrM}$ in Equation 4-5 refers to the linearized slope of the graph in Figure 4-4, at helical Mach numbers above 0.9. The helical Mach number at 75% span of the blade is provided by Equation 4-6, which indicates that it is dependent on the flight Mach number (M_0) and the imaginary advance ratio (J_{im1}).

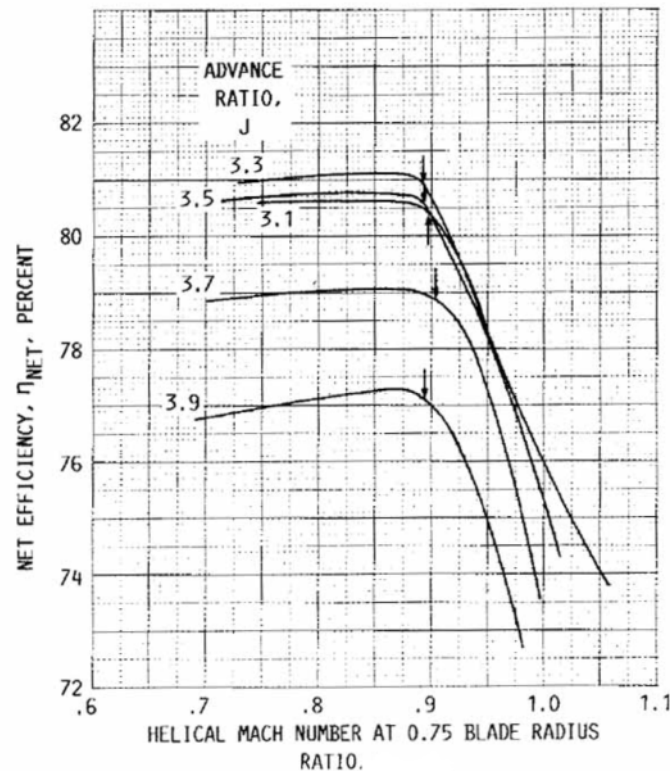


Figure 4- 4: net propeller efficiency correction as a function of helical Mach number[16]

$$\eta_{net} = \eta_{allow} - (M_{H0.75} - M_{*H0.75}) Slope_{corrM} \text{ for } M_{H0.75} > M_{*H0.75} \quad 4-5$$

$$M_{H0.75} = M_0 \left(1 + \left(\frac{0.75\pi}{J_{im1}} \right)^2 \right)^{0.5} \quad 4-6$$

In order, to predict the off-design behavior of the propeller (either forward or rear propeller) at a particular power setting and a shaft speed, a scaled map of the SR-7 propeller is used [111]. The design point choices of the coefficient of power, advance ratio and propeller efficiency provide the scaling factors for the un-scaled SR-7 map. At off-design conditions the propeller efficiency is derived from the scaled map (Figure 4-5 is a representative propeller map) and is a function of the propellers' diameter, shaft speed and required coefficient of power at a prescribed flight condition[16].

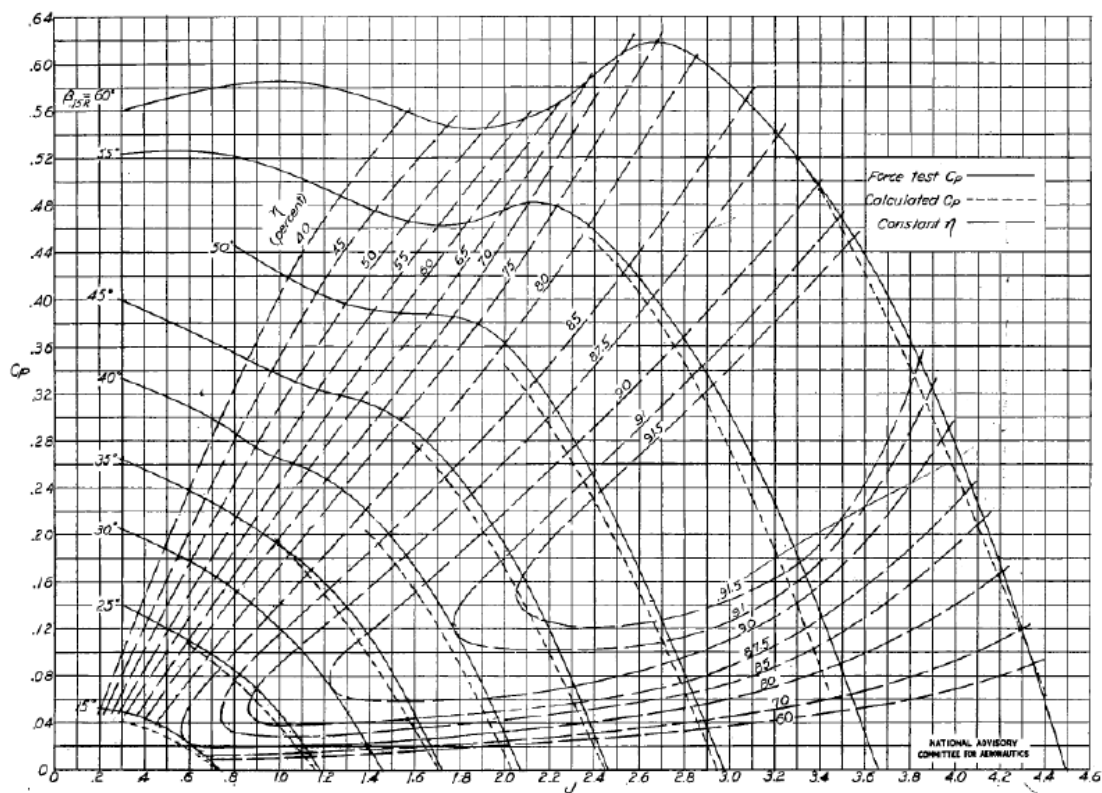


Figure 4- 5: representative single propeller map [16]

The original SR-7 map is scaled linearly at design point, in order to establish the operational bounds of both the forward and rear propellers, and is represented by Equation 4-7 to Equation 4-9. Where the constituent values of the unscaled map are indicated by $C_{pwr,map}$, η_{map} and J_{map} .

$$C_{pwr} = C_{pwr,map} SF_{Cp} \quad 4-7$$

$$\eta_{allow} = \eta_{map} SF_{\eta} \quad 4-8$$

$$J = J_{map} SF_j$$

4-9

In order, to define the allowable propeller efficiency (user defined input) a dedicated function is used to determine the allowable propeller efficiency, for both the forward and rear propellers. By digitizing Figure 4-6 and Figure 4-7 from NASA TM 83733 [111], it is possible to estimate the allowable propeller efficiency as a function of the power loading, number of blades and a technology factor. Figure 4-6 estimates the propeller efficiency of a single propeller array with a blade count lower than 8, whereas Figure 4-7 accounts for the propeller efficiency estimation for blade count higher than eight. The primary reason why a technology factor was added to this estimation is because these trends are representative of propeller technology circa 1980. In order to give an apt representation of the state of the art propeller design, a technology factor was introduced and is presented in Equation 4-10. In Equation 4-10, the technology factor ranges from unity to 1.3[16].

$$\eta_{allow} = 0.975 - \frac{\text{Power loading}(0.975 - f(\text{number of blades}))}{560 (TF)} \quad 4-10$$

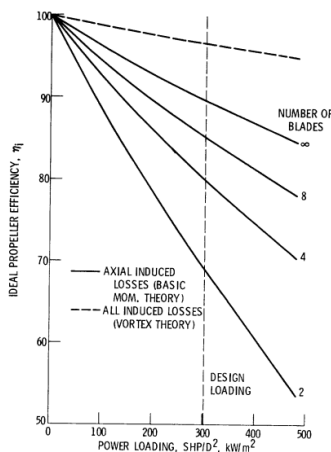


Figure 4- 6: Propeller efficiency as a function of the number of propeller blades and propeller loading

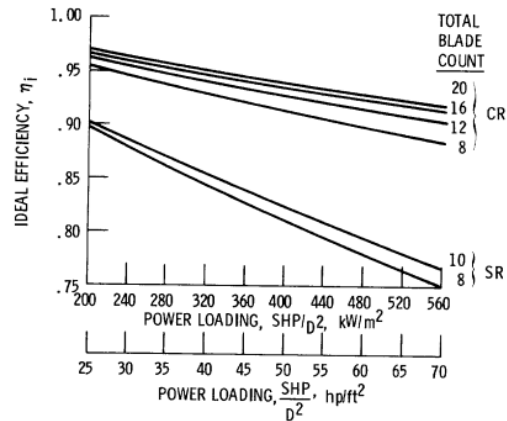


Figure 4- 7: Propeller efficiency estimation as a function of the number of propeller blades and propeller loading

Once the allowable propeller efficiency, for each array, is defined the net thrust for each propeller array can be estimated. The net thrust generated by each propeller array is estimated as function of the propeller disc area (A_{disc}), propeller rotational speed (n), Thrust coefficient (C_T), propeller diameter (D), density of air (ρ), net propeller efficiency (η_{net}) and

the imaginary advance ratio (J_{im}) as indicated by Equation 4-11[16]. Equation 4-11, refers to the net thrust generated by the forward propeller. In order to estimate the net thrust generated by the rear propeller, the subscripts are changed from 1 to 2.

$$F_{n_1} = \rho n_1^2 D_1^2 A_{disc1} \left(\frac{C_{T1} \eta_{net1}}{J_{im1}} \right) \quad 4-11$$

The theoretical area that produces the thrust, per propeller array, is determined by the propeller tip diameter (D_1) and hub to tip ratio of the forward propeller to nacelle diameter (D_1/D_h) and is determined in Equation 4-12.

$$A_{disc} = \frac{\pi}{4} D_1^2 \left(1 - \left(\frac{D_h}{D_1} \right)^2 \right) \quad 4-12$$

The coefficient of thrust (C_T) that contributes to the net thrust of each propeller array is determined by the shaft power transmitted ($P_{w_{mech}}$), air density (ρ), propeller diameter (D), shaft speed (n), and propeller disc area (A_{disc}). Equation 4-13, determines how the coefficient of thrust is estimated for each propeller array, as indicated by the value of the sub-script.

$$C_{T1} = \frac{P_{w_{mech1}}}{\rho n_1^3 D_1^3 A_{disc1}} \quad 4-13$$

It is also assumed that by EIS 2050 pylon blowing, for noise attenuation purposes [112], will feature in installed rear-fuselage GOR engine designs. Hence a methodology, has been introduced to account for the performance implications of pylon blowing. Figure 4-8 illustrates the hypothetical arrangement of the pylon blowing system.

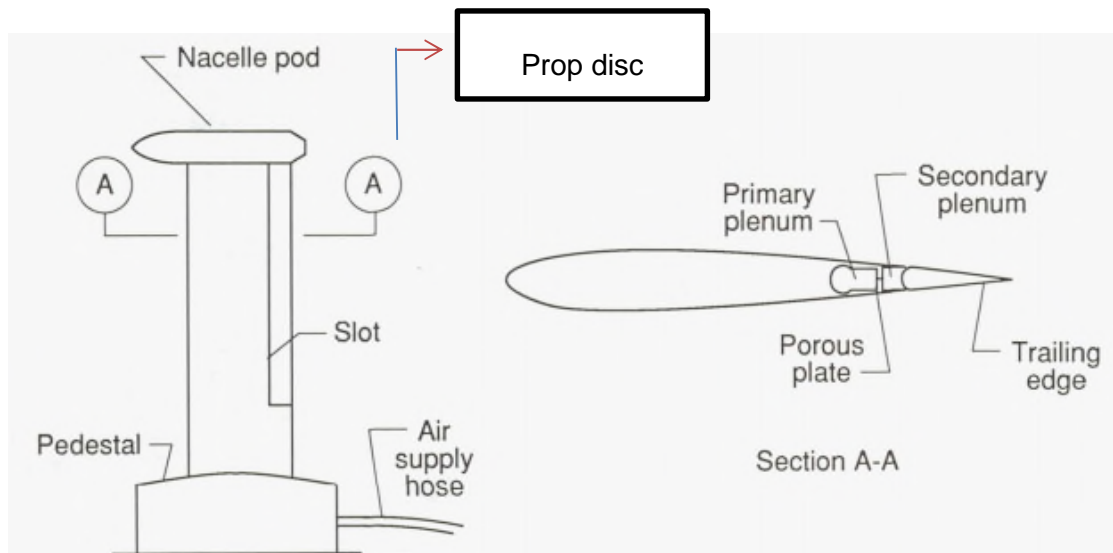


Figure 4- 8: General arrangement of an experimental trailing edge Pylon blower[113]

The methodology that has been earmarked to account for the pylon blowing performance effects is based on the results of the experimental work highlighted in NASA TM 4162 [113]. The main assumptions that will be employed are:

- Pylon blowing affects the coefficient of thrust (C_T) of the propellers at high flow deflections ($B_{@0.75 \text{ span}} > 40^\circ$) and at relatively high imaginary advance ratios ($J > 1.2$).
- The methodology does not account for high dynamic pressures and tip Mach numbers higher than 0.75, as the experiment was performed at low speed conditions.
- The pylon fairing is assumed to have the NACA 0012 profile.
- It is assumed that the velocity vector emanating from the trailing edge of the pylon fairing, matches that of free-stream conditions.
- It is assumed that the power required to power the pylon blowing system comes from the on-board fuel cells, therefore no power will be extracted from the engine.

As of now it is envisaged that when the flow deflection of the forward propeller of the CRP exceeds 40° and the advance ratio exceeds 1.2, the Pylon blower will be activated and it shall be deactivated when these conditions are not met. Due to the instantaneous increase in the angle of attack of the propeller blades (at high flow deflection and advance ratios) because of the pylon wake, the efficiency of the propeller reduces - and hence the thrust coefficient reduces as well [113]. Therefore, if pylon blowing is present, a correction of the thrust coefficient is required. The effects have been summarized in Figure 4-9, where the change between thrust coefficients for the pylon blowing were plotted as a function of advance ratios [113].

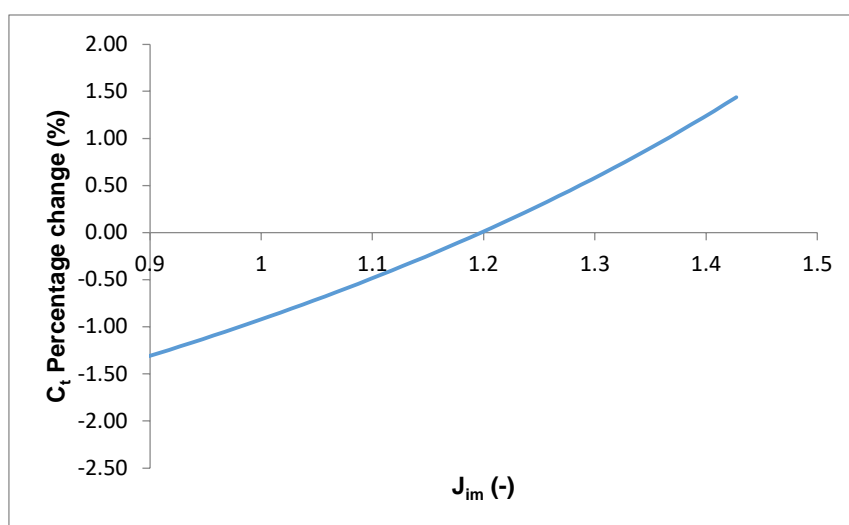


Figure 4- 9: Coefficient of thrust correction as a function of imaginary advance ratio.

Consequently, Equation 4-14 encapsulates how the performance effects of pylon blowing have been captured in the CRP model (for both the forward and rear propellers), where δ_{ct} represents the percentage correction to the coefficient of thrust and J_{im} refers to the imaginary advance ratio.

$$\delta_{ct} = 2.6863J_{im}^2 - 1.0988J_{im} - 2.5117 \quad \mathbf{4-14}$$

4.2.1.2 Rear Propeller performance prediction

Once the performance of the forward propeller has been ascertained the performance of the rear propeller can be calculated. The calculation of the thrust of the rear propeller can be deconstructed into four distinct steps, which are presented below.

4.2.1.2.1 Obtaining Flow conditions for the rear propeller

The inlet velocity conditions to any section of the rear propeller are defined by the flight velocity (V_0), the axial component of velocity induced by the forward propeller on the rear propeller ($V_{ind_{12A}}$) and the tangential component of velocity induced by the forward propeller on the rear propeller ($\Omega_{ind_{12}}$). The magnitude of these velocities are determined using a combination of momentum theory and a stream tube contraction model [108][114]. Equation 4-15, indicates that the axial velocity component induced by the forward propeller on the rear propeller can be derived from the net thrust of the forward propeller (F_{n1}), forward propeller disc area (A_{disc1}), air density (ρ), relative axial spacing between the forward and rear propeller (z_{12}/r) and the imaginary flight velocity incipient to the forward propeller (V_{oim1})[16].

$$V_{ind_{12A}} = \left(\left(\left(V_{oim1}^2 + \left(\frac{2 F_{n1}}{\rho A_{disc1}} \right) \right)^{0.5} - V_{oim1} \right) 0.5 \right) \left(1 + \frac{\frac{z_{12}}{r_1}}{\left(1 + \left(\frac{z_{12}}{r_1} \right)^2 \right)^{0.5}} \right) \quad \mathbf{4-15}$$

Once the axial induced velocity is ascertained, it is necessary to calculate the tangential induced velocity. Momentum theory considers that the torque applied by the actuator disk is equal to the change in angular momentum of the flow crossing the actuator disk[108] [115]. The torque balance of the propeller actuator disc, as per propeller theory, at any radial position (r) can be expressed by Equation 4-16[16], where Q refers to the torque applied by actuator disc.

$$Q(r) = 2\pi r (V_0 + V_{ind_A}(r)) V_{ind_T}(r) r \cdot dr \quad \mathbf{4-16}$$

Assuming that the tangential induced velocity is equivalent to the blade speed ($V_{ind_T}(r) = \Omega_{ind} r$) and the distribution of the axial induced velocity ($V_{ind_A}(r) = V_{ind_A}$) on the propeller blade is uniform from the hub to the tip of the propeller span, an integration of Equation 4-16

results in a definite integral that estimates the torque applied by each propeller disc. Equation 4-17 indicates the derived torque applied by the forward propeller at 75% span.

$$Q_1 = 0.5\pi\rho \left(V_{0im1} + \left(\left(\left(V_{0im1}^2 + \left(\frac{2Fn_1}{\rho A_{disk1}} \right)^{0.5} - V_{0im1} \right) 0.5 \right) \right) \right) \Omega_{ind_{11}} (r_1^4 - r_h^4) \quad \mathbf{4-17}$$

Finally, $\Omega_{ind_{12}}$ (induced tangential velocity of propeller 1 on propeller 2) is considered to be equal to $\Omega_{ind_{11}}$ and therefore considered not affected by the stream contraction [16].

4.2.1.2.2 Establishing rear propeller thrust coefficient and advance ratio

Since $V_{ind_{12A}}$ is equal for every blade element, an imaginary flight velocity (V_{0im2}) can be expressed by Equation 4-18[16].

$$V_{0im2} = V_0 + V_{ind_{12A}} \quad \mathbf{4-18}$$

Since $V_{ind_{12T}} = \Omega_{ind_{12}}r$, with constant $\Omega_{ind_{12}}$, an imaginary rotational speed (n_{im2}) can be defined by adding the tangential component of the velocity due to the rotation of the propeller and the tangential component of the induced velocity of the forward propeller. This relationship is expressed in Equation 4-19 [16].

$$2\pi r n_{im2} = 2\pi r n_2 + \Omega_{ind_{12A}}r \quad \mathbf{4-19}$$

Consequently, an imaginary advance ratio can be calculated for this imaginary operating condition, expressed by Equation 4-20 [16].

$$J_{im2} = V_{0im2}/n_{im2}D_2 \quad \mathbf{4-20}$$

The imaginary thrust coefficient ($C_{T_{im2}}$) and imaginary advance ratio (J_{im2}) define the operating point of the rear propeller on the propeller performance map. The power required for the rear propeller ($P_{w_{mech_{im2}}}$) is calculated by Equation 4-21, assuming the torque ratio (TR) between the forward and rear propeller is defined [16].

$$Q_{im2} = TR/(Q_1) = \frac{P_{w_{mech_{im2}}}}{n_{im2}} = \frac{P_{w_{mech}}}{n_2} \quad \mathbf{4-21}$$

Consequently, the imaginary thrust coefficient ($C_{T_{im2}}$) can be calculated by Equation 4-22 [16].

$$C_{tim2} = \frac{P_{w_{mech_{im2}}}}{\rho n_{im2}^3 D_2^3 A_{disk2}} \quad \text{with} \quad A_{disk2} = \frac{\pi}{4} D_2^2 \left(1 - \left(\frac{D_h}{D_2} \right)^2 \right) \quad \mathbf{4-22}$$

4.2.1.2.3 Obtaining net thrust of the Rear propeller

As mentioned earlier, the resultant force vectors for the real and imaginary cases are equal. This implies that the thrusts for both cases are equal and can be calculated by Equation 4-23. In addition, it is essential to correct the net propeller efficiency for compressibility effects using Equation 4-4 through to Equation 4-6.

$$F_{n_2} = \rho n_{im2}^2 D_2^2 A_{disk2} \left(\frac{C_{t_{im2}} \eta_{net_{im2}}}{J_{im2}} \right) \quad 4-23$$

4.2.1.2.4 Recalculate $V_{ind_{21A}}$

Once the thrust of the rear propeller is known, its corresponding induced velocity can be derived by Equation 4-24, which is similar to Equation 4-15.

$$V_{ind_{21A}} = \left(\left(\left(V_{0im2}^2 + \left(\frac{2 F_{n_2}}{\rho A_{disk2}} \right)^{0.5} - V_{0im2} \right) \right)^{0.5} \right) \left(1 + \frac{-\frac{z_{12}}{r_2}}{\left(1 + \left(\frac{z_{12}}{r_1} \right)^2 \right)^{0.5}} \right) \quad 4-24$$

Finally, the CRP performance calculation process can be repeated using $V_{ind_{21A}}$ in an iterative process. The procedure, highlighted in the aforementioned sections provides a brief overview of the methodology employed to estimate the performance of a CRP arrays for an EIS of 2050. In order for convergence to be achieved the guess of $V_{ind_{21A}}$ should be equivalent to the calculated value. Figure 4-10 shows a graphical overview of the entire process.

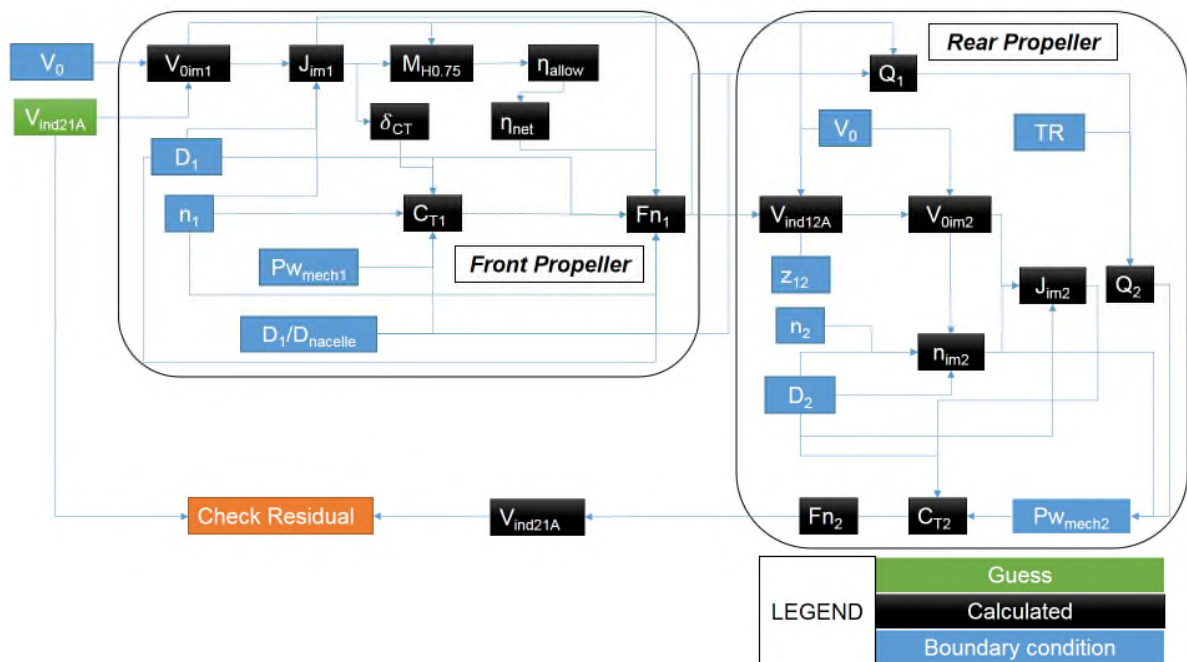


Figure 4- 10: Schematic overview of iterative process to determine CRP performance.

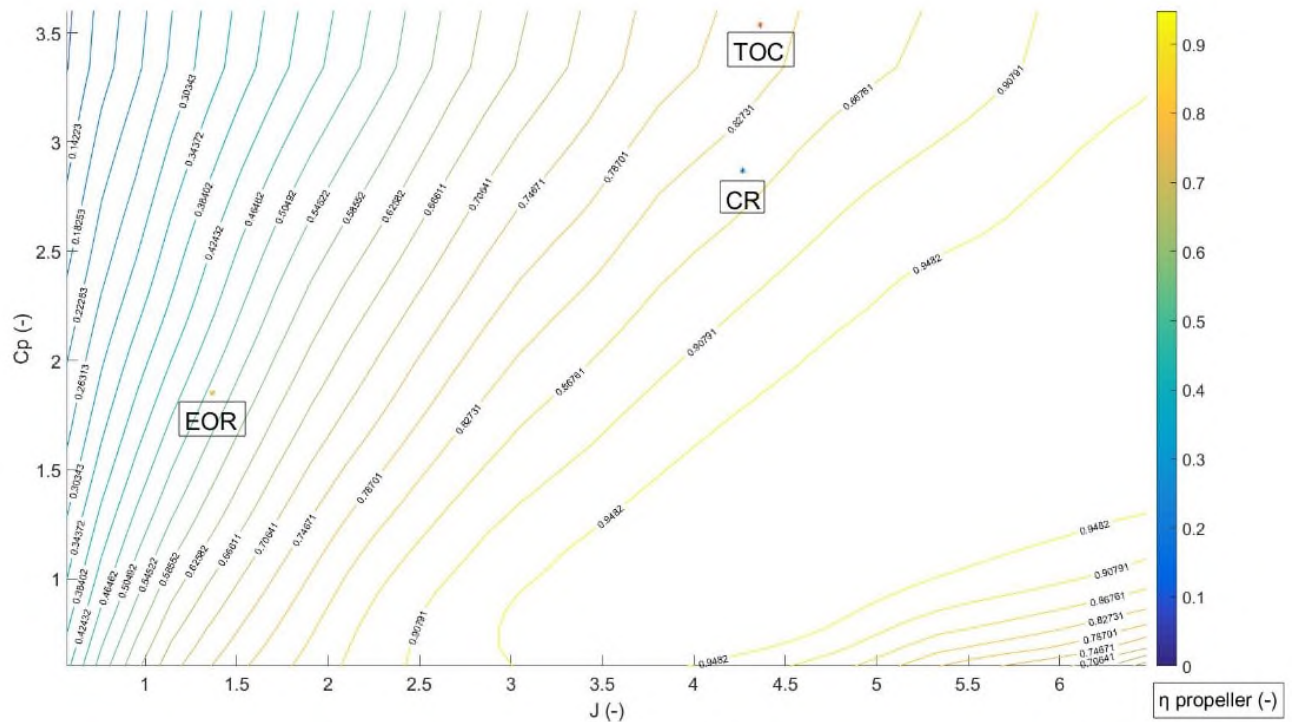


Figure 4- 12: Rear Propeller map at three operating conditions

In order to determine the off-design performance of the CRP array, the scaling factors described in Equations 4-7 to 4-9 are used to scale the map, and the corresponding propeller efficiencies for each propeller disc array are derived from each map separately. The bandwidth of the scaling factors for the coefficient of power and advance ratio tends from zero to three, which is dependent on the power demanded from the CRP array.

The aforementioned methods are used to estimate the performance of the CRP throughout the flight envelope, however it is not capable of estimating the performance of the CRP at static conditions as the performance of the CRP is highly dependent on the flight velocity. Therefore, to simulate static conditions a flight Mach number of 0.05 is chosen.

4.2.2 Differential planetary gearbox (DPGB) model

The differential planetary gearbox (DPGB) component model, within the geared open rotor, is considered to be an inline epicyclic gear train in a differential arrangement as opposed to a star arrangement [16]. In this configuration, it is assumed that the sun gear is connected to the concentric LP shaft and the ring and carrier gears are connected to the forward and rear propellers respectively. The design point performance of the DPGB is characterized by Equation 4-25 to Equation 4-28. The design point performance is estimated by specifying a torque ratio value (TR), which in turn dictates the ratio of the radii of the planet gears compared to the sun gear (k) or ($R_{carrier}/R_{sun}$). Consequently, operational speeds are assigned

to the ring (N_{ring}) and carrier ($N_{carrier}$) gears, which in turn establish the speed of the sun gear (N_{sun}). Finally, a torque balance is performed to derive the available power to the forward and rear propellers for a given mechanical transfer efficiency. This is characterized by Equation 4-27 to Equation 4-28.

$$k = 2 - \frac{TR}{-2 + 2TR} = R_{carrier}/R_{sun} \quad 4-25$$

$$N_{Sun} = N_{Ring}(1 + 2k) + N_{Carrier}2(1 + k) \quad 4-26$$

$$-Q_{Ring} = Q_{sun}(1 + 2k)\eta_{mech} \quad 4-27$$

$$Q_{carrier} = 2Q_{sun}(1 + k)\eta_{mech} \quad 4-28$$

The off-design operation of the DPGB is characterized by a map [62]. The provided map, illustrated in Figure 4-13, expresses the mechanical efficiency of a DPGB as function of the non-dimensional input torque and rpm. The variation in the mechanical transmission efficiency throughout the flight envelope leads to a variation in the steady state heat rejection of the DPGB, this relationship is quantified by Equation 4-29. Where the rejected heat $Heat_{DPGB}$ is expressed in kW, the power transmitted by the LPT P_{WSUN} is expressed in kW and the overall mechanical efficiency is dependent on the flight condition.

$$Heat_{DPGB} = P_{WSUN}(1 - \eta_{mech}) \quad 4-29$$

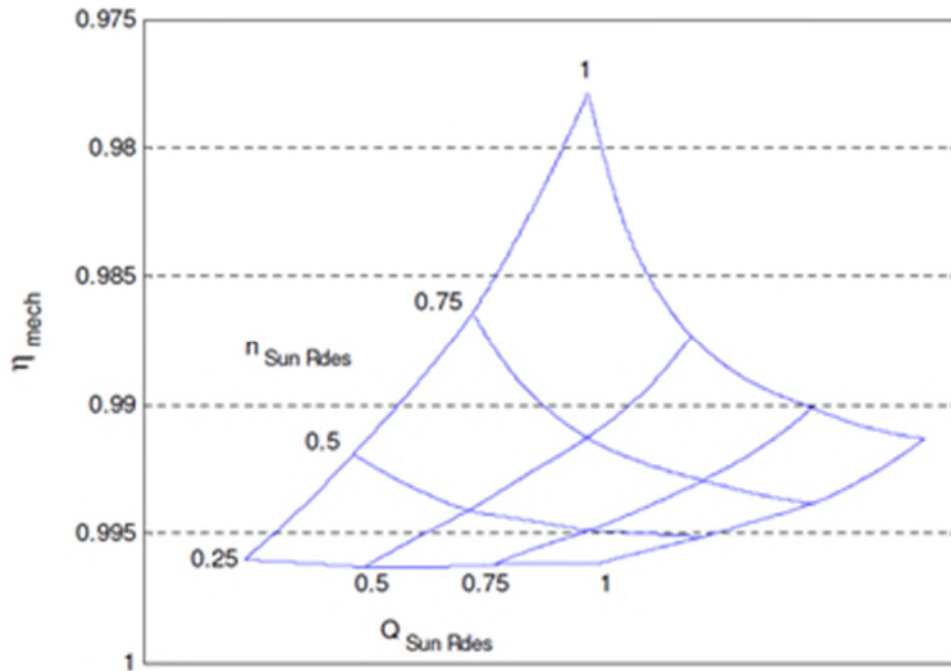


Figure 4- 13: Non-dimensional planetary gearbox map

4.2.3 DPGB cooling model

The scale effects of the core, when compared to an EIS2000 SR engine model, suggests that an independent air-oil cooling system would be necessary for high torque DPGB designs [16]. Moreover, it is considered that this air-oil cooling system would be independent of the air-oil-fuel cooling systems that would be used for the bearings, shafts and sumps of the rest of the core turbomachinery components. Due to this assumption, based on available literature, a separate air-oil cooling system has been included in the GOR model. A schematic of the modelled air-oil cooling system and the corresponding station numbers are illustrated in Figure 4-14. Essentially, the gearbox cooling system consists of a scoop inlet that ingests cool ambient air. This is facilitated by a single stage axial compressor, powered by a mechanical power off-take, which in turn pumps the relatively cooler air in to the cross-flow air-oil heat exchanger. Finally the spent air is ejected through a separate nozzle.

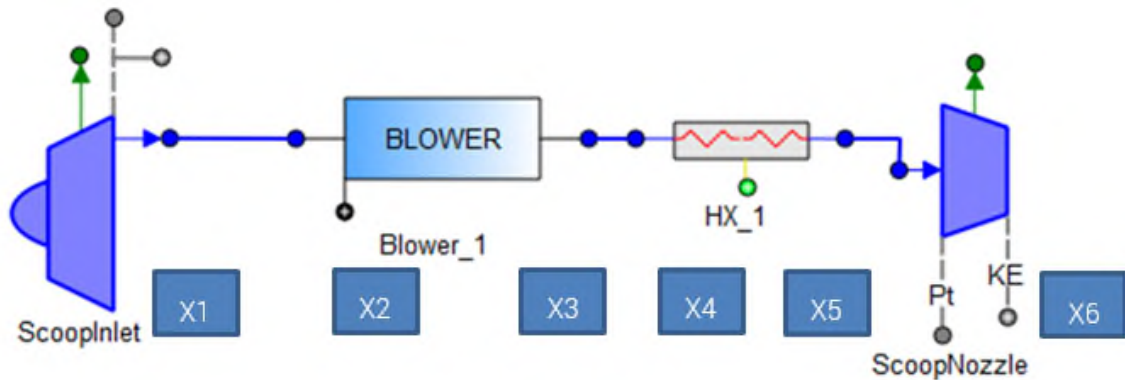


Figure 4- 14: PROOSIS schematic of DPGB cooling system

The assumptions and features that have been added with regards to modelling the air-oil cooling system are listed below:

- The, steady state, heat rejected from the DPGB is equivalent to the enthalpy rise across the heat exchanger.
- Total pressure loss and cooling effectiveness are prescribed, rather than being calculated as a function of the geometry of the heat exchanger, fluid properties of the oil and geometrical constraints.
- The current implementation of the 'blower' component does not account for the implementation of a map; therefore, it has a fixed efficiency (0.88) at all operating conditions[16].
- The 'blower' compressor component is activated below a fixed Mach number of 0.35, below which it is assumed that the ram compression is inadequate [16]. At these conditions the blower component extracts power from the HP spool in order to power

it. However in practice, the blower would be activated at an altitude lower than 15,000 feet.

- The scoop nozzle area scales as a function of the enthalpy rise across the heat exchanger at design point.
- There is no current limitation of the Scoop nozzle exhaust gas temperature (EGT).

The equations that are used to model the ScoopInlet and the ScoopNozzle are inherited from Turbo library 3.23 [95]. A rigorous design method to estimate the performance of the heat exchanger has been omitted. Instead, rudimentary pressure loss relationships and an enthalpy balance were imposed across the heat exchanger as indicated in Equation 4-30 to 4-31.

$$P_{X5} = P_{X4}(1 - dPqP) \quad 4-30$$

$$Heat_{DPGB} = W_{scoop} Cp(Tt_{X5} - Tt_{X4})\epsilon_{cooling} \quad 4-31$$

4.2.4 Nozzle duct pressure loss model

The root of the CRP array passes radially through the duct between the LPT and the core nozzle of the GOR (see Figure 4-15 for clarification). Generally, a fixed total pressure loss figure would suffice. However, as the total pressure loss would be a function of the blade speed and flow deflection a rudimentary model to account for these effects has been employed.

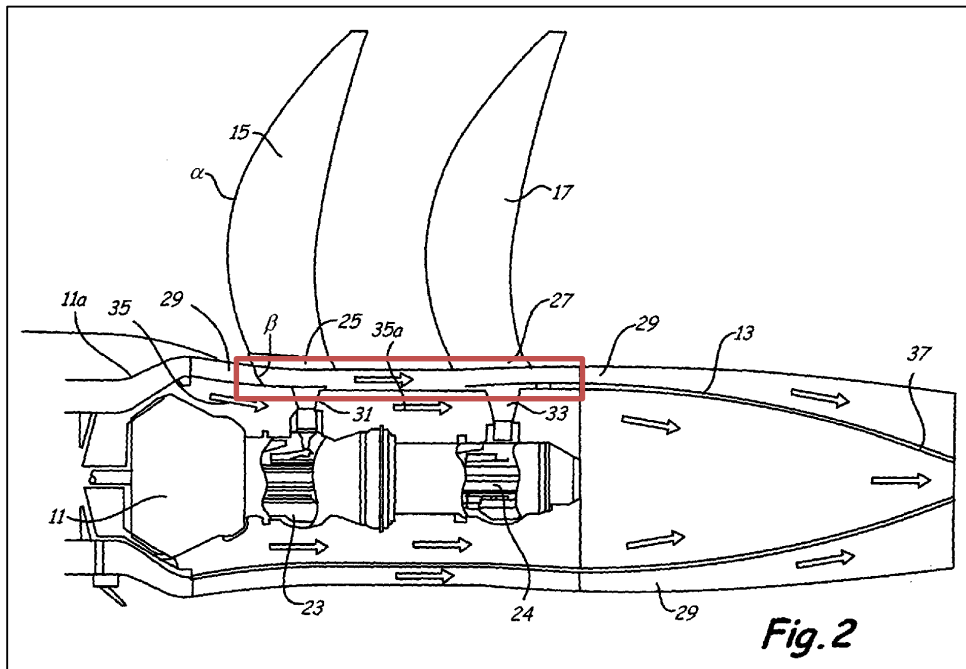


Figure 4- 15: Cross-section of the component under consideration[61]

The primary assumptions used in modelling the nozzle duct pressure loss effects are:

- It is assumed that the root section of the CRP's does not produce any useful work, and only contributes to the total pressure loss across the duct.
- The velocity triangle of the CRP at 75% span is assumed to be the same as that of the CRP cascade in the core section of the engine.
- The same aspect ratio is applied for both sets of blades.
- The pressure loss correlations are not valid for high deflection-impulse blading [116].

The total pressure loss (ξ_{total}) across the root CRP cascade is determined as a function of the flow deflection (ε) and the aspect ratio (b/H) of the cascade [116]. Equations 4-32 and 4-33 highlight the pressure loss approximations used. The magnitude of the total pressure ratio experienced within the model range from 1.25 at CR to 1.21 at EOR. In practice, it would be expected that some work would be transferred between the exhaust gases and the CRP root section, albeit a relatively small amount (325-375kW).

$$\xi_p = 0.025 \left(1 + \left(\frac{\varepsilon}{90} \right)^2 \right) \quad 4-32$$

$$\xi_{total} = \xi_p \left(1 + \left(\frac{3.2b}{H} \right) \right) \quad 4-33$$

4.3 Nutating Disc Engine Model

The design point methodology, for a naturally aspirated and turbo-charged ND engine systems are discussed in the following sections. It includes the discussion of a methodology to describe the thermodynamic performance of either a single disc or dual disc nutating disc engine system, a sizing methodology and a methodology to estimate the size and performance of the plenums that connect the axial compressors and turbines to the ND engine systems in the turbo-charged configurations.

4.3.1 Nutating disc performance model

The thermodynamic cycle that best describes a nutating disc engine system is similar to a dual cycle, where it is part Otto cycle and part Diesel cycle [1]. Figure 4-16 shows a P-V diagram that represents the thermodynamic processes within a single nutating disc engine system, as well as a top-down view of a single nutating disc engine system configuration in order to map the thermodynamic processes with the subcomponents of a single nutating disc engine system arrangement. The thermodynamic process in this instance has only been

described for a single disc engine system, however it can be extended to a dual disc or multi disc arrangement.

The thermodynamic processes of the cycle can be expressed as follows:

- Air enters a single disc ND engine system through an elbow duct, and is ported in to the ND compression chamber through a triangular admittance port located on the surface of the inlet wedge.
- Process 01-02, then accounts for the mass and time averaged adiabatic compression of the air.
- Once the compression process is completed, the compressed air is admitted in to an accumulation chamber, through a non-return valve or solenoid-controlled pneumatic valve. This admittance of air is expressed as the Process 02-03, and is represented as the adiabatic expansion of the compressed air from the compression chamber to the accumulator.
- Processes 03-04, represents the adiabatic expansion of the fluid from the accumulation chamber to the pre-combustion chamber, via a solenoid-controlled pneumatic valve[76].
- Once the compressed air has been admitted in to the accumulation chamber, fuel is added and via spark ignition constant volume combustion is achieved [1]. This process is represented by Process 04-05.
- It is assumed that the combustion process, will continue from the pre combustion chamber to a segment of the nutating disc expander. Hence it is assumed that, during this process the rate of heat addition to the working fluid and the rate of volumetric expansion would be equal, which consequently results in a constant pressure combustion process. This is represented by Process 05-06 [1].
- Once the flame front is extinguished, the expander section of the nutating disc adiabatically expands the working fluid, which is represented by process 06-07.
- Finally, the products of combustion are expelled through exhaust ports, located on the upper and lower casing of the single nutating disc engine configuration.

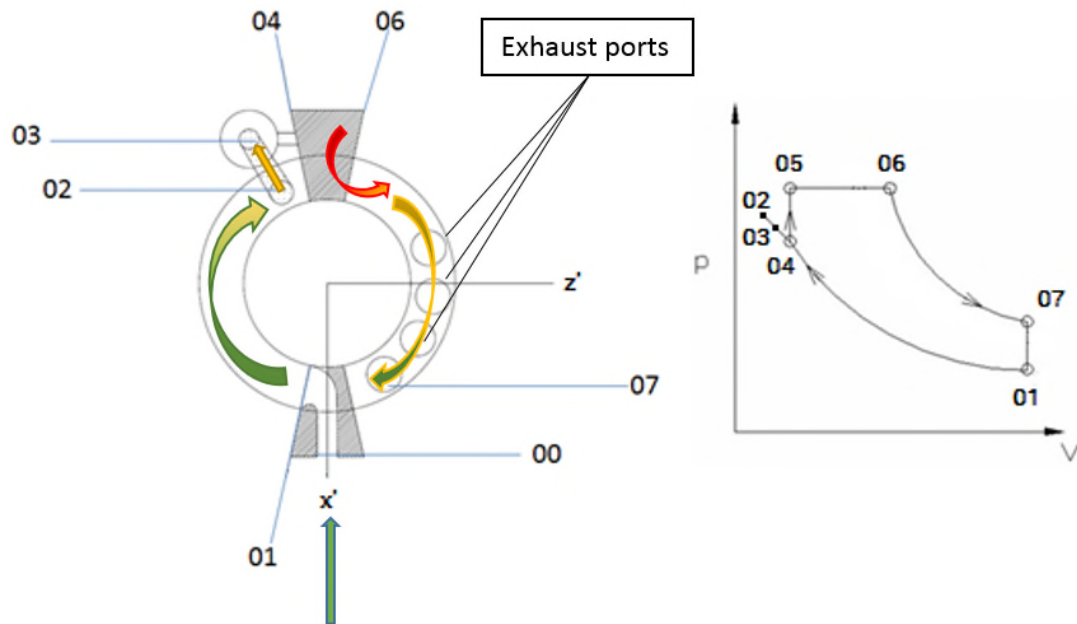


Figure 4- 16: Mapping thermodynamic stations to geometry of a naturally aspirated ND engine

The aforementioned thermodynamic processes occur on both sides of the single nutating disc structure and overlap each other by a phase angle of 90° . This in turn indicates that it is possible to achieve two complete cycles per shaft revolution (as the compression and expansion thermodynamic processes on one side of the disc last for 270°) as opposed to 2-stroke and 4-stroke internal combustion engines- where one can obtain one or half a complete cycle respectively [1].

When one considers a dual disc configuration, one disc is dedicated for compression and one disc is used for expansion. Furthermore, as opposed to the single disc configuration, the products of combustion are expelled through an elbow duct rather than exhaust ports. The choice of nutating disc engine system configuration, does not have a bearing on the fundamental performance of the nutating disc but affects the mass and thermal stressing of the components[1].

Before delving in to the fundamental thermodynamic equations that govern the performance of a ND engine system, it is necessary to list the assumptions and limitations that dictate the steady state performance. The assumptions are:

- The compression and expansion process is assumed to be adiabatic.
 - The limitation of this assumption is that since the compression and expansion process is dynamic, one fails to account for heat loss through the

casing in the compression and part of the expansion process.

- It is assumed that the adiabatic compression and expansion efficiency is chosen and is independent of the operating conditions.
 - The limitation of this assumption is that since adiabatic compression and expansion efficiency will be dictated by the amount of turbulence generated in the chambers of the nutating disc, the Reynolds number effect, efficacy of sealing and heat flux through the casing.
- It is assumed that the volumetric efficiency stays constant throughout the cycle, regardless of the operating speed.
 - Since the ND engine is a quasi-continuous flow machine, there will be a degree of mass accumulation in the displacement chambers. This aspect of positive displacement machines tends to vary the amount of air induced in to the machine per cycle as a function of the operating speed[117].
- It is assumed that the mechanical transmission efficiency remains constant at varying operating speeds.
 - Due to the complex nature of the transmission mechanism, between the expander and the compressor. A slight mass unbalance in the shaft can have implications on the shaft eccentricity and hence affect the mechanical transmission efficiency at different operating speeds.
- It is assumed that the total pressure loss in the inlet elbow duct is independent of the operating speed.
 - The total pressure loss in the inlet elbow duct will vary with the operating speed of the device.
- It is assumed that the volumetric compression ratio is fixed throughout the operation of the ND engine system.
 - Although the theoretical compression ratio remains constant, when defining the geometry of the ND engine. In reality, the actual volumetric compression ratio that determines the average pressure rise or drop in either the compressor or expander will depend on the efficiency of the seals, the timing of the valves in the process and the timing of the fuel injected in the process. Hence, the volumetric compression ratio could potentially change as a function of the operating speed.

- The scavenging efficiency term, commonly included as a separate term during the exhaust process is assumed to be included in the expansion process.
 - The scavenging efficiency will be determined by the volumetric flow rate and the characteristics of the exhaust valve or port [117].

The following equations are used to calculate the thermodynamic performance of either a single disc or dual-disc nutating disc engine system. Moreover, it must be mentioned that the station numbering is consistent with Figure 4-16. The mass and time averaged mass flow admitted in to the nutating disc engine is expressed by Equation 4-34 and it is a function of the volumetric efficiency (η_v), swept volume (V_{sw}), operational speed (N_s), intake density (ρ_{il}) and power cycles per shaft revolution (k)[1].

$$\dot{m}_a = k\eta_v\rho_{il}V_{sw}N_s \quad \mathbf{4-34}$$

Equation 4-35 to 4-38 indicate the volumetric ratios of the respective chambers, where Equation 4-35 indicates the volumetric compression ratio of the nutating disc engine (r_{12}). Equation 4-36 and Equation 4-37 indicate the volumetric expansion ratio from the end of the compression process to the accumulation chamber (r_{23}) and the volumetric expansion ratio from the accumulator to the combustion chamber (r_{34}), respectively. Equation 4-38 is indicative of whether the cycle is over or under-expanded (r_{71}) [1].

$$r_{12} = r_c = \frac{V_1}{V_2} > 1 \quad \mathbf{4-35}$$

$$r_{23} = \frac{V_2}{V_3} < 1 \quad \mathbf{4-36}$$

$$r_{34} = \frac{V_3}{V_4} < 1 \quad \mathbf{4-37}$$

$$r_{71} = \frac{V_7}{V_1} \quad \mathbf{4-38}$$

The properties of the working fluid (air) are evaluated by polynomial functions as a function of the average temperature (T_a, T_b) and the fuel to air ratio (FAR)[80]. Consequently, the isobaric (\overline{C}_p) and isochoric (\overline{C}_v) specific heat capacities and gas constant (R) are expressed by Equation 4-39 and Equation 4-40.

$$\overline{C}_p = C_p\left(\frac{T_a + T_b}{2}, FAR\right) \quad \mathbf{4-39}$$

$$\overline{C}_v = \overline{C}_p - R \quad \mathbf{4-40}$$

The inlet total pressure and total temperature are predicted by Equation 4-41 and Equation 4-42. Where the total inlet temperature is a function of the ambient atmospheric temperature (T_{at}) and the total inlet pressure is a function of both the ambient pressure (P_{at}) and the total pressure loss ($f_{pl,il}$) across the inlet.

$$T_{01} = T_{at} \quad \mathbf{4-41}$$

$$P_{01} = (1 - f_{pl,il})P_{at} \quad \mathbf{4-42}$$

The efficiency of the adiabatic compression process ($\eta_{s,c}$) and the compressor work (\dot{W}_c) are expressed by the following equations (Equation 4-43 to Equation 4-46). Where the pressure and stagnation temperature at the end of the compression process is expressed as P_{02} and T_{02} respectively.

$$T_{02,s} = T_{01} r_{12}^{\frac{R}{C_p}} \quad \mathbf{4-43}$$

$$P_{02} = P_{01} r_{12} \left(\frac{T_{02,s}}{T_{01}} \right) \quad \mathbf{4-44}$$

$$\eta_{s,c} = \frac{T_{02,s} - T_{01}}{T_{02} - T_{01}} \quad \mathbf{4-45}$$

$$\dot{W}_c = \dot{m}_a [\bar{C}_v (T_{02} - T_{01})] \quad \mathbf{4-46}$$

To evaluate the flow conditions in the accumulation chamber, one must adhere to the following equations. Where $P_{03,s}$ is the stagnation pressure after expansion from the end of the compression process to the accumulation chamber and $f_{pl,23}$ is the pressure drop across the non-return valves in between the compression chamber and the accumulation chamber. It must be mentioned that the same process is assumed to take place from the accumulation chamber to the pre-combustion chamber (from station 03 to 04), hence the equations have not been repeated[1].

$$P_{03,s} = P_{02} r_{23}^{\frac{\bar{C}_p}{\bar{C}_v}} \quad \mathbf{4-47}$$

$$P_{03} = P_{03,s} (1 - f_{pl,23}) \quad \mathbf{4-48}$$

$$T_{03} = T_{02} \left(\frac{P_{03}}{P_{02}} \right) (1/r_{23}) \quad \mathbf{4-49}$$

In order to model the combustion process, it is necessary to take the instantaneous maximum temperatures ($T_{06, mx}$, $T_{05, mx}$) into account that occur during the thermodynamic cycle - which is representative of a non-continuous combustion process. This is accounted for in the thermodynamic model by assigning heat loss factors ($f_{ql,cy}$) through the engine casing [1],

which ranges from 0 to 0.4. The following equations show the energy balance required to calculate the fuel flow. Furthermore, the ratio of constant volume combustion to constant pressure combustion is prescribed by choosing θ_1 , which can typically range from 10% to 90% [1]. θ_2 on the other hand determines the volumetric expansion ratio during the constant pressure combustion process and can also typically range from 10% to 90% [1]. The instantaneous temperature ratios (θ_2, θ_1), fuel to air ratio (FAR), fuel heating value (L_{hv}) and combustion efficiency (η_{bu}) are necessary to effectively predict the fuel flow (\dot{m}_f) for the thermodynamic cycle.

$$\frac{T_{mx}}{T_{at}} = \frac{T_{06,mx}}{T_{01}} \quad 4-50$$

$$\theta_1 = \frac{T_{06,mx} - T_{05,mx}}{T_{06,mx} - T_{04}} \quad 4-51$$

$$\dot{E}_{in} = (\dot{m}_a + \dot{m}_f)[\bar{C}_v(T_{05,mx} - T_{04}) + \bar{C}_p(T_{06,mx} - T_{05,mx})] = \dot{m}_f L_{hv} \eta_{bu} \quad 4-52$$

$$(FAR) = \frac{\dot{m}_f}{\dot{m}_a} \quad 4-53$$

$$f_{ql,cy} = \frac{T_{06,mx} - T_{06}}{T_{06,mx} - T_{at}} \quad 4-54$$

$$\theta_2 = \frac{T_{06} - T_{05}}{T_{06} - T_{04}} \quad 4-55$$

In order to calculate the total pressures (P_{05}, P_{06}) and volumetric expansion ratios (V_7/V_4) during the combustion process (part constant volume and part constant pressure combustion) the following equations have been used [1].

$$V_5 = V_4 \quad 4-56$$

$$P_{05} = P_{04} \left(\frac{T_{05}}{T_{04}} \right) \quad 4-57$$

$$P_{06} = P_{05} \quad 4-58$$

$$V_6 = V_5 \left(\frac{T_{06}}{T_{05}} \right) \quad 4-59$$

$$V_7 = r_{71} r_{23} r_{34} r_{12} V_4 \quad 4-60$$

To calculate the constant pressure expansion work (\dot{W}_{e56}), the following equation is used [1,117].

$$\dot{W}_{e56} = p_{05}(\dot{V}_6 - \dot{V}_5) = (\dot{m}_a + \dot{m}_f)R(T_{06} - T_{05}) \quad 4-61$$

In order to calculate the total pressures (P_{07}, P_{06}) and temperatures (T_{06}, T_{07}) during the adiabatic expansion process, the following set of equations are used. Furthermore, equations are provided to estimate the power produced by the expansion process ($\dot{W}_{e,67}$) and the net power (\dot{W}) produced by the ND engine core configuration for a given adiabatic expansion efficiency ($\eta_{s,e}$) and mechanical transfer efficiency (η_{me}), respectively[1].

$$T_{07,s} = T_{06} \left(\frac{V_6}{V_7} \right)^{\frac{R}{C_v}} \quad 4-62$$

$$P_{07} = P_{06} \left(\frac{T_{07,s}}{T_{06}} \right) \left(\frac{V_6}{V_7} \right) \quad 4-63$$

$$\eta_{s,e} = \frac{T_{06} - T_{07}}{T_{06} - T_{07,s}} \quad 4-64$$

$$\dot{W}_{e,67} = (\dot{m}_a + \dot{m}_f) \bar{C}_v (T_{06} - T_{07}) \quad 4-65$$

$$\dot{W} = \eta_{me} (\dot{W}_{e,56} + \dot{W}_{e,67} - \dot{W}_c) \quad 4-66$$

The output torque (Q) produced by the nutating disc engine is given by the following equation.

$$Q = \dot{W} / 2\pi N_s \quad 4-67$$

Figure 4-17 provides an overview of the methodology required to predict the output shaft power of the nutating disc engine, as well as an overview of the independent variables that are required to determine the performance of the nutating disc engine.

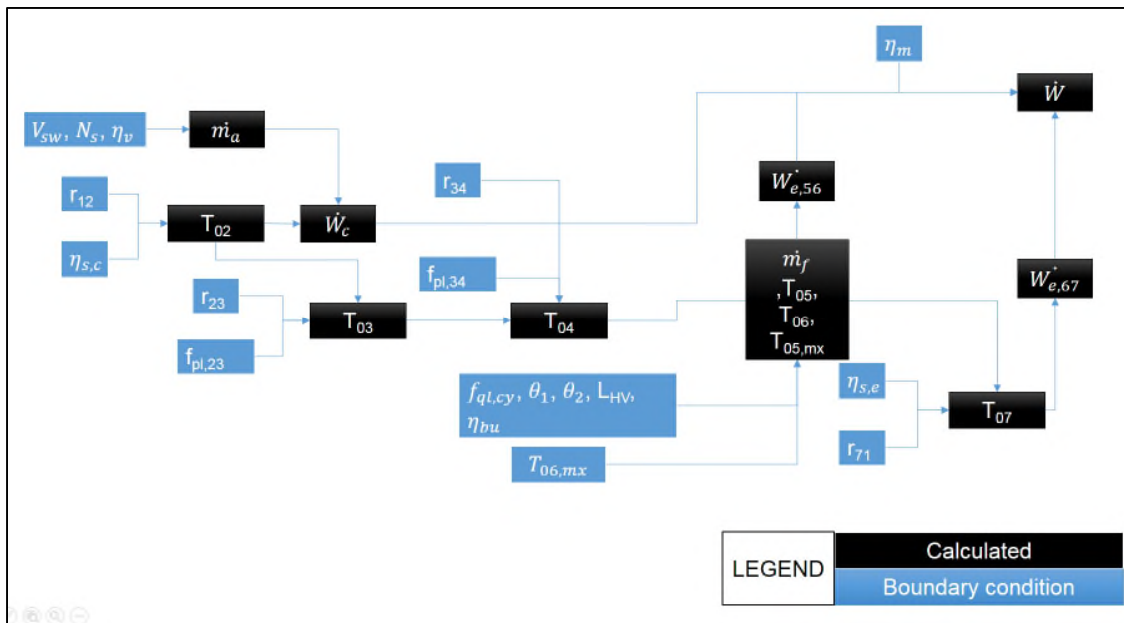


Figure 4- 17: Schematic overview of iterative process to determine ND engine performance.

The methodology proposed by Korakianitis et al., adequately describes the thermodynamic performance of a naturally aspirated nutating disc engine system. However, when the detail design of the nutating disc engine system is considered methodologies should be included to describe the relationship between the thermodynamic limits, geometric limits and the aerodynamic limits of the ND engine system.

This practise is akin to the detail design of turbomachinery, where initially a preliminary thermodynamic cycle study is conducted to determine the thermodynamic capability of a selected cycle, following which a 1D study is used to determine the size and aerodynamic feasibility of the turbomachinery component.

Therefore, in order to advance the ND engine system concept as well as examine its feasibility when it is incorporated in to the core of an aero-engine a methodology to derive the size of the dual disc ND engine system is developed. This methodology is presented in the subsequent section and directly addresses the primary contribution to knowledge of this thesis.

Prior to delving in to the sizing methodology, the magnitude of the primary independent design variables that are dictated by geometrical constraints are the swept volume (V_{sw}), the volumetric compression ratio (r_{12}) and the volumetric expansion ratio (r_{67}).

4.3.2 Swept volume estimation of the dual nutating disc engine system configuration

The assumptions and the consequent limitations of the proposed methodology are:

- It is assumed that there is no clearance between the tip radius of the nutating disc and the static structures like the casing and inlet wedges.
 - This assumption leads to an overestimation of the total swept volume of the ND engine system.
- The volume occupied by seals housed within the ND engine system have not been accounted for.
 - This leads to an overestimation of the swept volume of the ND engine system.
- The volume occupied by the accumulator and the pre-combustion chamber has not been accounted for.
 - This leads to an under estimation of the ND engine system swept volume

- The face of the wedge, housed between the ND casing and spherical section is assumed to be straight.
 - In reality this face will have a complex shape that is dictated by the motion of the nutating disc during operation. Therefore this contributes to an under estimation of the total swept volume.

The swept volume (V_{sw}) of the nutating disc engine system can be determined by defining the tip radius (r_t), hub radius (r_h), angle of nutation (α) and the wedge radius (r_l) of each disc in a Cartesian co-ordinate system. Figure 4-18 indicates the variables in the Cartesian co-ordinate system. In reality the internal nutating disc structure would lie in a position where the z' axis would not be perpendicular to the page in the left most depiction of **half** of the nutating disc internal structure and casing in Figure 4-18.

However, since the proposed methodology calculates the volume enclosed in between the **complete** casing, wedge and internal nutating disc structure the positioning of the internal nutating disc structure is placed parallel to the upper and lower casing walls for ease of derivation. Moreover, this assumption will have no influence on the final swept volume estimation due to the laws of symmetry.

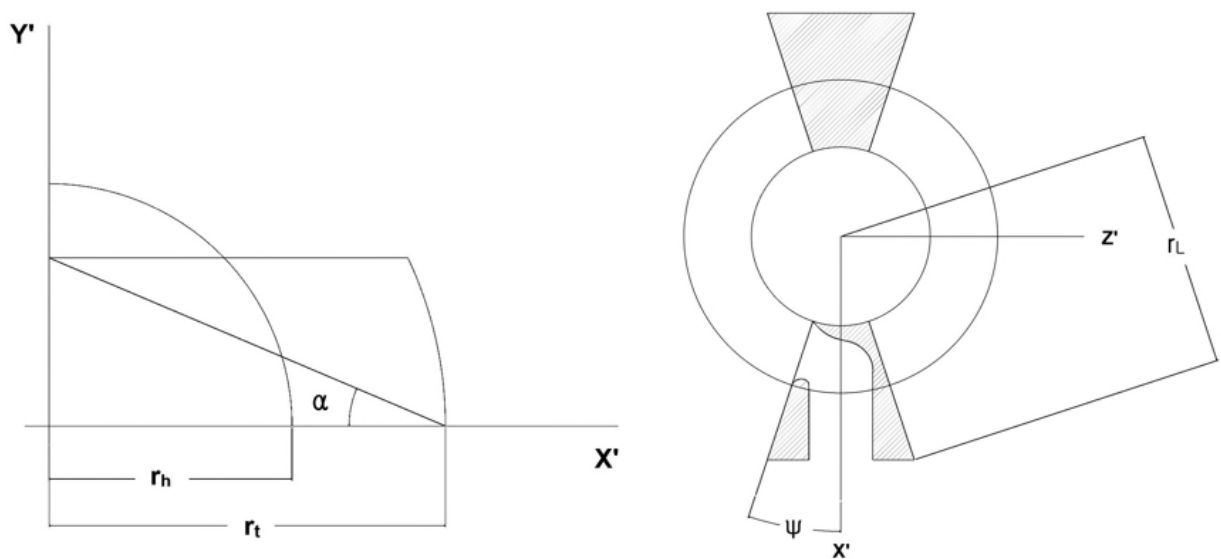


Figure 4- 18: Definition of the variables that determine the size of a single disc in Cartesian co-ordinate system

In order to effectively estimate the swept volume the volume of the nutating disc casing, volume of the wedges and volume of the internal nutating disc structure need to be determined. The derivation of these volumes will be shown in the following sub-sections.

4.3.2.1 Casing Volume estimation

The volume enclosed by the casing of a single nutating disc is expressed as a function of the tip radius and the angle of nutation. Figure 4-19 depicts what is meant by the casing volume. The casing volume is defined in Equation 4-68, where the angle of nutation is expressed in radians.

$$V_{casing} = 2\pi \left[r_t^3 \sin(\alpha) - \frac{[r_t \sin(\alpha)]^3}{3} \right] \quad 4-68$$

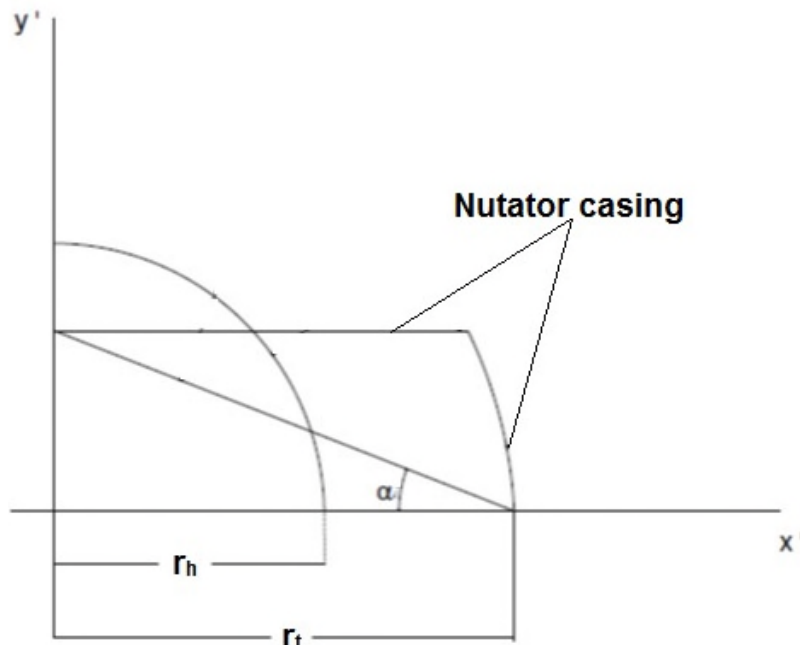


Figure 4- 19: Nutating disc casing definition in Cartesian co-ordinate system

4.3.2.2 Wedge Volume estimation

The wedge is placed in either the compressor or expander discs to admit or expel the working fluid. In each disc there exists two wedges, placed diametrically opposite each other, to admit the air through an 'elbow-duct' in the compressor disc and to expel the products of combustion in the expander disc.

The volume occupied by the wedge can be expressed as a function of the hub to tip ratio of the internal nutating disc structure (HT), the wedge angle (ψ) and the wedge radius to tip nutator radius ratio (l_f).

Figure 4-20 illustrates the definition of the arrangement of the wedge. The wedge volume is estimated by revolving the wedge by its wedge angle, this is indicated by Equation 4-72.

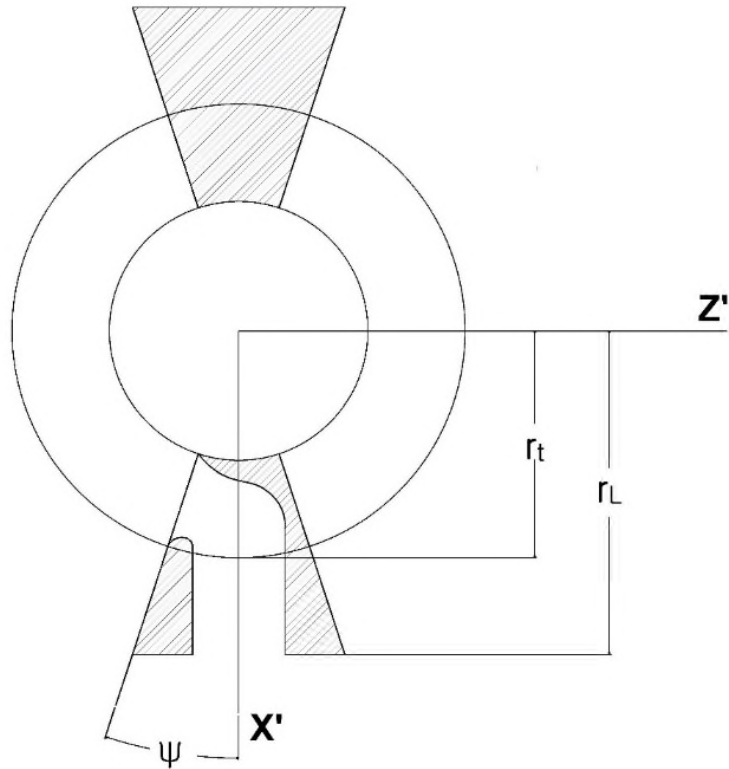


Figure 4- 20: Definition of wedge parameters

$$HT = \frac{r_h}{r_t} \quad 4-69$$

$$l_f = \frac{r_l}{r_t} \quad 4-70$$

$$\psi = \text{atan} \left(\frac{r_t - r_h}{2r_t l_f} \right) \left(\frac{180}{\pi} \right) \quad 4-71$$

$$V_{wedge} = \frac{2\pi\psi}{180} \left[\int_{-r_t \sin(\alpha)}^{r_t \sin(\alpha)} r_t^2 - y'^2 dy' - \int_{-r_t \sin(\alpha)}^{r_t \sin(\alpha)} r_h^2 - y'^2 dy' \right] \quad 4-72$$

4.3.2.3 Internal nutating disc structure volume estimation.

The nutating disc itself is housed within the casing at an angle corresponding to the angle of nutation and the crank angle. In order to estimate the volume that the nutating disc occupies within the casing the areas A_O and A_N are revolved around the y' axis, as indicated in Figure 4-21.

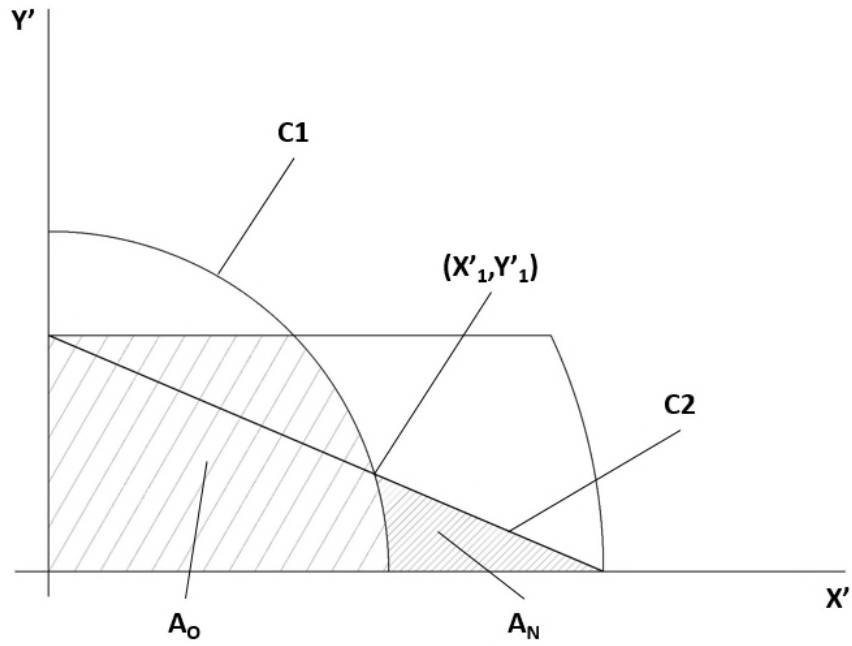


Figure 4- 21: Definition of the nutating disc areas that are revolved around the y' axis

The volume swept by A_N is defined by Equation 4-73, 4-74 and 4-75, where the upper limit in the volume of revolution integral (y'_1) is defined as a function of the internal nutating disc structure tip radius, hub to tip ratio and angle of nutation. The upper limit (y'_1) is defined parametrically by finding the spatial co-ordinates where curves C1 and C2, in Figure 4-21, intersect.

$$V_{A_n} = V_1 - V_2 \quad \mathbf{4-73}$$

$$V_1 = \pi \int_0^{y'_1} r_t^2 - 2r_t y' \tan(\alpha)^{-1} + y'^2 (\tan(\alpha))^{-2} dy' \quad \mathbf{4-74}$$

$$V_2 = \pi \int_0^{y'_1} r_h^2 - y'^2 dy' \quad \mathbf{4-75}$$

The upper limit of the integrals required to estimate the internal nutating structure volume is defined by the following equations.

$$a = [1 + \tan(\alpha)^{-2}]; b = [-2r_t \tan(\alpha)^{-1}]; c = [r_t^2 - r_h^2] \quad \mathbf{4-76}$$

$$y'_1 = \frac{[-b - [b^2 - 4ac]^{0.5}]}{2a} \quad \mathbf{4-77}$$

The volume of the solid that is defined when A_0 is revolved about the y' axis is indicated in Equation 4-78, where the upper limit of the integral is defined by the height of the casing.

Consequently the total volume occupied by the nutating disc in the casing is indicated in Equation 4-79.

$$V_{A_o} = \pi \int_0^{r_t \sin(\alpha)} r_h^2 - y'^2 dy' \quad \mathbf{4-78}$$

$$V_{ND} = V_{A_N} + V_{A_o} \quad \mathbf{4-79}$$

Therefore the volume displaced in a single nutating disc can be estimated by appropriate accounting of the internal volumes as shown in Equation 4-80.

$$V_{disp_{disc1}} = V_{casing} - 2(V_{ND} + V_{wedge}) \quad \mathbf{4-80}$$

In order to account for the volume displaced by the expander nutating disc compartment, in a dual disc arrangement, the overall volumetric expansion ratio (r_{71}) is defined so that the diameter of the expander disc is calculated [2].

$$r_{71} = \left(\frac{r_{disc1}}{r_{disc2}} \right)^3 \quad \mathbf{4-81}$$

Consequently if Equations 4-68 to 4-80 are used in terms of the expander disc, the corresponding volume displaced by the expander disc ($V_{disp_{disc2}}$) can be determined. Therefore the volume displaced by a dual disc nutating engine configuration is estimated by Equation 4-82. Furthermore, the swept volume estimated by a shaft revolution is expressed as function of the number of power cycles per shaft revolution (k).

$$V_{disp} = V_{disp_{disc1}} + V_{disp_{disc2}} \quad \mathbf{4-82}$$

$$V_{sw} = \frac{V_{disp}}{k} \quad \mathbf{4-83}$$

4.3.3 Volumetric compression ratio estimation

The assumptions and subsequent limitations associated with this methodology are:

- It is assumed that the parametric volumetric compression ratio derived is an approximation, rather than a definitive volumetric ratio.
 - In order to calculate the total volume enclosed at the beginning and at the end of the compression process a triple integral should be used to define the volume in the static frame of reference. The current proposed methodology sweeps the projected area on the X-Y plane by the crank angle of compression-without a guidance curve.
- It is assumed that the accumulator off-take port is located at the periphery of the ND casing, which corresponds to the tip radius.

- In reality, the volumetric compression ratio is determined by the radial position of the accumulator off-take port as well as the timing of the non-return check valve or solenoid controlled off-take port [78].

The volumetric compression ratio, can be expressed as a function of the tip radius, hub to tip ratio, angle of nutation and the crank angle per shaft revolution (ϕ). In order to account for the variation in the disc position, within the casing, as a function of the crank angle the tip and hub radii need to be projected from a dynamic frame of reference to a static frame of reference as shown in Figure 4-22.

The crank angle per shaft revolution is expressed as a function of the rotational speed (ω) in radians per second and time (t) in seconds. Consequently, the tip and hub radii are transformed from the dynamic frame of reference to the static frame of reference. These relationships are consequently defined in Equation 4-84 and Equation 4-85.

$$\phi = \omega t \quad \text{4-84}$$

$$r_{t(\phi)} = r_t \cos(\phi) \cos(\alpha); \quad r_{h(\phi)} = r_h \cos(\phi) \cos(\alpha) \quad \text{4-85}$$

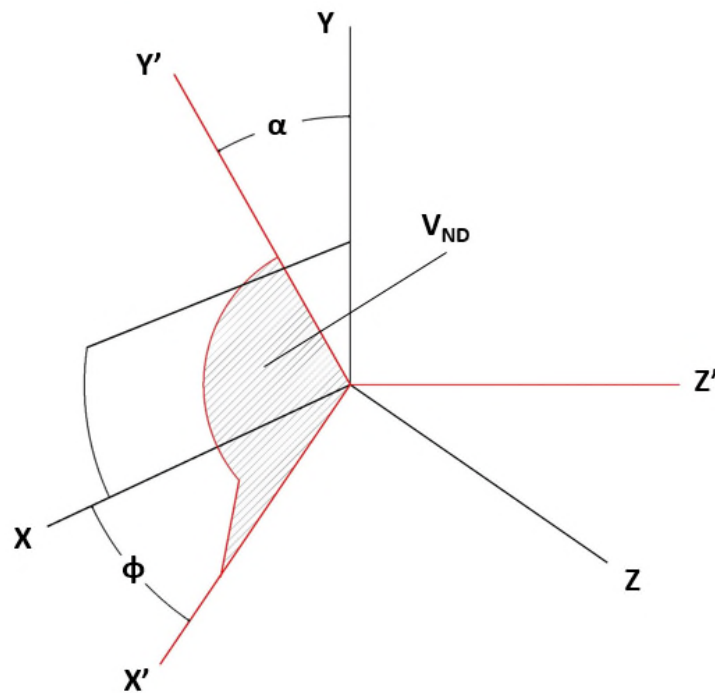


Figure 4- 22: Projection of the dynamic frame of reference on the static frame of reference

To make a representative approximation of the volumetric compression ratio the displaced volume is calculated at a crank angle corresponding to the beginning of compression process

(ϕ_i) and the displaced volume at the end of the compression process (ϕ_e). Figure 4-23 shows the two instances where the displaced volume should be calculated.

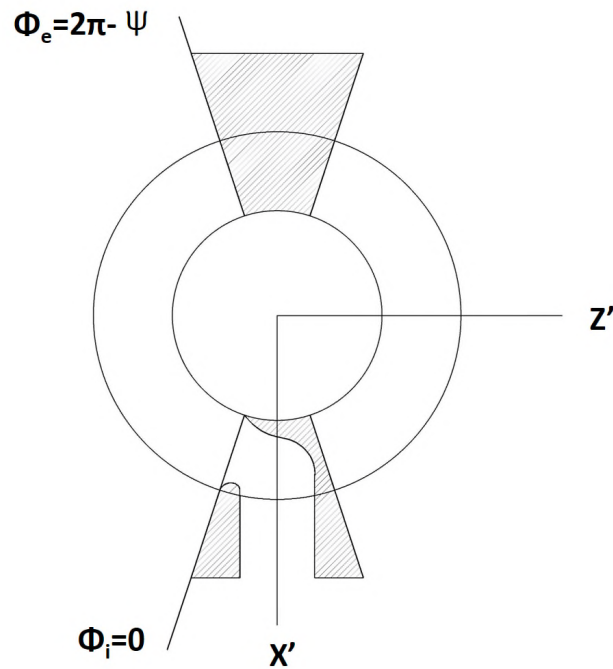


Figure 4- 23: Crank angles at which the displaced volumes are to be calculated

Therefore, using a refined definition of the tip radius and hub radius, in the static frame of reference, in Equations 4-68 to 4-80 an estimate of the volumetric compression ratio can be derived in conjunction with a technology factor ($TF=1.0$ to 2.0). $TF=1.0$ is chosen for the analyses. The technology factor corresponds to the maturity of bearing technology and casing materials that can allow for high volumetric compression ratios. Thus, an approximation of the volumetric compression ratio is presented in Equation 4-86. Figure 4-24 shows an equation flow chart to estimate the volumetric compression ratio. Essentially, the ND dimensions in the dynamic frame of reference are projected on to the static frame of reference and the enclosed ND area between the internal nutating disc structure and casing is swept across an angle corresponding to the start and end of the compression process. This displaced volume is derived at a crank angle corresponding to the beginning and end of the compression process.

$$r_{12} = (TF) \frac{V_{disp}(\phi_i)}{V_{disp}(\phi_e)} \quad \mathbf{4-86}$$

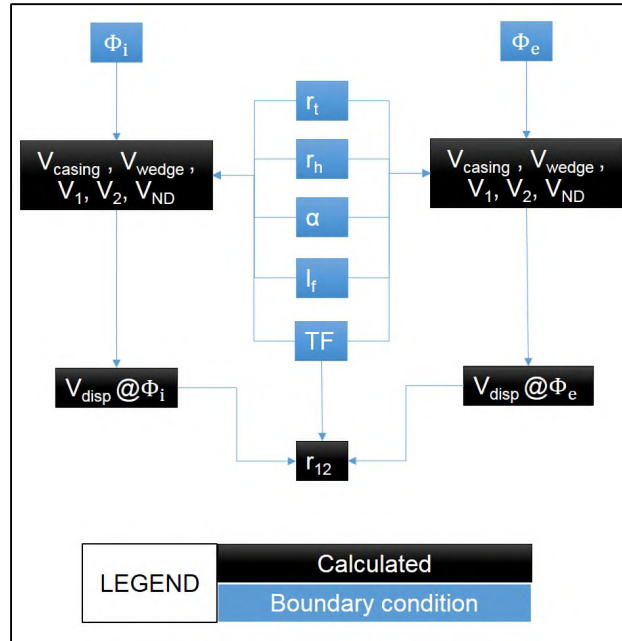


Figure 4- 24: Flow chart that schematically shows the volumetric compression ratio

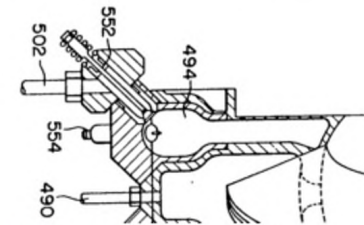
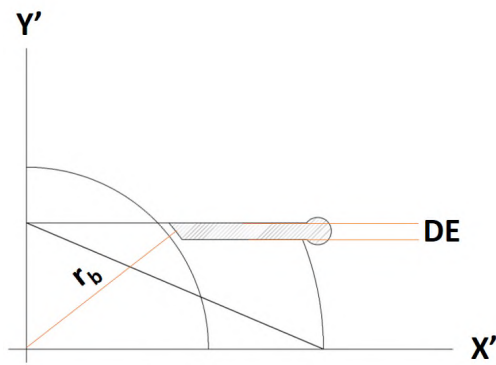
4.3.4 Combustion and expansion process estimation

The main assumption that has been accounted for in the hypothesis to estimate the combustion and expansion processes are:

- It is assumed that the crank angle at which the combustion process ceases is when the nutating disc no longer covers the exhaust port.
 - In reality, this boundary would be determined when flame front extinguishes, which would be determined by the local flame speed, rate of combustion, fuel to air ratio, geometry of the pre-combustor, size of the pre-combustor exhaust port and timing of fuel and air injection and ignition.
- It is assumed that the exhaust port of the pre-combustion chamber is rectangular in nature and found on the surface of the wedge in the expander disc.
 - In reality, the pre-combustion exhaust port will be triangular in nature and will be located close to the hub of the internal nutating disc structure[76]. This ensures that the pre-combustion chamber will be closed off for a relatively longer period during its operation, and thus facilitate a greater proportion of constant volume combustion during the combustion process.

The combustion process consists of a constant volume combustion process in the pre-chamber and a constant pressure combustion process through a portion of the expansion

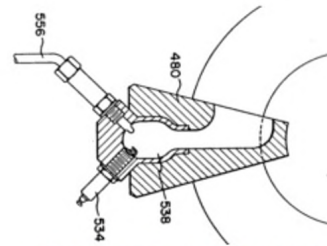
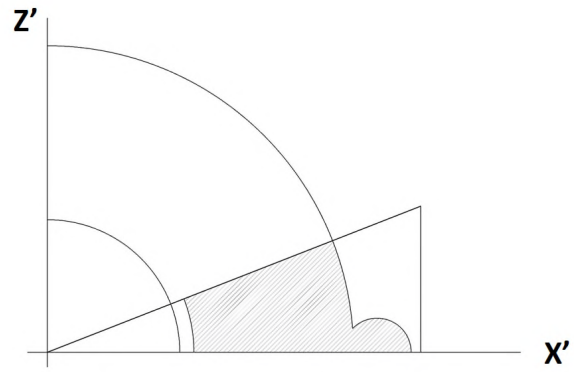
chamber. This would entail, that the volumetric expansion ratio of the nutating disc (per shaft revolution - assuming that the number of power cycles per shaft revolution is limited to 2 [78]) is in fact dictated by the crank angle duration of the combustion process. Figure 4-25 and Figure 4-26 indicates the idealized and real geometry of the pre-combustor in a Cartesian co-ordinate system.



Real pre-combustor cross-section

502: air injection
552: air injection valve

Figure 4- 25: y' - x' view of pre-combustor



Real pre-combustor cross-section

556: Fuel injection valve
534: Spark plug

Figure 4- 26: top-down view of the proposed pre-combustion chamber

In Figure 4-25, r_b represents the radius of the idealized burner exit port geometry and DE represents the height of the combustion chamber. The combustion chamber is positioned in such a way that the tip of the combustion chamber in the y' direction coincides with the casing. In order to estimate the crank angle per shaft revolution during the entire combustion process it is assumed that when the combustion process starts, the nutating disc structure completely overlays the hatched area shown in Figure 4-25 in the dynamic frame of reference. It is also assumed that the entire combustion process ceases the moment that the projected area of the nutating structure, from the dynamic frame of reference, no longer completely overlays the hatched area of combustion. This condition can be expressed mathematically by transforming r_t in the dynamic frame of reference onto the y' -axis of the static frame of reference. Consequently, when this dynamic radius coincides with the

minimum position of the combustor geometry, it can be mathematically assured that the projected area no longer overlays the combustor area, as expressed by Equation 4-87.

$$r_t \sin(\alpha) - DE = r_b \cos(\phi) \cos(\alpha) \quad \mathbf{4-87}$$

The crank angle per shaft revolution occupied during the combustion process is estimated as a function of the operational speed and crank angle per shaft revolution, and is expressed in Equation 4-88.

$$CA_{\text{combustion}} = \frac{180}{\pi} \arccos(\phi) \quad \mathbf{4-88}$$

Once the combustion crank angle is determined, the expansion ratio can be determined in a similar manner to that which was proposed in estimating the volumetric compression ratio. Therefore, it is possible to use Equation 4-84 to Equation 4-85 to estimate the expansion ratio. The only difference would be to specify the crank angle limits, within the derivation, such that two complete cycles are captured during one shaft revolution. The crank angle limits that need to be used in defining the volumetric expansion ratio are expressed in Figure 4-27. In addition, Figure 4-28 provides an overview of the methodology to estimate the volumetric expansion ratio.

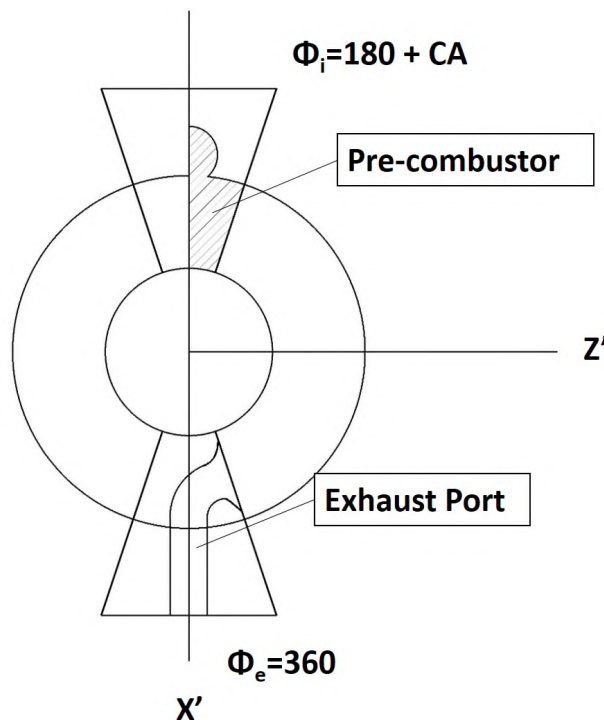


Figure 4- 27: Crank angle limits that define the volumetric expansion ratio

- The pressure loss effect in the ducts, plenum and runners are imposed, the total pressure loss at all flight conditions for inlet and exhaust plenum systems are estimated at 3%.
 - In reality the, the pressure loss would be dictated by the length of the ducts as well as the corrected non-dimensional mass flow [117].

It is necessary to have a toroidal shaped plenum upstream of the nutating disc array because the variations in pressure within the compression chamber of the nutating disc will cause some air to spill back towards the intermediate pressure compressor. Similarly, the interface between the expander disc and the intermediate pressure turbine also requires an exhaust plenum such that there is limited back-flow from the intermediate pressure turbine to the nutating discs in the architecture of the geared open rotor.

The following set of equations dictates the size of the inlet plenum chamber, exhaust plenum chamber and the corresponding connecting manifolds by assuming that there is no “throttle valve” (wide open throttle setting) between the plenum exit or entrance and the nutating disc engine entrance or exit. In addition to predicting the size of the plenum chamber the following equations predict the plenum resonance frequency [118].

The volume of the toroidal plenum (V_{plenum}) is estimated as a function of the number of nutating disc engine systems ($\#NDs$), maximum possible length (li_{max}) of the runner manifold, actual inlet or exhaust duct length ($L_{o,duct}$), inlet and exit areas ($A_{i||plenum}$) and the speed of sound (a). Figure 4-29, indicates the possible arrangement of multiple nutating disc engine systems in the meridional view of the engine core it also indicates the maximum length of the connecting and the axial length of the duct required to size the upstream plenum. Ideally, stacking the ND engine systems circumferentially would be the preferred option as seen in Figure 4-30. However, if the number of ND engine systems exceed the spatial constraints in the circumferential direction, it is assumed that the ND engine systems would form banks of ND engine systems that are stacked axially.

$$\cos \left[\frac{\omega li_{max}}{a} \right] = 0 \quad \mathbf{4-89}$$

$$\left(\frac{A_{i||plenum}}{A_{e||plenum}} \right) \cot \left[\frac{\omega L_{o,duct}}{a} \right] = \frac{\omega V_{plenum}}{a A_{e||plenum}} + 2\#NDs \tan \left[\frac{\omega li_{max}}{a} \right] \quad \mathbf{4-90}$$

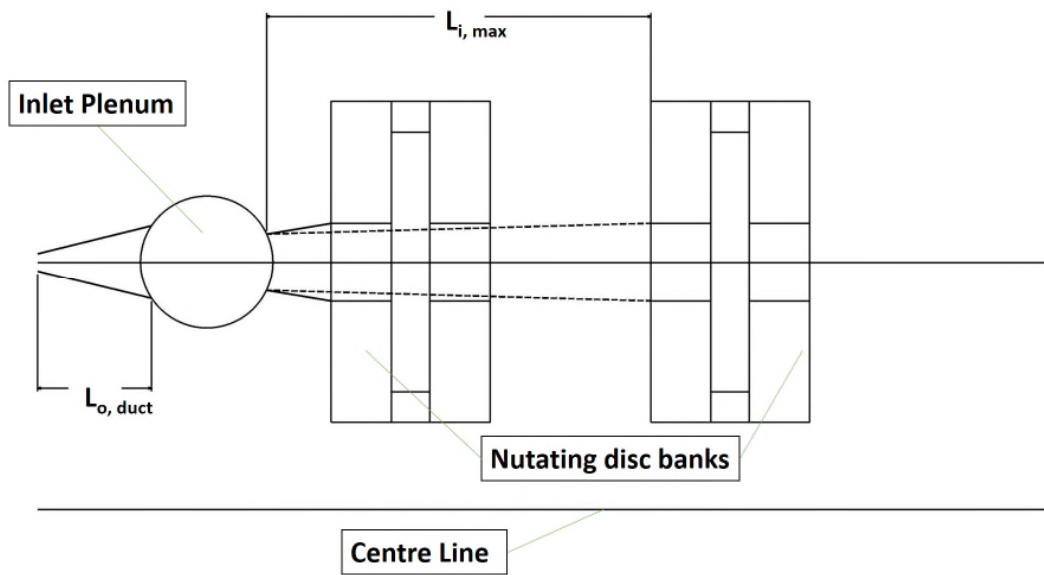


Figure 4- 29: Possible meridional view of the nutating disc engine systems in the core of a gas turbine

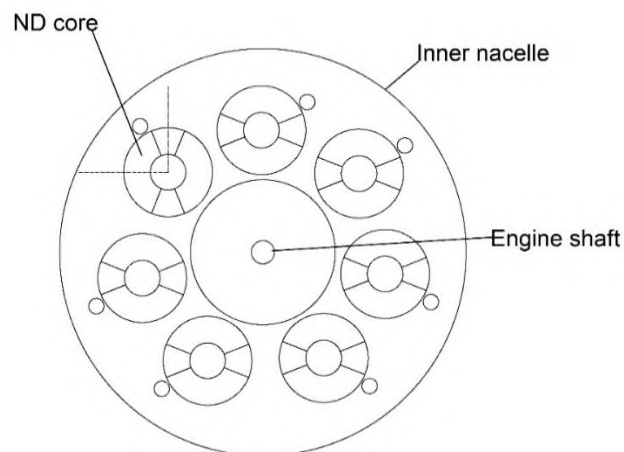


Figure 4- 30: Circumferential arrangement of the nutating disc engine systems corresponding to the centre line of the engine.

4.4 Intercooler and secondary combustor performance model

A nutating disc engine system within the architecture of a gas turbine benefits with the introduction of technologies that can augment the increment in the specific power of the core as well the reduction of overall engine mass. Within the scope of this thesis, the technologies that are considered in conjunction with a nutating disc engine system are:

- An intercooler system

- A secondary combustion system

The assumptions and limitations of the methods employed to estimate the performance of the intercooler and secondary combustor are:

- The effectiveness of the intercooler (on both the hot and cold side) are prescribed.
 - The limitation of this assumption, is that the effectiveness is determined by the wetted surface area of the heat exchanger stacks, the thickness of the elliptical tubes, the Reynolds number effect, magnitude of the mass flow and the degree of turbulence of the flow on both the hot and cold sides of the heat exchanger [25,87,119].
- The total pressure losses on both the hot side and cold side of the intercooler are prescribed.
 - In practice this would be dictated by the skin friction factor of the elliptical tubes, the Reynolds number effect and the degree of turbulence of the flow in both the hot and cold side of the heat exchanger tube stacks [119].
- The effects of fouling and ice accretion on the performance of the intercooler performance has not been accounted for.
 - During operation, at take-off conditions, the ingestion of foreign objects will affect the heat transfer area and consequently will affect the heat transfer effectiveness. In addition, during cruise, the possibility of ice accretion on the heat exchanger stacks will reduce the heat transfer effectiveness.
- The total pressure losses in the secondary combustor are prescribed, and are assumed not to vary at off-design conditions.
 - The total pressure loss, expected in a secondary flameless combustor will be primarily influenced by the cooling requirements of the combustor liner and the degree of re-circulation of the combustion products within the architecture of the flameless combustor[94].
- The combustion process in the secondary combustor is assumed to be adiabatic.
 - It is expected that the heat addition process would not be adiabatic as there would be heat loss through the combustor casing [24].

4.4.1 Intercooler performance model

The intercooler model consists of a two-pass cross-flow architecture. Figure 4-31 shows the layout of the intercooler configuration. It consists of an inflow diffuser duct, which reduces the velocity of the incoming hot flow thus allowing for more efficient heat transfer in the tubes. After the flow is diffused, the flow enters the first stack of elliptical tubular heat exchanger,

goes through a cross-over duct, then it passes through the upstream elliptical heat exchanger stack and is finally accelerated via a converging duct[87].

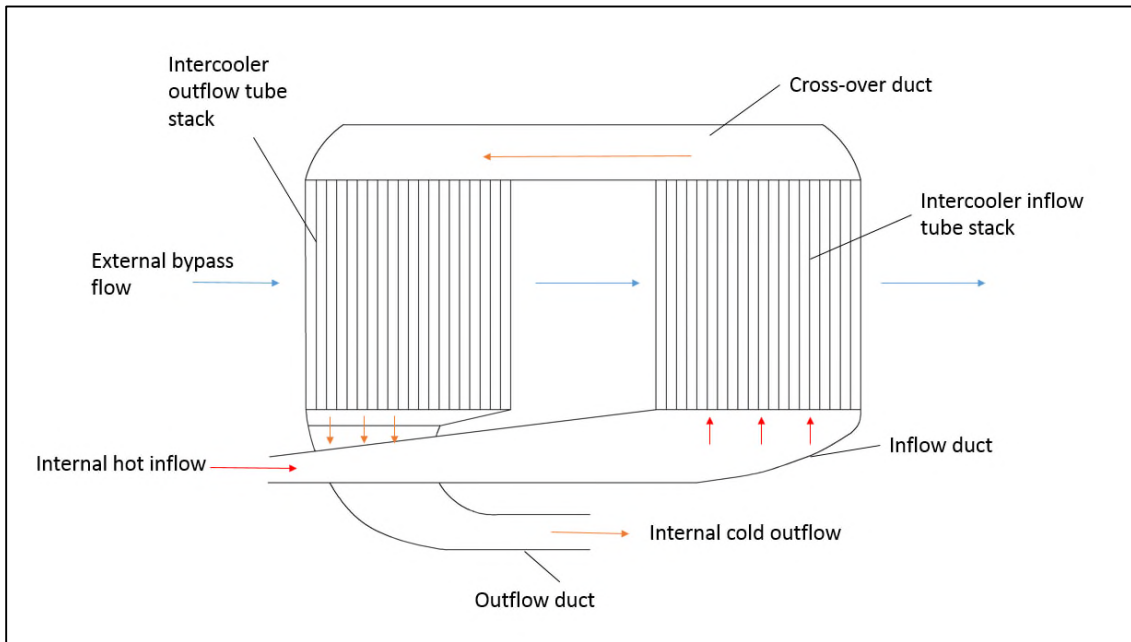


Figure 4- 31: Layout and flow path depiction of two-pass cross-flow intercooler

The preferred circumferential arrangement of the intercooler modules is postulated to be of the involute spiral type, as a consequence of its efficient circumferential spatial utilization[87]. Figure 4-32 indicates how the intercooler modules would be arranged in the circumferential direction.

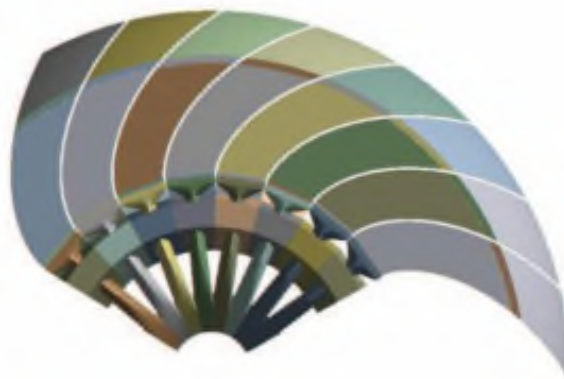


Figure 4- 32: Circumferential arrangement of the intercooler modules

The performance of the intercooler is estimated by prescribing the intercooler effectiveness and total to total pressure losses on the hot and cold sides. The temperature effectiveness (ζ) is determined by the ratio of the temperature change on the hot side ($T_{in,hot} - T_{out,hot}$) of

the heat exchanger and the temperature change between the hot side and cold side inlet temperatures ($T_{in,hot} - T_{in,cold}$), as seen in Equation 4-91. Equation 4-92 predicts the total pressure of the flow emanating from the cold or hot side of the intercooler module[89].

$$\zeta = \frac{T_{in,hot} - T_{out,hot}}{T_{in,hot} - T_{in,cold}} \quad 4-91$$

$$P_{out,cold \text{ or } hot} = P_{in,cold \text{ or } hot} (1 - dPqP_{cold \text{ or } hot}) \quad 4-92$$

In order to estimate the outlet temperatures of both the cold and hot side of the intercooler module, a power balance is performed between the hot and cold sides. Equation 4-93 and Equation 4-94 indicate how the power of each flow stream is derived and the corresponding power balance equation[89]. Figure 4-33 provides an overview of how the outlet temperatures of the Intercooler are determined.

$$Pwr_{cold \text{ or } hot} = W_{cold \text{ or } hot} (h_{out,cold \text{ or } hot} - h_{in,cold \text{ or } hot}) \quad 4-93$$

$$-Pwr_{hot} = Pwr_{cold} \quad 4-94$$

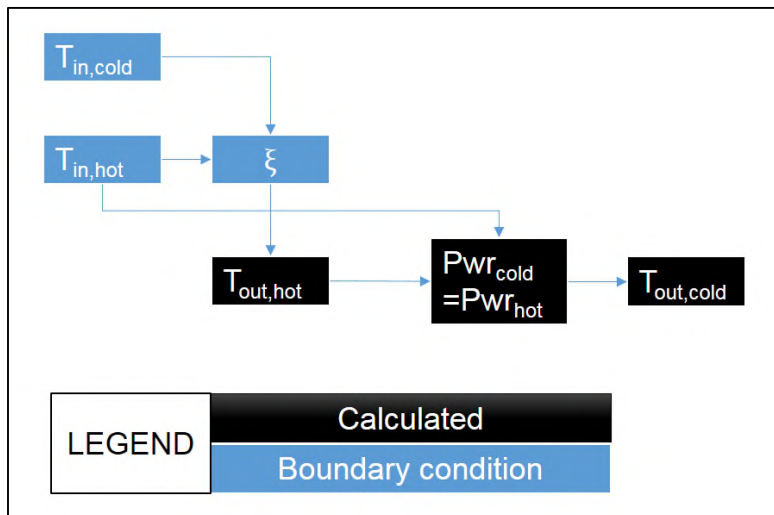


Figure 4- 33: Overview of the iterative process to determine the intercooler module performance

4.4.2 Secondary Combustor performance

When the secondary combustor is considered in conjunction with a ND engine core in a geared open rotor, it is postulated that the specific power of the core would increase as well as alleviating the excessively high flame temperatures in the ND core pre-combustion chamber. This technology, in conjunction with a ND core, would reduce the specific fuel consumption of the engine while concurrently theoretically reducing NOx emissions across the flight envelope.

The secondary combustor is assumed to be situated aft of the ND engine core and fore of the intermediate pressure turbine, within the architecture of a geared open rotor core, as seen in Figure 4-34.

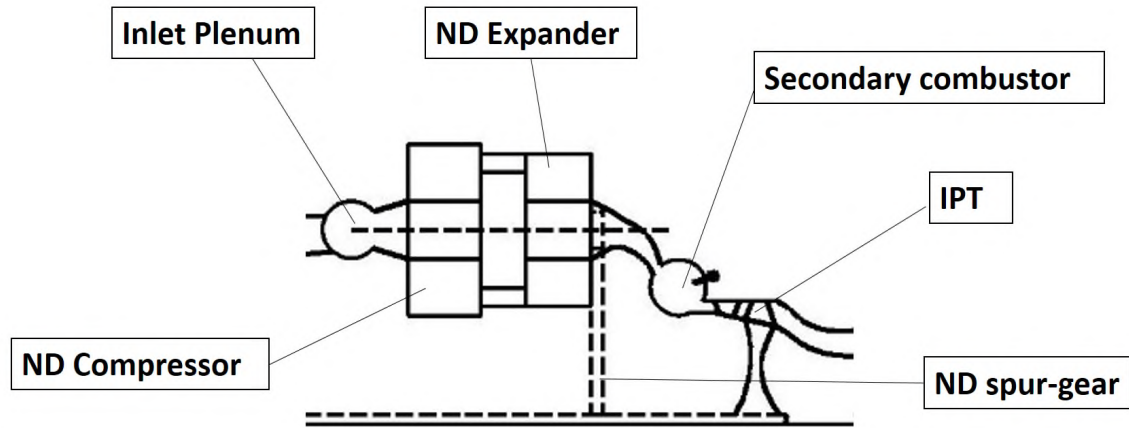


Figure 4- 34: Positioning of the secondary combustor within the gas turbine core

It is assumed that the secondary combustor (SC) is flameless in nature and can be characterized by oxy-poor flame combustion [94]. Essentially, the vitiated air emerging from ND engine core enters the combustor radially, as seen in Figure 4-35, and is entrained in the re-circulation zone, undergoes combustion and consequently exits the vortex towards the inlet guide vanes of the IPT [94]. The green arrow radially entering the SC, Figure 4-35, represents the expanded flow emerging from the ND core. Whereas the orange arrows represent the re-circulation zone and the red arrow represents the fuel injection zone. Finally the green arrow, axially exiting the component, represents the flow that the IGV of the IPT sees.

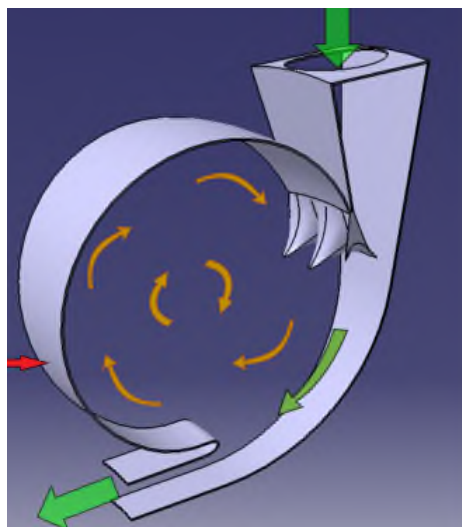


Figure 4- 35: Flow path definition within the secondary combustor[94]

The fuel flow of the secondary combustor is estimated by the energy balance equation, that is native to the Burner component within the Turbo library 3.2[89]. The total pressure loss across the SC module, is determined by implementing a weighted average of the total pressure loss estimates derived from a CFD investigation by Bueno et al. A weighted average is used to determine the significance of each phase of flight on the predicted performance of the SC module. Equation 4-95 indicates how the total pressure loss is determined for all phases of flight, where the total pressure loss for each flight phase is derived from the 3D-URANS study performed by Bueno et al [94] and the weight factors(WF) are derived from the work done by Kaiser et al. for a Y2050 short range aircraft with a range of 3500 nautical miles [96]. The weight factors are determined by the normalised time during the 3500 NM mission spent at cruise, end of runway and climb ($WF_{climb}=0.105$, $WF_{cruise}=0.881$, $WF_{take-off} = 0.014$).

$$dPqP_{SC} = WF_{climb}(dPqP_{SC,climb}) + WF_{cruise}(dPqP_{SC,cruise}) + WF_{take-off}(dPqP_{SC,take-off}) \quad 4-95$$

4.5 Component mass estimation methods

The mass of the Y2050 reference GOR engine and the Y2050 ND-GOR variant engines are derived by estimating the associated masses of the components that are used for each engine variant. The following subsections provide details of the methods that have been used to estimate the component masses. The assumptions and limitations associated with the component mass estimation methods are:

- The mass of the turbomachinery, axial flow compressors and turbines, are estimated using correlations that have been calibrated to determine the mass of engines for vertical take-off and landing engine applications[41].
 - At a detailed design level, fatigue and creep margins, dictate the size and therefore the mass of the blades, discs, shafts and casings of the axial turbomachinery. Thus, the mass of the component will be dictated by the mechanical constraints imposed on the design. In addition, when the mass of modular turbomachinery components are considered, auxiliary components that are usually placed around the core turbomachinery also contribute to the mass.
- The mass of the internal ND structure is estimated without accounting for mechanical limitations.
 - The mass of the internal ND structure should be determined by investigating the fatigue and creep limitations on the proposed design.
- The mass of the ND casing is estimated by assuming that it is a thick walled cylinder.

- The ND casing, should be determined by imposing design limitations, due to high cycle fatigue and creep considerations.
- The mass of the auxiliary components of the ND engine system, accumulator and associated ducting, are determined by assuming that the mass would scale with the mass of the internal ND structure.
 - The ND auxiliary components' mass would be determined by the mechanical constraints imposed by the peak operating pressures, temperatures and the operating speeds throughout the flight envelope
- The mass of the intercooler is determined by a correlation as opposed to the detail design of a two-path cross-flow intercooler design.
 - The mass of the intercooler, would depend on the choice of material, number of tubes, peak operating pressures, temperatures and the mass of the manifolds and cross-over ducts[25,87].
- The mass of the secondary combustor is assumed to be determined by the correlation suggested by Sargerser et al [41].
 - The mass of the re-circulating secondary combustor would need to be derived from low cycle fatigue and creep limitations associated with its design.
- The mass of the auxiliary systems, such as the pitch change mechanism, of the contra rotating propeller system are assumed to be included in the propeller mass estimation.
 - The mass of the CRP auxiliary systems would be determined by propeller gust load certification requirements.
- The mass of the turbomachinery components are derived using constants, that have been calibrated for high bypass ratio turbofans as per Sargerser et al [41].
 - The limitation of this approach is that the mass of the turbomachinery components will be overestimated. Hence this will provide a pessimistic estimation of the entire engine mass.

4.5.1 Axial Compressor Mass

The compressor mass is dependent on the number of stages, the average mean diameter, the compressor inlet tip blade speed and the entire compressor length to average mean diameter ratio. The correlation is provided in Equation 4-96 [41]. K_c , refers to the proportional constant and is equivalent to 24.2 for high bypass ratio turbofans. $U_{t,ref}$, refers to the reference blade tip speed and it is equivalent to 335 m/s. Equations 4-97 and 4-98 indicate how the mean diameter (D_m) of the compressor is calculated as well as the reference length to diameter ratio (L/D_{ref}).

$$W_c = K_c D_m^{2.2} N^{1.2} \left(\frac{U_t}{U_{t,ref}} \right)^c \left(1 + \left(\frac{\frac{L}{D_{m,in}}}{\left(\frac{L}{D_{m,in}} \right)_{REF}} \right) \right) \quad 4-96$$

$$\left(\frac{L}{D_{m,in}} \right)_{REF} = 0.2 + 0.081N \quad 4-97$$

$$D_m = 0.5(D_{m,in} + D_{m,out}) \quad 4-98$$

4.5.2 Centrifugal compressor size and mass model

It is postulated that when the primary flow entering the geared open rotor core, for the Y2050 intercooled-GOR- ND engine configuration, is split in to a bypass stream and a core stream to facilitate the functionality of the intercooled configuration. However, by doing so the last stage blade height of the axial compressor that would precede the ND engine system would significantly affect the polytropic efficiency of the compressor [32]. Therefore, a centrifugal compressor is considered instead. Equation 4-99 describes how the size of the centrifugal compressor is determined. Primarily the exit diameter (D_2) is a function of it's length to height ratio (L/D_2), relative component entry Mach number at the shroud ($M_{1shr,rel}$), entry diameters at the hub ($D_{1,h}$) and mid span ($D_{1,m}$) and empirical calibration constants (K_1 and K_2). The value of $M_{1shr,rel}$ ranges from 0.9 to 1.2 and the value of K_1 and K_2 is 0.28 and 0.8 respectively[120].

$$\left(\frac{L}{D_2} \right)^2 = K_1 (M_{1shr,rel} + K_2) \left(1 - \frac{D_{1,m}}{D_2} \right) (D_{1,shr} - D_{1,hub}) / D_2 \quad 4-99$$

The mass of the centrifugal compressor component is expressed as the sum of the centrifugal compressor and its casing mass. Equations 4-100 to 4-102, express the mass of the centrifugal compressor component as a function of its tip diameter and length to tip diameter ratio[121]. Moreover, as per the correlations provided by Onat et al the centrifugal compressor is assumed to be made out of titanium[121].

$$W_{centri} = \frac{\left(\frac{D_2}{2} (39.37) \right)^3}{13.1} \quad 4-100$$

$$W_{centri,casing} = \frac{16.3 \left(\frac{L}{D_2} \right) (D_2 (39.3701))^2}{2} \quad 4-101$$

$$W_{centri,total} = W_{centri} + W_{centri,casing} \quad 4-102$$

4.5.3 Annular Combustor or Secondary combustor

In order, to estimate the combustor mass by the methods outlined by Sargerreser et al. it is necessary to incorporate the combustor length to height ratio as well as the average mean diameter. Equation 4-103 outlines how the mass of the combustor is estimated. In Equation 4-103, $K_b=390$, $\left(\frac{L}{H}\right)_{REF} = 3.2$ and the exponent $a=0.5$ for high bypass ratio turbofans[41].

$$W_b = K_B D_m^2 \left[\frac{\frac{L}{H}}{\left(\frac{L}{H}\right)_{REF}} \right]^a \quad 4-103$$

4.5.4 Annular Turbine mass

To determine the mass of an axial flow turbine, by using Sargerser's methods, it is necessary to employ Equation 4-104. Where U_m is the mean blade speed of the multi stage turbine and K_t is a constant that is equivalent to a value of 7.9 for high bypass ratio turbofans. Furthermore, Equation 4-105 indicates how the mean blade speed is calculated[41].

$$W_T = K_T D_m^{2.5} N U_m^{0.6} \quad 4-104$$

$$U_m = 0.5(U_{m,in} + U_{m,out}) \quad 4-105$$

4.5.5 Supporting structures, controls and accessory mass

The supporting structures mass is calculated from Equation 4-106, where $K_B=0.18$ for high bypass ratio turbofans, however it has been modified to a 0.20 to account for the additional support structures associated with the GOR configuration. According to [41], Equation 4-106 calculates the combined mass of the engine mounts, bearings, bearing supports, shafts and transition sections.

$$W_s = K_B(W_{propeller} + W_c + W_b + W_T) \quad 4-106$$

In the case of calculating the mass of the controls and accessory mass, the approach of Lolis et al. was adopted [40] as opposed to the approach outlined by Sargerreser. It is assumed that the accessory mass is equivalent to 10% of the total engine mass.

4.5.6 Planetary and Bevel Gearbox mass estimation

As per the method highlighted by Sargerreser et al., the mass of an epicyclic planetary differential gearbox can be surmised by Equation 4-107. Where k_{gb} and K_w are constants and are equal to 0.001129 and 2 respectively. Furthermore Q_{sun} , corresponds to the torque imposed on the Sun gear of the epicyclic gear train. It is also assumed that Equation 4-108 is employed to assume the mass of the bevel gearbox, where Q_{shaft} is the torque produced

by each ND engine system and #ND signifies the number of modular nutating disc engine systems.

$$W_{gb} = K_w k_{gb} Q_{SUN} \quad \mathbf{4-107}$$

$$W_{ND_{gb}} = \#ND (K_w k_{gb} Q_{shaft}) \quad \mathbf{4-108}$$

4.5.7 Contra rotating propeller system mass and Nacelle mass

As per the methods highlighted by Bellocq [16], the mass of the contra rotating propeller system is approximated by assuming the number of blades, technology weight factor (WF [ranges from 0.8 to 1.2 [122]]), the rotational speed of each of the propellers, the diameter of the propellers and the power loading of the propellers. Equations 4-109 to 4-111 indicate how the propeller mass can be approximated. BnBF and BnBR refer to the number of blades for the front propeller and rear propeller array respectively. N_{mech} refers to the rotational speed of the propellers. D_F , D_R and D_N refers to the diameter of the forward, rear propeller and nacelle diameter respectively and are used to predict the weight of the forward and rear propeller arrays respectively (M_F, M_R) [16].

$$M_F = 4.55(D_F - D_N)^{2.6} BnBF \left(\frac{\pi(N_{mech}D_F)}{192} \right)^{0.3} \left(\frac{PowerLoading_F}{\frac{BnBF}{55}} \right)^{0.3} \quad \mathbf{4-109}$$

$$M_R = 4.55(D_R - D_N)^{2.6} BnBR \left(\frac{\pi(N_{mech}D_R)}{192} \right)^{0.3} \left(\frac{PowerLoading_R}{\frac{BnBR}{55}} \right)^{0.3} \quad \mathbf{4-110}$$

$$W_{propellers} = (M_F + M_R)WF \quad \mathbf{4-111}$$

Since there is no dedicated method, as per Sargerser, to determine the nacelle mass of a GOR type engine configuration. It is assumed that the nacelle mass of the GOR engine configuration equals to 10% of the total engine mass [11].

4.5.8 Nutating disc engine system mass

The mass of the internal nutating disc structure is determined by Equation 4-112, by multiplying the volume of the internal ND structure for both the compressor and expander discs by a material density. The internal nutating disc structure, refers to the nutating structure within the nutating disc casing that either compresses or expands the flow. It is assumed that the material, to be used for both the compressor and expander discs is

Hastalloy-X (nickel based alloy) due to the relatively high operating temperatures predicted within the high specific power core of the Y2050 GOR-ND engine configuration.

$$W_{disc\ 1\ or\ disc\ 2} = V_{disc\ 1\ or\ disc\ 2} \rho_{material} \quad \mathbf{4-112}$$

In order, to estimate the mass of the nutating disc casing for both the compressor and expander sections, the casing is assumed to adhere to Lamé's thick walled cylinder approximation[123]. Equations 4-113 to 4-115 predict the incumbent radial, hoop and axial stresses as a function of the peak operating pressure ($P_{ND,max}$), ambient pressure (P_{amb}), outer radius of the casing (r_o) and the inner radius of the casing (r_i)[123].

$$\sigma_h = \left(\frac{P_{ND,max} r_i^2 - P_{amb} r_o^2}{r_o^2 - r_i^2} \right) + \left((P_{ND,max} - P_{amb}) r_o^2 r_i^2 / (r_o^2 - r_i^2) r_o^2 \right) \quad \mathbf{4-113}$$

$$\sigma_r = \left(\frac{P_{ND,max} r_i^2 - P_{amb} r_o^2}{r_o^2 - r_i^2} \right) - \left((P_{ND,max} - P_{amb}) r_o^2 r_i^2 / (r_o^2 - r_i^2) r_o^2 \right) \quad \mathbf{4-114}$$

$$\sigma_a = P_{ND,max} \left(\frac{r_i^2}{r_o^2 - r_i^2} \right) \quad \mathbf{4-115}$$

Once the axial, radial and hoop stresses are determined, the highest stress value is benchmarked against the ultimate tensile stress of Hastalloy-X (with a factor of safety of 1.5) to determine the casing thickness of either the compressor or expander discs[124]. Equations 4-116 to 4-118 determine the height of the nutating disc casing, volume of the casing and its mass.

$$H_{ND\ disc\ 1\ or\ disc\ 2} = 2r_{t,disc\ 1\ or\ 2} \sin(\alpha) \quad \mathbf{4-116}$$

$$V_{casing\ disc\ 1\ or\ 2} = \pi(r_o^2 - r_i^2) H_{ND\ disc\ 1\ or\ disc\ 2} \quad \mathbf{4-117}$$

$$W_{casing\ disc\ 1\ or\ 2} = V_{casing\ disc\ 1\ or\ 2} \rho_{material} \quad \mathbf{4-118}$$

Once the mass of the casing is derived the mass of the wedges on the compressor and expander must be estimated. In addition, the mass of the accessory components of the ND engine system have to be estimated. Equation 4-119 estimates the mass of the wedge by applying a material density ($\rho_{material}$) to the volume of the wedge (V_{wedge}). To account for the space occupied by the inlet and exhaust elbow ducts on the compressor and expander disc respectively a void fraction (VF) of 0.5 is applied as well. The mass of the accessory components such as the accumulator, bearings, Z-shaft and cooling systems is accounted for by Equation 4-120. Finally, the mass of the entire ND engine system array can be estimated by Equation 4-121.

$$W_{wedge\ disc\ 1\ or\ 2} = VF(V_{wedge\ disc\ 1\ or\ 2} \rho_{material}) \quad \mathbf{4-119}$$

$$W_{accessories} = 0.5(W_{disc1} + W_{disc2} + W_{casing1} + W_{casing2} + W_{wedge1} + W_{wedge2}) \quad \mathbf{4-120}$$

$$W_{ND_{total}} = \#NDS(W_{disc1} + W_{disc2} + W_{casing1} + W_{casing2} + W_{wedge1} + W_{wedge2} + W_{accessories}) \quad \mathbf{4-121}$$

In addition, to estimating the mass of the ND engine system, the mass of the upstream and downstream plenums need to be estimated. It is assumed that both the upstream and downstream plenums will have a toroidal pressure vessel. The corresponding mass of the plenums are derived by estimating the maximum stresses (Equation 4-122) seen by each plenum arrangement, which is then benchmarked against the ultimate tensile stress of the material with a factor of safety (FS=1.5) that adequately accounts for the expected cyclic pressure variations within the component. In Equation 4-122, P , represents the peak total pressure, R represents the radius of the toroidal structure from the center line of the engine, r represents the loop radius of the torus and t represents the thickness of the toroidal shell[125].

$$\sigma_{v,max} = \frac{Pr}{2t} \sqrt{\left(\frac{2R-r}{R-r}\right)^2 - \left(\frac{2R-r}{R-r}\right)} + 1 \quad \mathbf{4-122}$$

4.5.9 Intercooler mass

The mass of the two-pass involute spiral cross-flow intercooler is derived from a scaled correlation for recuperators based on the work of Grieb and Syed [126,127]. It is assumed that the material that would be used for the intercooler module is Titanium, as it offers a high strength to mass ratio. Equation 4-123 indicates the estimation of the intercooler mass as a function of its effectiveness (ξ), mass flow on the cold side (W_{cold}) and technology factor (TF [ranges from 0.8 to 1.2, unity was used throughout]). It was derived by curve fitting the data used by Syed et al. in determining the specific mass of a titanium intercooler[127].

$$W_{intercooler} = TF(0.0002\xi^3 - 0.0218\xi^2 + 1.0248\xi - 14.583)W_{cold} \quad \mathbf{4-123}$$

Once the component masses of the individual components have been derived, they can be utilized to estimate the mass of a series of ND engine core based engine configurations.

4.6 Relative Fuel burn estimation

It is assumed that the reference Y2050 geared open rotor engine and 2050 ND engine core based engine configurations will be mounted on to the rear of the fuselage of a short range aircraft that can ferry 180 passengers across 3500NM in the year 2050[107]. By Y2050, it is assumed that, for a short range aircraft, via the introduction of carbon-fibre reinforced polymers, fly-by-light systems, improvement in cabin furnishing mass, hybrid laminar flow

control, high aspect ratio wings and fuel cell systems the lift to drag ratio of a short range aircraft will significantly increase[6].

To benchmark the fuel burn benefits that Y2050 GOR-ND engine core configurations deliver relative to the reference Y2050 geared open rotor configuration, when installed on the same aircraft configuration and flies the same mission range, non-linear trade burn factors are imposed. Non-linear trade burn factors account for changes at engine design level by resizing the aircraft to account for the change in fuel burn and engine mass. Figure 4-36, schematically represents the process to estimate the fuel burn while taking in to account the aircraft-engine 'snowballing' effect. The non-linear trade burn trade factors used within this study were provided by the ULTIMATE project[96]. A detailed example of how the nonlinear trade factors were used is provided in Appendix-D. Furthermore, the operational profile of the mission as well as the fuel utility policy has been laid out in [107]

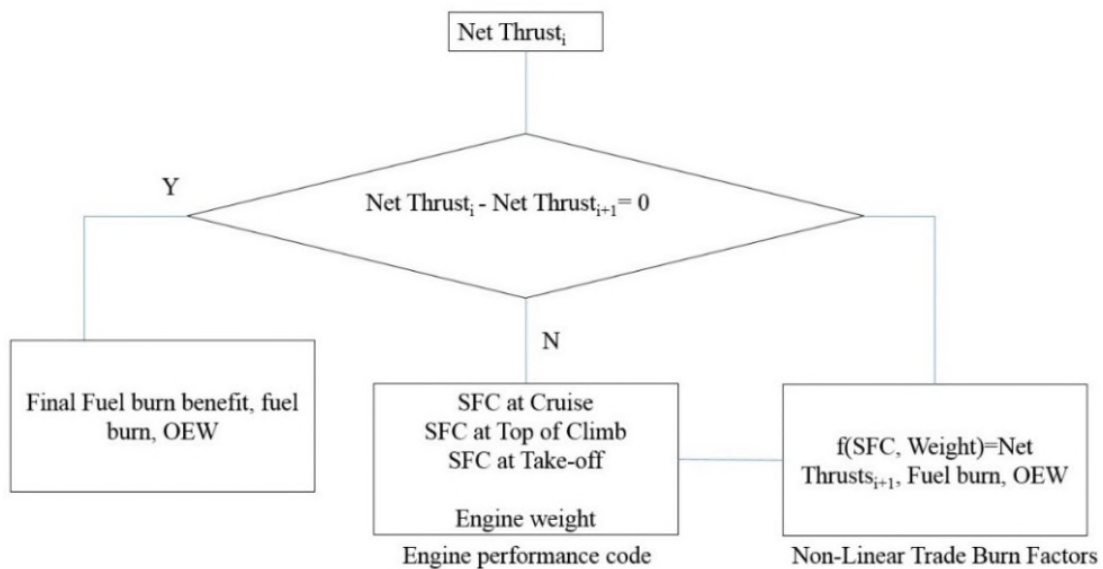


Figure 4- 36: Schematic representation of procedure to estimate relative fuel burn benefits for Y2050 GOR-ND engine system configurations

5 Results and Discussion

This chapter includes an overview of the performance of the baseline Y2000 short range engine, Y2050 reference engine and Y2050 GOR-ND engine system variants. In addition, a qualitative discussion of the potential noise and NO_x emission impact for each aero-engine configuration.

The structure of this chapter is as follows:

- Description of the performance of the baseline Y2000 short range engine.
- Description of the performance estimate of the reference GOR 2050 engine.
 - Description of the design considerations and iterations employed to size the final reference GOR2050 configuration.
 - A parametric analysis of the contra rotating propeller array with regards to its effect on overall engine performance and mass is determined.
- Validation and Calibration of the preliminary nutating disc engine system performance and sizing model.
 - Entails a validation of the thermodynamic model.
 - Verification of geometric sizing models used for the Nutating disc engine system.
 - Parametric assessment of introduced parameters, depicting their sensitivity on the geometry and cycle.
- Differentiation between a GOR configuration that has a nutating disc engine system that powers the LP-spool GOR (ND LP-drive) and a GOR configuration that has a nutating disc engine system that powers the IP-drive (ND IP-drive).
 - Entails the procedure to ensure both ND engine system configurations outperform the fuel burn estimate of the reference Y2050 GOR variant.
 - Performance of both ND engine system configurations and a discussion of the benefits and shortcomings of each configuration.
- Performance of the Y2050 GOR with a nutating disc engine system that powers the IP-spool (Y2050 GOR IP-drive) is discussed.
 - A sensitivity study to show the effect of design point TSFC and mass estimates, based on the choice of ND engine system design variables
 - A parametric study to show the topography of the design space.
 - a qualitative discussion of the potential of each configuration in terms of emission profile
- Performance of the Y2050 GOR with an intercooled nutating disc engine system that powers the IP-spool (Y2050 GOR IP-IC-drive) is discussed.

- A parametric study to show the topography of the design space is shown and discussed.
- A qualitative discussion of the potential of the configuration in terms of NO_x and noise emission profile is highlighted.
- Performance of the Y2050 GOR with a re-heated nutating disc engine system that powers the IP-spool (Y2050 GOR IP-SC-drive) is discussed.
 - A parametric study to show the topography of the design space is shown and discussed.
 - A qualitative discussion of the potential of the engine arrangement in terms of NO_x and noise emission profile is discussed.
- Performance of the Y2050 GOR with an intercooled-re-heated nutating disc engine system that powers the IP-spool (Y2050 GOR IP-SC-IC-drive) is discussed.
 - A parametric study to show the topography of the design space is shown and discussed.
 - A qualitative discussion of the potential of the engine arrangement in terms of NO_x and noise emission profile is discussed.
- Discussion with regards to the benefits and shortcomings of each IP-drive configuration.
 - A quantitative comparative assessment of all the ND engine system configurations is conducted.
 - A qualitative assessment of each proposed engine configuration, in order to determine which engine configuration would potentially advance past the current technology readiness level.

5.1 Year 2000 short range engine

In order to benchmark the TSFC and mass estimates of Y2050 GOR ND engine system configurations against a comparable Y2000 short range turbofan, a Y2000 short range turbofan model was constructed in PROOSIS using Turbo library 3.2.3[89,95]. The performance model that has been constructed is similar to a CFM56-5b type performance model. In a previous EU project, NEWAC, the performance of a CFM56-5b type model has been highlighted at top of climb (TOC), mid-cruise (CR) and end of runway conditions (EOR) [97]. Therefore, a representative engine model is created to replicate the performance stipulated in [97]. In order to create an engine performance model that effectively replicates the NEWAC dataset, the engine performance model within PROOSIS has been transformed in to a representative PROOSIS engine deck. Its subsequent performance has been matched to the NEWAC data by means of an optimization algorithm in Isight[128]. As a consequence an optimizer was chosen to achieve a relatively good match, Figure 5-1 shows the structure

of the Isight model that **matched** the performance of the PROOSIS model with the NEWAC data set.

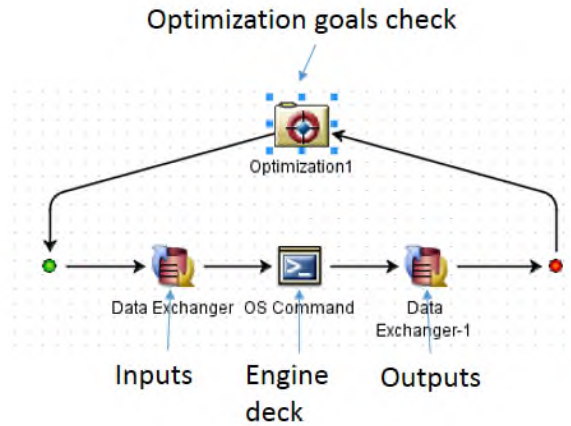


Figure 5- 1: schematic of optimizer flow path in the Isight environment

In order to benchmark an appropriate match between the SRTF2000 model and the NEWAC data, it was assumed that the net thrusts, OPRs and TSFC's at TOC, CR and EOR had to be **matched** as a final outcome. To achieve these targets a 'Pointer' algorithm was chosen. Table 6-1 indicates the settings that were specified for the algorithm, in the optimization GUI within Isight.

Table 5- 1: Optimizer global variables

<u>Option</u>	<u>Value</u>
Average analysis time [sec]	1.0
Topography type	unknown
Max failed runs	500

A Pointer algorithm was chosen as the preferred optimizer in this instance, because it is ideally suited for continuous and dis-continuous design spaces. The Pointer algorithm approaches these 'unknown' design topographies by employing a hybrid search method, essentially by coupling the following optimization methods [128]:

- A genetic algorithm
- Nelder and Mead downhill simplex
- Sequential quadratic programming (NLPQL)
- Linear solver

Once the appropriate choice of algorithm had been ascertained, a series of input variables were defined together with upper and lower bounds of the same within Isight. Since the performance of the turbomachinery associated with high-spool shaft had been omitted in the NEWAC dataset, the pressure ratio of the HPC and adiabatic efficiencies of the HPC and HPT were included in the design variables together with scaling factors for the associated turbomachinery components (for range of acceptable scaling factors please refer to the documentation of Proosis [95]). Table 5-2 shows the number of input variables used within the framework of the optimizer. It should be noted that the NcRdes, NcRdesmap and BETA or ZETA variables for all turbomachinery components are incorporated such that the operational speed line and surge margin are selected in such that the off-design conditions of the NEWAC data are matched. Furthermore, the bypass ($C_{x,20}$) and core nozzle ($C_{x,18}$) discharge coefficients are also included as variables, in accordance with the discharge coefficient range in literature [32,60] in the optimizer such that the NEWAC dataset is matched. It must be mentioned that the nomenclature that is used for the in Table 5-2 corresponds to PROOSIS component nomenclature, which is based on ARP755-A naming practices[95,98].

Table 5- 2: Design Variable bounds used for Isight matching

<u>Parameter</u>	<u>Units</u>	<u>Lower bound</u>	<u>Upper bound</u>
Booster NcRdes	-	0.95	1.05
Booster NcRdesMap	-	0.95	1.05
Booster BETA	-	0.4	0.6
HPC PR	-	13.0	13.8
HPC η_{isen}	-	0.86	0.89
HPC NcrDesmap	-	0.95	1.05
HPC NcRdes	-	0.95	1.05
HPC Wbld	-	0.1	0.15
Combustor outlet temp. (COT)	K	1550	1570
HPT η_{isen}	-	0.87	0.89
HPT NcrDesmap	-	0.95	1.05

<u>Parameter</u>	<u>Units</u>	<u>Lower bound</u>	<u>Upper bound</u>
HPT NcRdes	-	0.95	1.05
HPT ZETA	-	0.4	0.6
LPT NcrDesmap	-	0.95	1.05
LPT NcRdes	-	0.95	1.05
LPT ZETA	-	0.4	0.65
CX _{,18}	-	0.98	0.998
CX _{, 20}	-	0.98	0.998

In order to guide the optimizer to the desired solution, certain constraints were imposed on the Isight model. Details of the applied constraints are given in Table 5-3.

Table 5- 3: Constraints imposed on optimizer

<u>Parameter</u>	<u>Units</u>	<u>Lower bound</u>	<u>Upper bound</u>
TSFC at TOC	g/(kN*s)	17.7	19.1
TSFC at CR	g/(kN*s)	16.5	17.5
TSFC at EOR	g/(kN*s)	13.0	14.0

Finally, the targets for the multi-objective optimizer needed to be specified, Table 5-4 indicates the values. In order to ensure that the chosen targets were given, a similar degree of weighting within the construct of the objective function was ensured.

Table 5- 4: Scale and Weight factors used in optimization

<u>Parameter</u>	<u>Units</u>	<u>Direction</u>	<u>Target</u>
FN at TOC (N)	N	target	30140
OPR at TOC (-)	-	target	35.5
OPR at CR (-)	-	target	27.85
OPR at EOR (-)	-	target	27.7
TSFC at TOC	g/(kNs)	target	18.71

<u>Parameter</u>	<u>Units</u>	<u>Direction</u>	<u>Target</u>
TSFC at CR		target	17.11
TSFC at EOR		target	13.59

As a result of the matching exercise in Isight, the performance overview of the derived Y2000 baseline engine performance model for intra-European missions is highlighted in Table 5-5. The engine performance model of the SRTF2000 replicated the performance of an equivalent CFM56-5B engine, with PROOSIS and Isight. The performance results of the engine model at three distinct operating conditions are highlighted in Table 5-5. Furthermore, the design point for the performance model was assumed to be at TOC and the subsequent performance points at EOR and CR were assumed to be off-design conditions. The station numbering with regards to the SRTF2000 engine configuration are consistent with the practices outlined in ARP755A [98].

Table 5- 5: SRTF2000 engine specification

<u>Component</u>	<u>Parameter</u>	<u>Units</u>	<u>SRTF2000 (TOC)</u>	<u>SRTF2000 (CR)</u>	<u>SRTF2000 (EOR)</u>
General Information	Mach	-	0.78	0.78	0.25
	Altitude	m	10700	10700	0
	dT ISA	K	10	10	15
	HP shaft mech. losses	W	67113	67113	67113
	NL	RPM	4888	4405	5000
	Total net thrust	kN	30.1	21.9	96.1
	BPR	-	4.63	5.12	5.10
	OPR	-	35.68	28.38	28.21
HPC	Pressure ratio	-	13.58	12.15	12.60
	Isentropic efficiency	-	0.87	0.89	0.88

<u>Component</u>	<u>Parameter</u>	<u>Units</u>	<u>SRTF2000 (TOC)</u>	<u>SRTF2000 (CR)</u>	<u>SRTF2000 (EOR)</u>
	Exit temperature	K	789	717	848
	NH	RPM	14064	12891	14460
	HPC Wbld 1	(%)	12.4	12.4	12.4
Combustor	FHV	MJ/kg	42.8	42.8	42.8
	Efficiency	-	0.9995	0.9995	0.9995
	dP40qP30	-	0.043	0.043	0.043
	COT	K	1572	1393	1642
HPT	TET	K	1530	1357	1599
	Isentropic efficiency	-	0.88	0.87	0.88
	Tblade	K	1336	1185	1398
Performance output	Thermal efficiency	-	0.46	0.46	0.41
	Propulsive efficiency	-	0.65	0.73	0.39
	Overall efficiency	-	0.29	0.31	0.16
	Specific thrust	m/s	200	191	267
	Engine air mass flow	kg/s	150.7	114.8	360.40
	TSFC	g/kN/s	18.92	18.01	14.00

It can be seen that the final SRTF2000 engine performance falls in line with the NEWAC data. The blade metal temperature at EOR conditions is excessive but if the inclusion of a thermal barrier coating (TBC) had been considered explicitly, the blade metal temperature would be under the 1340 K limit specified in [60]. Table 5-6 compares the targets of the optimization with the NEWAC data, and it can be seen that the average absolute deviation

from the NEWAC data is 1.5%. Figure 5-2, further shows the closeness of fit between the SRTF2000 performance model and the provided NEWAC dataset in the form of a radar plot.

Table 5- 6: SRTF2000 comparison versus NEWAC data specification

<u>Condition</u>	<u>Parameter</u>	<u>Units</u>	<u>VITAL</u>	<u>SRTF2000</u>
TOC	OPR	-	35.50	35.68
	TSFC	g/(kN*s)	18.71	18.92
	Fn	N	30.14	30.08
CR	OPR	-	27.85	28.38
	TSFC	g/(kN*s)	17.11	18.01
	Fn	N	21.90	21.90
EOR	OPR	-	27.70	28.21
	TSFC	g/(kN*s)	13.59	14.00
	Fn	N	96.06	96.06

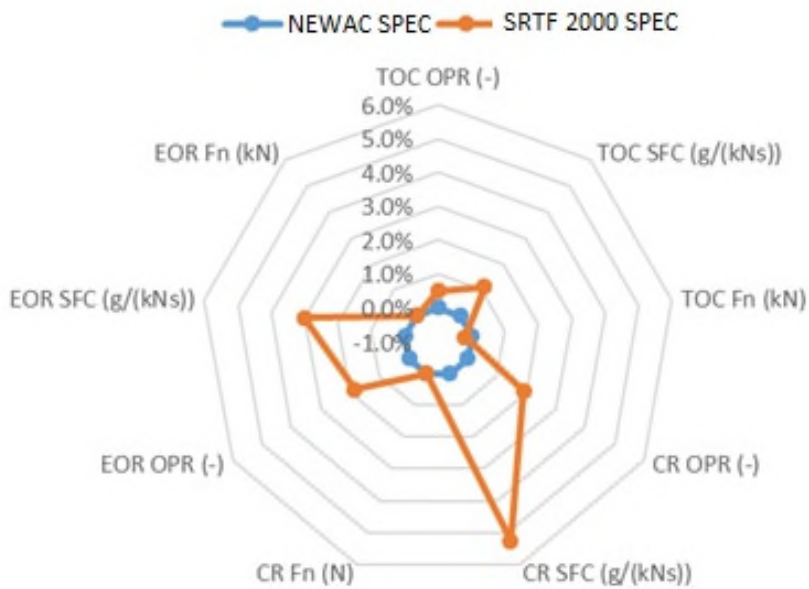


Figure 5- 2: Radar plot indicating the closeness of fit between the SRTF2000 model and the NEWAC dataset.

Although there is an absolute average deviation between the SRTF2000 model and the NEWAC dataset of 1.5%, there are certain parameters that exceeded the NEWAC performance estimates by 5%. The primary reasons for this deviation is:

- The maps chosen to derive the off-design performance can vary between the NEWAC and SRTF2000 modelling approaches.

The rotational speeds for the HP and LP spool specified for the baseline engine configuration in Table 5-5, are derived from the EASA type certificate data sheet, by scaling the stated operational speeds to replicate 100% absolute rotational speeds (Table 5-7). Furthermore, the exit hub to tip ratios of the HPT and LPT are derived from a scaled cutaway of the CFM56-5B engine [106]. Finally, a representative exit axial flow Mach number is chosen at EOR conditions to determine the exit area and rim speeds of the HPT and LPT respectively. Table 5-7 shows how the derived design compares to the accepted values of exit AN² and associated rim speeds, as per Walsh and Fletcher [32], which must not exceed 5.0e+07 rpm²m² and 400 m/s respectively.

Table 5- 7: Absolute rotational speeds of SRTF2000 and component parameters at EOR

<u>Parameter</u>	<u>Units</u>	<u>HPT</u>	<u>LPT</u>
Operating Point	-	EOR	EOR
U _{tip}	m/s	575	212
N	RPM	14460	5000
AN ²	RPM ² m ²	26.3 X 10 ⁶ (exit)	9.57 X 10 ⁶ (exit)

Once the performance of the SRTF2000 was deemed a suitable match with the NEWAC dataset, the mass of the engine configuration was determined using the EOR conditions of the engine model. The mass of the engine is estimated at EOR because the highest absolute mechanical loads are expected at EOR conditions.

The software that is used to determine the dry and total mass of the engine configuration is WeiCo 9.6, which was supplied by Chalmers university under the confines of the ULTIMATE project [39]. Weico 9.6 estimates the mass of the engine by using 1D methods to size the gas path, discs, shafts, components and the nacelle[39]. The dry and total mass estimate of the SRTF2000 engine configuration is 2339kg and 3086kg respectively[61]. The subsequent meridional view of the SRTF2000 is shown in Figure 5-3 [61].

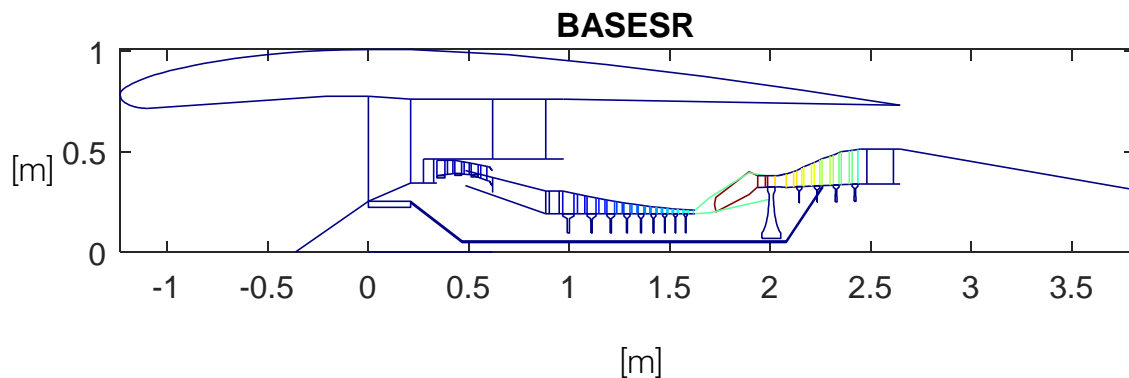


Figure 5- 3: SRTF2000 meridional view [61]

5.2 Year 2050 reference GOR engine

The envisaged advanced tube and wing (ATW) aircraft design for short range intra-European missions (SR) in year 2050 is deemed to feature a geared open rotor propulsor [107]. Revolutionary concepts in short range aircraft design and manufacturing that are assumed to be introduced by entry into service (EIS) of 2050 claim to significantly reduce the drag of the short range aircraft, while maintaining similar levels of payload capacities as of year 2000 [96]. This in turn leads to a reduced net thrust requirement from the propulsors throughout the flight envelope. This thrust reduction coupled with an industry outlook to have operational GORs by the year 2050, demands the modelling of a rear fuselage mounted GOR2050 engine model. In order to model the GOR2050, a unique approach is required.

The necessity of this approach mainly stems from a difference between the thrust levels envisaged by the original equipment manufacturer (OEM) in 2050 [60] and the thrust requirements (as per [107]) needed by an assumed EIS 2050 short range aircraft. As a result, the modelling of the performance of the GOR2050 needs to be flexible in order to account for the aircraft-engine snowballing effect. In order to do so, three phases of modelling the GOR2050 were adopted.

This approach to modelling the engine (in fact any conventional engine configuration) is beneficial in making robust engine models that are capable of incorporating the snowballing effect incumbent due to improvements in preliminary aircraft and engine designs. This section of defining year 2050 short range engine technology levels was performed within the confines of the ULTIMATE project.

Within the scope of the preliminary work done in ULTIMATE, perceived reference engine cycle parameters, performance estimates and subsequent meridional engine views for the GOR2050 engine were outlined by Safran Aircraft Engines. The proposed engine

configuration, as per [60], claimed that the GOR2050 would be 34.2% more efficient than a CFM56-5B engine (year 2000 baseline engine). Consequently, the first step in the global modelling approach for the GOR2050 is to match the quoted performance model as stated in [60], to ensure that the technology levels assumed for the modular engine components are consistent with what is expected by the year 2050. The engine model, to match the performance estimates in [60], was constructed using PROOSIS and is referred to as the M-GOR2050 configuration. As mentioned in Section 2.2, it is assumed that the reference GOR is of a pusher variant and will be fuselage mounted similar to the engine arrangement on an MD-88 or a B7J7 aircraft [60].

Under the collaborative efforts in ULTIMATE continual improvements to the mass and drag estimates of the short range aircraft model, for a fixed 3500NM mission, led to a series of iterations of possible engine design thrust levels. Therefore, the second step, in the global modelling approach, involves creating a range of scaled engine models based on the technology levels derived from the M-GOR2050 configuration engine model such that the payload requirements of the 3500NM could be met by a year 2050 SR aircraft. Details of how exactly the engines are scaled are provided in the following sub-sections.

Finally, once a short range aircraft configuration was sized, an engine model was assembled to meet final reference engine thrust requirements throughout the flight envelope [96]. A matching procedure was used on derived engine model such that it produced an engine configuration, that met the thrust and fuel burn demands of the frozen reference short range aircraft [96]. The matching procedure entails using an optimization algorithm to ensure that the engine model meets the thrust demands of the aircraft.

The term 'matched optimization procedure' is coined because the Pointer based optimization algorithm is used to match the aircraft requirements and the engine model outputs. This step was necessary as the final engine model will be used in assessing the relative benefits of the advanced core technology enabled engines. Figure 5-4 highlights the global modelling approach undertaken to produce the final GOR2050 engine model.

Once the final engine model is presented, parametric studies are conducted on the LP system to show the sensitivity of its design parameters on propulsive efficiency, benefits or penalties, for the reference GOR2050 configuration.

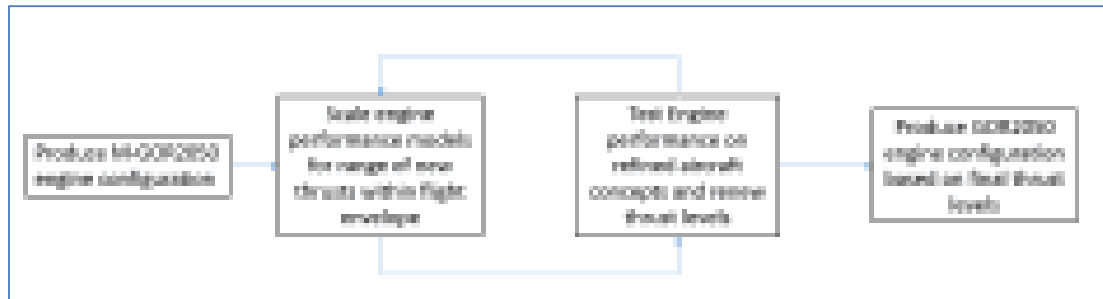


Figure 5- 4: Schematic of global overview of modelling procedure to produce the GOR2050 configuration

5.2.1 Performance overview of the M-GOR2050 engine configuration

The cycle parameters for the industry based reference GOR2050 design at cruise (CR) conditions are provided in Table 5-8 as an outcome of the perceived technology limits predicted by Safran Aircraft Engines in the year 2050[60]. Since there is no comparable power-plant in service in year 2000 the industry-reference 2050 short-range engine is instead benchmarked against an EIS 2025 GOR, as outlined in Table 5-8 [60]. In addition, as per the perceived industry outlook, a proposed meridional view of a potential reference Y2050 GOR configuration is presented in Figure 5-5. Particular design features of the industry perceived GOR2050 include the following:

- The engine is mounted towards the aft of the fuselage, similar to that of the engine arrangement on an MD-88 or a Boeing 7J7 aircraft. The reason for the positioning of the engine is two fold; the primary one attributed to poor ground clearance if the engine was mounted under the wing and the second being a relatively better cabin noise signature if the engine is rear-fuselage mounted[61].
- The high speed power turbine (PWT) powers a pusher contra rotating propeller (CRP) array through an epicyclic reduction gear box. This configuration is preferred over a CRP array being powered by a contra-rotating LPT stage due to stability reasons associated during the operation of a multi-stage contra rotating turbine[16]. In addition, it is assumed that the epicyclic gearbox is located fore of the contra rotating propellers such that there is an added degree of freedom of design when it comes to the relative spacing between the fore and aft propellers for noise purposes. In addition, another reason why the epicyclic gearbox is placed fore of the CRP array is due to relatively less laborious lubrication system[61].
- A zero bleed configuration for environmental cabin systems (ECS) demands; it is assumed that no overboard bleed is taken from the core and instead a power offtake is obtained from the high pressure (HP) spool to meet envisaged 2050 ECS demands[60,61].

- The diameter of the rear propeller is assumed to be clipped by 20% relative to the front propeller. A reason as to why this has been done stems from the perceived noise level benefits in the landing and take-off (LTO) cycle as the front propeller tip vortex interaction with the rear propeller leading edge is significantly reduced [16].

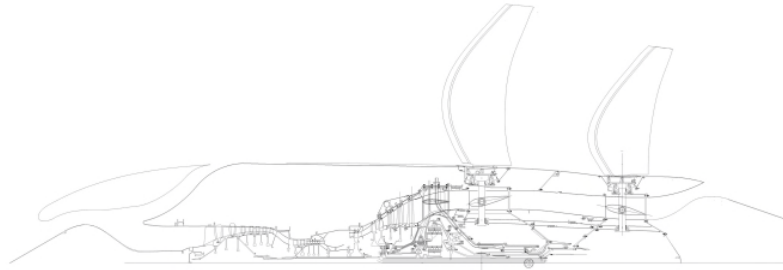


Figure 5- 5: Visualization of the potential industry GOR2050 general arrangement by Safran Aircraft Engines [60]



Figure 5- 6: Visualization of the mounting location on an Y2050 SR aircraft[107]

Table 5- 8: industry based reference GOR2050 design parameters at mid-cruise[60]

			Reference open rotor (EIS 2025)	ULTIMATE Baseline open rotor (EIS 2050)	Comments
General	Mach	-	0.75	0.75	
	Altitude	km	11.9	11.9	
	FHV	MJ/kg	42.8	42.8	
	HP shaft power extraction	kW	77.5	77.5	Bleedless configuration
	Total net thrust	N	16707	16707	Typical cruise condition (500NM mission)
	BPR	-	100.5		Approximate value based on Froude theory for propeller airflow
	OPR	-	48.4	48.4	Typical cruise condition (500NM mission)
	Gearbox eff	-	0.987	0.987	
Propellers	Propeller diameter	m	4.27	4.27	1st propeller diameter (2nd propeller with 20% clipping)
	Propeller net efficiency	-	0.872	0.9	Net propeller thrust * V0 / shaft power
Compressors	IPC pressure ratio	-	8.8	8.8	
	IPC polytropic efficiency	-	0.924	0.924	
	HPC pressure ratio	-	5.58	5.58	
	HPC polytropic efficiency	-	0.899	0.899	
Turbines	HPT TET	K	1714	1730	
	HPT isentropic efficiency	-	0.917	0.917	
	IPT isentropic efficiency	-	0.948	0.948	
	PWT isentropic efficiency	-	0.945	0.945	
Outputs	Core efficiency	-	0.543	0.548	
	Transfer efficiency	-	0.825	0.849	
	Thermal efficiency	-	0.448	0.465	
	Propulsive efficiency	-	0.947	0.948	
	Thermopropulsive eff.	-	0.424	0.441	
	SFC	g/kN/s	11.87	11.44	-3.7%
	kg/daN/h	0.427	0.412		

Limited information, for the industry GOR2050 engine, is provided with regards to off-design conditions within [60]. However, through internal communications with Safran Aircraft Engines updated performance figures at CR, TOC and EOR are provided and have been included in Table 5-9[61]. It must be mentioned that the HPT TET stated in Table 5-8 has been revised from 1730K to 1606K. The primary reason for this is because the TET figure had been misquoted in [60].

Table 5- 9: Operational envelope as specified by Safran Aircraft Engines

<u>Property</u>	<u>Units</u>	<u>EOR</u>	<u>Typical Cruise</u>	<u>MCL at Cruise</u>
Altitude	ft	1150	39000	39000
Mach	-	0.2	0.75	0.75
Delta ISA	K	28	0	10
TET	K	1740	1606	1730
OPR	-	38.5	48.4	53.6

The primary step in defining the final GOR2050 cycle performance is to create a M-GOR2050 engine performance model such that it matches the technology limits set out by the industry perceived GOR2050 limits. Therefore, as a consequence of a matching exercise a general overview of the performance of the M-GOR2050 configuration is depicted in Table 5-10. Further details with regards to the performance of the M-GOR2050 configuration can be found in Appendix A.

Table 5- 10: M-GOR2050 general performance figures compared to industry GOR2050 performance figures

	<u>Parameter</u>	<u>Units</u>	<u>CR</u>			<u>TOC</u>	<u>EOR</u>
			<u>SN</u>	<u>model</u>	<u>Dev. (%)</u>	<u>model</u>	<u>model</u>
General	Mach no	-	0.75	0.75	0.00	0.75	0.2
	Altitude	km	11.9	11.9	0.00	11.9	0.35
	dT ISA	K	0	0	0.00	10	28
	FHV	MJ/kg	42.8	42.8	0.00	42.8	42.8

	<u>Parameter</u>	<u>Units</u>	<u>CR</u>			<u>TOC</u>	<u>EOR</u>
			<u>SN</u>	<u>model</u>	<u>Dev. (%)</u>	<u>model</u>	<u>model</u>
	HP shaft power extraction	kW	77.5	77.5	0.00	77.5	322.7
	Total Thrust	N	16707	16707	0.00	18669	72321
	OPR	-	48.4	48.4	0.00	53.6	35.1
	TSFC	g/kNs	11.44	11.44	0.04	12.11	7.44
	W	kg/s		9.5		10.11	22.24
	TET	(K)	1606	1606	0.00	1735	1877

Figure 5-7 depicts a radar plot that shows the closeness of fit between the M-GOR2050 performance estimates and the industry reference GOR2050 configuration in relative terms.

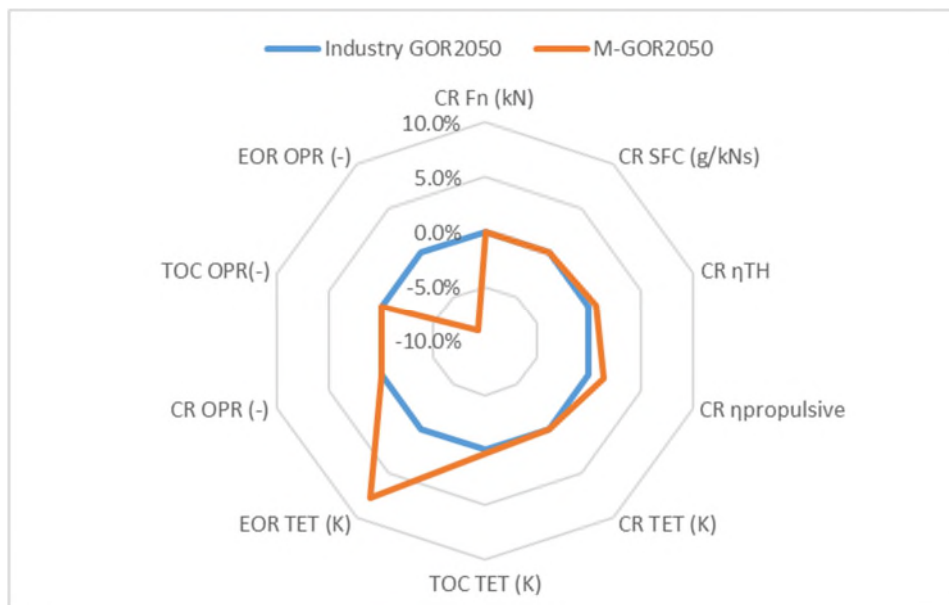


Figure 5- 7: Radar plot that indicates the closeness of fit between M-GOR2050 configuration and industry reference GOR2050 configuration

It can be seen that the TET and OPR at EOR conditions are over predicted and under predicted respectively. The primary reason for this divergence can be attributed to:

- The off-design performance, as per PROOSIS, is derived from scaling component BETA maps. Whereas the OEM has used proprietary MFT maps to derive the performance of the GOR, this can lead to divergence in the EOR values.

- It is assumed that the rotational speed of the propellers are the same across the flight envelope, this directly affects the efficiency of the CRP array. Whereas the rotational speed of the OEM model at off-design varies throughout the operational envelope.

When the M-GOR2050 configuration is compared to the industry GOR2050 there is an overall absolute average divergence of 0.1%. The M-GOR2050 engine model includes certain design considerations and sensitivities for the CRP propeller array and the axial turbines. Hence the following sub-sections shall comment on these design considerations or sensitivities

5.2.1.1 Contra rotating propeller performance

An important aspect of modelling the contra rotating propeller (CRP) array is the assumption that the CRP rotates at a fixed speed throughout the flight envelope and the pitch control mechanism (PCM) will vary the pitch angle during operation to ensure that the desired gross thrust from the propeller is achieved. It was seen that by changing the rotational speed throughout the flight envelope considerable changes were observed in the pitch angle of the front and rear propellers at 75% span, while minimal changes were observed in the gross thrust and propeller efficiencies. Table 5-11 shows a brief comparative study that shows the effect of varying the propeller speeds at off-design conditions for the M-GOR2050 configuration. In the 'varying rpm' case study the CRP speeds were changed at TOC and EOR conditions by 14% and 27% respectively. This in turn, had a significant impact on the pitch angle of the front and rear propellers. However, the gross thrust produced at EOR and TOC conditions deviates less than 0.3%. An optimization with regards to optimal speed and pitch angle deviation in the flight envelope can lead to a reduced mass impact of the PCM.

Table 5- 11: Effect of varying CRP speeds on the pitch setting throughout the flight envelope

<u>Parameter</u>	<u>M-GOR2050 Varying RPM test case</u>	<u>M-GOR2050 Constant RPM test case</u>	<u>Dev. (%)</u>
	CR		
Forward Prop pitch (deg.)	28	28	0.0%
Rear Prop pitch (deg.)	30	30	0.0%
rpm (-)	731	731	0.0%

<u>Parameter</u>	<u>M-GOR2050 Varying RPM test case</u>	<u>M-GOR2050 Constant RPM test case</u>	<u>Dev. (%)</u>
TSFC (g/kNs)	11.44	11.44	0.0%
Fg Propellers (N)	16691	16691	0.0%
	TOC		
Forward Prop pitch (deg.)	31	28	-10.0%
Rear Prop pitch (deg.)	33	30	-8.0%
rpm (-)	831	731	13.7%
TSFC (g/kNs)	12.11	12.38	2.2%
Fg Propellers (N)	18376	18312	-0.3%
	EOR		
Forward Prop pitch (deg.)	61	55	-10.0%
Rear Prop pitch (deg.)	62	57	-7.5%
rpm (-)	931	731	27.4%
TSFC (g/kNs)	7.44	7.76	4.3%
Fg Propellers (N)	69462	69592	0.2%

The operation of the front and rear propellers can be depicted by propeller maps, which are scaled representations of SR7 maps [111] without the consideration of compressibility effects.

The scaled propeller maps in Figure 5-8 and 5-9 show the coefficient of power vs advance ratio amidst efficiency contours, for both the forward and rear propeller respectively for the M-GOR2050 engine model.

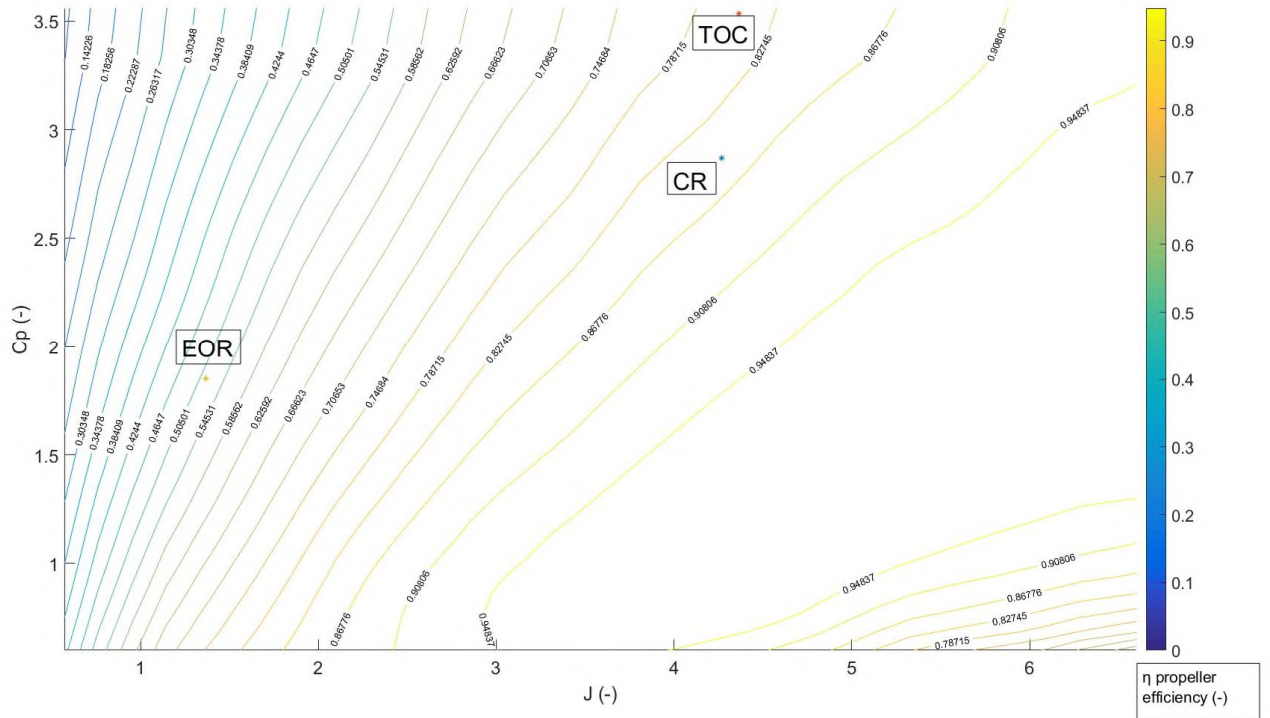


Figure 5- 8: Scaled forward propeller performance map of the M-GOR2050 at three operating conditions

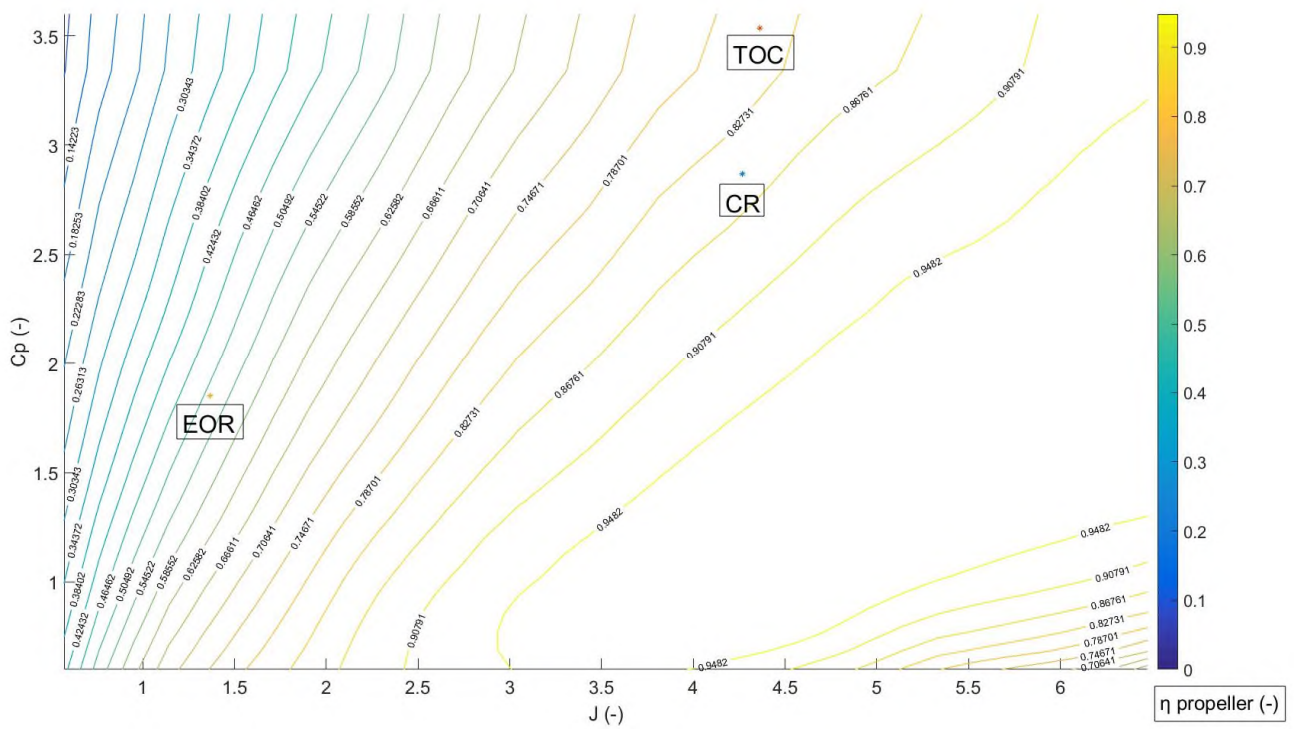


Figure 5- 9: Scaled rear propeller performance map of the M-GOR2050 at three operating conditions

5.2.1.2 Axial Turbines

The design considerations and sensitivities for the three axial turbines within the M-GOR2050 are presented in the following sub sections. The design considerations are addressed for the HPT, IPT and LPT respectively.

5.2.1.2.1 High Pressure Turbine

The design considerations and sensitivities specific to the HPC component, for the M-GOR2050 model are:

- A cooling air constant (CAc) value of 0.05 for the HPT component in PROOSIS, which is representative of the technology level of the internal convection cooling in TURBO library 3.2, was chosen.
- A relative total inlet temperature (T_{rel}) that the rotor would encounter during operation, in order to account for the rotating frame of reference. A value of 90% of the stator outlet temperature was used in the HPT component [89].
- It is considered that by EIS 2050 ceramic matrix composite materials would be used in the NGV of the HPT, hence there would only be internal convection cooling requirements for the same [60]. In addition, based on industry recommendations, the limiting blade metal temperature of the HPT rotor is 1400 K, after accounting for the application of thermal barrier coating (TBC). Therefore a limit of the M-GOR2050 design was chosen to ensure that the blade metal temperature at EOR conditions did not exceed 1400K.
- The HPC delivery bleed is assumed to be split between the NGV and the HPT by 45% and 55% respectively. In addition, it is assumed that 80% of the bleed flow is reintroduced into the gas path and does work in the subsequent components downstream. The 20% mass flow deficit is assumed to address platform cooling needs and the sealant needs for the HP system. Although the aforementioned method estimates the blade metal temperature of the rotor, it has the following limitations:
 - Additional cooling benefits that stem from film cooling are not explicitly shown
 - The cooling benefit that stems from the addition of TBC are not seen.
 - Radial variations in the stator outlet temperature (SOT) have not been accounted for with a combustor pattern factor as in [116].
 - The effects of pre-swirling the coolant flow prior to admittance in the HPT rotor has not been accounted for.
 - Although the capability of cooled cooling air (CCA) has been included within the modelling capabilities of the component model, it has not been utilized

within the scope of this work. This was because the HPC fractional bleeds were consistent with those mentioned in [32], and hence did not appear to warrant the use of CCA.

- In addition, it must be mentioned that the implications of a shrouded design's impact on the component isentropic efficiency bears no impact on the modelling assumptions.
- During the course of the matching procedure, the HPC compressor discharge pressure fractional bleed was changed in order to ensure that the calculated rotor blade metal temperature does not exceed the limit stipulated in [60] at either CR, TOC or EOR. In addition, a parametric study was conducted to ensure that the operational speeds of the HPT were mechanically sound in terms of rim speeds and AN^2 limitations. Figure 5-10 indicates the variation of AN^2 as a function of exit axial Mach number of the component, for a fixed exit hub to tip ratio of 0.875. It can be seen that the AN^2 limit of $50 \times 10^6 \text{ rpm}^2 \text{ m}^2$, as stipulated by Walsh and Fletcher ([32]) is not violated, when a HP rotational speed of 15000 at EOR is chosen. Figure 5-11 indicates the variation of the average HPT hub speed, for a fixed entry axial Mach number of 0.3 for the component, against an entry hub to tip ratio variation. It can be seen that the HPT rim speed falls below the limit mentioned in [32].

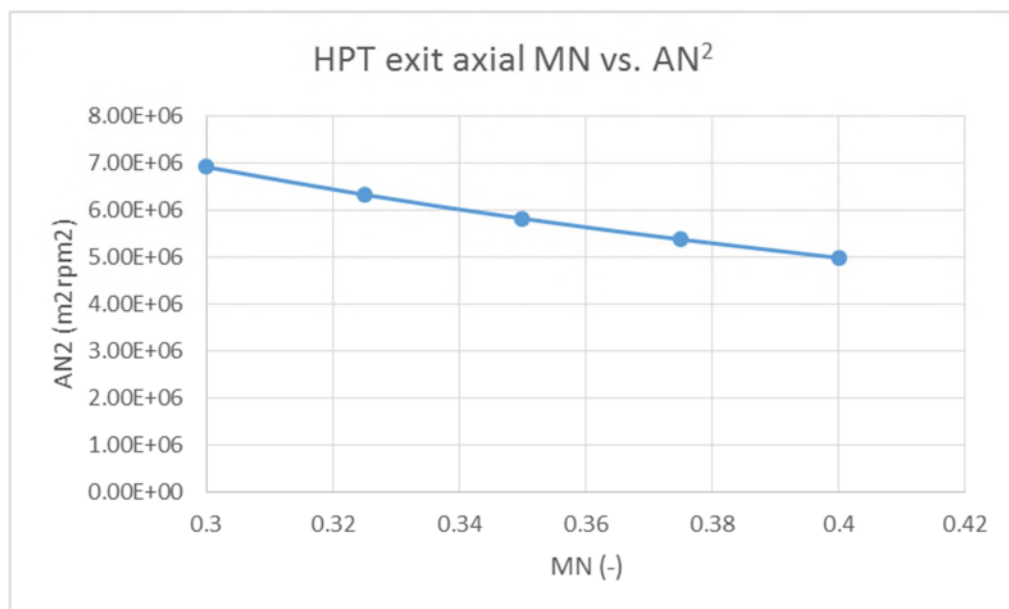


Figure 5- 10: HPT exit AN^2 variation as a function of axial exit Mach number

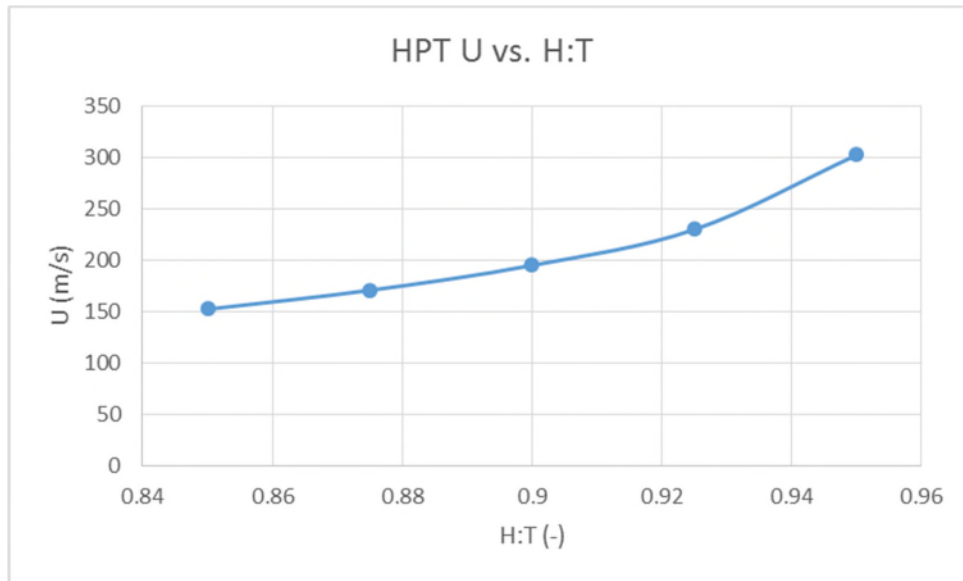


Figure 5- 11: HPT rotor blade speed variation as a function of the exit hub:tip ratio

5.2.1.2.2 Intermediate Pressure Turbine

The design considerations and sensitivities particular to IPT of the M-GOR2050 are:

- A cooling air constant (CAc) value of 0.05 was chosen
- A $T_{t,rel}$ value of 0.90 was chosen.
- 45% of the fractional bleed is used in NGV and 55% in the rotor.
- 94% of the IPT return bleed is assumed to do work in the gas path.
- The 6% deficit of the flow is assumed to address the platform cooling requirements as well as the IP sealing requirements.
- Assuming a component exit hub to tip ratio of 0.8 and an axial exit Mach number of 0.35, it was seen that the AN^2 limitations and rim speed limitations at EOR conditions aren't violated. Similar to the HPT component a parametric study was conducted to see whether changes in either the exit axial Mach number or the exit hub to tip ratio had any adverse effect on the imposed first order AN^2 mechanical constraint. It was seen that limits weren't violated for a rotational speed of 10000 rpm at EOR conditions.

5.2.1.2.3 Low Pressure Turbine

The low pressure turbine (LPT), within the M-2050GOR model, is assumed to be a high speed LPT as opposed to direct drive turbofans [16]. Within PROOSIS it is modelled as an equivalent single stage (EqSS) turbine using a scaled map of Δ enthalpy vs corrected mass flow. The reference map used for this component is an AGARD two stage turbine [105]. The LPT powers the CRP array through an epicyclic gearbox, which is located aft of the LPT. It

must be noted that the following assumptions have been accounted for within the scope of the current model:

- It is assumed that the LPT design will feature a shrouded design, however the implications on component efficiency have not been considered.
- The IPC bleed offtake is assumed to account for the LP system sealing and cooling requirements.
- It is assumed that the LPT is a high speed component, as opposed to conventional low speed LPTs in most turbofan engines

It is assumed that the LPT will operate at a constant absolute speed throughout the flight envelope. The reason for this is that the LPT is coupled to the CRP array, which rotates at a fixed rpm throughout the flight envelope, through a fixed reduction ratio planetary differential gearbox (DPGB).

This assumption would certainly have an effect on the component level efficiency of the LPT throughout the flight envelope. However, by using a scaled reference map it is possible to estimate the efficiency variation at off-design conditions. Figure 5-12 shows the working points of the LPT.

However, in practice the LPT rpm schedule is controlled by four target power conditions, namely maximum power at low and high altitude conditions and intermediate and low power conditions[61].

Consequently, the LPT is not operating on a single set of points. It must be mentioned that the x-axis in Figure 5-12 is the product of the non-dimensional corrected speed and the corrected mass flow. Conversely, the y-axis is the measure of the change of the specific enthalpy.

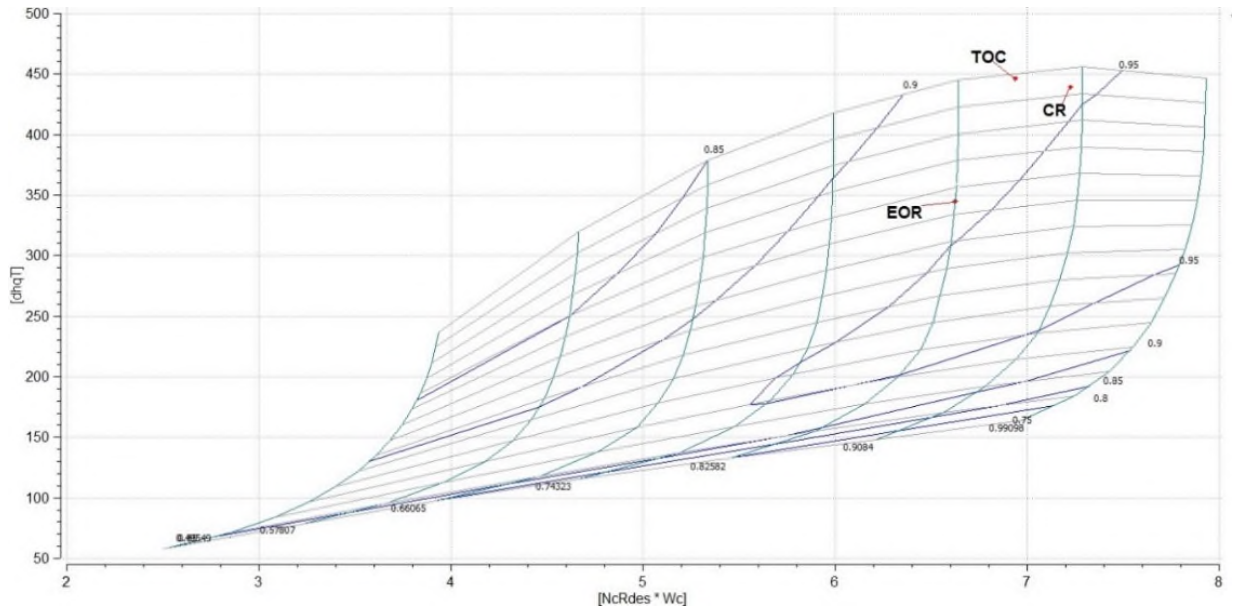


Figure 5- 12: Representative operating points on the LPT component map

As in the case of the HPT, a parametric study was conducted to ensure that the operational speeds of the LPT were mechanically sound in terms of rim speeds and AN^2 limitations.

Figure 5-13 indicates the variation of AN^2 as a function of exit axial Mach number of the component, for a fixed exit hub to tip ratio of 0.75. It can be seen that the AN^2 limit stipulated by [32] is not violated, when a LP rotational speed of 6760 is chosen.

Figure 5-14 indicates the variation of the average LPT hub speed, for a fixed entry axial Mach number of 0.40 for the component, against an entry hub to tip ratio variation. It can be seen that the LPT rim speed falls below the limit mentioned, 400 m/s, in [32].

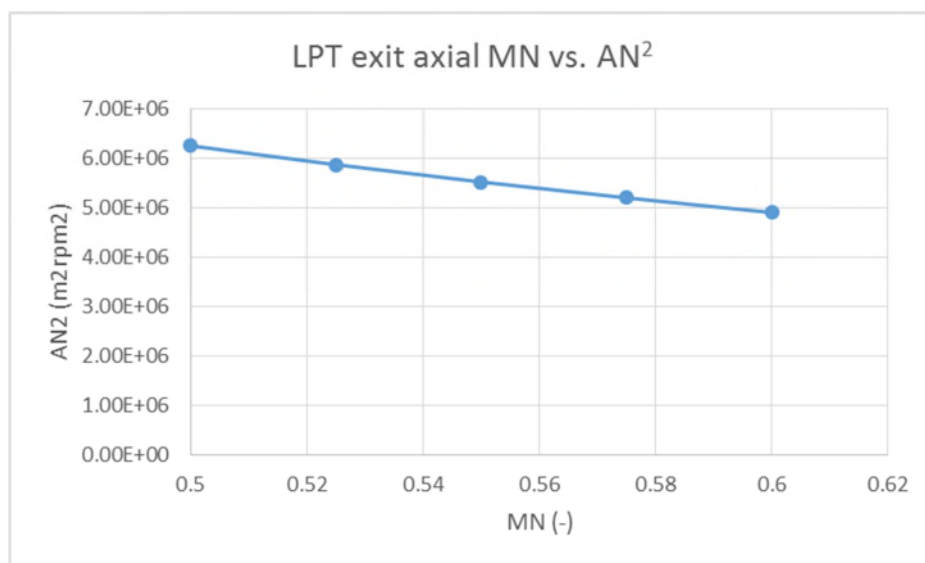


Figure 5- 13: LPT exit AN^2 variation as a function of exit Mach number

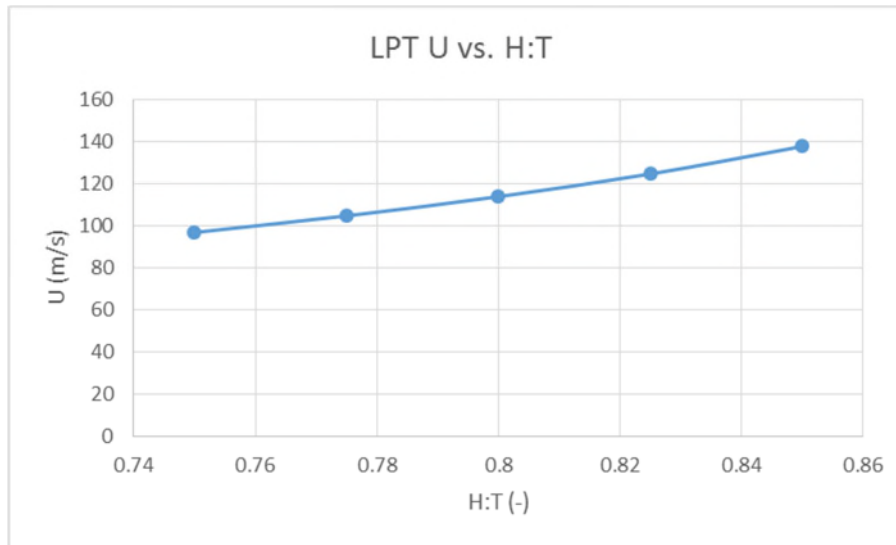


Figure 5- 14: LPT exit hub speed variation as a function of the exit hub:tip ratio

Once the technology levels of the components, not specified by Table 5-8, has been determined via the M-GOR2050 engine model a series of engine models at different TOC thrust levels were created. This was done to facilitate the sizing of the Y2050 short range aircraft, under the scope of the ULTIMATE project. The considerations for the design choices of these engine configurations are presented in the following section. Since the purpose of these engine models were to assist with the aircraft sizing they bear the designation S-GOR2050-XX, where XX refers to thrust level of the engines in kN.

5.2.2 Performance overview of the S-GOR2050-XX engine configurations

The stipulated TOC design point thrust levels, were stipulated under the scope of the ULTIMATE project in order to size the Y2050 short-range aircraft. The design point shifted from CR to TOC, as limiting propeller loading figures have been quoted at TOC[18]. The TOC thrust ratings of the range of engines, engine configuration specification and flight conditions are specified by Table 5-12. It is considered that by Y2050 the need to off-take power from the engine to run the ECS system, will be obsolete. As the potential introduction of hydrogen fuel-cells would power the ECS systems as well as other auxiliary systems that have traditionally relied on engine power-off take [107].

Table 5- 12: S-GOR2050-XX design point thrust ratings and flight conditions

<u>Design point Thrust ratings</u>					
<u>Configuration</u>	<u>Fn [N]</u>	<u>POT [W]</u>	<u>Altitude [m]</u>	<u>Delta ISA [k]</u>	<u>Mach [-]</u>
S-GOR2050-18	18000	0	10688	10	0.73
S-GOR2050-22	22200	0	10688	10	0.73
S-GOR2050-25	25000	0	10688	10	0.73

In order to produce S-GOR2050-XX models that reflect the technology levels highlighted in the M-GOR2050 engine model, certain scaling methods were employed. The scaling methods and assumptions are listed below:

- The design point conditions (for all components) are assumed to be at TOC conditions, as opposed to the design point of mid-CR of the M-GOR2050 engine model.
- All the inter-component total pressure ratios (duct pressure ratio and burner pressure ratios) are maintained as those of the M-GOR2050 engine model. Moreover, at off-design conditions, the pressure ratios of the ducts and burners are not scaled with the corrected mass flow.
- The pressure ratio split between the IPC and the HPC at TOC conditions for the M-GOR2050 engine model has been maintained for all the S-GOR2050 design points.
- The TET at TOC for all design points, is allowed to vary between 1700K and 1750K.
- The polytropic efficiencies and isentropic efficiencies for the IPC, IPT and LPT at TOC conditions for the M-GOR2050 engine are used for all design-points.
- The polytropic efficiency of the HPC is scaled as a function of the last stage blade height of the M-GOR2050 engine model. This is carried out by assigning a hub-to-tip ratio (0.895) and an axial Mach number (0.25) at the exit of the HPC (which does not include the diffuser between the HPC and the combustion chamber). The blade height of the last stage of the HPC is calculated to be 12.25 mm for the M-GOR2050.
- The last stage blade height of the HPC is calculated without considering tip-clearance. Once the last stage blade height of the HPC is ascertained, the polytropic efficiency is scaled for the S-GOR2050-XX engine model series using the methodology stipulated in [19], which corrects the HPC polytropic efficiency as a function of its last stage blade height. This method has been extended to encompass last stage HPC blade heights above 13mm. In this instance Figure 5-15 has been adjusted to account for zero efficiency correction for the blade height from the M-

GOR2050 engine model (Figure 5-16). One key assumption is that this correlation is applicable for TOC, mid-cruise and EOR sizing conditions

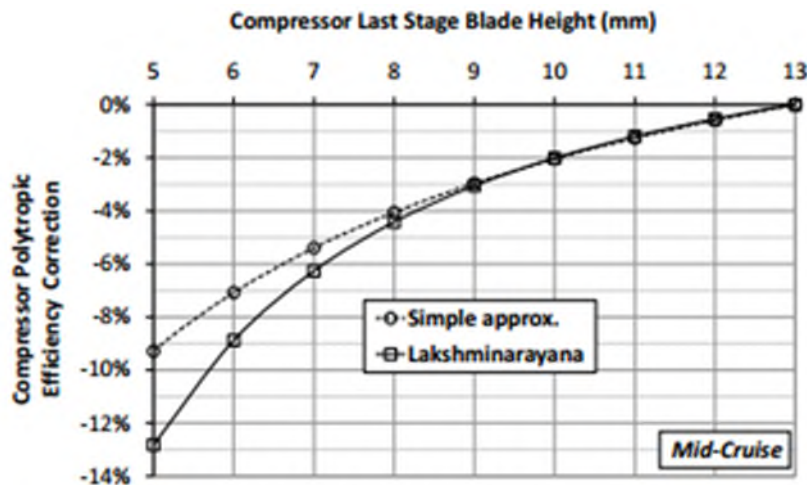


Figure 5- 15: HPC polytropic efficiency correction as a function of last stage blade height[19]

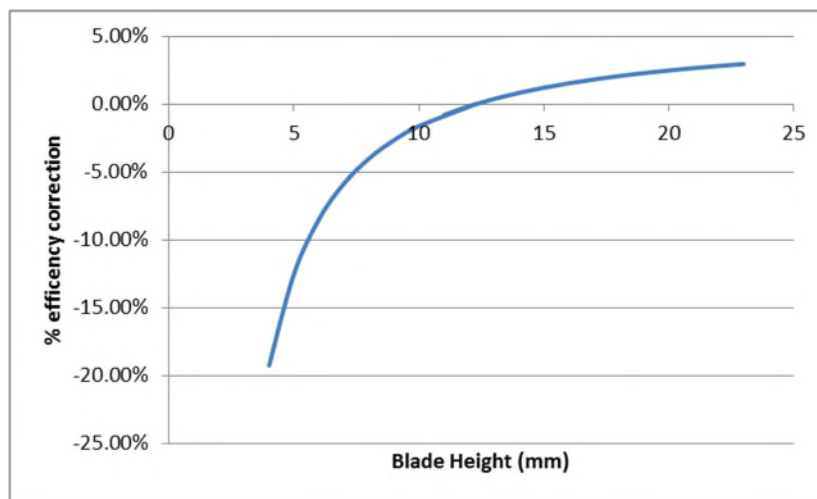


Figure 5- 16: Re-datum (as per the last stage blade height of the M-GOR2050 engine model) HPC polytropic efficiency correction as a function of last stage blade height.

Equation 5-1, indicates the coefficients of the curve fit employed in Figure 5-16 to predict the HPC polytropic efficiency correction as a function of last stage blade height for the S-GOR2050 engines. Where, b represents the last stage blade height and δ represents the efficiency penalty. In addition, Equation 5-2 estimates the scale effects imparted on the polytropic efficiency of the HPT component [20].

$$\delta_{poly,HPC} = 0.056977 - (0.5547b^{-1}) - (1.7724b^{-2}) \quad 5-1$$

$$\delta_{poly,HPT} = 0.5 \delta_{poly,HPC} \quad 5-2$$

- The forward propeller loading at TOC for the M-GOR2050 engine model is imposed for all S-GOR2050 engine design point conditions.
- The HPT, IPT and LPT cooling constants and the relative gas temperature of the M-GOR2050 engine are used in all the reference engine cases.
- All the cooling bleed flow percentages are maintained as the M-GOR2050 engine model.
- The blade metal temperatures at end of runway conditions are ensured not to exceed 1400K as proposed by [60].

In order to provide competitive TSFC reductions, relative to the M-GOR2050 engine model, a ‘targeted optimization study’ was done for each of the engines in the stipulated thrust classes of the S-GOR2050-XX engine series. The term ‘targeted optimization’ is coined because the sole purpose of employing an optimization routine was to provide engine configurations that were more competitive than the M-GOR2050 engine model. The ‘targeted optimizations’, were not subject to a setting dependency study and the optimizations did not account for mechanical, vibrational, noise constraints, emission and mass constraints at a preliminary design level.

In order to perform the targeted optimization cases a user ‘deck’ is created within PROOSIS, that has three distinct operating points (Design point at TOC, off-design at mid-cruise and EOR conditions). The user deck comprises three files: the input file, the executable and the output file. The deck is then introduced into the Isight environment (the I-sight schematic is similar to Figure 5-1) and a targeted optimization study is performed within the Isight environment.

Similar to the ‘matching’ approach taken for the SRTF2000 engine configuration a Pointer algorithm was chosen for the targeted optimization of the S-GOR2050-XX engine configurations within I-sight. Table 5-13 indicates the upper and lower bounds for the variables used for all three cases. The reasoning for choosing the upper and lower bounds of the targeted optimization are:

- The lower limit of the nozzle pressure ratio was chosen, such that the LPT design point pressure ratio was adequate enough to meet the power demands of the CRP array. This occurs because the LPT pressure ratio is directly proportional to the core nozzle pressure ratio. The upper limit of the nozzle pressure ratio was chosen such that the LPT pressure ratio increase does not correspond to an adverse LPT exit area, which could potentially violate the exit AN^2 limitation in [32].
- The lower limit of the propeller rotational speeds were imposed, such that high propeller pitch settings that lead to blade stall are avoided. The upper limit for the

propeller rotational speed is imposed because the LPT rotational speed is directly proportional to the propeller rotational speed, which in turn can violate the exit LPT AN^2 limitation.

- The lower limit of the HPC PR was imposed such that a relatively high design point OPR could be obtained, while maintaining appropriate last stage blade heights. The upper limit of the design point HPC PR was imposed such that the polytropic efficiency corrections due to last stage blade height limitations do not become too exaggerated.
- The lower limits for TETs at the three operating points were imposed such that the TSFC benefits derived from the S-GOR2050-XX series would be competitive, while ensuring that the HPC and IPC do not surge at any of the three operating points. In addition, the upper limits are chosen such that the blade metal temperatures at EOR conditions do not exceed 1400K and all engines maintain the same HPT cooling technology level.
- The torque ratio (TR) limits were imposed in accordance to the perceived technology limits indicated by Bellocq et al.[16]

Table 5- 13: Upper and lower bounds imposed on design variables within the optimization

<u>Property</u>	<u>Units</u>	<u>Lower bound</u>	<u>Upper bound</u>
Nozzle PR at TOC	-	1.10	1.3
Propeller Nmech at TOC	RPM	400	1200
HPC PR at TOC	-	5.0	6.0
TET at CR	K	1550	1700
TET at TOC	K	1700	1750
TET at EOR	K	1800	1900
TR at TOC	-	1.15	1.3

Finally, the targeted optimization, with the aforementioned settings, were set to run in the Isight environment for all the S-GOR2050-XX engine configurations. An overview of the targeted optimization studies are presented in Table 5-14 for all three engine configurations at TOC conditions. Details of all three engine cycles are presented in Appendix-A.

Table 5- 14: Overview of S-GOR2050-XX series engine models at TOC

	<u>Parameter</u>	<u>Units</u>	<u>TOC</u>		
			<u>S-GOR2050-18</u>	<u>S-GOR2050-22</u>	<u>S-GOR2050-25</u>
General	Mach no	-	0.73	0.73	0.73
	Altitude	m	10688	10688	10688
	dT ISA	K	10	10	10
	FHV	MJ/kg	42.8	42.8	42.8
	Total Thrust	N	18000	22200	25000
	OPR	-	52.78	55.82	59.22
	TSFC	g/kNs	10.85	10.61	10.35
	W	kg/s	8.23	10.04	11.19
	TET	(K)	1750	1750	1750
	HPC last stage blade height	mm	10.29	11.10	11.44

In addition, to the design point performance, Table 5-15 indicates the engines' performance at EOR conditions. It can be seen that the blade metal temperature of the 25kN engine is right at the limit of 1400K and the surge margin of the IPC compressor is rather small at EOR conditions (surge margin variance shown in Table 5-15). The reason why the surge margin at EOR is rather small is because the component map of the IPC is more representative of a booster map rather than a 7 stage IPC component [60].

However, the low surge margin at EOR can be rectified by the inclusion of VSVs and blow-off valves, which are currently not included within the scope of this study. Conversely, this issue can be rectified by rescaling the map- at the expense of component efficiency- in order to restore the surge margin. Another issue that must be highlighted, is that the TET at EOR conditions for all the three engines is capped at 1880K, the reason being that it is assumed that the engine family range would use the same level of technology in terms of adequate blade cooling. Hence, the TET at EOR is kept constant.

Table 5- 15: Overview of S-GOR2050-XX series engine models at EOR

	Parameter	Units	EOR		
			S-GOR2050-18	S-GOR2050-22	S-GOR2050-25
GENERAL	Mach no	-	0.2	0.2	0.2
	Altitude	m	350	350	350
	dT ISA	K	28	28	28
	FHV	MJ/kg	42.8	42.8	42.8
	HP shaft power extraction	W	0	0	0
	Total Thrust	N	59180	72344	81403
	OPR	-	34.43	36.19	38.09
	TSFC	g/(kN*s)	6.58	6.46	6.26
IPC	IPC polytropic efficiency (EP23)	-	0.940	0.939	0.938
	IPC Surge Margin	%	8.1	7.6	6.9
HPC	HPC polytropic efficiency (EP27)	-	0.888	0.893	0.895
	HPC Surge Margin	%	20.9	21.0	21.0
HPT	MN	-	0.3	0.3	0.3
	AN2	rpm ² m ²	4.16 X 10 ⁵	7.64 X 10 ⁵	3.15 X 10 ⁵

	<u>Parameter</u>	<u>Units</u>	<u>EOR</u>		
			<u>S-GOR2050-18</u>	<u>S-GOR2050-22</u>	<u>S-GOR2050-25</u>
	HPT Tblade (Tm41)	K	1393	1397	1402
IPT	MN	-	0.45	0.45	0.45
	AN2	rpm ² m ²	3.77E+05	4.87E+05	1.19E+06
LPT	MN	-	0.55	0.55	0.55
	AN2	rpm ² m ²	1.95E+06	4.73E+06	3.80E+06
	EGT	K	898	893	881

Once the engine performance of the S-GOR2050-XX configurations were established, the final Y2050 short range aircraft configuration was developed while a rubberized aircraft model was concurrently created in the form of Y2050 short range non-linear fuel burn factors. The non-linear fuel burn trade factors are used in the forthcoming sections to determine the relative fuel burn benefits the Y2050 GOR-combined cycle configuration possess over a representative Y2000 short range mission and a reference Y2050 short range mission. The following sub section details the performance of the frozen reference Y2050 GOR engine, from which the fuel burn benefits of Y2050 GOR- combined cycle configurations will be measured against.

5.2.3 Performance overview of the reference Y2050 GOR

Based on the Y2050 aircraft sizing requirements [107], the final design point thrust requirement was by the ULTIMATE project by linearly extrapolating the thrust and performance figures provided by the S-GOR2050-XX engine series. Table 5-16 indicates the final frozen engine performance demanded by the Y2050 short range aircraft for a 3500 NM mission at mid-CR, TOC and EOR [96].

Table 5- 16: Frozen global engine specification demanded by Y2050 SR aircraft

<u>Parameter</u>	<u>Units</u>	<u>TOC</u>	<u>MID-CR</u>	<u>EOR</u>	<u>SLS</u>
Altitude	ft	35000	37000	0	0
Mach Number	-	0.73	0.71	0.2	0.1

<u>Parameter</u>	<u>Units</u>	<u>TOC</u>	<u>MID-CR</u>	<u>EOR</u>	<u>SLS</u>
Delta ISA	K	10	0	15	0
Thrust	kN	17.34	13.85	78.94	105.2
TSFC	g/(kN*s)	10.78	10.43	6.10	5.39

Since the new design point thrust level falls outside the realm of the previously investigated thrust levels, an engine design was created to match the performance highlighted in Table 5-16 and shall be referred to as the reference GOR2050 engine configuration.

In order, to meet the performance estimates highlighted in Table 5-16 a matching exercise was undertaken using the Pointer optimizer algorithm in the I-sight environment. Similar to the procedure used to derive the performance of the S-GOR2050-XX engine series, a representative engine deck in PROOSIS was created and an optimization process was initiated in the I-sight environment such that the final engine matched the performance demanded by the final frozen Y2050 SR aircraft. Table 5-17 indicates the variables, constraints and objectives employed in estimating the reference GOR2050 performance.

Table 5- 17: Design variable ranges, constraints and optimizer objectives set within the I-sight environment

<u>Property</u>	<u>Units</u>	<u>Lower bound</u>	<u>Upper bound</u>
Nozzle PR	-	1.10	1.35
Ring Nmech	rpm	450	1200
HPC PR	-	5.0	6.0
TET at CR	K	1550	1700
TET at TOC	K	1700	1750
TR	-	1.15	1.3
<u>Constraint</u>	<u>Units</u>	<u>Lower bound</u>	<u>Upper bound</u>
Fn at CR	N	13500	14500
Fn at EOR	N	77500	79000
TSFC at CR	g/(kN*s)	10.35	10.65

<u>Property</u>	<u>Units</u>	<u>Lower bound</u>	<u>Upper bound</u>
TSFC at EOR	g/(kN*s)	5.8	6.4
<u>Objectives</u>	<u>Units</u>	<u>Value</u>	
Fn at CR	N	13850	
Fn at EOR	N	78940	

Similar to the approach taken for the S-GOR2050-XX engine series the optimizer was employed with the 'Pointer' algorithm to find an engine configuration that matched the required performance of the frozen Y2050 SR aircraft. Table 5-18 shows an overview of the performance of the reference GOR2050 engine configuration at TOC, mid-CR and EOR. A detailed overview of the GOR2050 performance is shown in Appendix-A.

Table 5- 18: Reference GOR2050 performance overview at TOC, CR and EOR

	<u>Parameter</u>	<u>Units</u>	<u>TOC</u>	<u>CR</u>	<u>EOR</u>
GENERAL	Mach no	-	0.73	0.71	0.2
	Altitude	m	10688	11277.6	0
	dT ISA	K	10	0	15
	HP shaft power extraction	kW	0	0	0
	Total Thrust	kN	17.34	13.85	78.95
	OPR	-	41.14	36.81	33.40
	TET	K	1750	1628	1950
	HPT Tblade (Tm41)	K	1233	1139	1374
	W	Kg/s	7.08	6.17	17.43
	TSFC	g/(kN*s)	10.75	10.41	6.44

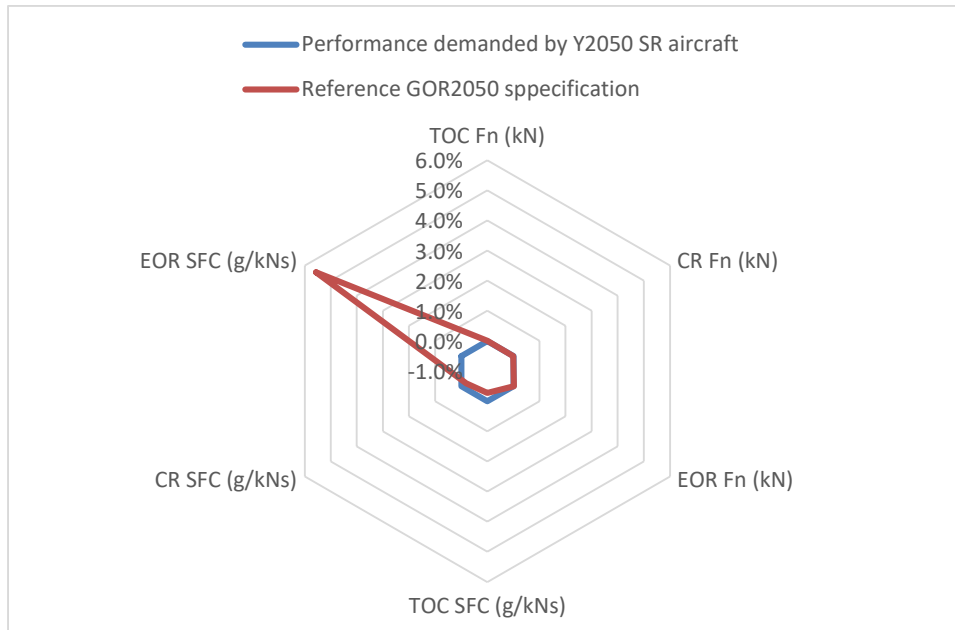


Figure 5- 17: Radar plot indicating the quality of fit of the GOR2050 engine

Figure 5-17 shows the quality of fit of the final reference GOR2050 engine configuration with regards to what is demanded by the aircraft. It is seen that the fit at TOC and mid-CR conditions are acceptable, however the TSFC at EOR is over estimated on the order of 5%. The primary reason for this can be attributed to the initial scaling factors employed for the component maps as well as the type of component maps themselves when compared to the Thrust demands of the Y2050 short range aircraft.

Once the performance of the GOR2050 was deemed a suitable match with the required performance for the Y2050 SR-aircraft, the mass of the engine configuration was determined using the TOC, CR and EOR conditions of the engine model. The software that is used to determine the dry and total mass of the engine configuration is Weico 9.6, which was supplied by Chalmers University under the scope of project ULTIMATE [39]. Weico 9.6, predicts the mass of the turbomachinery components using gas path sizing methods, disc and corresponding shaft sizing methods that are well documented in literature. However, the mass of the CRP and the associated core ducts are predicted by the methods outlined by Bellocq et al. The dry and total mass estimate of the GOR2050 engine configuration is 2820kg and 3197kg respectively [61]. The subsequent meridional view of the GOR2050 is shown in Figure 5-18 [61]. In addition, Figure 5-19 shows a representative breakdown of the constituent component masses of the GOR2050 engine configuration as predicted by Weico 9.6 [39].

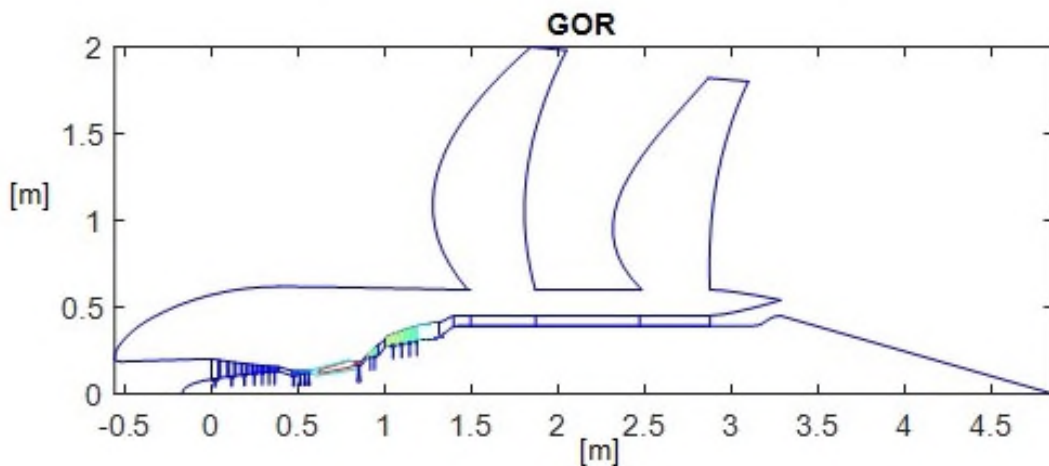


Figure 5- 18: Engine cross-section of the reference GOR2050 engine configuration[61]

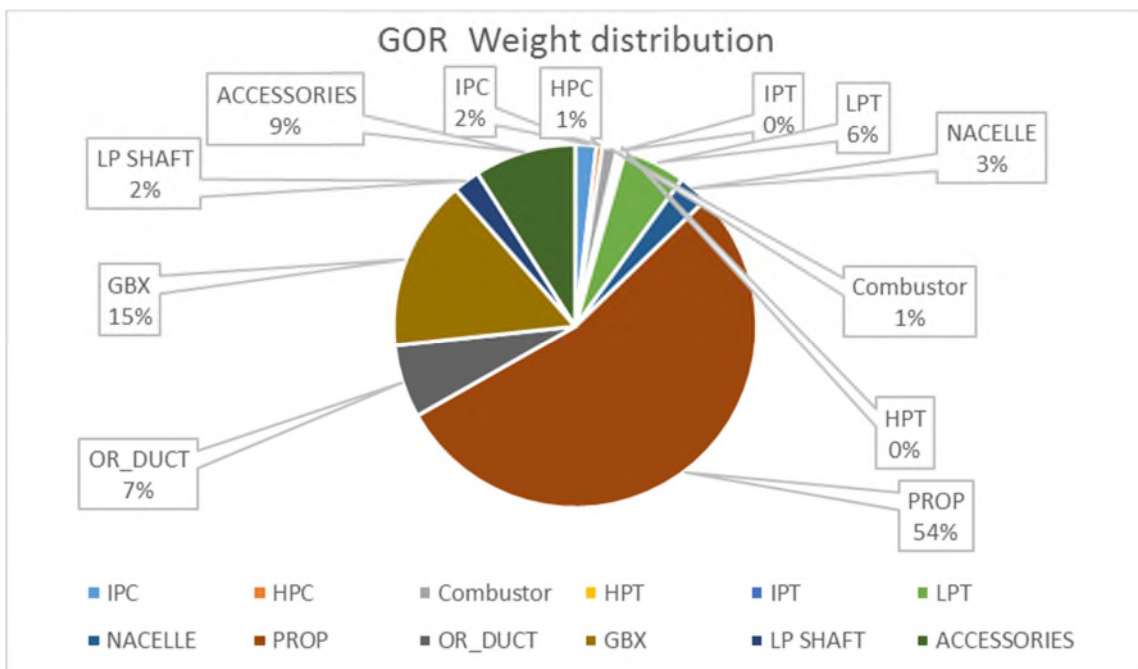


Figure 5- 19: Relative mass breakdown of the reference GOR2050 components[61]

Once the final reference GOR2050 engine has been established it is necessary to determine, what potential fuel burn benefits or penalties are associated with the design choices of the LP-system. An analysis of this nature spotlights the sensitivities of design choices, at a preliminary design stage, on the propulsive efficiency of a potential reference GOR2050 engine configuration. Moreover, it will highlight the potential impact that the design choice sensitivities will have on the SRIA fuel burn targets. In addition, Appendix-E provides a comparative overview between SRTF2000 and GOR2050 engine configurations. The

following section, shall include a parametric study of the reference GOR2050 engine configuration to encapsulate the design sensitivities of the LP-propulsion system.

5.2.4 Design Sensitivity of the LP- system of the reference GOR2050 engine

A parametric design sensitivity is carried out on the variables that most severely influence the propulsive efficiency of the reference GOR2050 engine. As per the fidelity of the modelling of a reference GO2050 engine model, highlighted in section 4.2, the variables that influence the performance and engine mass are highlighted in Figure 5-20.

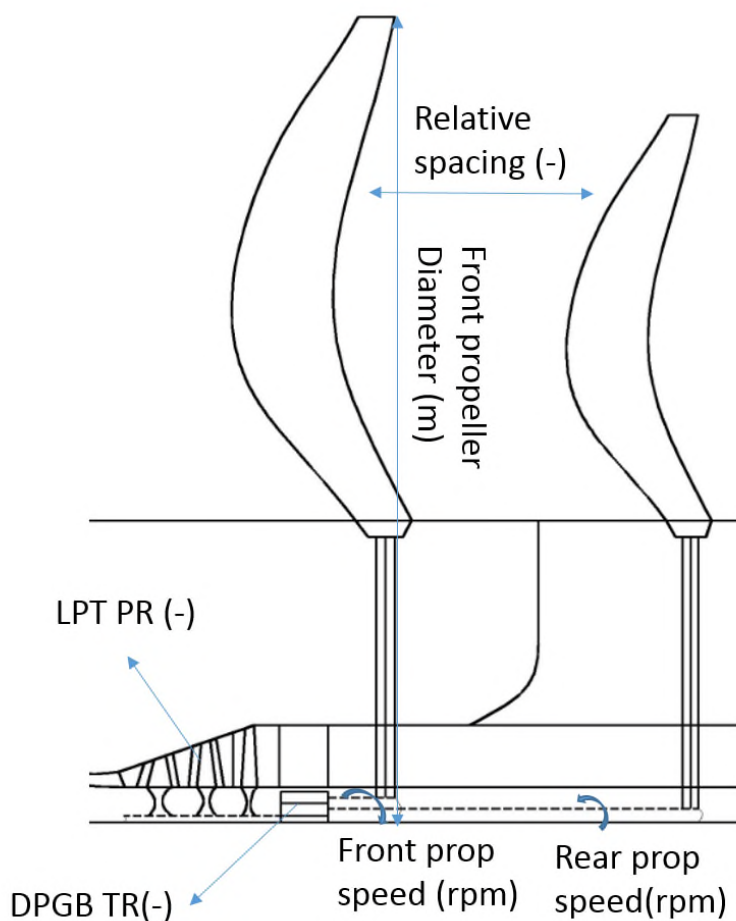


Figure 5- 20: Overview of LP-system design parameters

The parametric design sensitivity study is conducted at TOC conditions for the reference GOR2050 engine configuration. Table 5-19, indicates the lower bounds, upper bounds and the reference values of the LP-design parameters used in the parametric design sensitivity study. The parametric studies are conducted such that the sensitivities of the chosen two design choices are benchmarked against the TOC TSFC and the engine mass estimated at

TOC, while keeping the rest of the variables at reference GOR2050 values. For example, as per Table 5-19, the values of the LPT pressure ratio (PR) and propeller speed are varied while keeping the rest of the variables at reference GOR2050 conditions.

Table 5- 19: Overview of the variables used in the GOR2050 LP-system parametric study

<u>Property</u>	<u>Units</u>	<u>Lower bound</u>	<u>Reference GOR2050</u>	<u>Upper bound</u>
LPT PR	(-)	4.5	7	7.5
Propeller speed	(rpm)	400	452	1000
relative spacing	(-)	0.10	0.27	0.30
Torque Ratio	(-)	1.05	1.1	1.29
Percentage clipping	(%)	10	20	60
Front Propeller diameter	(m)	3.18	3.98	4.78

The underpinning reasons for choosing the upper and lower bounds of the parametric study are:

- The upper bound for the LPT pressure ratio is chosen such that the LPT AN² constraints are not violated. The lower bound was chosen such that adequate levels of convergence would be achieved in the PROOSIS experiment, which is facilitated by the LPT in meeting the power demands of the CRP.
- The lower bound of the propeller speed corresponds to excessively high pitch settings that correspond to possible blade stall. The upper bound corresponds to excessive LPT AN² values. The propeller speed are chosen to be of the same magnitude for the front and rear propeller for most analyses henceforth, unless explicitly mentioned otherwise. Moreover, it is assumed that the front propeller rotates clockwise and the rear propeller rotates anti-clockwise.
- The upper bound of relative spacing corresponds to a case where the magnitude of the induced velocities would be reduced relative to the reference case. In addition, the lower bound corresponds to a spacing case where the induced velocities would be increased relative to the reference case.
- The rear propeller of the GOR2050 engine configuration is clipped relative to the front propeller, primarily to reduce the propeller vortex interaction between the front and rear propeller for noise alleviation [16,60]. The upper bound of the relative clipping corresponds to a setting where the rear propeller power loading becomes mechanically infeasible [18]. The lower bound of rear propeller clipping corresponds to a lower rear propeller power loading case relative to the reference case.
- The front propeller diameter upper bound value and lower bound value corresponds to a lower front propeller power loading and higher front propeller power loading relative to the reference case.

The results of the parametric sensitivities studies, with regards to the effect of the design sensitivities are compared to the reference GOR2050 engine mass (**3197 kg**) and TOC TSFC (**10.75 g/kNs**). Therefore the results of the parametric studies will be displayed in relative terms to the reference values. Figure 5-21 shows the relative change of TOC TSFC as a function of the LPT pressure ratio and the propeller speeds. The figure displayed in Figure 5-21 is a result of a 3rd order polynomial fit.

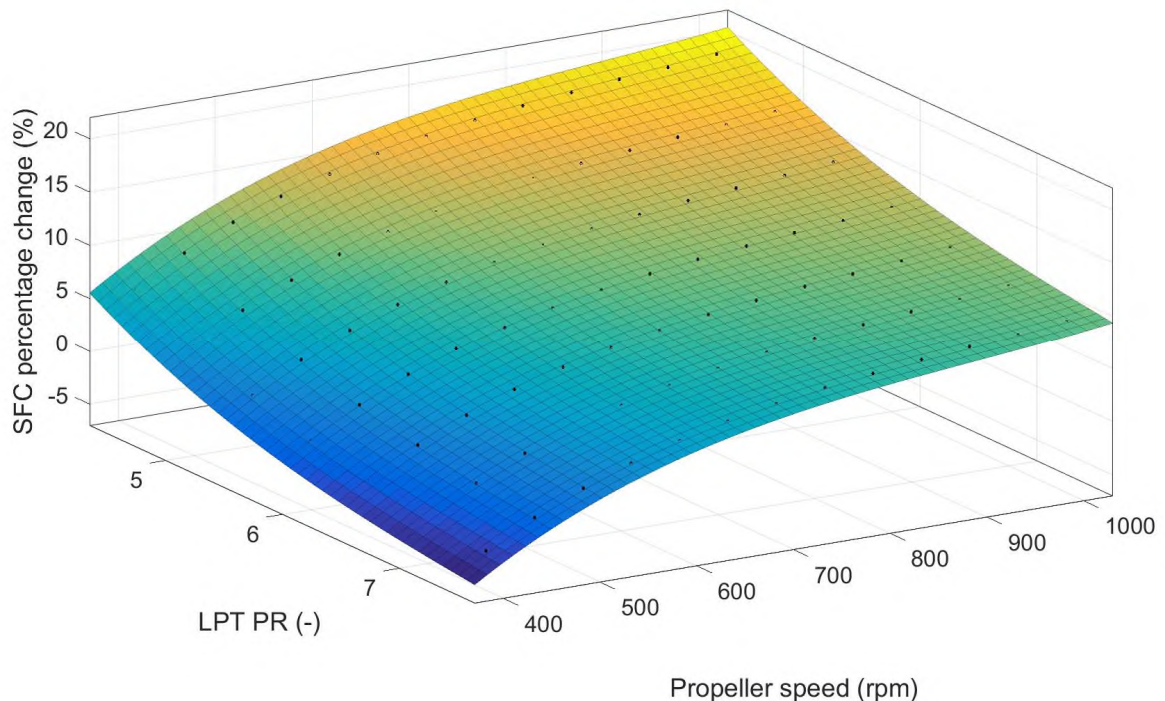


Figure 5- 21: Relative change in TOC TSFC as a function of the LPT PR and propeller speed.

The following trends and observations with regards to Figure 5-21 can be made:

- For a fixed propeller rotational speed, as the LPT pressure ratio increases the TSFC reduces. This trend occurs because as the LPT pressure ratio increases the specific power of the core increases for a fixed thrust level, which in turn causes the TSFC to decrease.
- For a fixed LPT pressure ratio, as the propeller speed increases the TSFC increases. This occurs because as the propeller speed increases the pitch setting and advance ratio reduces, which leads to higher helical Mach numbers and consequently a less efficient contra rotating propeller array and a higher relative TSFC at TOC.
- The magnitude of change of the relative TSFC brought about by changes in the propeller speed is greater than the magnitude of change of the relative TSFC brought about by changes in LPT pressure ratio.

Figure 5-22 shows the relative change of the engine mass as a function of the LPT pressure ratio and the propeller speed. The figure displayed in Figure 5-22 is a result of a 2nd order polynomial fit.

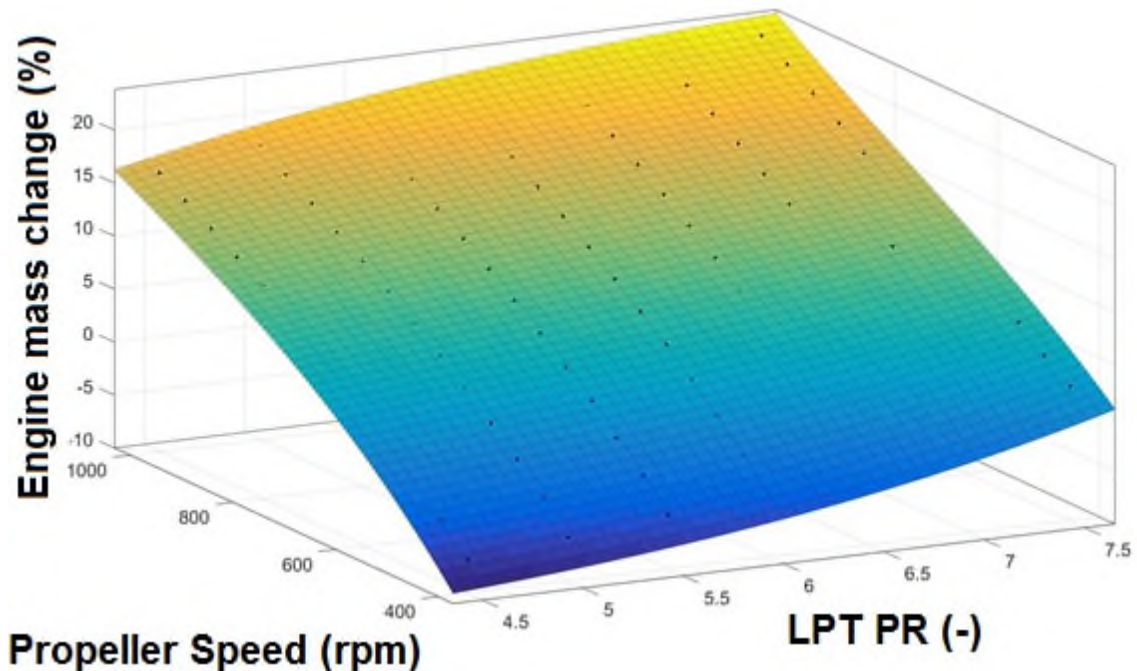


Figure 5- 22: Relative change in engine mass as a function of the LPT PR and propeller speed.

The following trends and observations with regards to Figure 5-22 can be made:

- For a fixed LPT pressure ratio, as the propeller speed is decreased the engine mass decreases. This occurs because the mass of the contra rotating propeller array is directly proportional to the operating speed as indicated by Equation 4-109- 4-111 [16].
- For a fixed propeller speed, as the LPT pressure ratio increases the relative mass of the engine configuration increases. This is because as the LPT pressure ratio increases the exit area of the LPT increases, for a fixed exit hub to tip ratio and exit axial Mach number. Consequently, the mean component diameter increases and the mass of the LPT and engine increases.
- The magnitude of change of the relative engine mass brought about by changes in the propeller speed is greater than the magnitude of change of the relative engine mass brought about by changes in LPT pressure ratio.

Figure 5-23 shows the relative change of TOC TSFC as a function of the relative propeller spacing and the propeller speeds. The figure displayed in Figure 5-23 is a result of a 3rd order polynomial fit.

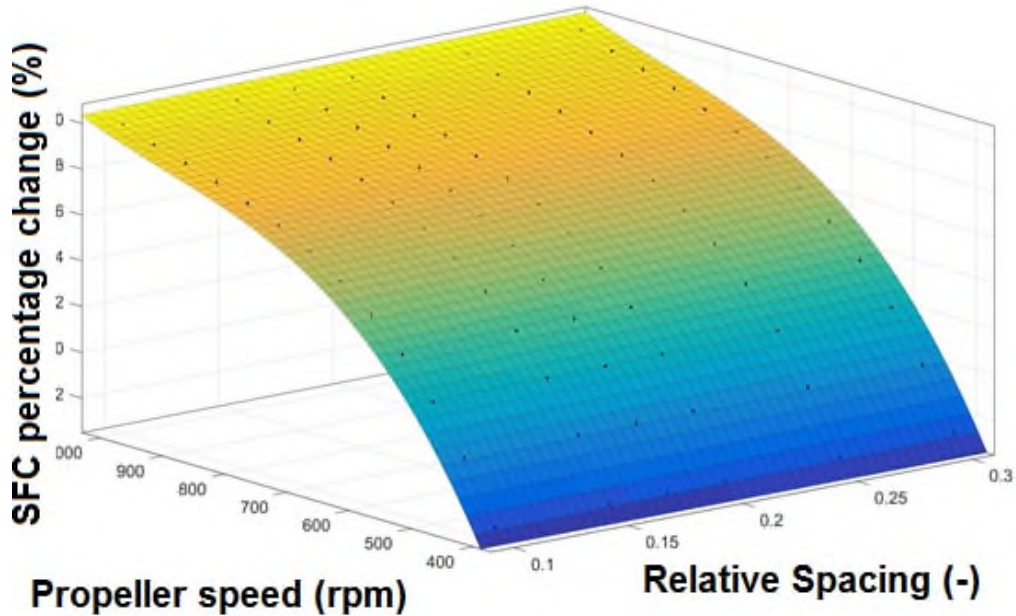


Figure 5- 23: Relative change in TOC TSFC as a function of the relative propeller spacing and propeller speed.

The trends seen in Figure 5-23, with regards to the effects of propeller operating speed on the TOC TSFC of the engine configuration is similar to the trend shown in Figure 5-21. Since the effect of relative propeller spacing is not obvious in Figure 5-23, the effect of relative propeller spacing for a propeller speed of 700 rpm is seen in Figure 5-24.

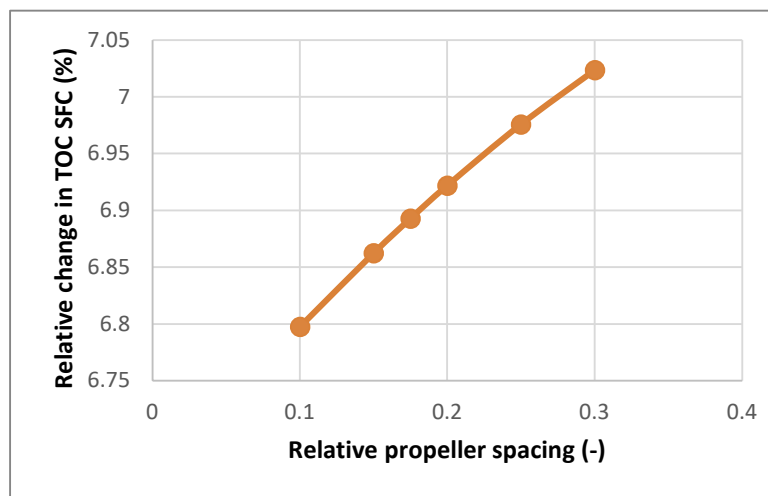


Figure 5- 24: Relative change in TOC TSFC as a function of relative propeller spacing at a rotational speed of 700 rpm

The trend seen in Figure 5-24, indicates that as the relative propeller spacing increases the relative TSFC increases. The reason for this trend is because as the rear propeller is placed further aft of the front propeller lower magnitude of swirl is recovered by the rear propeller which leads to a relatively less efficient contra rotating propeller array and higher TSFC. Similar to the effects that the propeller speeds has on the TSFC of the GOR2050 engine, the effects of engine mass is dominated by the propeller speeds as opposed to the relative propeller spacing by an order of magnitude. Thus the effects of relative propeller spacing on the entire engine mass, for a fixed thrust class, can be deemed as a second order effect at a preliminary design level. In reality, as the space between the propellers increase the shaft length of the rear propeller increases and the mass will increase.

Figure 5-25 shows the effects of the design point torque ratio with regards to the relative TOC TSFC benefits. As the torque ratio increases the power loading of the front propeller increases and the propeller loading of the rear propeller decreases, which in turn causes the average propeller loading of the CRP array to decrease, for a 20% propeller clipping. The average power loading of the CRP array is directly proportional to the overall efficiency of the contra rotating propeller array, therefore as the torque ratio increases the average contra rotating propeller loading decreases and the relative TSFC increases, as seen in Figure 5-25.

The mass of the contra rotating propeller is proportional to the propeller loading of the front and rear propeller. As the torque ratio increases the mass of the CRP array decreases due to the effect of the reduction of the average propeller loading. Concurrently the mass of the DPGB increases, due to the increase in the torque of the front propeller. These two effects counteract each other and lead to a net mass decrease across the span of the investigated torque ratios, however the relative mass change range across the investigated torque ratios was less than half a percentage point.

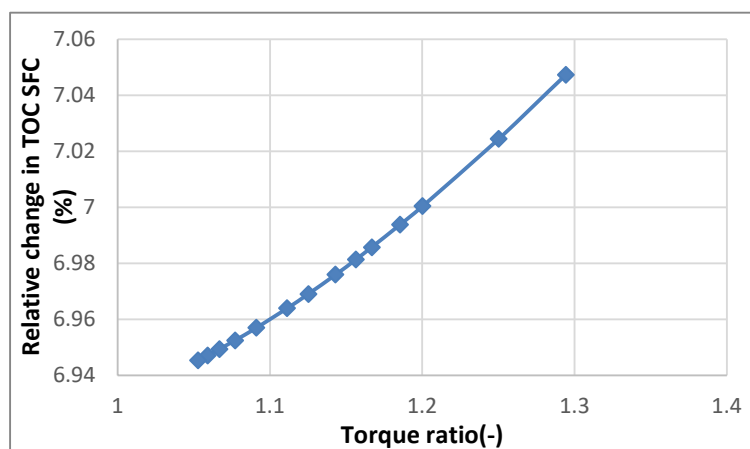


Figure 5- 25: Relative TSFC effect as a function of Torque ratio at propeller speed of 700 rpm.

Figure 5-26, shows the effect of the relative TSFC benefit or penalty as a function of the degree of rear propeller clipping to the front propeller and the rotational speed of the propellers. It can be seen that as the degree of rear propeller clipping decreases the relative TSFC decreases. The reason for this trend is because as the degree of clipping reduces, more swirl is recovered by the rear propeller, as there is more rear propeller span to do so. This in turn leads to a more efficient CRP array, and consequently relatively lower TSFC values. Generally, the degree of rear propeller clipping is governed by noise legislation impositions within the LTO envelope, and clipping alleviates the magnitude of propeller tip vortex interaction between the front and rear propeller[16]. Moreover, based on the trends depicted in Figure 5-26, it is seen that the effect of the propeller speed on the relative TOC TSFC outweighs the effect of the degree of clipping.

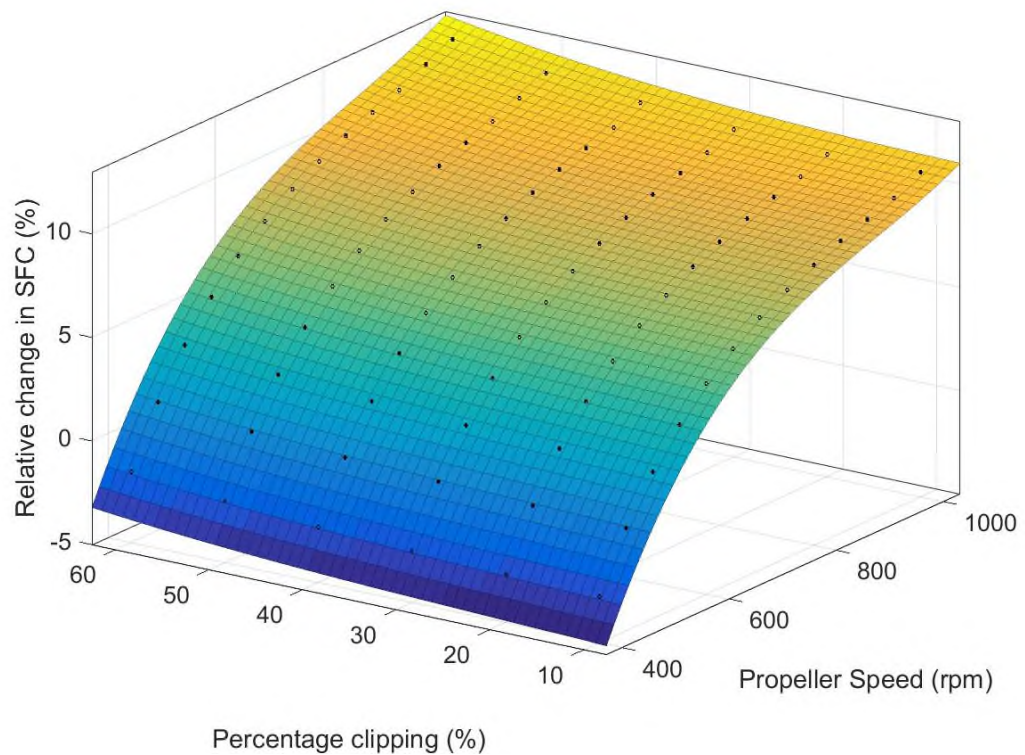


Figure 5- 26: Relative change in TOC TSFC as a function of the rear propeller clipping and propeller speed.

Figure 5-27, shows the relative change in engine mass as a function of the rear propeller clipping and the propeller clipping. As the degree of the rear propeller clipping increases the mass of the engine reduces drastically, as the mass of the rear propeller array is directly proportional to the diameter of the rear propeller. Another important observation is that the magnitude of relative engine mass change is the similar for changes in propeller clipping and changes in propeller speed.

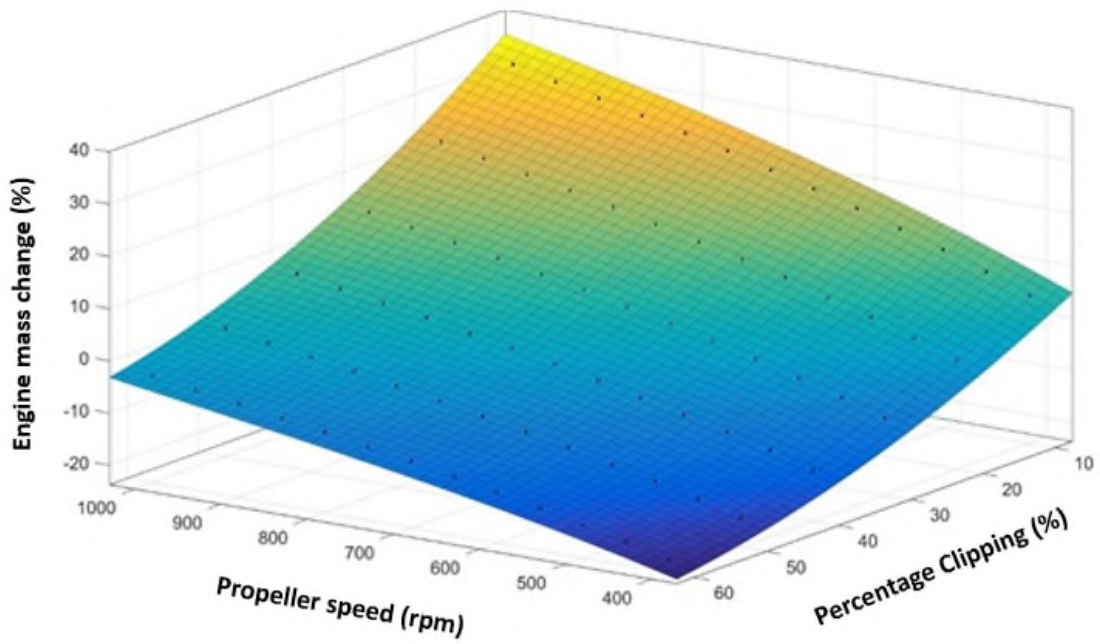


Figure 5- 27: Relative change in engine mass as a function of the rear propeller clipping and propeller speed.

Figure 5-28, indicates the relative change in TOC TSFC as a function of the front propeller diameter and the propeller speed.

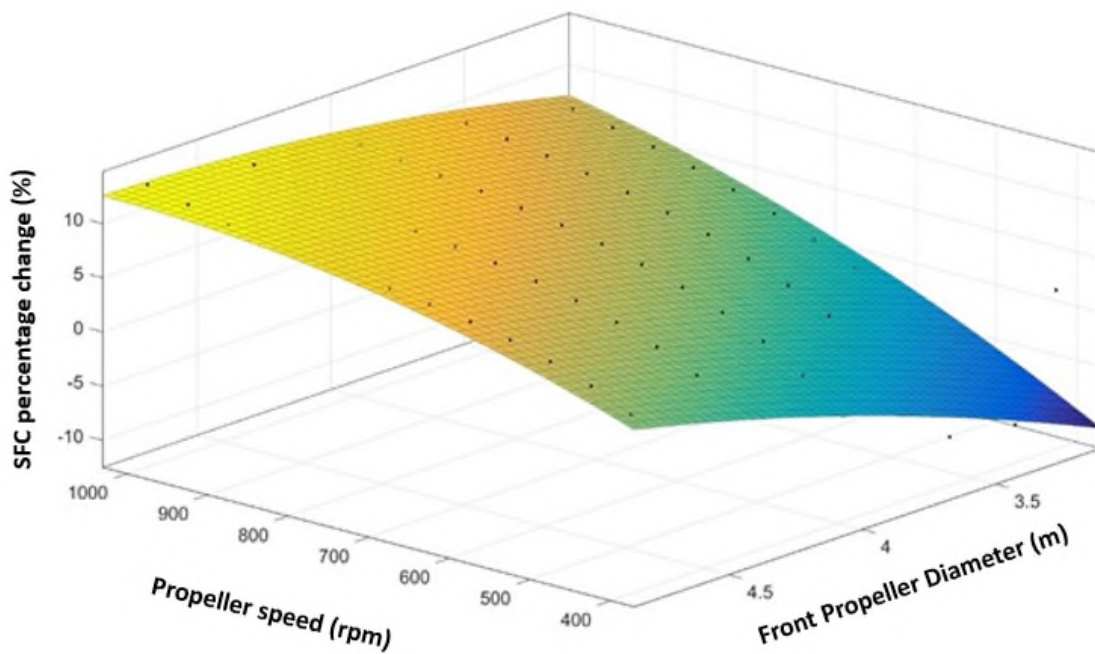


Figure 5- 28: Relative change in TSFC as a function of the front propeller diameter and speed.

As the front propeller diameter decreases the relative TSFC decreases as the average CRP power loading increases significantly. The effect of the change in the front propeller diameter on the relative TSFC is more severe than that of the operational speed. However in reality, the diameter of the front propeller would be constrained by the mechanical constraints imposed by the increased power loading.

Figure 5-29, provides an interesting overview of the two most dominant variables on the overall engine mass. As the propeller diameter decreases the mass of the entire engine as the mass of the CRP array is directly proportional to the diameter of the front and rear propellers. It can be seen that the effect on the relative engine mass is more severe with changes in front propeller diameter (at a fixed clipping) as opposed to changes in the propeller speeds.

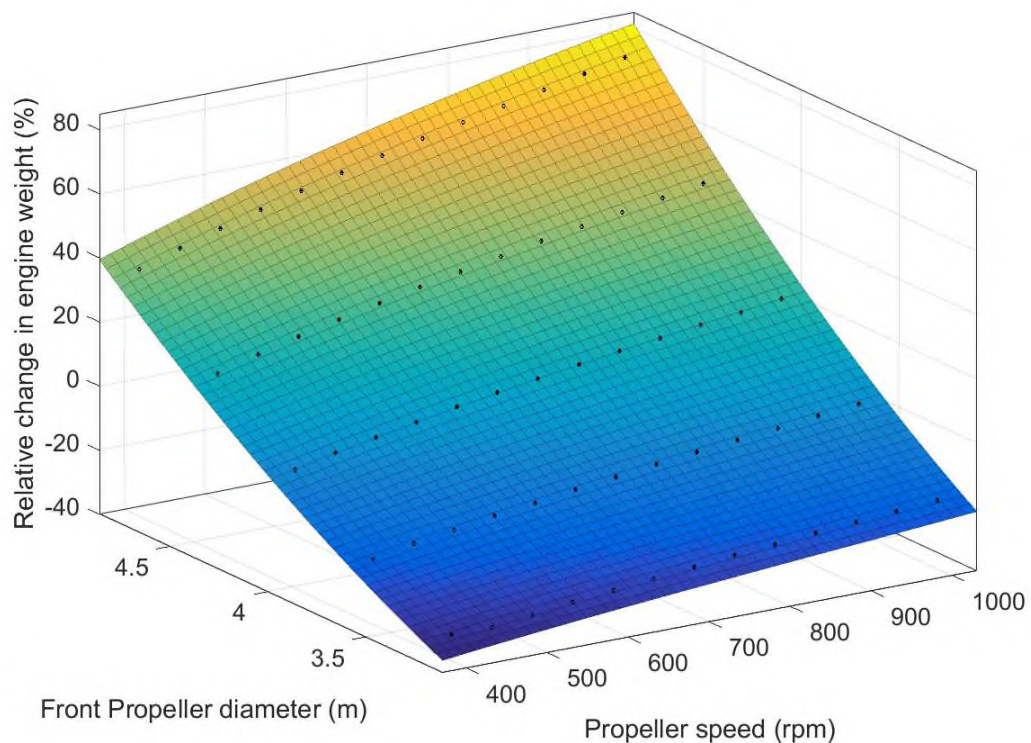


Figure 5- 29: Relative change in engine weight as a function of propeller speed and front propeller diameter.

A consistent assumption that has been made throughout all analyses with regards to all stages of the GOR2050 engine configurations is that the chosen operational rotational speed is kept constant throughout the flight envelope. However, by effectively changing the propeller rotational speeds throughout the flight envelope relative fuel burn benefits can be achieved. Figure 5-30, indicates the relative change in fuel burn compared to a reference GOR2050 configuration, when the propeller rotational speeds at EOR and CR conditions are

changed. In order to determine the relative fuel burn benefits the linear fuel burn trade factors provided in [96] were used for a 3500NM mission and the TOC design values were assumed to be the same as those specified in Table 5-19.

From Figure 5-30, it can be seen that changes in the mid-cruise propeller speed have a significant impact on the relative fuel burn as opposed to the EOR propeller speeds. This is primarily due to the fact the relative time spent in the cruise phase of flight is greater than the EOR segment by an order of magnitude. Therefore, it is expected that the change in propeller operational speed will have a greater influence on the relative fuel burn. However, the primary message intended by Figure 5-30 is to highlight the potential fuel burn benefits or penalties by making changes to the rotational speeds at off-design conditions. Furthermore, an additional degree of freedom in terms of potential trajectory optimization could be individually changing the operational rotational speeds of the front and rear propellers separately to achieve better fuel burn benefits. A technology enabler to account for this could be a hybrid-electric transmission system or a series of torque splitters (similar to what is used in automatic transmission cars).

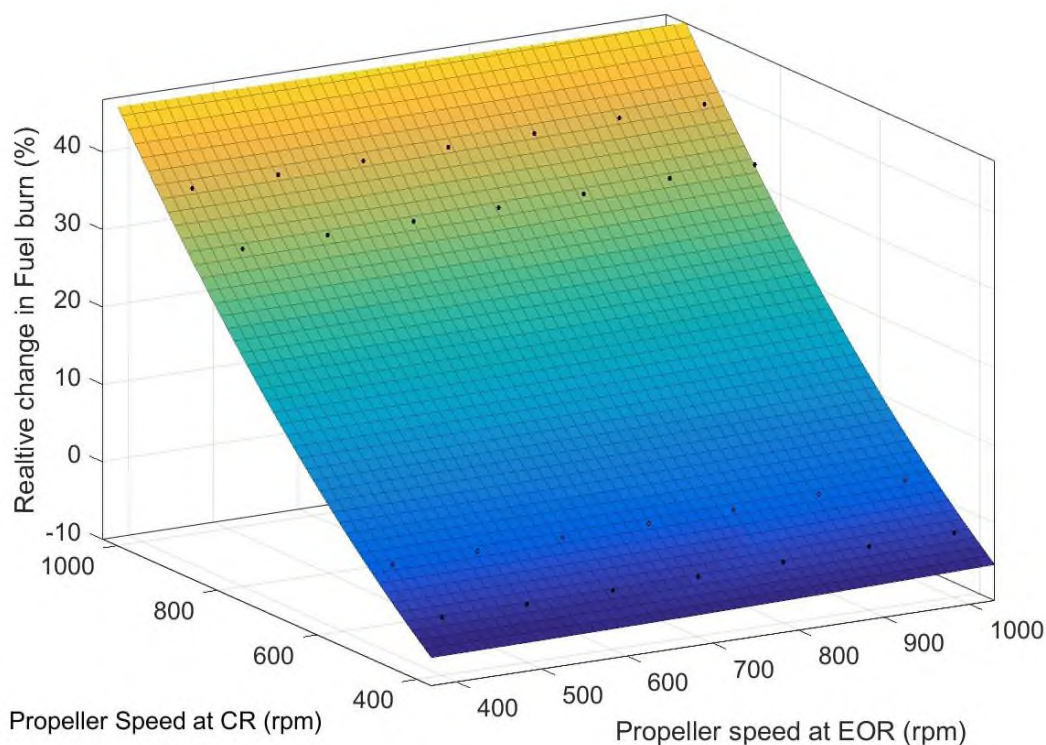


Figure 5- 30: Relative change in Fuel burn by variation of operational speed at CR and EOR

5.2.4.1 Overview of the GOR2050 design sensitivity study

The GOR2050 design variables that have the most significant impact on the relative TOC TSFC, in descending order, are:

- Front propeller diameter variation, however it is curtailed at relatively low propeller diameters due to mechanical limitations as the average power loading increases[18].
- Propeller speed variations, it is curtailed at high rotational speeds as the LP AN^2 limitation is violated at relatively high rotational speeds. In addition, it is curtailed at relatively low propeller rotational speeds as the occurrence of blade stall is prominent.
- LPT pressure ratio variations, it is curtailed at high LPT pressure ratio values as excessive expansion of the LPT causes the AN^2 value to be violated.
- Rear propeller clipping variations have a marked effect on the relative TSFC variation. The upper limit of the propeller clipping is governed by noise limitations and the lower limit is governed by the mechanical limitations of the rear propeller array.
- Relative propeller spacing and design point torque ratio variations, have almost a second order effect on the relative change in TSFC. However, the relative spacing between the propellers and the torque ratio have implications on noise limitations and mechanical considerations of the DPGB.

The GOR2050 design variables that have the most significant impact on the relative change in engine mass, in descending order, are:

- Front propeller diameter variations, have the most significant impact on the overall engine mass of the GOR2050 engine configuration, in terms of the LP-system.
- Rear propeller clipping and propeller speed variations, are the second most influential parameters with regards to engine mass. Where an increase in the degree of clipping and an increase in the operational speed contributes to an increase in the overall engine mass.
- LPT pressure ratio variations impact the mass of a GOR2050 engine configuration. The engine mass variation is directly proportional to the change in LPT pressure ratio.
- Variations in the relative propeller spacing and torque ratio have a second order effect on the mass of the engine configuration. Rather, these variables are essential in ensuring noise limitations and mechanical constraints are respected at a preliminary design phase.

When the frozen reference GOR2050 engine configuration is coupled to a year 2050 short-range aircraft the relative mission fuel burn benefit is 58.9%, when compared to a year 2000 baseline. The aforementioned LP-system design trends for relative TOC TSFC and engine

mass provides an insight in to the potential design space that can be explored to help attain designs that could achieve the ambitious relative fuel burn target of 68%.

Careful considerations must be aligned with mechanical, noise and emission constraints in order to provide a holistic view to whether the 68% fuel burn benefit target can be realistically achieved. In addition, the possible impact of varying the propeller operational speeds throughout the flight envelope show the possibility of attaining further fuel burn benefits by scheduling the speeds throughout the flight envelope.

Once the potential of varying the LP-system design parameters have been explored, with regards to its potential of reaching the 68% fuel burn reduction target it is necessary to focus on design improvements to the engine core that would further the overall efficiency of the aero-engine and help meet this target by the year 2050.

Consequently, the following sections shall introduce the validation/calibration of the ND performance and sizing models. Then the performance of said cycles are benchmarked against a comparable reference GOR2050 engine configuration and a baseline year 2000 engine configuration.

5.3 Quasi 1-D nutating disc engine system performance and sizing model

Prior to delving in to the performance benefits and feasibility of the nutating disc engine system within the architecture of the GOR2050 engine configuration, it is necessary to highlight the performance and sizing of a naturally aspirated nutating disc engine system against what is available in literature.

The amount of available literature to verify the proposed methodologies is meagre. Therefore two calibration approaches are presented, to ensure that confluence is ensured between the proposed thermodynamic model and a reference nutating disc geometry. The first validation approach is a recreation of the parametric study performed by Korakianitis et al. [1] by using the methodology outlined in section 4.3.

Figure 5-31 shows the closeness of fit between a naturally aspirated ND engine system modelled in PROOSIS and Korakianitis models. Each line in the parametric study shows the variation in the design point thermal efficiency (η_{th}) with respect to the specific power (\dot{W}') when the volumetric compression ratio is changed from 6 to 27 in increments of 3.

The solid lines in Figure 6-31 refer to the parametric study performed by Korakianitis et al, where one input variable from the reference case is changed and the volumetric compression ratio is changed from 6 to 27 in steps of 3. The input variables for the parametric studies and the reference values can be found in Table 5-20.

Table 5- 20: Input variables for the reference case in [1]

Reference case		Parametric case	
Variable	Value	Variable	Value
T_{at}	288 K	$T_{06_{mx}}$	1200 K
p_{at}	101.3 kPa	$T_{06_{mx}}$	1600 K
$f_{pl,il}$	0.02	$T_{06_{mx}}$	2000 K
$T_{06_{mx}}$	2400 K	r_{71}	0.5 K
$\eta_c = \eta_t$	0.9	r_{71}	1.5 K
$f_{ql, cy}$	0.2	r_{71}	2
$\Theta_1 = \theta_2$	0.5	r_{71}	2.5
$r_{23} = r_{34}$	0.9	$\Theta_1 = \theta_2$	0.9
$f_{pl,,23} = f_{pl,,34}$	0.05	$\Theta_1 = \theta_2$	0.1
r_{71}	1	$f_{ql, cy}$	0.4
ΔISA	0 K	$f_{ql, cy}$	0.1

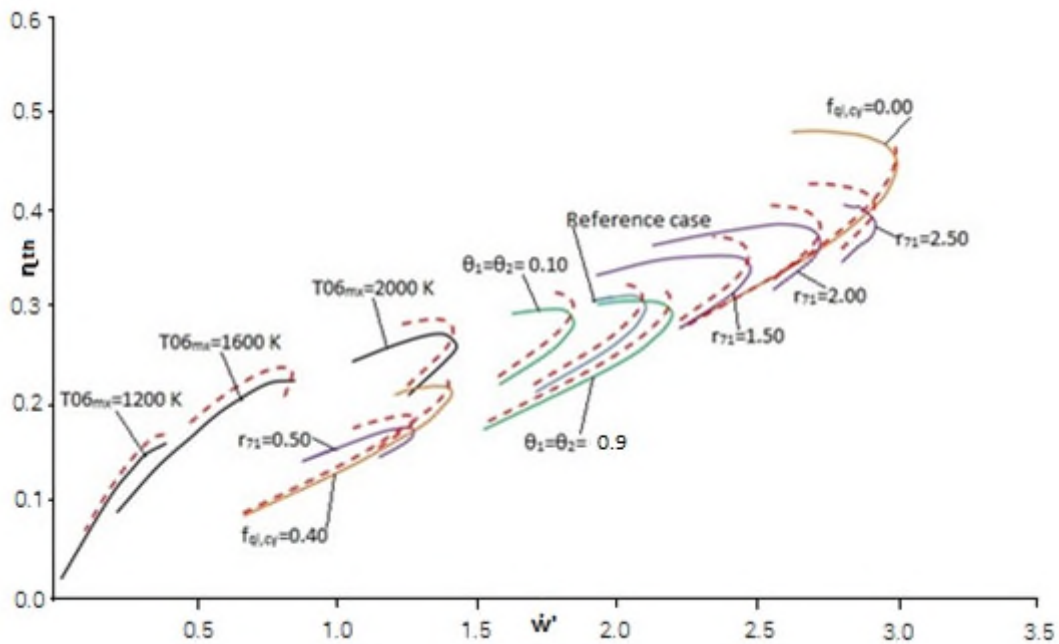


Figure 5- 31: PROOSIS model fit compared to the parametric study in [1]

The dashed lines presented in Figure 5-31 represent the parametric study carried out in PROOSIS. It can be seen that the trends produced by the PROOSIS models follow the trends shown in the baseline parametric study. The average absolute difference between the PROOSIS models and the baseline parametric study for thermal efficiency was less than 5% and less than 1% for the specific power. The sources of error stem from:

- Digitizing the plot presented in [1].
- The fuel heating value of ‘heavy diesel’ has not been explicitly mentioned in [1], this is one of the reasons for the variance in thermal efficiency. For this study a fuel heating value of 43,000 kJ/kg was used.
- The right hand side of *equation (25)* in reference [1] is incorrect as pointed out by Heywood [117] . This has been corrected in Equation 4-42 for implementation within the PROOSIS models.

Based on the satisfactory trends, in Figure 5-31, and the low values of percentage difference the PROOSIS models provide acceptable levels of confidence in the proposed thermodynamic model.

Since data for the absolute validation of the sizing methodology is un-available, at this stage only a calibration of the proposed methodologies against NASA’s published prototype test data is provided in Table 5-21 [67].

Table 5- 21: Calibration of proposed sizing methodology

<u>Feature</u>	<u>NASA test configuration</u>	<u>Proposed methodology</u>	<u>Difference</u>
# of discs	2	2	0%
disc (in)	8	8	0%
compression ratio (-)	10.0	9.9	1%
nutating angle (deg.)	20	20	0%
Brake horsepower (BHP)	107	107	0%
Total engine displacement (in ³)	232	240	3%
Weight (lb)	145	154	7%

The calibration of the proposed methodology, indicates that the displaced volume is over estimated. This is primarily because of the simplification of the ‘leading edge’ of the nutating

disc periphery and the inlet wedge geometry. Furthermore, the volume occupied by the seals is not accounted for. In addition, an independent study performed by Nadhira et al. [84] shows a good fit of the estimation of the ND engine system displacement methodology when benchmarked against a swept volume assessment performed by CAD software.

The source of error, for the mass estimate, can be attributed to the lack of knowledge of the material properties as well as the relative percentage of mass that stems from the ND engine accessories. Based on the methodology highlighted in section 4.5.8, the distribution of a dual disc nutating disc engine configuration component mass is highlighted in Figure 5-32.

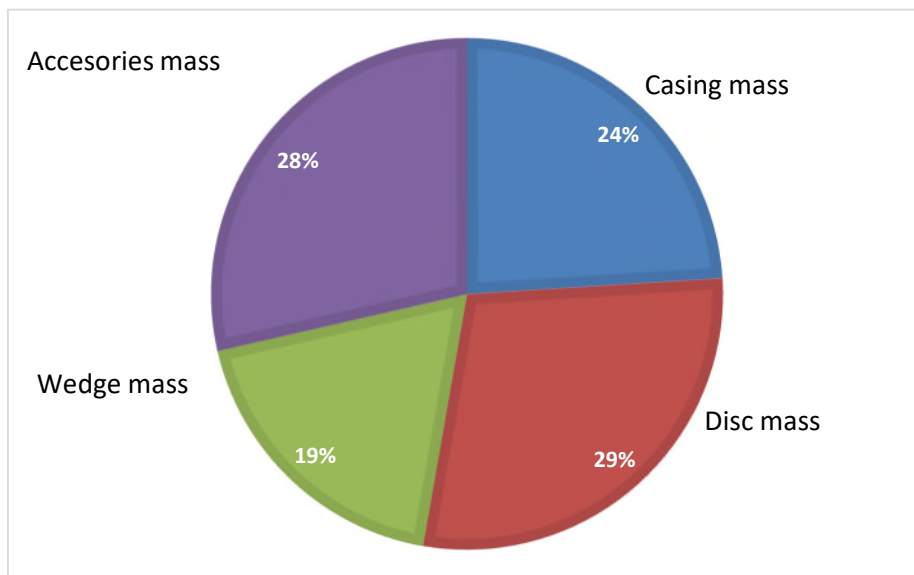


Figure 5- 32: Component mass distribution of the naturally aspirated, and calibrated, dual disc nutating disc engine configuration

In indicating the sensitivity of the ND engine system sizing parameters on the size and performance of the ND engine system a parametric analysis is conducted and presented in the following sub-section.

5.3.1 Parametric analysis for ND sizing methodology

A parametric analysis is conducted to show the influence of the compressor disc tip radius and angle of nutation on the swept volume of a single disc, at a fixed hub to tip ratio. From Figure 5-33 it can be seen that, for a fixed tip radius, as the angle of nutation increases the swept volume increases linearly. In addition, for a fixed angle of nutation, the swept volume increases exponentially with an increase in compressor disc tip radius.

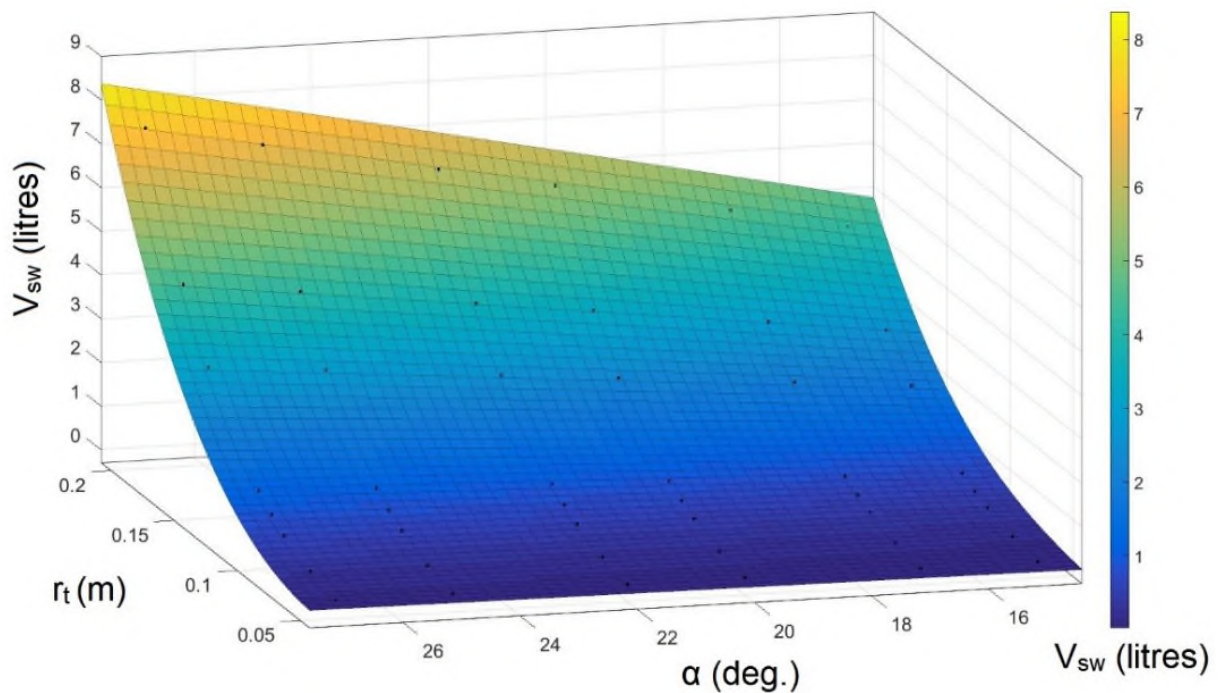


Figure 5- 33: Variation of swept volume as a function of the ND compressor tip radius and angle of nutation

Intuitively, it would seem that as the disc hub to tip ratio reduces the swept volume of the compressor disc would increase. However, in Figure 5-34, as the hub to tip ratio increases the swept volume increases. This occurs as the inlet radii factor of the wedge, l_f , is fixed in the parametric study, the wedge angle reduces as the hub to tip ratio increases. This consequently leads to an increased swept volume for the compressor disc.

The variation of the swept volume (cubic metres) of a single nutating disc engine chamber can be expressed as a function of it's' tip radius (in metres), hub to tip ratio, wedge angle (in degrees) and angle of nutation (in degrees).

The swept volume per nutating disc is estimated by employing a third order polynomial fit of the swept volume derived by using the methods highlighted in section 4.3. The presented equation (Equation 5-3) is valid for tip radii from 0.05m to 0.2m and at angles of nutation from 15 degrees to 27 degrees.

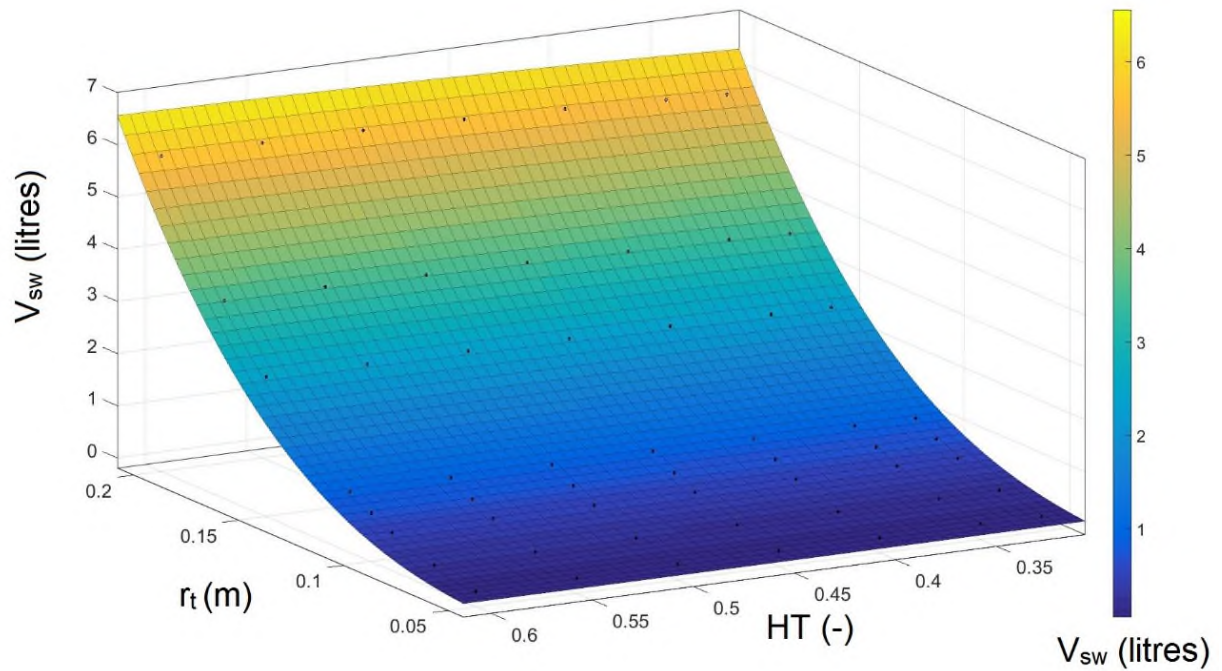


Figure 5- 34: Variation of swept volume as a function of the ND compressor tip radius and hub to tip ratio

$$V_{sw} = p00 + p10r_t + p01\alpha + p20r_t^2 + p11r_t\alpha + p02\alpha^2 + p30r_t^3 + p21r_t^2\alpha + p12r_t\alpha^2 + p03\alpha^3 \quad \mathbf{5-3}$$

To account for variance in hub to tip radius ratios, response surface equations for the swept volume of a single disc are presented at varying hub to tip radius ratios and wedge angles in Table 5-22. It is recommended to quadratically interpolate the swept volume estimate at hub to tip radius ratios not presented.

Table 5- 22: Coefficients to estimate the swept volume of a single disc at varying hub to tip ratios.

<i>HT ψ</i>	<i>p00</i>	<i>p10</i>	<i>p01</i>	<i>p20</i>	<i>p11</i>	<i>p02</i>	<i>p30</i>	<i>p21</i>	<i>p12</i>	<i>p03</i>
<u>0.32 18.3</u>	1.187	1.476	0.2356	0.6093	0.3039	-0.00052	0.08306	0.1090	-0.00042	-0.00012
<u>0.35 7.5</u>	1.197	1.488	0.2332	0.6141	0.3025	-0.00235	0.83560	0.1088	-0.00235	0.00068
<u>0.40 6.3</u>	1.211	1.502	0.2360	0.6225	0.3049	-0.00535	0.08739	0.1098	-0.00462	-0.00028
<u>0.45 5.0</u>	1.227	1.523	0.2350	0.6276	0.3183	-0.00816	0.08696	0.1254	-0.00828	-0.00120
<u>0.50 3.7</u>	1.238	1.537	0.2403	0.6334	0.3252	-0.00713	0.08704	0.1286	-0.00708	-0.00183
<u>0.55 2.3</u>	1.244	1.544	0.2425	0.6366	0.3302	-0.00611	0.08749	0.1304	-0.00623	-0.00078

Figure 5-35, reveals the relative change of the volumetric compression ratio of the compressor disc (reference $r_{12} = 10.0$) as a function of the compressor discs hub to tip ratio and the angle of nutation. Generally as the angle of nutation increases, for a fixed hub to tip ratio, the relative volumetric compression ratio increases. This occurs because the area projected on to the static frame of reference at the end of the compression process is lower at high angles of nutation relative to low angles of nutation.

As the hub to tip ratio increases the volumetric compression ratio increases. This seems contra-intuitive, however since the wedge factor (l_f) is kept constant the overall wedge angle of the nutating disc compressor reduces as the hub to tip ratio increases and the consequent volumetric compression ratio increases.

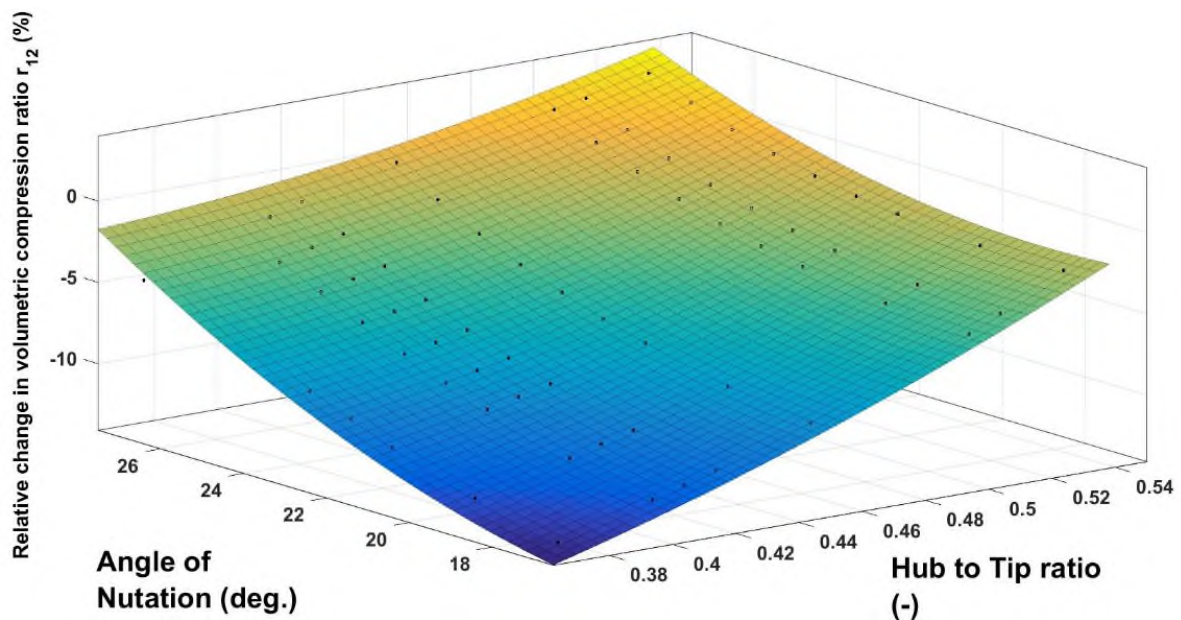


Figure 5- 35: Relative change in the compressor disc volumetric compression ratio as a function of the angle of nutation and the hub to tip ratio.

The aforementioned figure (Figure 5-35) provides an overview of the potential impact the geometric design choices would potentially have on the performance of a nutating disc compressor, and consequently on the nutating disc core. However, the aforementioned trend is an approximation assuming that the accumulator off-take port coincides with the periphery of the nutating disc compressor and with the angle ϕ_e , as shown in Figure 5-36. In practice, the volumetric compression ratio would be governed by the radial and circumferential position of the accumulator off-take manifold in conjunction with the timing of the solenoid controlled valve located at the junction of the accumulator manifold and the upper or lower surface of the nutating compressor disc.

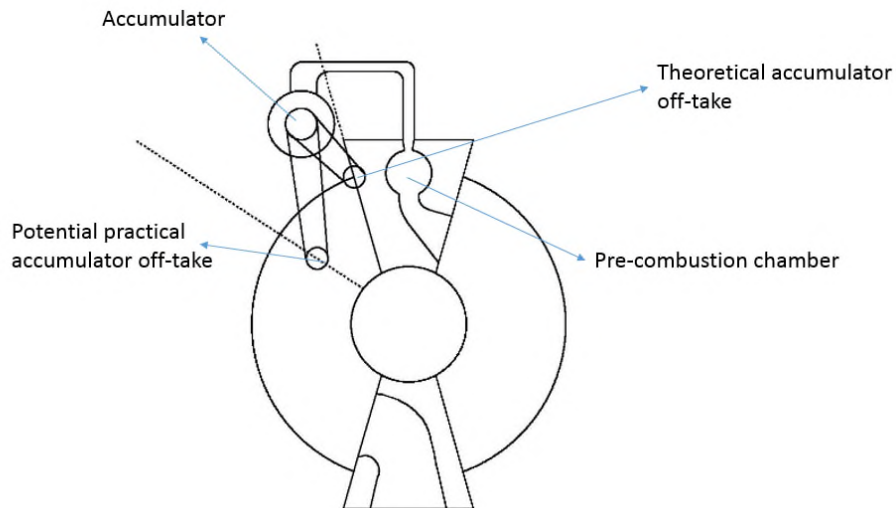


Figure 5- 36: Top-down view of nutating disc compressor, with theoretical and potential practical compressor off-take.

When the combustion system of the dual nutating disc engine system is considered, Figure 5-38 shows the variation in the combustion crank angle as a function of the height of the combustion chamber exit aperture (DE) and the ratio of the hub radius of the expander disc to the burner radius (r_b) housed in the expander disc (XR). Figure 5-37 depicts the variables under consideration as well as the idealized combustion chamber geometry.

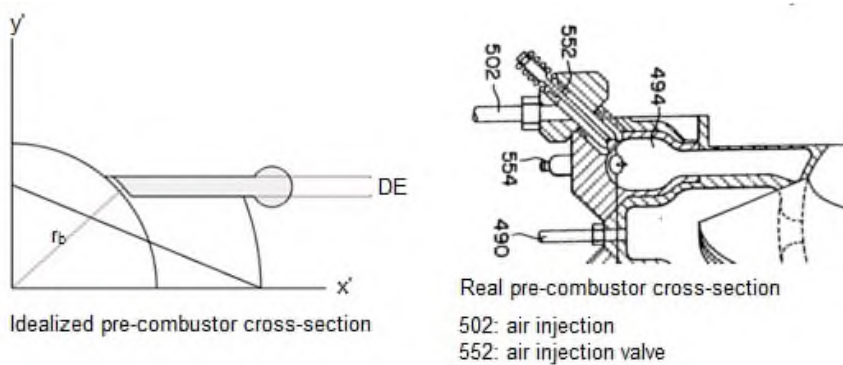


Figure 5- 37: Variables used in parametric analysis

The reference value of the combustion crank angle, in Figure 5-38, is 74.6° and the reference value for XR and DE are 1.04 and 5.5 mm respectively. For a fixed value of the burner radius ratio (XR), as the height of the pre-combustion chamber aperture increases the crank angle increases. For a fixed shaft power output and inlet mass flow, as the combustion crank angle increases the relative time for the entire combustion process increases. Consequently the fuel to air ratio during combustion and the peak cycle temperature decreases. Similarly, as the value of XR increases for a fixed combustion chamber aperture height, the relative

combustion crank angle increases as it takes a relatively longer time for the nutating disc in the expander chamber to no-longer cover the combustion chamber exit aperture.

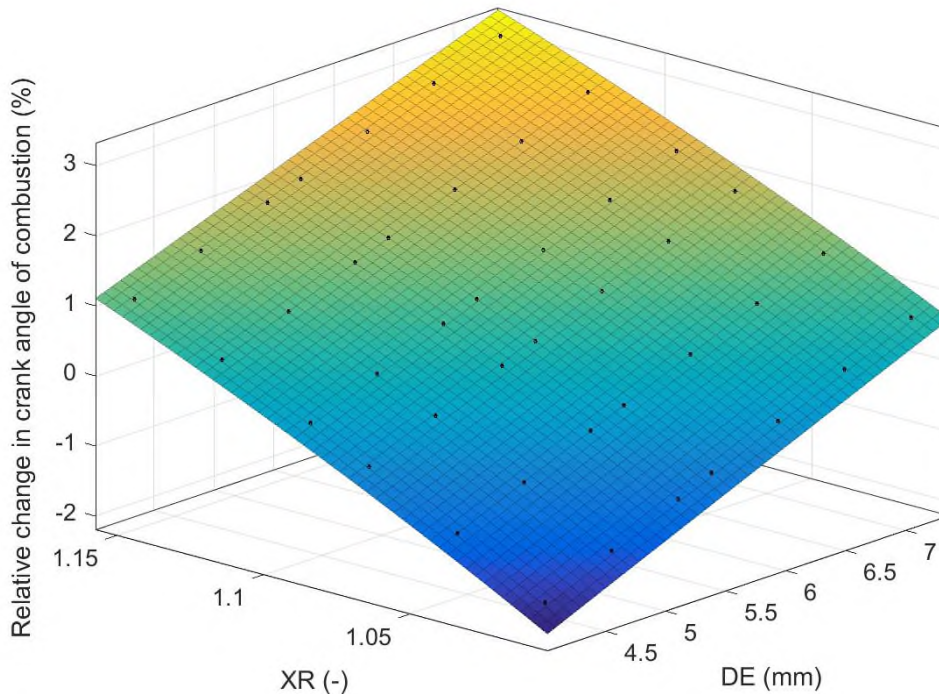


Figure 5- 38: Relative change in combustion crank angle as a function of the combustion chamber exit aperture height and the ratio of the expander hub radius and the burner radius

Despite estimating the combustion crank angle per shaft revolution, there are many uncertainties associated with the combustion process that can only be resolved with experimental analysis. For instance, the heat release during the constant volume combustion process is a function of the surface to area volume ratio of the combustor, effectiveness of the external coolant and frequency of fuel injection. The amount of heat lost to the surroundings during the combustion process has a significant impact on the performance of the cycle, the sensitivity of this feature shall be discussed in the forthcoming sections. In addition, we do not know enough about the heat release characteristics during the constant pressure combustion process, which is generally defined by the ND pre-combustor geometry, which will in turn dictate whether the constant pressure combustion process includes a total pressure loss or not. Therefore, significant research effort should be made to quantify the aforementioned gaps in knowledge, the details of how to do so shall be highlighted in chapter 7.

Once the sensitivities of the design parameters, are introduced it is necessary to investigate the combined performance of the ND engine system within the architecture of the reference

GOR2050 configuration. The following sections, provide an insight in to the performance benefits/penalties associated with the inclusion of the ND engine system in GOR2050 type engine configuration.

5.4 Y2050 GOR-ND IP-drive and Y2050 GOR-ND LP-drive configurations

The inclusion of the ND engine system can be considered in the architecture of a reference GOR2050 engine configuration to mechanically power either the LP or IP drive. Figure 5-39 shows the potential arrangement of a scaled Y2050 GOR ND IP-drive variant. The IP-drive configuration, replaces the entire HP spool in the reference GOR2050 engine configuration with a series of nutating disc engine systems arranged circumferentially around the IP-shaft. In addition, the nutating disc systems' z-shafts are aligned parallel to the IP-shaft, which would facilitate a similar oil circuit system for all cores. Moreover, the shaft power from the nutating disc engine systems are transmitted to the IP-shaft by a series of spur gears. The meridional view shown in Figure 5-39, was derived from the outcome of a targeted optimization. Details with regards to the scope of the optimization shall be presented in the following subsections.

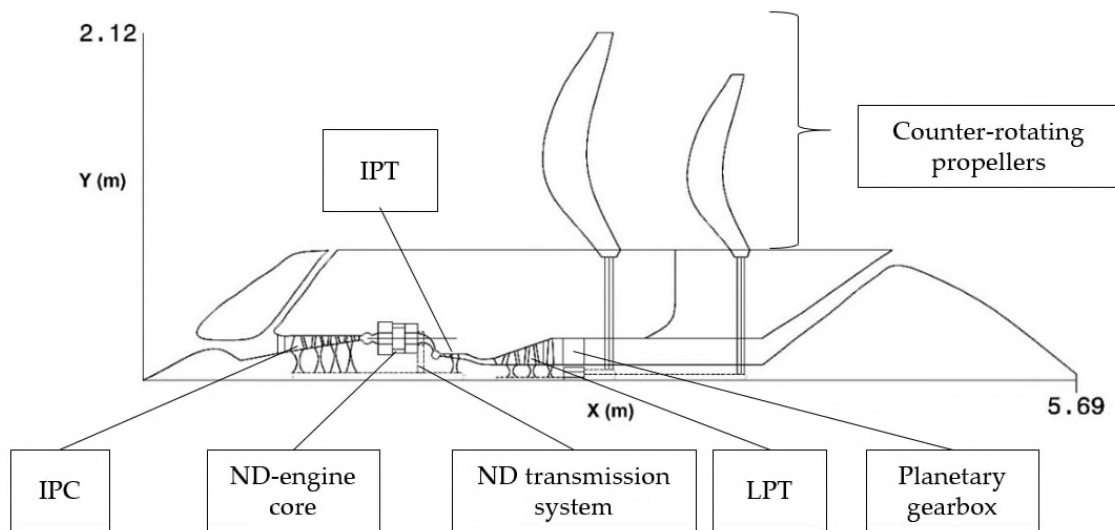


Figure 5- 39: Scaled meridional view of the Y2050 GOR-ND IP-drive

Figure 5-40 shows the potential arrangement of a scaled Y2050 GOR ND LP-drive variant. Similar to the IP-drive variant, the nutating disc engine system replaces the HP spool of a reference GOR2050 engine configuration. The excess shaft power produced by the ND engine systems, arranged circumferentially around the LP-shaft, is mechanically transmitted to the LP-shaft through a series of bevel gears. The pinions of the bevel gears that are

perpendicular to the engine centre line, pass through the OGV of the LPT, which is housed in the LPT turbine frame. The scaled meridional view of the LP-drive configuration is derived from a targeted optimization, which will be explained in the subsequent sub section.

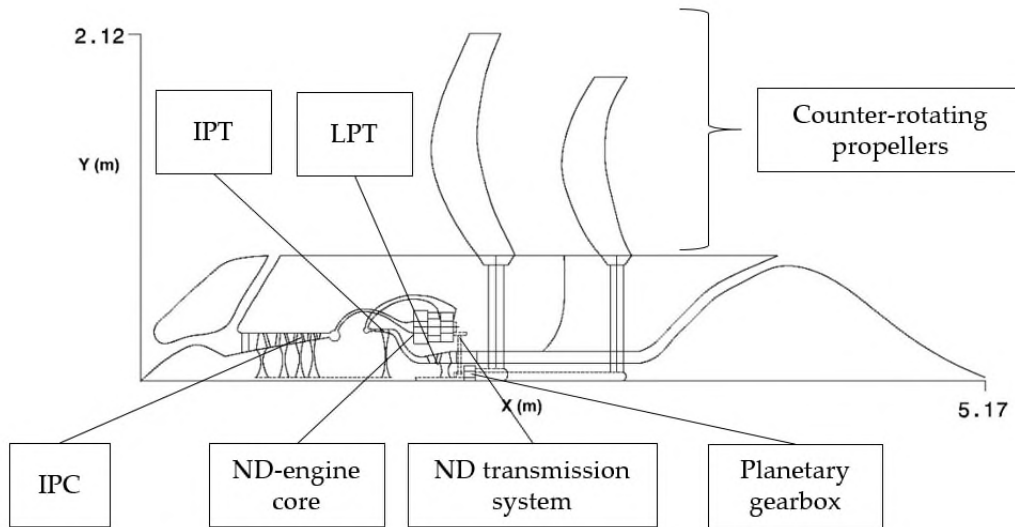


Figure 5- 40: Scaled meridional view of the Y2050 GOR-ND LP-drive

5.4.1 Determining the performance of Y2050 GOR-ND IP-drive and Y2050 GOR-ND LP-drive engines

In order to compare the two types of engine variants, the following steps have been employed:

- A design point (TOC) engine deck and off-design point engine deck was created for the IP-drive, using the created PROOSIS model.
- The non-linear trade burn factors are included within the structure of the decks to quantify the relative fuel burn benefits relative to the reference GOR2050 engine configuration.
- A targeted optimization was performed to ensure that the IP-drive variant consumed relatively less fuel compared to the reference GOR2050 engine for a 3500 NM mission.
- The same technology levels, in terms of net thrusts, mass flows and ND engine system parameters are applied to the LP-drive variant.
- A quantitative and qualitative comparison is undertaken for the IP-drive and LP-drive variants.

Figure 5-41, provides an overview of the sequence of execution that is necessary for the targeted optimization of the IP-drive variant. Initially the design point design parameters are altered and the design point deck is executed, following which the off-design deck is executed. Then the TSFCs at three operating conditions and engine mass estimation are used with the non-linear fuel trade factors (NLTF) for Y2050 short range aircraft platforms, following which the design point and off-design thrusts are updated till the thrust predicted by the NLTF and the thrusts included in to the two decks match. Finally the relative fuel burn figure is acquired. A key difference employed in the IP-drive engine model and all ND-engine system engine variants henceforth, is that the mass of the engine is estimated using the methods out lined in section 4.5. This method of mass estimation was favoured over using Weico 9.6 because, it provided a greater sensitivity to the design choices of the turbo-compounded engine cycle. A comparison between the mass estimation method using Weico 9.6 and the methods outlined in section 4.5 for the reference GOR2050 engine configuration are provided in Figure 5-42.

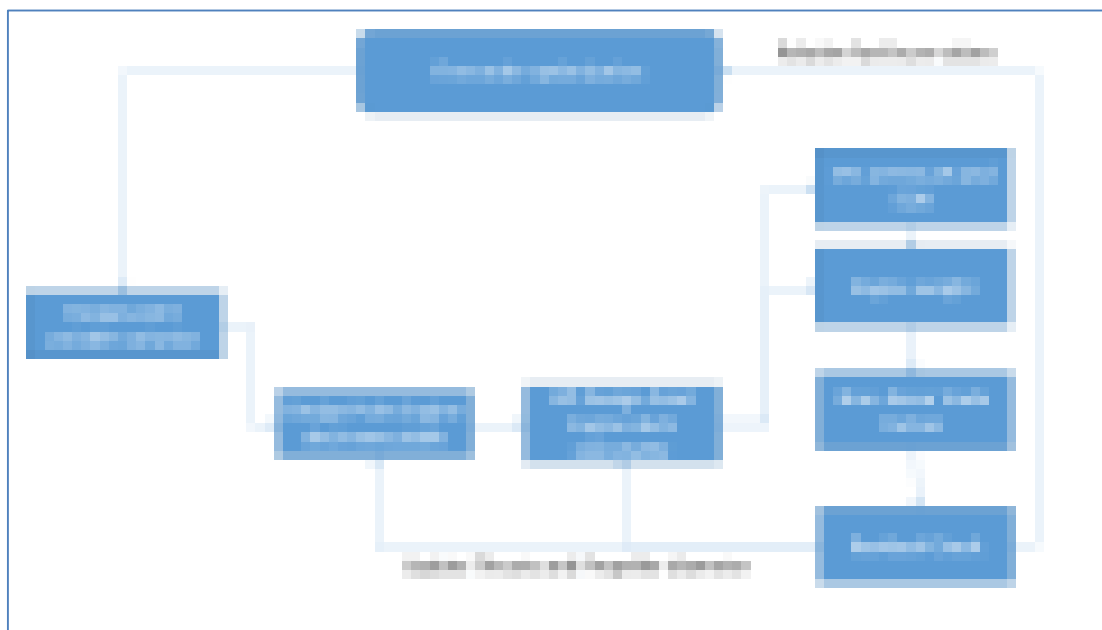


Figure 5- 41: Overview of first order optimization employed to derive fuel burn estimates of the IP-drive configuration

Based on the relative distribution of the relative engine component masses, shown in Figure 5-42, between the approximation of Weico 9.6 and the methodology outlined in section 4.5, it can be seen that the relative dry masses of the combustor, CRP, IPC, HPC, IPT and HPT modules are comparable. However, the estimated mass of the LPT and associated differential planetary gearbox by the method outlined in section 4.5 under predict the relative mass of the aforementioned components. This discrepancy is attributed to the fact that the

methods employed to predict the mass of the LPT and DPGB in Weico 9.6 utilizes a sizing approach that includes the mechanical constraints imposed at EOR conditions. Whereas the component engine masses, predicted by section 4.5, estimate the mass of the components at TOC conditions. This discrepancy in the LPT and PDGB module engine mass is alleviated by altering the magnitude of the scaling factor (K_b) in estimating the supporting structure mass as well as the scaling factor of the nacelle mass, to 0.22 and 15% of total engine weight respectively . This can be seen in Figure 5-42, where the relative mass of the nacelle and supporting structures are of a greater proportion of the engine mass when compared to the mass distribution estimated by Weico 9.6. One key impact the method utilized to predict the Y2050 ND engine system variant masses will have is that the engine masses will be optimistic.

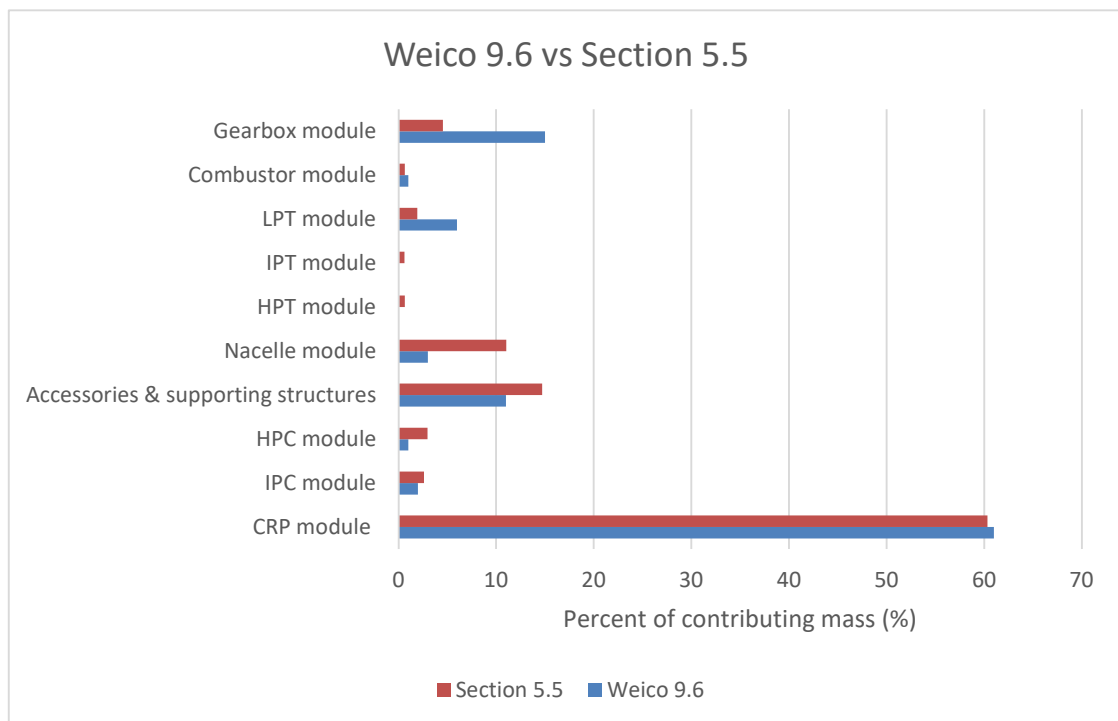


Figure 5- 42: Comparison between the relative mass distribution predicted by Weico 9.6 and methods outlined in Section 5.5 for the reference GOR2050.

The design parameters of the IP-drive variant at TOC conditions and their associated ranges that were incorporated in the targeted optimization procedure are outlined in Table 5-23. Moreover, the constraints and objectives of the targeted optimization are provided in Table 5-23. The process was deemed a targeted optimization because the primary purpose was to derive a nutating disc engine system aero-engine configuration that outperformed the reference year 2050 GOR. Ideally, prior to providing an optimized engine configuration it is necessary to include mechanical design constraints, emission, noise and vibrational

constraints on the model. Since these detailed constraints were not available, the primary objective of the targeted optimization was to provide an IP-drive design that burnt relatively less fuel when compared to the reference GOR2050 configuration. The optimization process was carried out within the I-sight environment, using the 'Pointer' algorithm similar to that used in the reference GOR 2050 configuration [128].

Table 5- 23: Design parameter bounds, constraints and objective for the IP-drive variant at TOC conditions

First-order design parameters bounds at TOC			
<u>Property</u>	<u>Units</u>	<u>Lower bound</u>	<u>Upper bound</u>
# of ND cores	(-)	4	12
IPC PR	(-)	4	7
IPT Nmech	(rpm)	10000	25000
Propeller speed	(rpm)	400	1000
Inlet W	(kg/s)	8	12
LPT PR	(-)	4.5	7.5
ND r_{23}	(-)	0.9	0.95
ND accumulator dpqp	(-)	0.02	0.05
ND r_{34}	(-)	0.95	0.98
ND compressor $\eta_{s,c}$	(-)	0.87	0.92
ND expander $\eta_{s,e}$	(-)	0.87	0.92
ND expander r_t	(m)	0.05	0.11
ND expander HT	(-)	0.35	0.5
ND expander α	(deg)	17	25
ND expander $f_{ql,cy}$	(-)	0.05	0.2
ND expander θ_1	(-)	0.1	0.9
ND expander θ_2	(-)	0.1	0.9
ND compressor l_f	(-)	1.02	1.15
Constraints			
<u>Property</u>	<u>Units</u>	<u>Lower bound</u>	<u>Upper bound</u>
IPT PR	(-)	1.2	5
Engine mass	(kg)	3000	5000
TOC TSFC	(g/kNs)	5	10.75
ND gearbox reduction ratio	(-)	1.5	3.0
Inlet ND axial Mach number	(-)	0.1	1.0
Objective: minimize relative FB			

The lower bound and upper bounds for the number of nutating discs were imposed to ensure that the mass of the ND core module segment would be appropriate to derive relative fuel burn benefits from. Furthermore, the lower bound of the number of nutating discs were constrained by ensuring that the flow entering the ND core was not sonic. A choked condition can occur when the number of nutating disc systems are such that the mass flow that enters

each ND engine system accelerates excessively from inlet plenum conditions to the inlet elbow duct of the nutating disc system. The IPC design point pressure ratio lower bound was imposed so that the mass of the ND engine system, for a given thrust level, would not become excessive. The upper bound for the IPC pressure ratio is imposed such that the last stage blade height of the IPC would not be excessively compromised such that the polytropic efficiency of the component would be affected. The upper and lower bounds of the IPT rotational speed were chosen such that it facilitated the optimizer to relatively quickly meet the nutating disc gearbox reduction ratio constraint. The rotational speed of the propellers at TOC were chosen for reasons similar to those mentioned in section 5.2.3. The inlet mass flow at TOC conditions were chosen such that it was comparable with the reference GOR2050 values. The LPT pressure ratio lower bound was chosen such that adequate expansion occurs to power the counter rotating propellers. The LPT pressure ratio upper bound was chosen such that the LPT AN² limitation wasn't violated. The upper and lower bounds corresponding to the ND-engine system are chosen in the ranges stipulated by Korakianitis et al.[1]. The lower bound of the IPT pressure ratio constraint was imposed to allow for adequate expansion across the IPT. The ND- engine gearbox reduction ratio constraints were imposed such that the transmission system for the ND would be mechanically feasible in terms of the spur gear arrangement for the IP-drive variant[129].

Table 5-24, provides an overview of the TOC performance of the Y2050 GOR-ND IP-drive configuration as a consequence of the targeted optimization process. In addition, Table 5-24 provides an overview of the Y2050 GOR-ND LP-drive configuration for the same TOC thrust levels and similar technology levels. Besides, the changes made to the design parameters in the optimization process, the boundary conditions corresponding to the technology levels of the IP-drive variant are exactly the same as that of the reference GOR2050 engine configuration.

Table 5- 24: Overview of the performance of the Y2050 GOR-ND IP-drive and LP-drive configurations

<u>Property</u>	<u>Units</u>	<u>Y2050 GOR-ND IP-drive</u>	<u>Y2050 GOR-ND LP-drive</u>
# of ND cores	(-)	6	6
IPC PR	(-)	6.5	6.5
IPT N _{mech}	(rpm)	10328	10328
Propeller speed	(rpm)	400	400
Inlet W	(kg/s)	10.3	10.3
LPT PR	(-)	7.5	2.0
ND r ₂₃	(-)	0.9	0.9
ND accumulator dP _{qP}	(-)	0.048	0.048
ND r ₃₄	(-)	0.90	0.90
ND compressor η _{s,c}	(-)	0.9	0.9

Property	Units	Y2050 GOR-ND IP-drive	Y2050 GOR-ND LP-drive
ND expander $\eta_{s,e}$	(-)	0.9	0.9
ND compressor r_t	(m)	0.102	0.102
ND expander r_t	(m)	0.085	0.085
ND expander HT	(-)	0.43	0.43
ND expander α	(deg)	25	25
ND expander $f_{gl,cy}$	(-)	0.1	0.1
ND expander θ_1	(-)	0.5	0.5
ND expander θ_2	(-)	0.5	0.5
ND compressor l_f	(-)	1.13	1.13
TOC F_n	(kN)	17.04	17.04
ND $T_{06_{mx}}$	(K)	1657	1800
TOC TSFC	(g/kNs)	10.14	13.14
Engine mass	(kg)	3209	3067
Front propeller diameter	(m)	3.98	3.98

Based on the performance of the two engine variants at TOC, it can be seen that the LP-drive has a comparatively worse TSFC. The reason for this, is that the power demanded by the counter rotating propellers is far greater than that demanded by the IPC. Consequently, for a constant thrust and inlet mass flow, in both configurations, the peak cycle temperature in the LP-drive is much higher than that of the IP-drive. This in turn leads to a higher fuel to air ratio and comparatively higher TSFC in the LP-drive variant. Another interesting observation, is that the mass of the LP-drive is lower than that of the IP-drive variant. This can be attributed to the fact that the LPT pressure ratio is significantly reduced relative to the IP-drive variant. As a consequence the LPT mass reduces from three stages to one stage.

Besides the reduced mass and increased TOC TSFC of the LP-drive configuration relative to the IP-drive configuration the following issues are incumbent with the LP-drive design:

- The tortuous path that the manifolds, stemming from the inlet plenum to the ND engine system and the ND-engine system to the exit plenum, take correspond to relatively higher total pressure losses, and further penalties on specific fuel consumption.
- The relatively higher peak cycle temperatures necessitate a more robust cooling system as well as relatively higher impact of creep-fatigue related lifing issues.
- When one considers the standard axial modular component approach to maintenance, the ND-core would be included with the LPT component of the LP-drive. This would make the access to the LPT component rather difficult. However, the IP-drive would facilitate the standard modular approach to maintenance and relatively easier access to components.

- The relatively higher peak cycle temperatures are indicative of higher flame temperatures in the LP-drive relative to the IP-drive, which are directly proportional to the degree of NO_x generated during operation [24], if the residence time and the combustor delivery temperature is the same for both configurations.
- Propeller speed schedules throughout the flight envelope, would entail the LP-drive configuration to have variable setting blow-off valves upstream of the ND engine system to ensure that the ND engine system operates within the designated speed schedule throughout the flight envelope. This leads to additional complexities to the configuration as well as reduced part load performance.

Due to the relative performance benefits and qualitative benefits the IP-drive has over the LP-drive, the following sections focuses on the design sensitivities associated with Y2050 GOR-ND IP-drive engine and its variants.

5.5 Performance and mass sensitivities of the Y2050 GOR-ND IP-drive engine configuration

The overview of the Y2050 GOR-ND IP-drive performance at TOC conditions, in Table 5-24, indicate that the IP-drive variant should outperform the reference GOR2050 engine configuration. Therefore, sensitivity studies are necessary to quantify the relative impact the design variables have on the TSFC and engine mass. This provides a hierarchy for the design variables that have the largest impact on mission fuel burn. The design sensitivity studies are carried out for the nutating disc system initially, after which the impact of the nutating disc systems' interaction with the rest of the core turbomachinery are investigated.

The nutating disc engine system design variables can be grouped in to TSFC dependent and engine mass dependent variables. Within the investigated range of the design variables, the variables that have the largest impact on the design point TSFC are the volumetric expansion ratios between the compressor and accumulator (r_{23}), the volumetric expansion ratio between the accumulator and the pre-combustion chamber (r_{34}), the adiabatic efficiency of the compressor ($\eta_{s,c}$), adiabatic efficiency of the expander ($\eta_{s,e}$), the heat loss factor through the combustion chamber casing ($f_{ql,cy}$), the maximum temperature change ratio during combustion (θ_1) and the average temperature change ratio during combustion (θ_2).

In practice, the compressor and expander adiabatic efficiencies will be dictated by the efficacy of sealing, severity of turbulence, surface roughness of the compressor disc, Reynolds number effect and the heat flux through the casing during compression and expansion processes. Likewise, the heat loss factor through the combustion chamber would be dictated by the surface area to volume ratio of the combustion chamber, maximum firing

temperature and the effectiveness of the associated cooling system. The maximum temperature change ratio, in practice, will depend on the volume of the pre-combustion chamber, maximum firing temperature, operational speed, angle of nutation and the hub to tip radius of the expander disc.

The average temperature change ratio during combustion is governed by the volumetric expansion ratio, firing frequency and wedge angle of the expander disc. In practice, the expansion ratio r_{23} and r_{34} will be dictated by the settings of the solenoid controlled valve that meters compressed air from the compressor to the accumulator and accumulator to the pre combustion chamber [2]. The total pressure loss of the accumulator would be dictated by the frequency of air admittance and discharge of the accumulator coupled with the scale of large eddy formation within the accumulator during operation.

A sensitivity study with regards to the aforementioned variables indicate that the volumetric expansion ratios (r_{23} and r_{34}), isentropic compression efficiency, heat loss through the combustion chamber casing and the average temperature change ratio significantly contributes to the design point TSFC. Figure 5-43 indicates the variation of the TSFC dependent nutating disc system design variables, where the reference case corresponds to Table 5-24. Intuitively, as the isentropic efficiencies and heat loss factor increases the TSFC decreases and increases respectively.

As the maximum temperature change ratio (θ_1) increases the TSFC increases as the ratio of constant volume combustion to constant pressure combustion decreases. However, when the average temperature change ratio (θ_2) increases the TSFC decreases. This phenomenon occurs because the volumetric expansion ratio increases with an increase in the average temperature change ratio, which in turn causes more work to be produced by the nutating disc engine system.

In addition, as the volumetric expansion ratio between the compressor and accumulator and the volumetric expansion ratio between the accumulator and pre-combustion chamber tends towards unity the relative TOC TSFC reduces, as relatively less heat is dissipated to the surroundings. In practice, the actual volumetric expansion ratios are expected not to vary considerably because the solenoid controlled air metering valve can change the operating metering pressure as a function of the operating conditions. Thus it can maintain relatively fixed levels of volumetric expansion ratios throughout the flight envelope. As the accumulator total pressure loss increases, the relative TSFC increases as the relative ratio of specific enthalpy to entropy decreases.

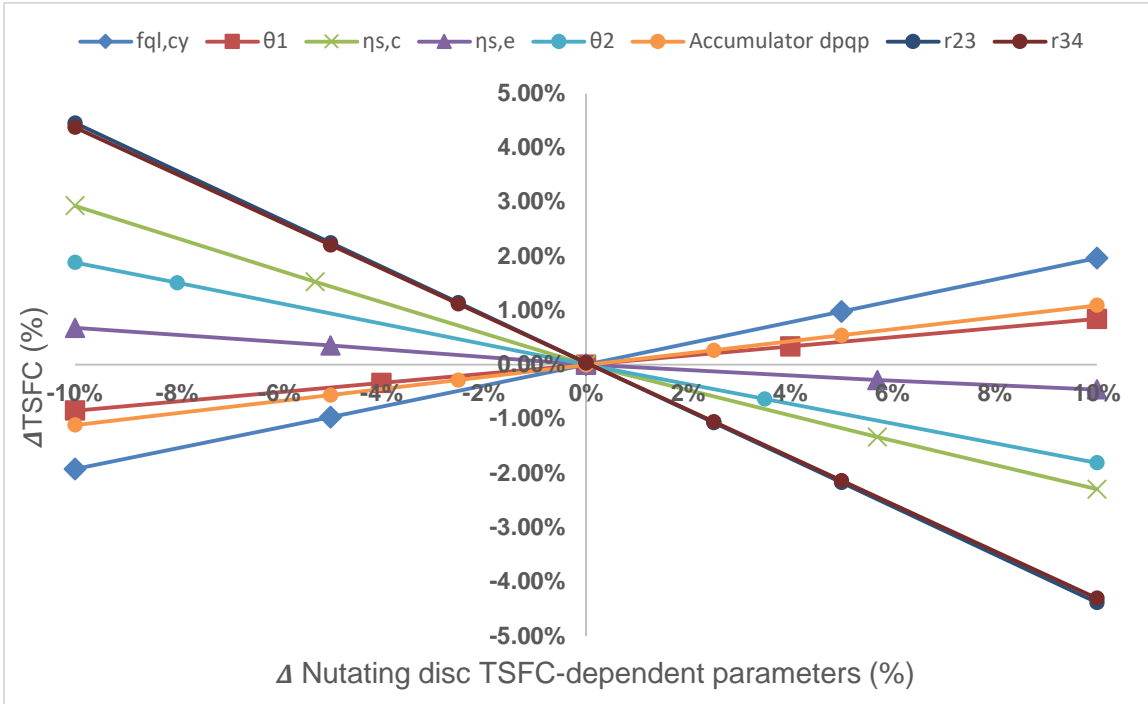


Figure 5- 43: Sensitivity study of the TOC TSFC dependent nutating disc system design variables

The nutating disc system design variables that have the largest impact on the ND engine system design mass are the disc tip radius (r_t), the wedge inlet factor (I_f), the hub to tip ratio (HT) and the angle of nutation (α). The sensitivity study presented in Figure 5-44 indicates the severity the design choices have on the overall mass of the engine.

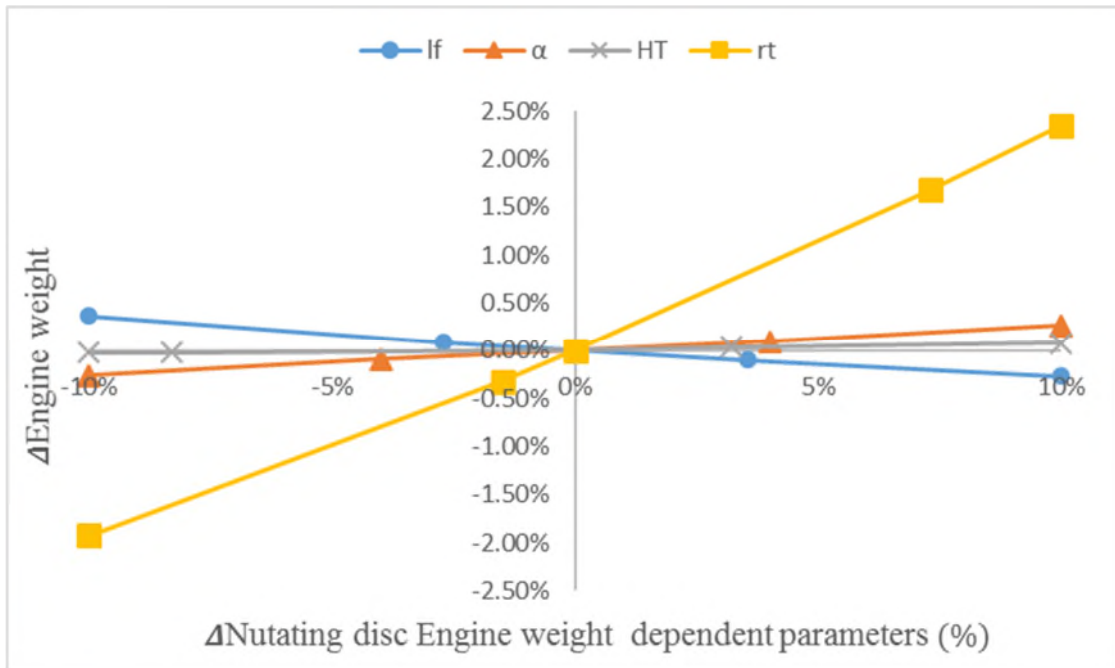


Figure 5- 44: sensitivity of the engine weight dependent ND system design variables

The outcome of the sensitivity study indicates that as the tip radius, hub to tip ratio and angle of nutation increase the mass increases. The effect of the angle of nutation and the tip radius causes the relative engine mass to increase quadratically. However, the hub to tip ratio and the inlet factor have a linear trend with regards to its effect on overall engine mass. The counterintuitive trend of engine mass decrease as the wedge inlet factor increases, corresponds to a decrease in the wedge angle for a fixed hub to tip ratio. In addition, the severity of the tip radius impact on mass significantly outweighs the other mass dependent parameters.

To truly appreciate the influence of the choice of nutating disc design parameters, a fuel burn analysis is conducted for the design presented in Table 5-24 as well as a design that leads to an optimistic design and a design that leads to a pessimistic design configuration. The design choices for optimistic design case are chosen based on TSFC dependent variables of the nutating disc engine system that produces relatively low specific fuel consumption-based on the allowable ranges dictated by Korakianitis et al. Similarly, the optimistic design choices for the mass dependent ND engine system variables are chosen based on the size of the nominal ND engine compressor and expander, at lower angles of nutation and hub to tip ratios. Likewise, for the pessimistic design case the ND TSFC dependent variables were chosen based on the allowable ranges as dictated by Korakianitis, which produces relatively higher TSFC. The mass dependent ND engine system variables, for the design case that yields a pessimistic design, were chosen such that the size of the ND compressor disc is double the nominal case and the angle of nutation and hub to tip ratios were higher than the nominal case.

The relative fuel burn analysis is conducted on a representative Y2050 short range aircraft for a mission range of 3500NM. Furthermore, the relative fuel burn analysis is conducted using the non-linear fuel burn trade factors provided by ULTIMATE and are presented in Table 5-25 [96].

Table 5- 25: relative fuel burn benefits of Y2050 GOR-ND IP-drive design variants

<u>Parameter</u>	<u>Pessimistic design</u>	<u>Nominal design</u>	<u>Optimistic design</u>
TOC Fn (kN)	20.5	17.0	16.0
ND compressor r_t (m)	0.2	0.1	0.1
ND compressor HT (-)	0.50	0.43	0.32

<u>Parameter</u>	<u>Pessimistic design</u>	<u>Nominal design</u>	<u>Optimistic design</u>
ND compressor l_f (-)	1.13	1.13	1.13
ND compressor α (-)	27	25	17
ND compressor $\eta_{s,c}$ (-)	0.8	0.9	0.95
ND expander r_t (m)	0.2	0.1	0.1
ND r_{23}	0.99	0.9	0.81
ND r_{34}	0.99	0.9	0.81
ND expander HT (-)	0.5	0.43	0.32
ND expander α (-)	27	25	17
ND expander l_f (-)	1.13	1.13	1.13
ND expander $\eta_{s,e}$ (-)	0.8	0.9	0.95
ND expander $f_{q,cy}$ (-)	0.2	0.1	0.05
ND expander θ_1 (-)	0.9	0.5	0.1
ND expander θ_2 (-)	0.1	0.5	0.9
TSFC (g/kN/s)	15.00	10.14	7.39
Engine mass (kg)	5191	3208	2939
Front propeller diameter (m)	4.18	3.98	3.92
ND Nmech (rpm)	2335	17963	44977
<u>Off-design</u>			
Fn at Cruise(kN)	16.0	13.7	13.1
Mach no.	0.71	0.71	0.71
altitude (m)	11278	11278	11278
Delta ISA (K)	0	0	0

<u>Parameter</u>	<u>Pessimistic design</u>	<u>Nominal design</u>	<u>Optimistic design</u>
Fn at Take-off(kN)	92.3	77.8	73.0
Mach no.	0.2	0.2	0.2
altitude (m)	0	0	0
Delta ISA (K)	15	15	15
TSFC at cruise (g/kN/s)	14.29	9.59	6.93
TSFC at Take-off (g/kN/s)	7.38	4.89	3.52
Fuel burn relative to GOR2050 (%)	55.9	-9.4	-36.7
Fuel Burn relative to Y2000 (%)	-35.9	-62.8	-74.0

It is apparent that the vast possible variation in relative fuel burn values are highly dependent on the technology level of the TSFC dependent and mass dependent design variables. An intriguing observation is how the operating speed of each nutating disc engine system scales with the degree of optimism of the design. This is wholly attributed to the fact that in the pessimistic design regime the swept volume increases, therefore for a fixed mass flow rate the operational speed will decrease.

The operational speed of the nutating disc engine system is generally proportional to the bearing loading life, thus it is assumed with the current state of the art bearing design a more pessimistic design case seems more favourable. However, by Y2050 it can be postulated that advances in bearing technology would sustain higher loads, higher temperatures and higher operational speeds which could be representative of the nominal 2050 GORIP-drive engine configuration. A key assumption in estimating the off-design performance of the aforementioned cases is that the turbomachinery performance is based off of scaled component maps and that the ND engine system design parameters remain the same as that chosen at design point. For example, it is assumed that the efficiencies, gear reduction ratios and heat release ratios remain constant. In practice, this would not be the case and further work with regards to the part load performance of a nutating disc engine system is crucial.

When the feasibility of the presented engine design configurations are benchmarked against the 2050 fuel burn reduction target of -68%, which stems from the combined benefits of advances in Y2050 aircraft and potential Y2050 novel engine configurations, the reference 2050 GORIP-drive engine misses the mark and the optimistic case meets it [6]. Figure 5-45 indicates the relative fuel burn benefits derived from all three 2050 GORIP-drive design cases, the fuel burn target and the reference GOR 2050 engine design configuration relative to a short range turbofan in the Y2000.

In order to meet the lofty fuel burn targets stipulated by the optimistic 2050 GORIP-drive, sealing technology needs to mature to a point where there is minimal leakage. In addition, minimal amounts of turbulence generation in the compression and expansion chamber coupled with minimal heat loss through the casings should be achieved. Furthermore, the cycle should be more inclined towards constant volume combustion, minimal heat loss through the combustion chamber and a larger volumetric expansion ratio. Lastly, bearing technology needs to mature to sustain the high loads and speeds seen in the optimistic design case.

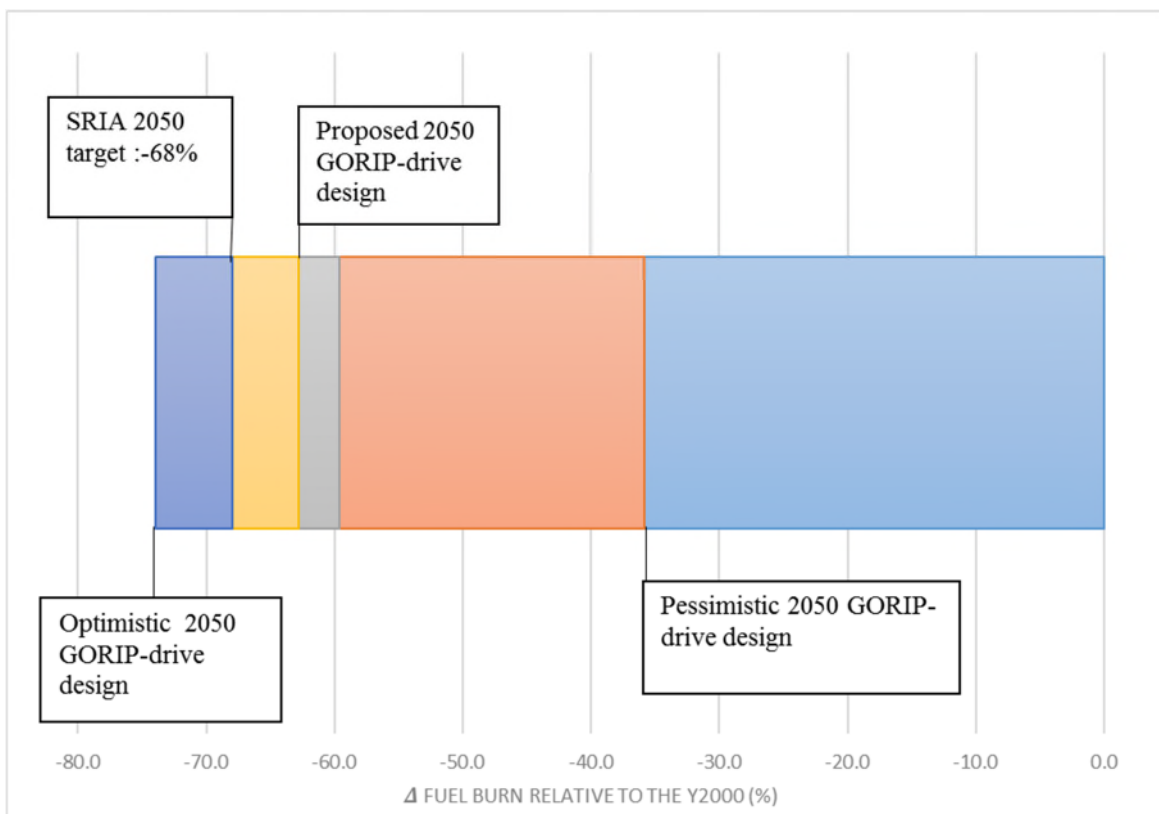


Figure 5- 45: Fuel burn targets and estimates relative to an Y2000 reference

A constituent breakdown of the effects of the independent variables that contribute to the mission fuel burn of the nominal 2050 GOR IP-drive design is provided in Figure 5-46. The

heat loss through the combustor and the ratio of constant volume combustion and constant pressure combustion have the most significant impact on the fuel burn estimate of the engine configuration. The ranges of the investigated design parameters are consistent with those used in Figure 5-31.

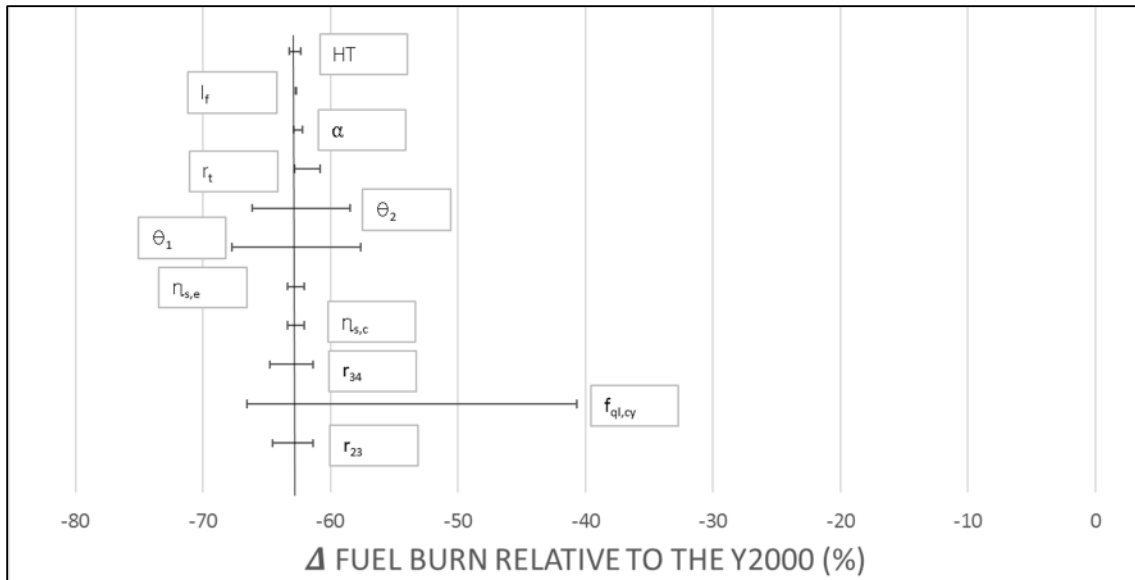


Figure 5- 46: relative uncertainty of ND engine system design variables in the nominal 2050 GORIP-drive design

The other core design parameters (both TSFC-dependent and mass-dependent) considered in conjunction with the nutating disc engine system design parameters are the inlet mass flow and IPC pressure ratio at TOC. Figure 5-47 shows the effect that Inlet mass flow and IPC pressure ratio has on the relative TOC specific fuel consumption, where the reference TSFC corresponds to **10.14 g/kNs**, while maintaining the technology levels of the nominal IP-drive engine as that of the reference case in Table 5-25. The upper bound for the IPC pressure ratio and lower bound for the mass flow, in Figure 5-47, was chosen as it represented a potential last stage blade height limitation. For a fixed mass flow, as the IPC pressure ratio increases the relative TOC TSFC increases. This trend occurs because, as the IPC pressure ratio increases the density of the air entering the ND engine system increases, thus for a fixed mass flow rate the swept volume and operational speed of the ND engine system decreases. Since the radius of the compressor disc is fixed, an increase in ND inlet air density corresponds to a decrease in size of the expander disc. This corresponds to less high-grade turbine work being extracted from the ND engine system and more turbine work being extracted from the IPT. Thus the relative TSFC increases. For a fixed IPC pressure ratio, as the mass flow rate decreases for a fixed TOC thrust level the swept volume decreases, for a fixed ND engine system inlet air density and ND compressor radius.

This in turn corresponds to a smaller expander disc and lower ND turbine work. However the ratio of ND-turbine work and IPT turbine work are maintained despite variation in the inlet mass flow. As a consequence of lower turbine work demands from the ND engine system, the firing temperature and fuel flow rates decrease.

This trend continues till a minima in the relative TOC TSFC is reached (~9 kg/s). Further decrease in the core mass flow causes the effects of compressor work to overshadow the turbine work increment benefits. The relative TSFC variation versus the variation in design point mass flow is similar to the Thrust-TSFC loops, commonly seen in the preliminary design space explorations of ducted aero-gas turbine engines[32]. An additional observation, is that the magnitude of TOC TSFC change is similar to that of the core ND engine system design parameters.

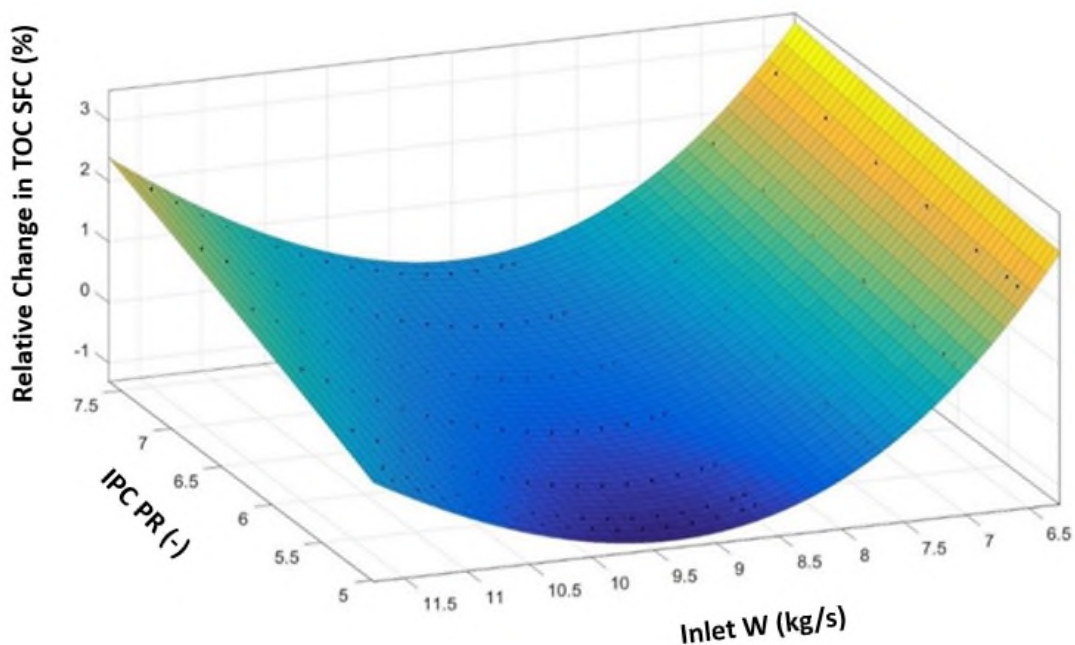


Figure 5- 47: Relative change in TOC TSFC as a function of the IPC pressure ratio and inlet mass flow.

Figure 5-48, shows the variation in the relative mass of the Y2050 GOR-ND IP-drive variant as a function of the IPC pressure ratio and the inlet mass flow. As the mass flow increase the relative mass of the configuration increases, as expected. In addition, for a fixed mass flow as the IPC pressure ratio increases the relative engine mass increases. The effect of the inlet mass flow on the engine mass has a greater influence than that of the IPC pressure ratio.

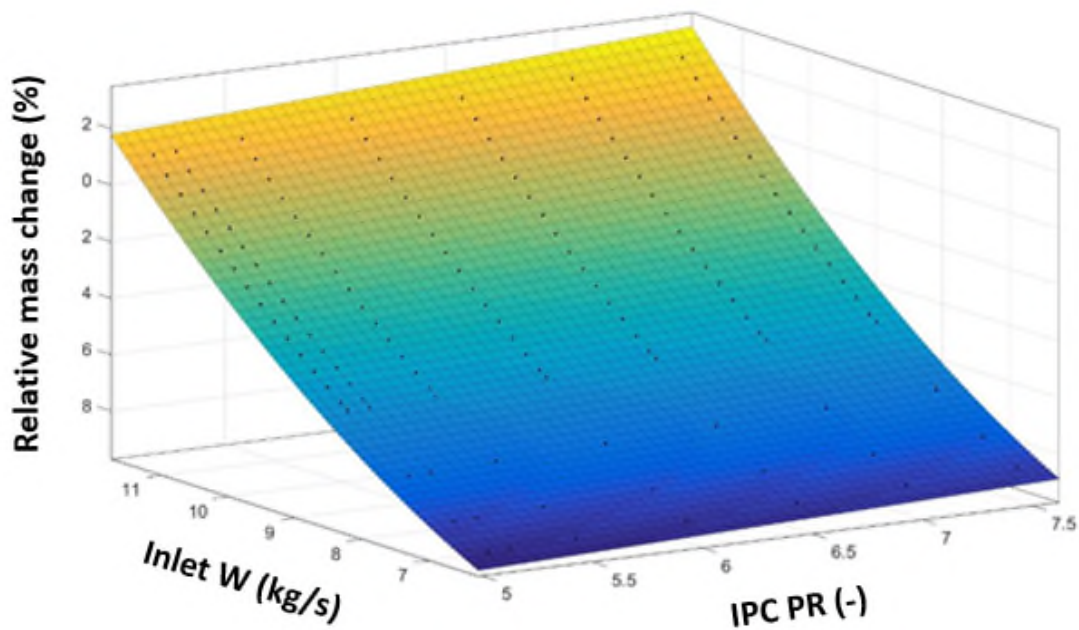


Figure 5- 48: Relative change in TOC TSFC as a function of the IPC pressure ratio and inlet mass flow.

Table 5-26, provide an overview of certain values for the reference GOR2050 engine and the Y2050 GOR-ND IP-drive engine models at EOR conditions. These variables provide an insight with regards to the potential impact of the noise and emissions pattern within the LTO envelope. A comprehensive analysis has not been performed to estimate the noise and emissions characteristics within the LTO envelope, therefore a qualitative assessment of the IP-drive engine relative to the reference GOR2050 engine has been provided.

Within the architecture of a geared open rotor the primary source of noise is attributed to the counter rotating propeller array and a relatively minor proportion to the core exhaust jet stream[16,115]. Generally, the magnitude of the noise pattern is directly proportional with the velocity of the core exhaust jet stream [32]. Since both engine configurations, highlighted in Table 5-26, have the same operational speed it can be postulated that the noise signature of both engine configurations are comparable in the LTO regime.

However, the core exhaust jet velocity in the IP-drive is comparably much higher than the reference GOR2050 configuration at EOR conditions, which in turn indicates a relatively noisier engine within the LTO envelope. Since detailed analysis to quantify the relative increase in the potential noise signature has not been done, a potential research brief is presented in chapter 7.

In terms of NO_x emissions within the LTO regime, it is generally postulated that the degree of NO_x emissions scales with compressor delivery temperature (CDT) and peak cycle temperature, assuming that the firing temperature is proportional to the peak cycle temperature and the effects of residence time is not accounted for [24,32]. The compressor delivery temperature prescribed for the IP-drive configuration corresponds to the temperature of air that enters the ND pre-combustion chamber during EOR conditions.

Based on the figures depicted in Table 5-26, it can be seen that the CDT and peak cycle temperature of the IP-drive are higher than that of the reference GOR2050 engine. Therefore, it is possible to expect relatively more NO_x emissions by the IP-drive in the LTO envelope. The aforementioned statement is qualitative in nature, and a thorough quantitative assessment of the same needs to be addressed in order to verify the degree of NO_x emissions.

Table 5- 26: Noise dependent and NO_x emission dependent parameters

<u>EOR Conditions</u>			
<u>Property</u>	<u>Units</u>	<u>Reference GOR2050</u>	<u>Y2050 GOR-ND IP-drive</u>
Propeller Nmech	(rpm)	400	400
Core nozzle exit velocity	(m/s)	210	322
CDT (T25)	(K)	911	1057
Peak cycle Temperature	(K)	2019	2041

Since NO_x emission criteria form a considerable part of the potential SRIA legislation, reducing the ND engine system delivery temperature and peak cycle temperature should be incorporated in to the design of the Y2050 GOR-ND IP-drive engine configuration. The incorporation of intercooling technologies and inter turbine reheat technologies have historically been investigated to address comparable issues within the architecture of ducted aero gas turbines[91,130]. Therefore, the following sections will investigate the performance benefits as well as the qualitative emission and noise estimates by incorporating intercooling and secondary combustion to the architecture of a Y2050 GOR-ND IP-drive configuration. Therefore the following engine configurations shall be introduced and analysed in the subsequent sections:

- Y2050 GOR-ND IP-IC-drive engine configuration, consists of an involute-spiral crossflow intercooler introduced in to the architecture of the IP-drive engine variant.

- Y2050 GOR-ND IP-SC-drive engine configuration, consists of a reverse-flow secondary combustion system integrated in to the architecture of the IP-drive engine variant.
- Y2050 GOR-ND IP-IC-SC-drive engine configuration, consists of a recirculating-flow secondary combustion system and an involute-spiral crossflow intercooler introduced in to the architecture of the IP-drive engine variant.

5.6 Performance and mass sensitivities of the Y2050 GOR-ND IP-IC-drive engine configuration

Figure 5-49 indicates the scaled arrangement of a Y2050 GOR-ND IP-IC-drive engine configuration. Similar to the approach taken in determining the performance of the Y2050 GOR-ND IP-drive engine configuration, a targeted optimization of the PROOSIS Y2050 GOR-ND IP-IC drive engine model was created to ensure that the configuration outperformed the reference GOR2050 engine configuration.

Key features of the Y2050 GOR-ND IP-IC-drive engine configuration include the following:

- Splitting the flow entering the core of the GOR in to a bypass stream and a core flow, after a booster stage. This arrangement was preferred over having a separate duct located on the nacelle to provide relatively cooler air for the intercooler because an additional duct located on the nacelle would have distorted the flow seen by the counter rotating propeller array. Therefore, the proposed arrangement provided a relatively simpler and compact arrangement.
- An axi-centrifugal intermediate pressure compressor is preferred over an axial compressor because as a consequence of splitting the core flow the last stage blade height of the IPC in an axial compressor, in the proposed arrangement, would be rather small and would consequently impact the polytropic efficiency of the IPC component adversely.
- The exit plane of the LPT and the intercooler exit bypass duct is a mixed nozzle. However, it is assumed that the intercooler bypass exit area is a variable area nozzle to minimize the pressure loss due to the mixing flows.

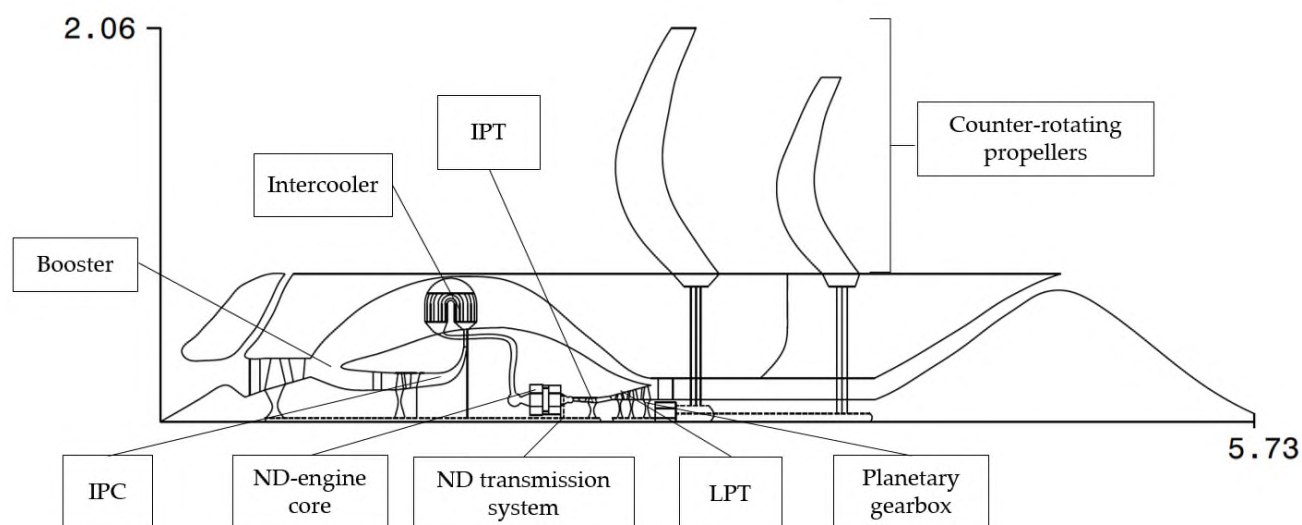


Figure 5- 49: Scaled meridional view of the Y2050 GOR-ND IP-IC-drive engine configuration

The primary design parameters of the IP-IC-drive variant at TOC conditions and their associated ranges that were incorporated in the targeted optimization are outlined in Table 5-23. Furthermore, the constraints and objectives of the targeted optimization are provided in Table 5-23 (refer to section 5.4). The ranges of the additional design parameters as a result of incorporating the intercooler component are shown in Table 5-27. The upper and lower bounds of the targeted optimization study were prescribed based on aerospace mandated bounds, by a year 2050 timeframe, for cross-flow heat exchangers as per [60,119,130]. The upper and lower bounds for the booster pressure ratio are determined by the acceptable pressure ratio limits for a single stage axial compressor and axi-centrifugal compressors [33,131]. The inlet mass flow rates range, in Table 5-27, were chosen such that the derived IPT pressure ratio was above unity. The bypass ratio, for the targeted optimization study, was also chosen such that the IPT pressure ratios were above unity. Similar to the targeted optimization described in section 5.4, the ‘pointer’ optimizing algorithm in Isight was chosen.

Table 5- 27: Ranges of the TOC design variables for the targeted optimization for the Y2050 GOR-IP-IC-drive configuration

<u>Design parameters bounds at TOC</u>			
<u>Property</u>	<u>Units</u>	<u>Lower bound</u>	<u>Upper bound</u>
IC effectiveness	(-)	0.45	0.75
IC hot side dpqp	(-)	0.01	0.05
IC cold side dpqp	(-)	0.01	0.05
Booster PR	(-)	1.1	1.7
Axi-centrifugal IPC PR	(-)	6.5	9.5
BPR	(-)	0.5	2.5

Design parameters bounds at TOC			
<u>Property</u>	<u>Units</u>	<u>Lower bound</u>	<u>Upper bound</u>
Inlet W	(kg/s)	15	23
Objective: minimize relative FB			

Table 5-28, provides an overview of the performance of the Y2050 GOR-ND IP-IC-drive engine performance at TOC, CR and EOR conditions. In addition the total engine mass and relative fuel burn benefit for a 3500 NM mission is shown. The key observations about the IP-IC drive performance figures is that the number of nutating disc engine systems dropped from 6 to 4, which can be attributed to the lower core flow entering the ND engine system array when compared to the IP-drive engine variant.

The operational speed of the IP shaft also increased, relative to the GOR-ND IP-drive configuration, as the turbomachinery tends closer to the centre line of the engine because of the introduction of the bypass ratio.

Table 5- 28: Performance overview of Y2050 GOR-ND IP-IC-drive engine performance

Design point TOC		
<u>Property</u>	<u>Units</u>	<u>Y2050 GOR-ND IP-IC-drive</u>
# of ND cores	(-)	4
Booster PR	(-)	1.3
IPC PR	(-)	8.5
BPR	(-)	1.56
IPT Nmech	(rpm)	30185
Propeller speed	(rpm)	400
Inlet W	(kg/s)	21
LPT PR	(-)	7
Propeller diameter	(m)	4.01
ND r23	(-)	0.9
ND accumulator dPqP	(-)	0.027
ND r34	(-)	0.95
ND compressor $\eta_{s,c}$	(-)	0.9
ND expander $\eta_{s,e}$	(-)	0.9
ND compressor r_t	(m)	0.074
ND expander HT	(-)	0.37
ND expander α	(deg)	25
ND expander $f_{q,cy}$	(-)	0.05
ND expander θ_1	(-)	0.25
ND expander θ_2	(-)	0.9
ND compressor l_f	(-)	1.04
IC effectiveness	(-)	0.55
IC dPqP cold side	(-)	0.05
IC upstream duct dPqP	(-)	0.02
IC downstream duct dPqP	(-)	0.02

Design point TOC		
Property	Units	Y2050 GOR-ND IP-IC-drive
IC dPqP hot side	(-)	0.03
TOC Fn	(kN)	17.6
ND T06mx	(K)	1782
TOC TSFC	(g/kNs)	9.39
Engine mass	(kg)	4313
Off-design conditions		
CR Fn	(kN)	14.2
CR TSFC	(g/kNs)	9.09
EOR Fn	(kN)	80
EOR TSFC	(g/kNs)	3.71
Fuel burn		
Delta FB2050	(%)	-11.6
Delta FB2000	(%)	-63.7

Just as in the case of the Y2050 GOR ND-IP-drive, the relative fuel burn of the IP-IC-drive variant is heavily dependent on the technology level of the design variables chosen. Therefore, it is reasonable to expect a similar level of relative fuel burn uncertainty as depicted in Figure 5-46.

An uncertainty break down of how each independent design variable for the IP-IC-drive configuration, besides the nutating disc engine system design variables, affects potential fuel burn is found in Figure 5-50. The BPR has the most sensitive impact on the fuel burn estimate of the engine configuration. As an increase in the nominal BPR causes the fuel flow to increase and core engine mass to decrease for a fixed thrust level. The ranges of the investigated design parameters are consistent with those used in Table 5-27

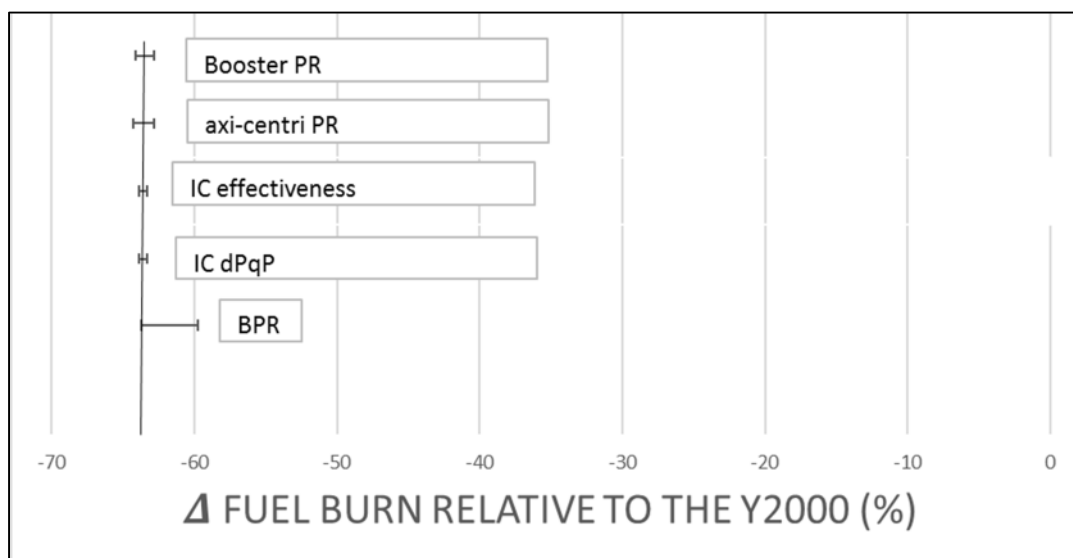


Figure 5- 50: Relative breakdown of key intercooler design variables

The relative trends of the ND-engine system design parameters, in the IP-IC-drive, in terms of their effect on TSFC and engine mass are the same as those discussed in section 5.4. As in the case of the Y2050 GOR-ND IP-drive engine configuration the effect of other core design parameters, besides the ND-engine system parameters, should be considered with regards to their impact on TOC TSFC and engine mass.

Therefore the effects of the engine mass flow, booster pressure ratio, axi-centrifugal pressure ratio, intercooler effectiveness, intercooler total hot and cold pressure losses and bypass ratio on the relative TSFC and mass of the IP-IC-drive combination are investigated. The effects of inlet mass flow and axi-centrifugal pressure ratio on the relative TSFC are depicted in Figure 5-51. Refer to section 5.5 for an explanation of the trends, as they are the same.

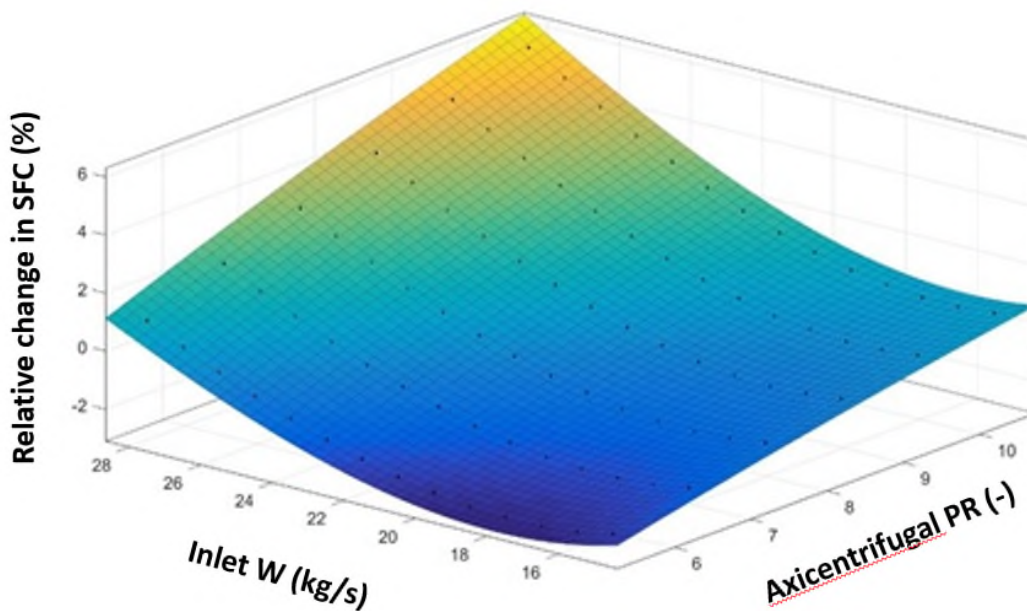


Figure 5- 51: Relative change in TSFC as a function of axi-centrifugal PR and inlet mass flow.

Figure 5-52, show the relative change in engine mass as a function of the inlet mass flow and IPC pressure ratio. It would be intuitive to expect that the trends to be similar to that depicted in Figure 5-48 in section 5.5.

However it can be seen that as the axi-centrifugal compressor ratio increases the relative engine mass decreases. This occurs because the rate at which the ND engine system decreases in mass as function of increasing the axi-centrifugal pressure ratio is greater than the relative increase in mass of the axi-centrifugal compressor. Therefore, as the axi-centrifugal compressor pressure ratio increases the relative engine mass decreases. In addition, as the inlet mass flow increases the mass of the engine increases as expected.

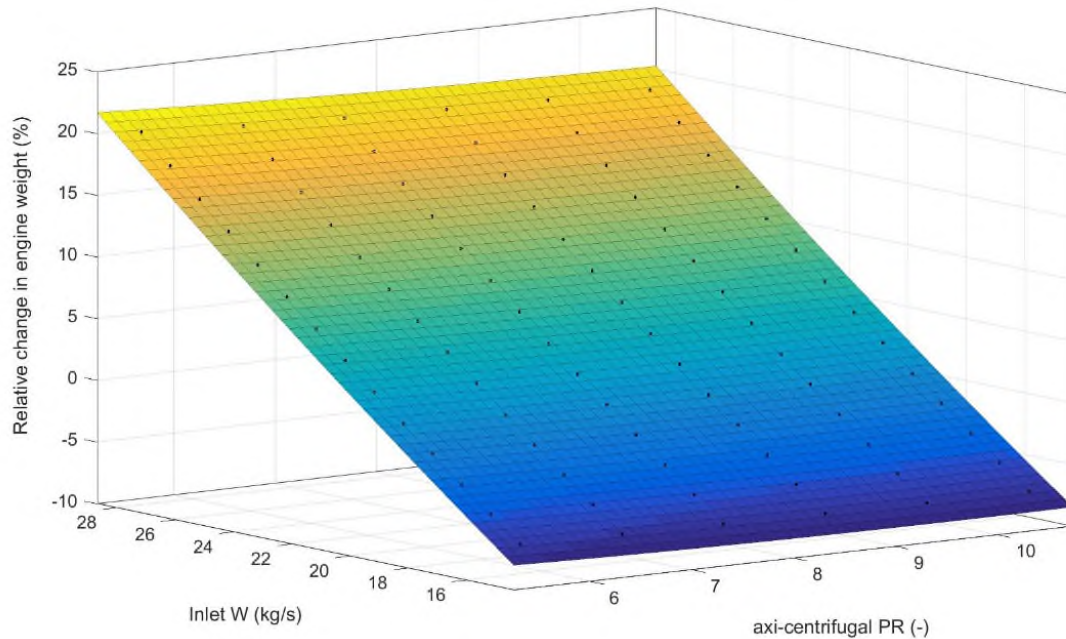


Figure 5- 52: Relative change in the IP-IC-drive engine mass as a function of the inlet mass flow and axi-centrifugal pressure ratio

Figure 5-53, indicates the relative TSFC variation as a function of the booster pressure ratio and the axi-centrifugal pressure ratio. For a fixed thrust rating at TOC and nutating disc compressor radius, as either pressure ratio is reduced the relative TSFC reduces as well.

This is attributed to the fact that as the pressure ratio decreases the density of the air entering the ND engine system will decrease, swept volume of the ND engine system increase, ND expansion ratio increases and the subsequent percentage of work extracted from the core relative to the IPT would increase.

Another observation that can be drawn from Figure 5-53, is that the effect of varying the booster pressure ratio and the axi-centrifugal pressure ratio has an equally similar effect on the relative TSFC.

Figure 5-54, shows the relative change in engine mass as a function of the booster pressure ratio and axi-centrifugal pressure ratio. It can be seen that the as the booster pressure ratio and axi-centrifugal pressure ratio increases the mass of the entire engine decreases. This occurs because the density of the air entering the nutating disc engine system increases and consequently the size of the expander disc decreases. It also can be observed that the rate of change of the relative engine mass as a function of the booster pressure ratio is steeper than that of the relative engine mass as a function of the axi-centrifugal pressure ratio. This occurs because the rate of booster mass increment as a function of increased pressure ratio

is much lower than that of the axi-centrifugal component. Hence, it can be surmised that a change in booster pressure ratio has a higher impact on the relative engine mass.

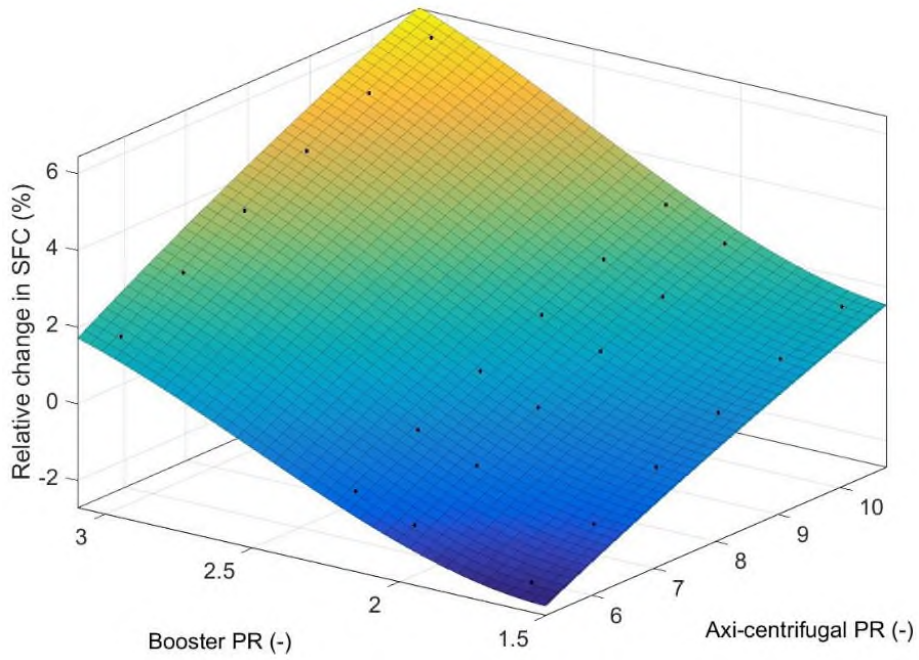


Figure 5- 53: Relative change in TSFC as a function of axi-centrifugal PR and booster PR.

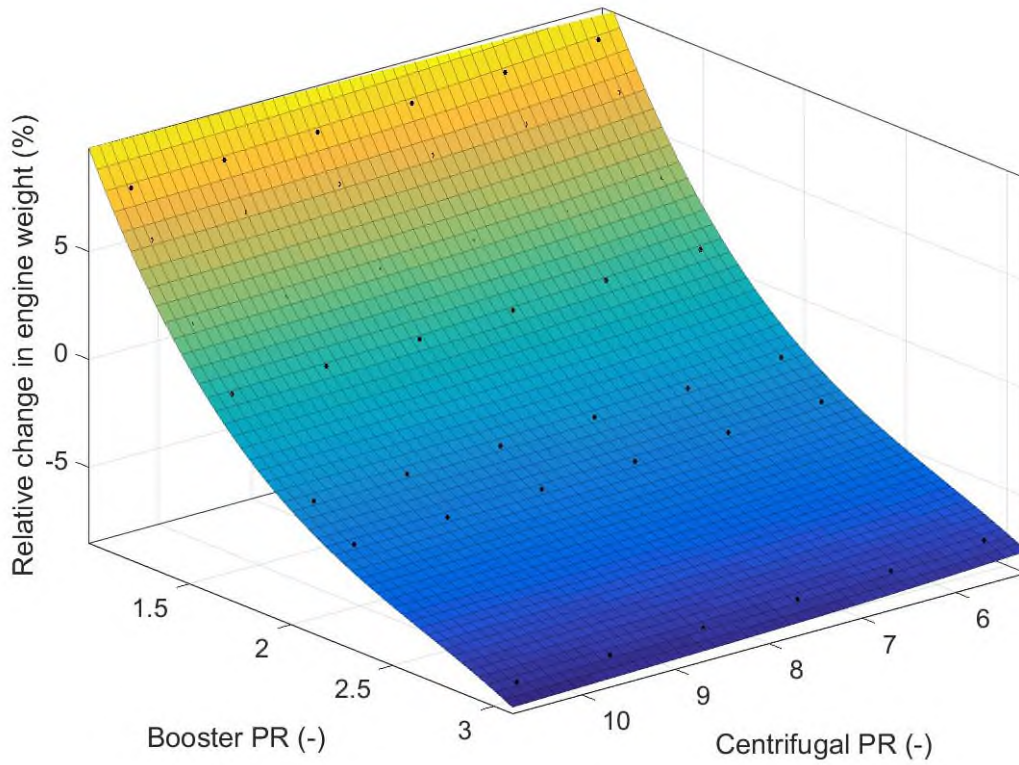


Figure 5- 54: relative change in engine weight as a function of booster and axi-centrifugal pressure ratios.

When the relationship between the BPR and axi-centrifugal pressure ratio is considered in relation to the relative TSFC, Figure 5-55 can be investigated. The bypass ratio is defined as the ratio of the mass flow in the intercooler duct and the mass flow entering in to the axi-centrifugal compressor. The effect on the axi-centrifugal pressure ratio on the relative TSFC is consistent with the trends seen in Figure 5-53. When the BPR decreases, for a fixed thrust and a fixed nutating compressor radius the mass flow entering the ND engine system increases and the swept volume of the ND engine system increases. As the nutating disc compressor radius is fixed in this analysis, the expander disc volume increases and higher grade ND power is extracted in relation to the IPT. However it can be seen as the BPR is reduced further than ~ 1 , the relative TSFC starts to increase. This occurs because the work demanded of the ND expander increases as such, for a fixed thrust and ND compressor size, that it causes the ND expander to deliver over expanded flow to the IPT. This in turn causes IPT pressure ratios to tend lower than unity, therefore under the context of the model the compressor work would increase and the relative TSFC would also increase.

In actuality, an IPT pressure ratio does not tend below unity. Thus, the core specific thrust or the ND compressor size must increase to accommodate a feasible design. Consequently, for a fixed specific thrust rating and ND compressor size there exists a BPR that corresponds to minimum TSFC. In addition, within the feasible design space of Figure 5-55, the degree of variation in BPR has a greater impact on the relative TSFC than the axi-centrifugal pressure ratio.

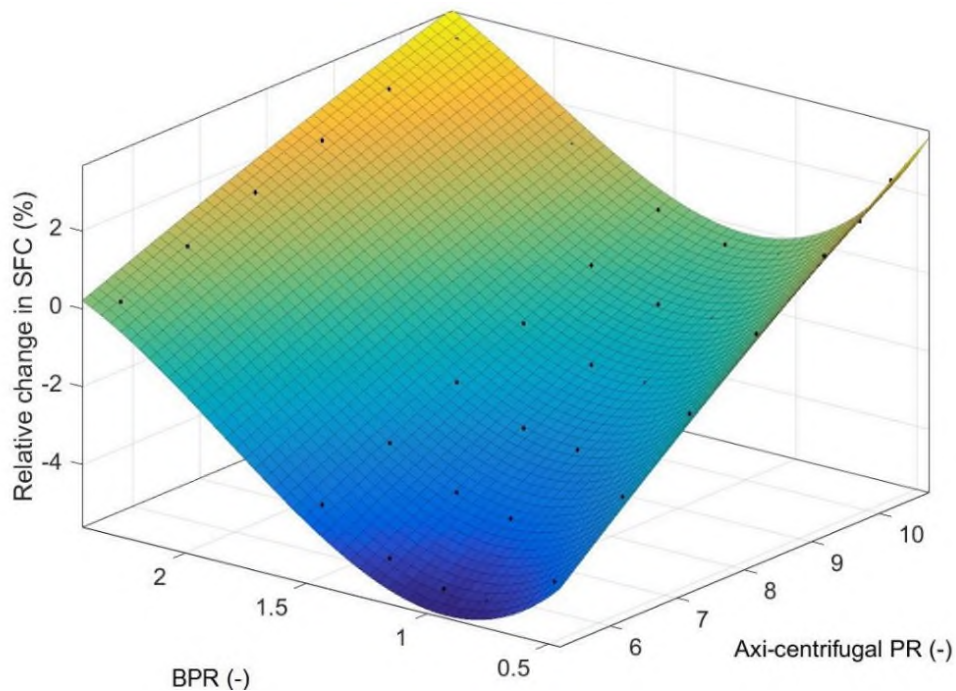


Figure 5- 55: Relative change in TSFC as a function of axi-centrifugal PR and BPR.

Similar to the format that has been followed so far, Figure 5-56 shows the impact of the BPR and axi-centrifugal PR on the relative change in engine mass. Unsurprisingly, as the BPR increases the relative engine mass decreases as the size of the core turbomachinery reduces significantly and hence their constituent masses.

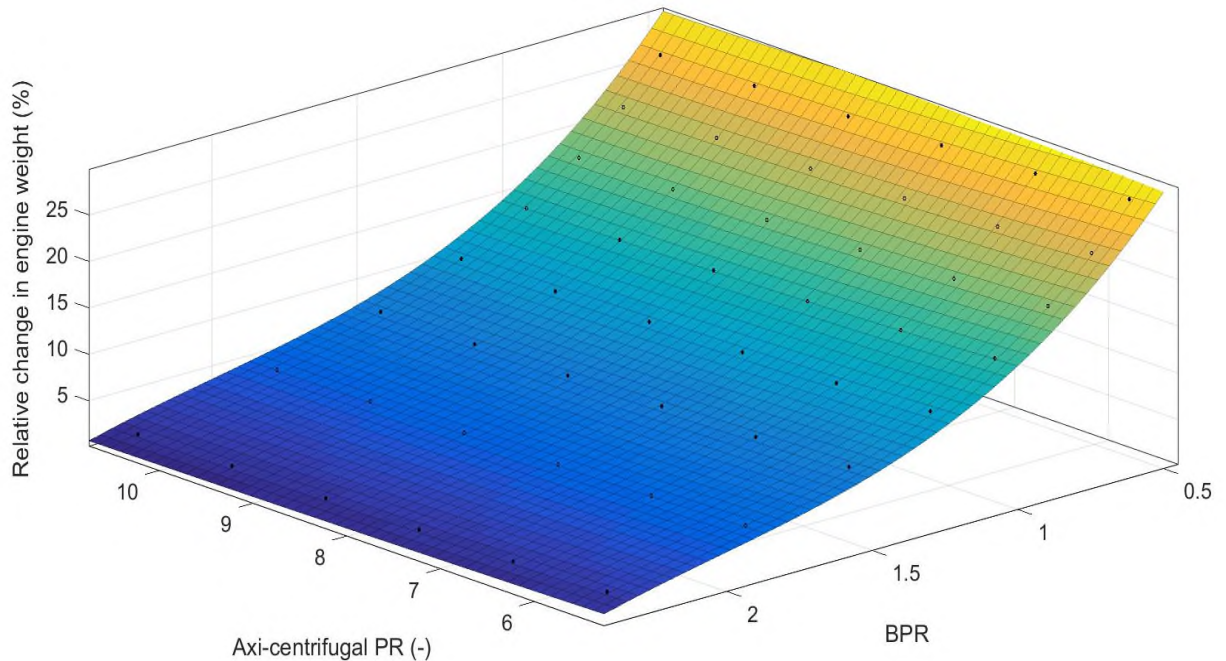


Figure 5- 56: Relative change in engine mass as a function of axi-centrifugal PR and BPR

Figure 5-57, reveals the relationship between the core mass flow and the BPR on the relative TSFC for the IP-IC-drive configuration. As the BPR decreases the relative TSFC decreases, for a fixed mass flow, based on the fact that a higher percentage of higher grade ND engine system power is extracted. However there exists a BPR for each mass flow which corresponds to the minimum TSFC. This value increases with the mass flow.

Thus, for a fixed thrust level and ND compressor radius as the mass flow increases the boundary at which the ND core expander would over expand the flow occurs at higher BPRs. Similarly, as per Figure 5-57, as the BPR increases the inlet mass flow that corresponds to a minimum TSFC corresponds to a higher value.

As the mass flow decreases, for a relatively high BPR value (~2) and fixed ND compressor radius, the specific power increases and the relative TSFC decreases to a minimal value. After which further decrease in the mass flow yields an increase in the relative TSFC as the flow over expands and forces the IPT to tend to a value below unity. Therefore, the limits of the design space and design flexibility are dictated by the volumetric capacity of the ND engine system.

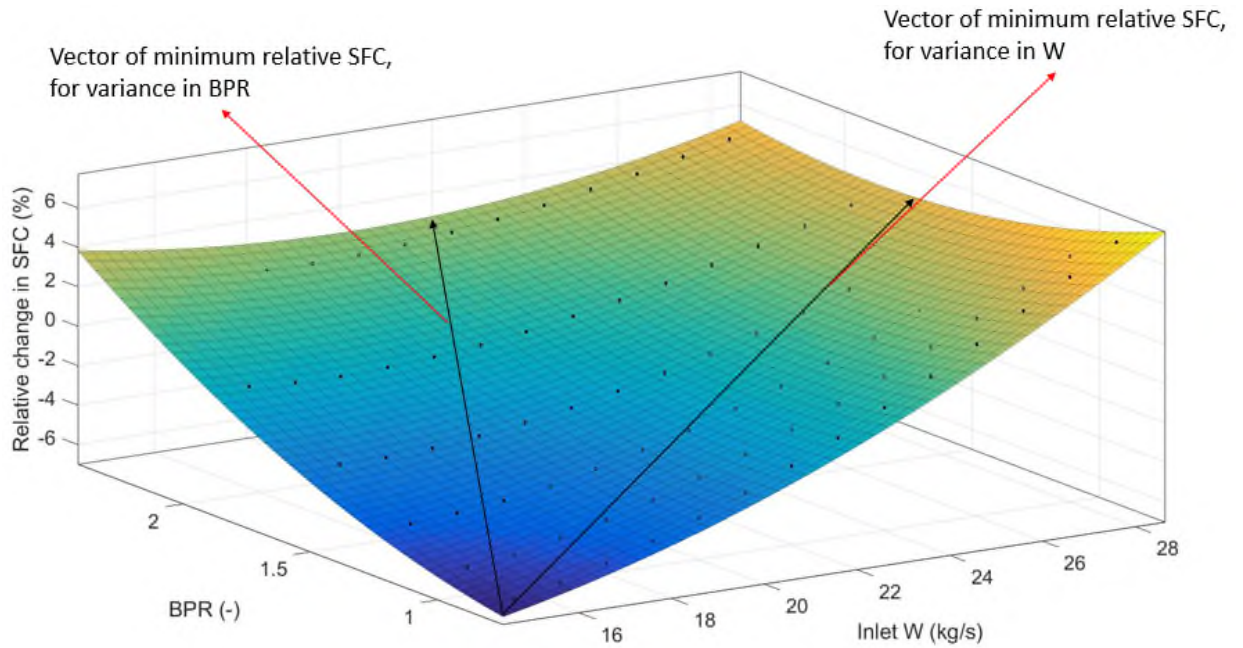


Figure 5- 57: Relative change is TSFC as a function of BPR and mass flow.

Figure 5-58, shows the impact that the BPR and the inlet mass flow has on the relative engine mass. As expected, when the BPR increases and the core mass flow decreases the relative engine mass decreases. The magnitude of the inlet mass flow on the relative engine mass is more severe than the BPR.

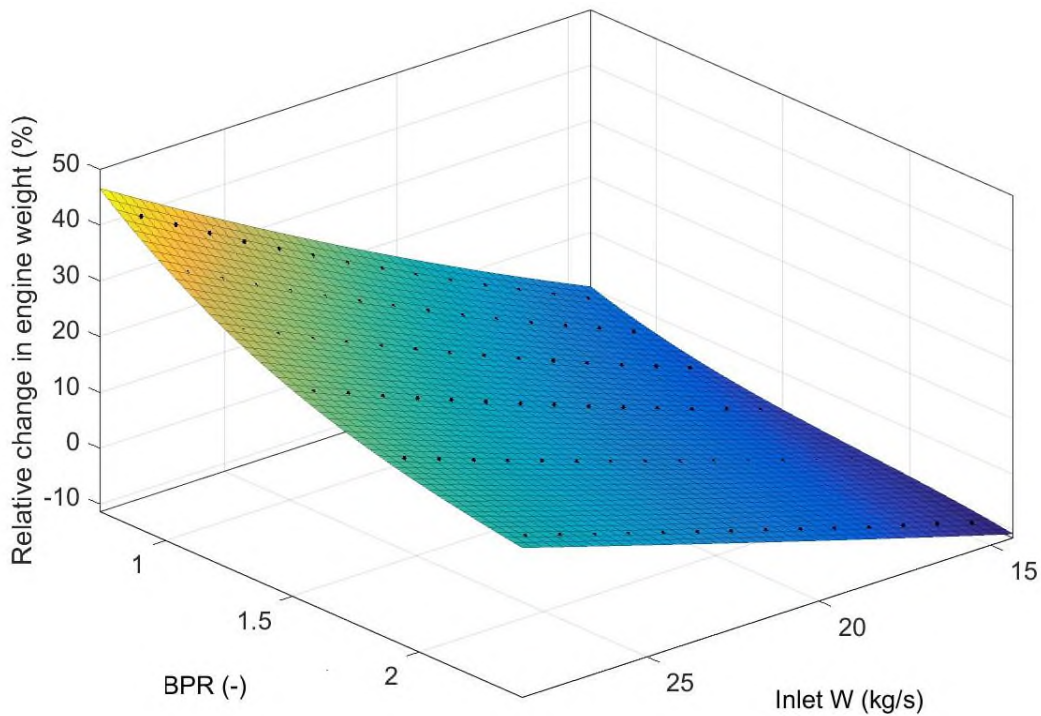


Figure 5- 58: Relative change is weight as a function of BPR and mass flow.

Key design parameters that influence the design of the intercooler are the effectiveness of the cross-flow intercooler and the pressure loss across the tubular banks on the cold side of the intercooler. Figure, 5-59 shows the relative impact that the design point temperature effectiveness and cold side pressure loss has on the relative TSFC of the Y2050 GORND-IP-IC configuration. As the total pressure loss across the intercooler banks increases, the relative TSFC increases as expected. However, as the intercooler effectiveness increases the relative TSFC increases. This seems counterintuitive, however as the effectiveness increases, for a fixed total pressure loss, the temperature of the air entering the ND engine system decreases and the density of the air increases. This in turn causes the swept volume to decrease, for a fixed ND engine system compressor radius, and the percentage of work from the ND engine system to decrease. In addition, the magnitude of variance of the relative TSFC as a function of the intercooler design parameters are not as sensitive compared to the other core design parameters discussed in this section.

The effect of the design point intercooler temperature effectiveness and cold side total pressure loss on the relative engine mass is less than a percentage point, and has not been shown, as the effect is considered to be second order.

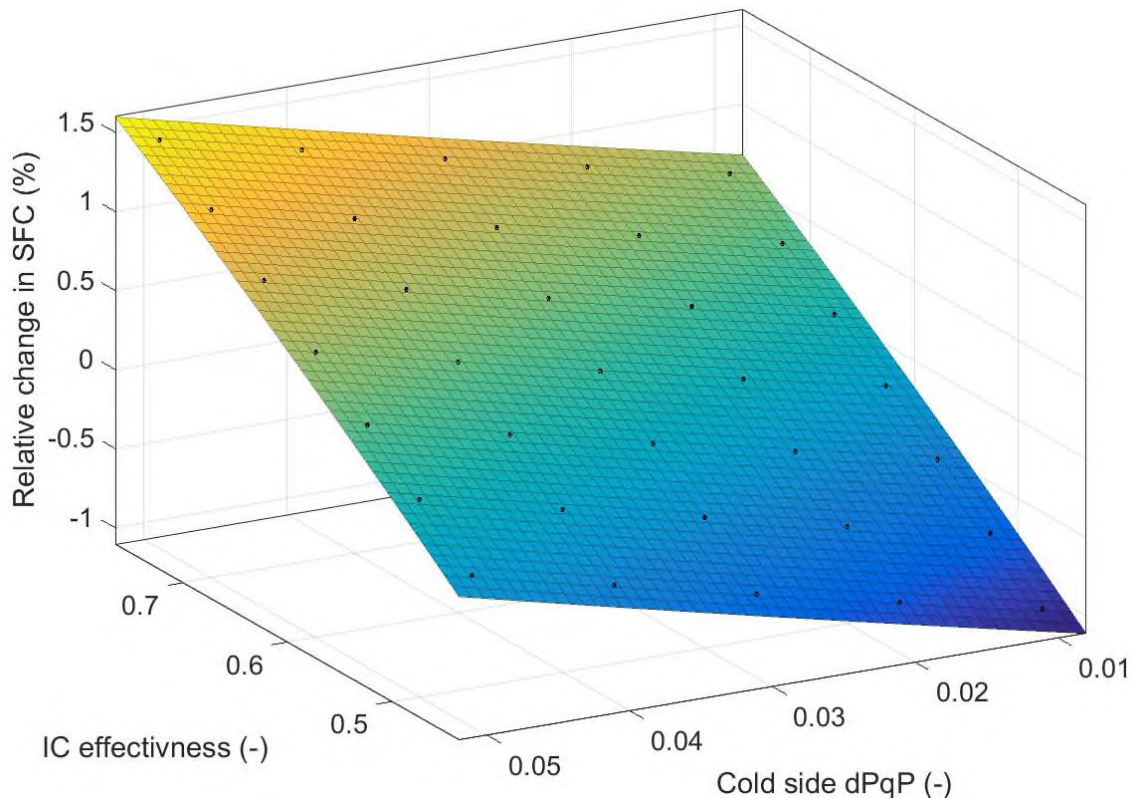


Figure 5- 59: relative change of TOC TSFC as a function of cold side total pressure loss and intercooler effectiveness.

Once the trends related to the core design parameters of the IP-IC-drive configuration, other than that of the ND engine system design parameters have been addressed, the off-design impact of some of the design variables must be considered. Within the IP-IC-drive configuration the most uncertain would be the impact of the IC effectiveness and pressure loss, which have been prescribed.

Figure 5-60, shows the impact that variance in the pressure loss and effectiveness have on the relative TSFC at mid cruise and end of runway conditions. It can be seen that the effect of the effectiveness and total pressure loss, on the relative TSFC, is more significant at EOR conditions.

This can be attributed to the fact that at EOR conditions the inlet mass flow is higher than at cruise. As a consequence, the heat that is transferred from the hot flow stream to the cold flow stream will fluctuate more for the investigated ranges of effectiveness and total pressure losses. The trends illustrated in Figure 5-60, are consistent with those seen in Figure 5-59. However the magnitude of change of the relative TSFC is just over a percentage point, which indicates a second order impact on the relative fuel burn.

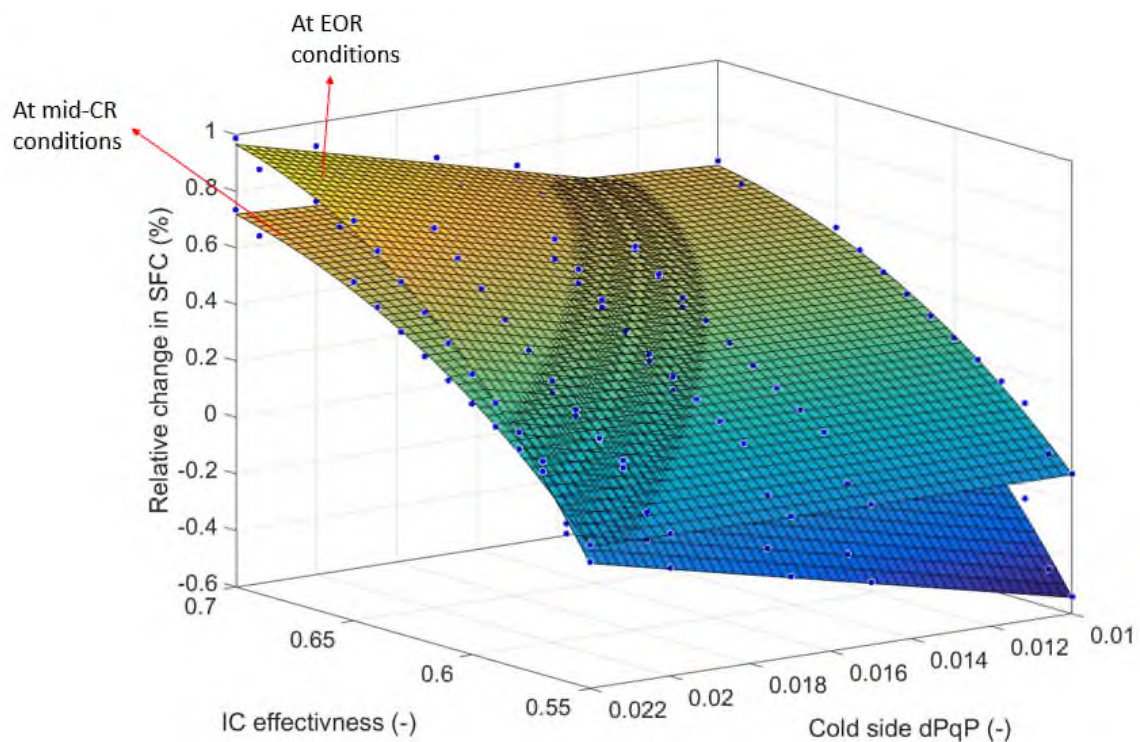


Figure 5- 60: Relative change in the mid-CR and EOR TSFC as a function of the total pressure loss and effectiveness of the IC.

Table 5-29, shows how the Y2050 GOR-ND IP-IC-drive compares with the reference GOR2050 engine configuration and the Y2050 GOR-ND IP-drive configuration at EOR

conditions. Table 5-29 provides a qualitative comparative overview of the magnitude of the NO_x and noise emissions within the LTO envelope.

Table 5- 29: Parameter comparison of three engines at EOR conditions

<u>EOR Conditions</u>				
<u>Property</u>	<u>Units</u>	<u>Reference GOR2050</u>	<u>Y2050 GOR-ND IP- drive</u>	<u>Y2050 GOR-ND IP-IC-drive</u>
Propeller Nmech	(rpm)	400	400	400
Core nozzle exit velocity	(m/s)	210	322	382
CDT (T25)	(K)	911	1057	965
Peak cycle Temperature	(K)	2019	2041	2111

Table 5-29, indicates that the compressor delivery temperature did indeed reduce as a consequence of introducing the intercooler. This will assist in alleviating potential NO_x emissions issues relative to the Y2050 GOR-ND IP-drive configuration, provided combustor residence times are comparable. However, even though the compressor delivery temperature decreased, the peak cycle temperature increased. This occurs, because of increased specific power of the core as a consequence of the introduction of the intercooler. A relatively higher peak cycle temperature, indicates that the average firing temperature in the IP-IC-drive configuration would be higher than that of the IP-drive. This corresponds to potentially relatively higher NO_x emissions relative to the IP-drive. However detailed NO_x assessments in the LTO cycle, are needed to quantify this claim.

When the potential noise emissions in the IP-IC drive are considered, the IP-IC drive would be relatively noisier than the IP-drive as the core exit velocity increased relatively. However detailed noise assessments in the LTO cycle, are needed to quantify this claim.

Based on the qualitative overview of the possible NO_x and noise emissions in the LTO envelope, the peak cycle of the IP-IC drive cycle must be reduced in order for it to be more attractive from a noise and NO_x perspective. Therefore, a secondary combustor is incorporated in to the architecture of the IP-IC drive in order to reduce the peak cycle temperature.

Firstly, the feasibility of a secondary combustor integrated in to the architecture of an IP-drive is considered to see whether the peak cycle temperature can be reduced as well as the core exit velocity (next section) Secondly, the feasibility of intercooling and secondary combustion will be considered (penultimate section of the chapter).

5.7 Performance and mass sensitivities of the Y2050 GOR-ND IP-SC-drive engine configuration

Figure 5-61 indicates the scaled arrangement of a Y2050 GOR-ND IP-SC-drive engine configuration. Similar to the approach taken in determining the performance of the Y2050 GOR-ND IP-drive engine configuration, a targeted optimization of the PROOSIS Y2050 GOR-ND IP-SC drive engine model was created to ensure that the configuration outperformed the reference GOR2050 engine configuration.

The primary design parameters of the IP-SC-drive variant at TOC conditions and their associated ranges that were incorporated in the targeted optimization are outlined in Table 5-23. In addition, the constraints and objectives of the targeted optimization are provided in Table 5-23 (refer to section 5.4). The ranges of the additional design parameters as a result of incorporating the secondary combustion component (SC) are shown in Table 5-30. The bounds of the secondary combustor in terms of its fuel flow is determined by the stability of the model in PROOSIS. The total pressure loss bounds are determined by the accepted range as per [94]. The IPC pressure ratio and inlet mass flow upper and lower bounds were determined based on the last stage blade height limit and the stability of the PROOSIS model. The optimizer settings, were arranged in the same manner as the Y2050 GOR-ND IP-drive and Y2050 GOR-ND IP-IC-drive configurations.

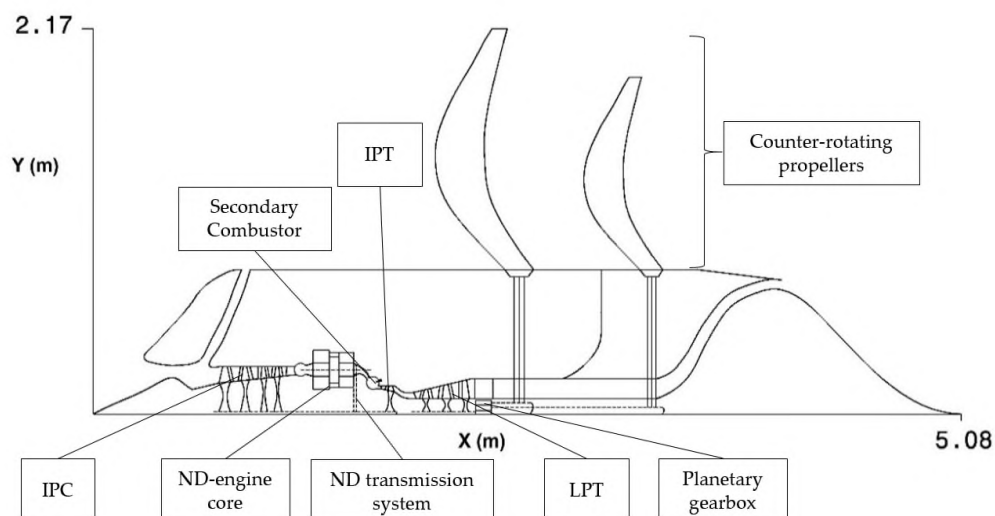


Figure 5- 61: Scaled meridional view of the Y2050 GOR-ND IP-SC-drive engine configuration

Table 5- 30: Y2050 GOR-ND-IP-SC design point parameters for targeted optimization.

<u>Design parameters bounds at TOC</u>			
<u>Property</u>	<u>Units</u>	<u>Lower bound</u>	<u>Upper bound</u>
SC fuel W	(kg/s)	0.001	0.01
SC dpqp	(-)	0.001	0.03
IPC PR	(-)	4.5	7.0
Inlet W	(kg/s)	8	12
<u>Objective: minimize relative FB</u>			

Table 5-31, highlights the performance overview of the Y2050 GOR-ND IP-SC engine configurations. Based on the design selection of the optimizer, it seems that an optimistic engine configuration has been chosen. Similar to the IP-drive engine configuration, the IP-SC-drive configuration reverted back to six nutating disc engine systems, in order to prevent the inlet conditions to the ND engine systems to be sonic. In addition, the peak cycle temperature has been reduced, in comparison to the IP-drive. This showcases the intended effect of reducing peak cycle temperatures within the framework of this configuration. Similar to what was depicted in Figure 5-45, it is possible to expect similar levels of uncertainty with regards to absolute fuel burn values.

The uncertainty of the fuel burn estimate for the 2050 GOR-ND-IP-SC-drive, attributed to each design variable, is provided in Figure 5-62. The secondary fuel flow has the most significant impact on the fuel burn estimate of the engine configuration, as expected. The ranges of the investigated design parameters are consistent with those used in Table 5-30.

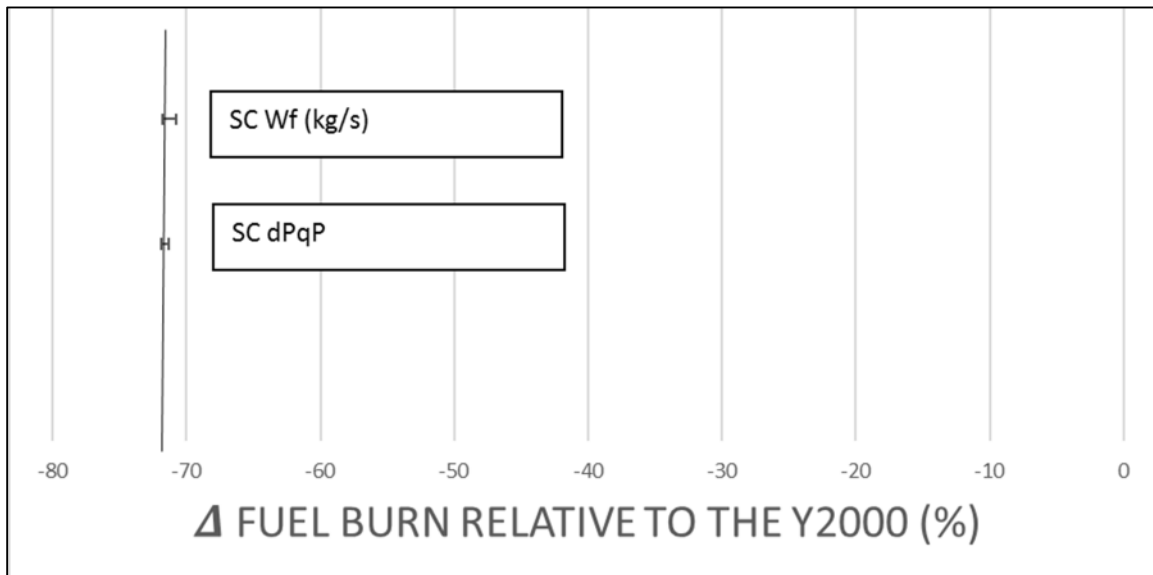


Figure 5- 62: Relative uncertainty of key secondary combustor design variables

Table 5- 31: Performance overview of the Y2050 GOR-ND IP-SC- drive configuration.

<u>Design point TOC</u>		
<u>Property</u>	<u>Units</u>	<u>Y2050 GOR-ND IP-SC-drive</u>
# of ND cores	(-)	6
IPC PR	(-)	6.5
SC Fuel W	(kg/s)	0.008
SC dPqP	(-)	0.02
IPT Nmech	(rpm)	10000
Propeller speed	(rpm)	400
Inlet W	(kg/s)	10.01
LPT PR	(-)	5
Front Propeller diameter	(m)	3.97
ND r23	(-)	0.96
ND accumulator dPqP	(-)	0.05
ND r34	(-)	0.93
ND compressor $\eta_{s,c}$	(-)	0.9
ND expander $\eta_{s,e}$	(-)	0.87
ND compressor r_t	(m)	0.11
ND expander HT	(-)	0.38
ND expander α	(deg)	25
ND expander $f_{ql,cy}$	(-)	0.05
ND expander θ_1	(-)	0.12
ND expander θ_2	(-)	0.87
ND compressor I_f	(-)	1.05

<u>Design point TOC</u>		
<u>Property</u>	<u>Units</u>	<u>Y2050 GOR-ND IP-SC-drive</u>
TOC Fn	(kN)	16.4
ND T06mx	(K)	1544
TOC TSFC	(g/kNs)	7.89
Engine mass	(kg)	3382
<u>Off-design conditions</u>		
CR Fn	(kN)	13.3
CR TSFC	(g/kNs)	7.39
EOR Fn	(kN)	74.7
EOR TSFC	(g/kNs)	4.29
<u>Fuel burn</u>		
Delta FB2050	(%)	-31.2
Delta FB2000	(%)	-71.7

The relationship of TOC TSFC and the engine mass is investigated as a function of the other core design parameters such as the IPC pressure ratio, secondary combustor fuel flow, mass flow and secondary combustor total pressure loss. This was done in order to provide a scale of the significance each design variable has on the potential fuel burn of the engine configuration. Figure 5-63 shows the effect of the relative TSFC as a function of the mass flow and secondary combustor pressure loss.

For a fixed secondary combustor total pressure loss, as the mass flow rate decreases for a fixed TOC thrust level the swept volume decreases, for a fixed ND engine system inlet air density and ND compressor radius. This in turn corresponds to a smaller expander disc and lower ND turbine work. However the ratio of ND-turbine work and IPT turbine work are maintained despite variation in the inlet mass flow. As a consequence of lower turbine work demands from the ND engine system, the firing temperature and fuel flow rates decrease.

This trend continues till a minima in the relative TOC TSFC is reached (~10 kg/s). Further decrease in the core mass flow causes the effects of compressor work to overshadow the

turbine work increment benefits. As expected, as the total pressure loss in the secondary combustor increases the relative TOC TSFC increases. The effect of the aforementioned parameters on the relative mass are not depicted as they follow the expected trends, i.e., as the mass flow and SC total pressure loss (dP_{qP}) decreases the relative mass decreases. The influence of the mass flow on the mass outweighs the influence that the SC pressure loss has on the relative engine mass. The influence of the SC total pressure loss can be considered as second order.

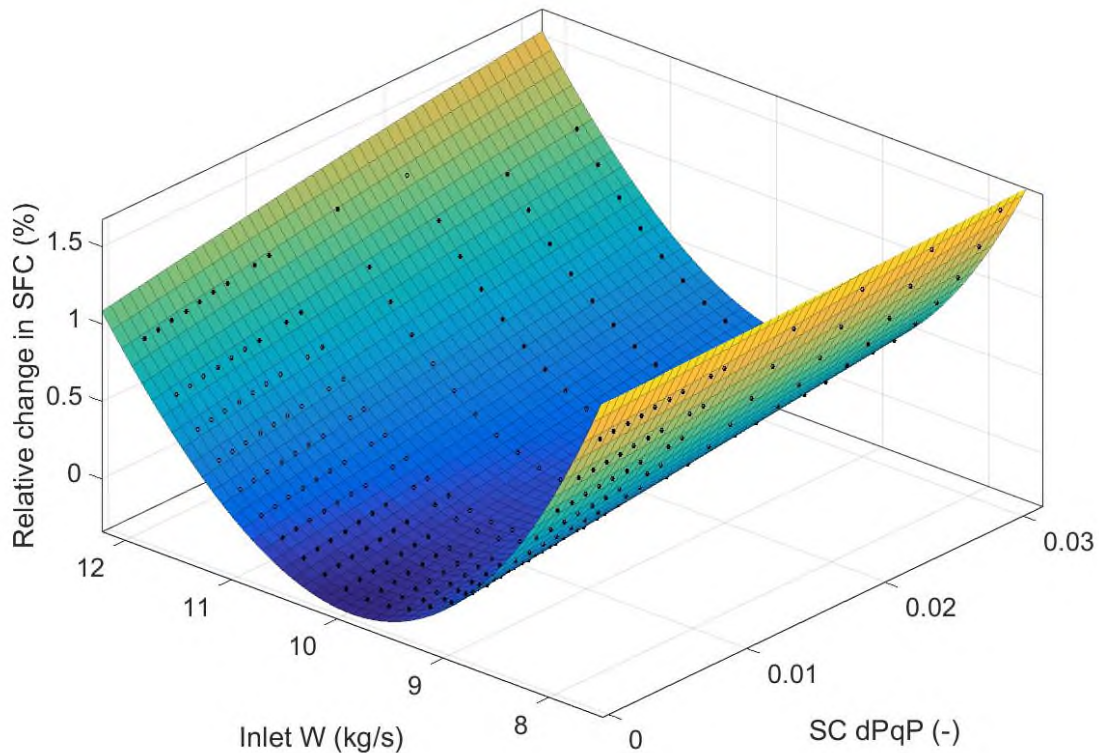


Figure 5- 63: relative change in TOC TSFC as a function of the SC dP_{qP} and inlet mass flow.

Figure 5-64 shows the relative TSFC impact as a function of the mass flow and SC fuel flow at TOC conditions. As the fuel flow increases in the SC chamber the relative TSFC increases because the analysis is considered at a fixed thrust level.

When the fuel flow is fixed, the variance of mass flow exhibits a similar trend as that of Figure 5-63. Another pertinent observation about Figure 5-64, is that the impact of the SC fuel flow has a far larger impact on the relative TSFC as opposed to the inlet mass flow.

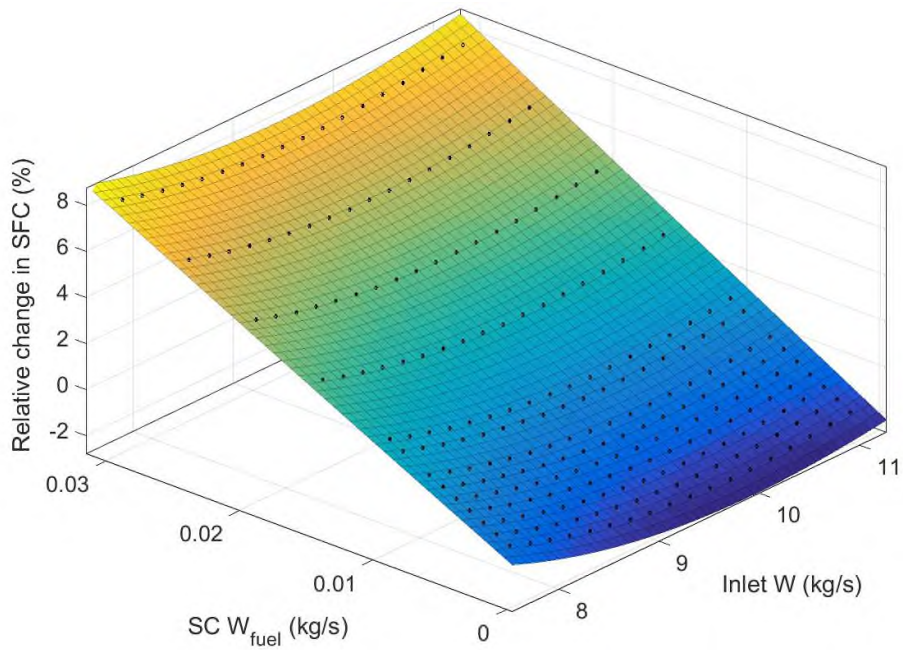


Figure 5- 64: Relative TOC TSFC variation as a function of the SC fuel flow and the inlet mass flow.

Figure 5-65, indicates the variance in the relative engine mass as a function of the SC fuel flow and the inlet mass flow. It can be seen that the as the SC fuel flow increases the relative engine mass increases. This is attributed to the increased IPT pressure ratio, which in turn causes the mass of the IPT component to increase as well as the relative engine mass. It can also be seen that the effect of the inlet mass flow dominates the secondary combustor fuel flow in terms of the relative engine mass.

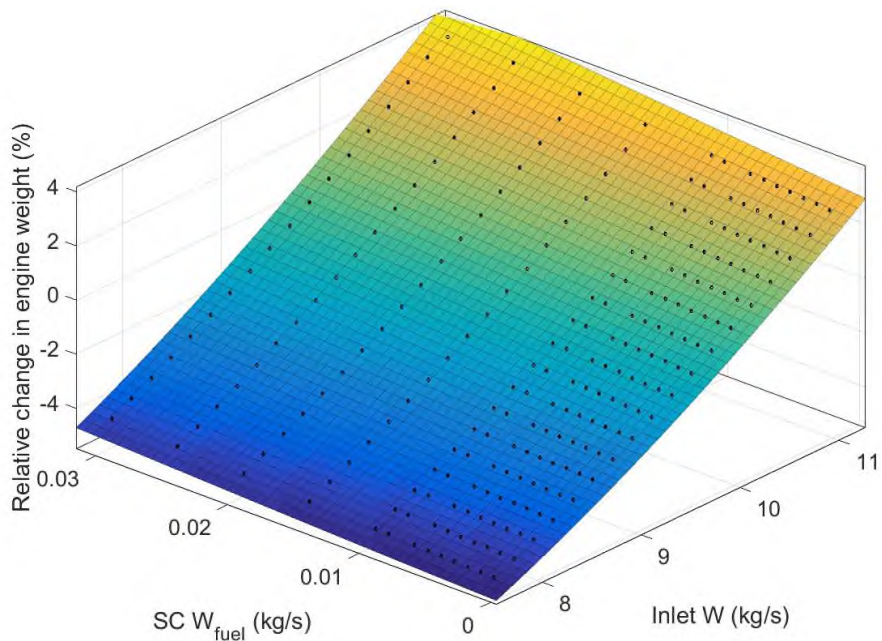


Figure 5- 65: Relative change in engine weight as a function of the inlet mass flow and SC fuel flow.

When one considers the effect of SC fuel flow on the off-design performance of the Y2050 GOR-ND IP-SC configuration, it can be seen that the effect of the relative TSFC change at CR is dominant when compared to that at EOR. This is seen in Figure 5-66. Also, as expected for fixed thrust levels, as the fuel flow increases the relative TSFC increases.

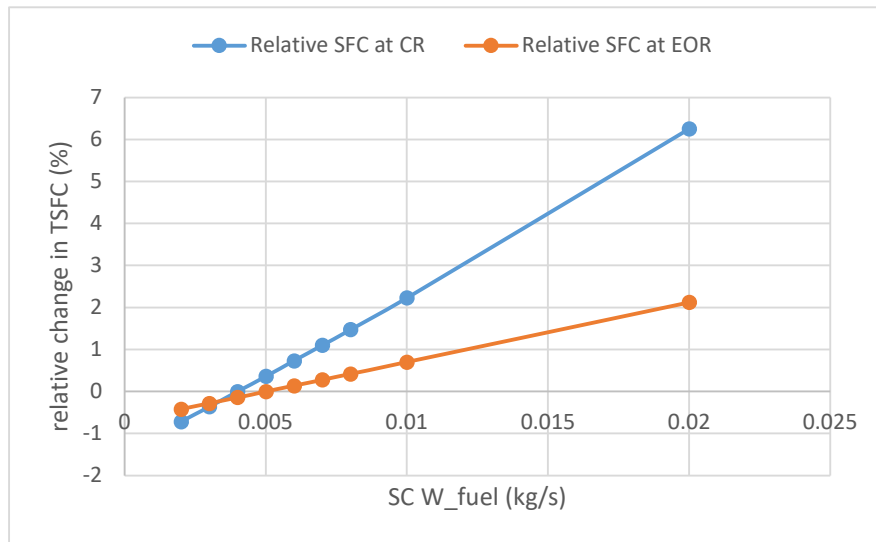


Figure 5- 66: Relative change in TSFC as a function of the SC fuel flow

Table 5-32, depicts the EOR conditions of the Y2050 GOR-ND IP-SC configuration when compared to the reference GOR2050, IP-drive and IP-IC-drive Y2050 GOR-ND engine variants. The peak cycle temperatures have reduced compared to the other configurations. The ND compressor delivery temperature increased considerably, which can be attributed to the optimistic engine configuration chosen by the targeted optimization process. Table 5-32 certainly indicates that the elevated peak cycle temperature inherent to the IP-IC-drive engine variant can be mitigated by the introduction of secondary combustion. In addition, the relative noise signature attributed to the core of the engine would be higher than that of all other engine configurations.

Table 5- 32: Comparative overview of three engine configurations at EOR conditions

<u>EOR Conditions</u>					
<u>Property</u>	<u>Units</u>	<u>Reference GOR2050</u>	<u>Y2050 GOR-ND IP-drive</u>	<u>Y2050 GOR-ND IP-IC-drive</u>	<u>Y2050 GOR-ND IP-SC-drive</u>
Propeller Nmech	(rpm)	400	400	400	400

<u>EOR Conditions</u>					
<u>Property</u>	<u>Units</u>	<u>Reference GOR2050</u>	<u>Y2050 GOR- ND IP-drive</u>	<u>Y2050 GOR- ND IP-IC-drive</u>	<u>Y2050 GOR-ND IP-SC-drive</u>
Core nozzle exit velocity	(m/s)	210	322	382	394
CDT (T25)	(K)	911	1057	965	1075
Peak cycle Temperature	(K)	2019	2041	2111	1965

Based on the outcome of section 5.6 and 5.5, it has become apparent that intercooling reduces the ND compressor delivery temperature and secondary combustion reduces the peak cycle temperatures. Therefore the performance benefits of both technologies utilized in conjunction have been investigated in the following section.

5.8 Performance and mass sensitivities of the Y2050 GOR-ND IP-IC-SC-drive engine configuration

Figure 5-67 indicates the scaled arrangement of a year 2050 GOR-ND IP-IC-SC-drive engine configuration. Similar to the approach taken in determining the performance of the Y2050 GOR-ND IP-drive engine configuration, a targeted optimization of the PROOSIS Y2050 GOR-ND IP-IC-SC-drive engine model was created to ensure that the configuration outperformed the reference GOR2050 engine configuration.

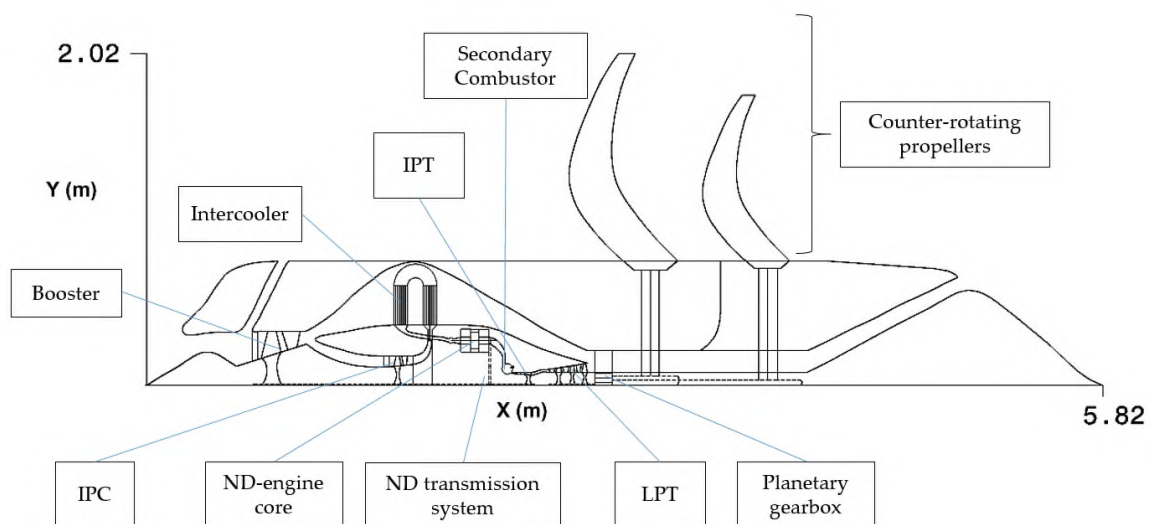


Figure 5- 67: Scaled meridional view of the Y2050 GOR-ND IP-IC-SC-drive engine configuration

The Y2050 GOR-ND IP-IC-SC engine configuration inherits its' design features from the IP-IC-drive and IP-SC-drive respectively. Similar to deriving the performance of the IP-drive, IP-IC-drive and IP-SC-drive engine configurations a targeted optimization is performed on the IP-IC-SC-drive configuration.

The bounds of the design parameters, limits and objectives for the targeted optimization coincide with the values outlined in Table 5-23, Table 5-27 and Table 5-30. The optimization algorithm had the same settings and duration as outlined in sections 5.5 to 5.7.

Table 5-33, provides an overview of the performance of the Y2050 GOR-ND IP-IC-SC-drive engine configuration. It can be seen that the targeted optimization favoured fewer ND engine systems, similar to the IP-IC-drive configuration. In addition, the specific mass of the IP-IC-SC-drive engine configuration is lesser than all the aforementioned engine configurations.

Table 5- 33: Overview of the performance of the Y2050 GOR-ND IP-IC-SC-drive engine configuration

<u>Design point TOC</u>		
<u>Property</u>	<u>Units</u>	<u>Y2050 GOR-ND IP-SC-drive</u>
# of ND cores	(-)	4
IPC PR	(-)	8.5
IC effectiveness	(-)	0.7
Upstream IC dPqP	(-)	0.02
Downstream IC dPqP	(-)	0.02
Hot side IC dPqP	(-)	0.03
Booster PR	(-)	1.63
Cold side IC dPqP	(-)	0.03
BPR	(-)	1.86
SC Fuel W	(kg/s)	0.005
SC dPqP	(-)	0.02
IPT Nmech	(rpm)	15000
Propeller speed	(rpm)	400

<u>Design point TOC</u>		
<u>Property</u>	<u>Units</u>	<u>Y2050 GOR-ND IP-SC-drive</u>
Inlet W	(kg/s)	20
LPT PR	(-)	7.1
Propeller diameter	(m)	3.98
ND r_{23}	(-)	0.95
ND accumulator dPqP	(-)	0.03
ND r_{34}	(-)	0.96
ND compressor $\eta_{s,c}$	(-)	0.89
ND expander $\eta_{s,e}$	(-)	0.81
ND compressor r_t	(m)	0.07
ND expander HT	(-)	0.33
ND expander α	(deg)	25
ND expander $f_{q1,cy}$	(-)	0.05
ND expander θ_1	(-)	0.21
ND expander θ_2	(-)	0.92
ND compressor l_f	(-)	1.01
TOC Fn	(kN)	17.1
ND T06 _{mx}	(K)	1746
TOC TSFC	(g/kNs)	9.44
Engine mass	(kg)	3370
<u>Off-design conditions</u>		
CR Fn	(kN)	13.8
CR TSFC	(g/kNs)	8.99

<u>Design point TOC</u>		
<u>Property</u>	<u>Units</u>	<u>Y2050 GOR-ND IP-SC-drive</u>
EOR Fn	(kN)	77.8
EOR TSFC	(g/kNs)	4.38
<u>Fuel burn</u>		
Delta FB2050	(%)	-14.2
Delta FB2000	(%)	-64.7

Section 5.6 and Section 5.6 have shown the impact of the design core parameters, other than the ND engine system parameters, on the performance of each respective configuration. The relative TOC TSFC and engine mass trends seen in section 5.6 and section 5.7 are comparable, when looking at each technology addition individually.

However, the effects of these complementary technologies in conjunction on the design space has not been shown. Hence, Figure 5-68 shows the relative TOC TSFC variance as a function of the BPR and the secondary combustor fuel flow. The aforementioned design variables were chosen as they had the most significant impact on the relative TOC TSFC in sections 5.6 and 5.7.

As the BPR decreases, the relative TSFC decreases significantly, as relatively higher mass flow is admitted in to the core, the swept volume of the ND engine system increases and the ratio of ND engine system shaft work to IPT work increases. Similarly, as the secondary combustor fuel flow rate increases the relative TSFC increases, primarily due to the analysis being conducted at a fixed thrust. Furthermore, the impact that the BPR has on the relative TSFC is much greater than that of the secondary combustor fuel flow.

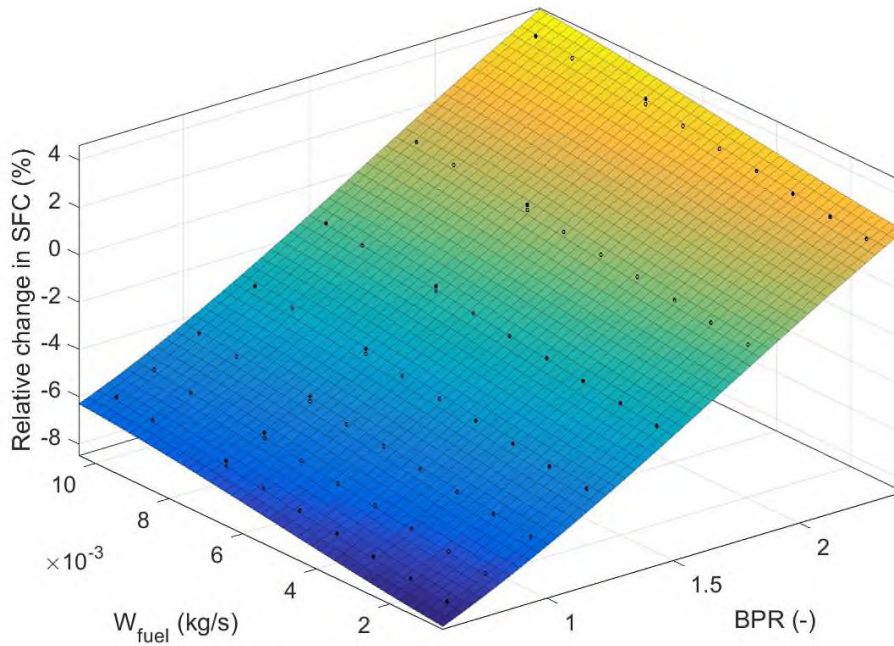


Figure 5- 68: Relative change in TOC TSFC as a function of the SC fuel flow rate and the BPR.

Figure 5-69, shows the relative change in the engine mass as a function of the secondary combustor fuel flow rate and the BPR. As the BPR decreases the relative engine mass increases, as the mass of the ND engine core increases. In addition, as the secondary fuel flow increases the relative engine mass also increases. However, the magnitude of the relative change in engine mass is most significant when the BPR is changed.

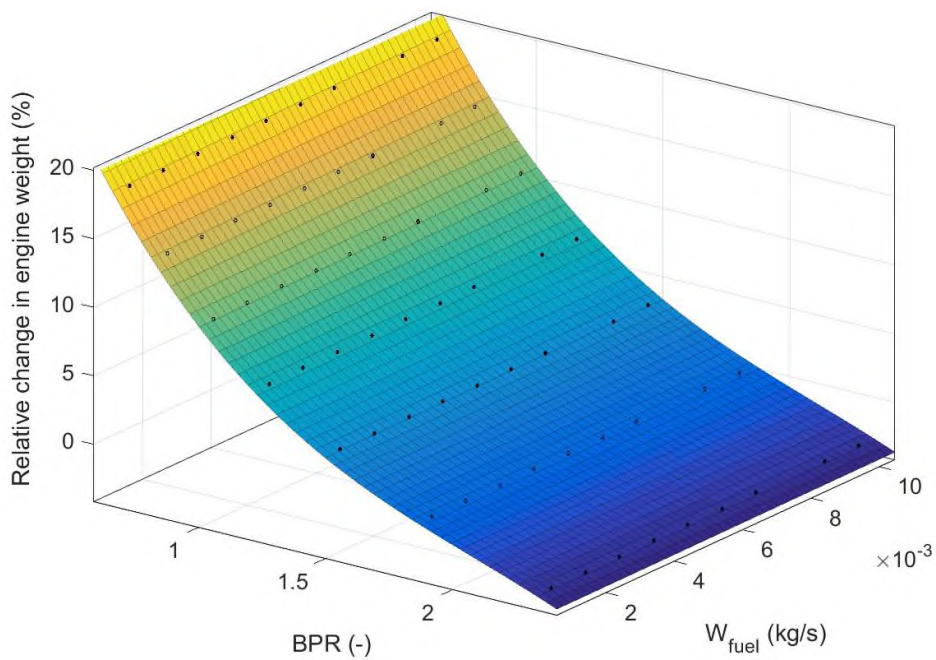


Figure 5- 69: Relative change in engine weight as a function of BPR and secondary fuel flow

Table 5-34, shows how the IP-IC-SC-drive compares to the rest of the engine configurations at EOR conditions. The compressor delivery temperature has reduced relative to the other configurations. However, the nozzle exit velocity has risen considerably therefore the IP-IC-SC-drive noise signature attributed to the core would be considerably worse than the other engines. Bear in mind that the comparisons shown in Table 5-34, are an outcome of a targeted optimization approximation for each configuration. Therefore, the following section will show the fuel burn estimates, CDT, peak cycle temperatures as a consequence of similar technology levels of the ND engine system and associated technologies. In addition, the following section shall provide a possible failure case assessment of the various ND engine system configurations presented.

Table 5- 34: Parameter comparison of four engines at EOR conditions

<u>EOR Conditions</u>						
<u>Property</u>	<u>Units</u>	<u>Reference GOR2050</u>	<u>Y2050 GOR-ND IP- drive</u>	<u>Y2050 GOR- ND IP-IC- drive</u>	<u>Y2050 GOR- ND IP-SC- drive</u>	<u>Y2050 GOR-ND IP-IC-SC- drive</u>
Propeller Nmech	(rpm)	400	400	400	400	400
Core nozzle exit velocity	(m/s)	210	322	382	394	519
CDT (T25)	(K)	911	1057	965	1075	805
Peak cycle Temperature	(K)	2019	2041	2111	1965	2085

5.9 Y2050 GOR-ND configuration overview and quasi-qualitative configuration assessment

Since the targeted optimization, for all the engine configurations provided a more competitive engine configuration for each engine configuration relative to the reference GOR2050 engine, their design parameters and consequently their technology levels are different. Therefore in order to compare like for like, a comparison of all the proposed configurations must be carried out at similar technology levels. Table 5-35, provides an overview of the design parameters used in the comparative analysis of all the proposed configurations. The

thrust levels chosen for this study are the same as that of the reference GOR 2050 configuration.

Table 5- 35: Parameters used in comparative study for Y2050 GOR-ND IP-drive variants

<u>Engine Configurations</u>			<u>Property</u>	<u>Units</u>	<u>Values</u>
Y2050 GOR- ND IP-IC- SC- drive	Y2050 GOR- ND IP-IC-drive	Y2050 GOR- ND IP-drive & Y2050 GOR-ND IP- SC-drive	<u>Design Point TOC</u>		
			# of ND cores	(-)	6
			Compressor PR	(-)	11.05
			IPT Nmech	(rpm)	15000
			Propeller speed	(rpm)	400
			Inlet W	(kg/s)	16
			LPT PR	(-)	3.5
			Propeller diameter	(m)	3.98
			ND r_{23}	(-)	0.9
			ND accumulator dPqP	(-)	0.05
			ND r_{34}	(-)	0.97
			ND compressor $\eta_{s,c}$	(-)	0.9
			ND expander $\eta_{s,e}$	(-)	0.9
			ND expander r_t	(m)	0.102
			ND expander HT	(-)	0.43
			ND expander α	(deg)	25
			ND expander $f_{ql,cy}$	(-)	0.1
			ND expander θ_1	(-)	0.5
ND expander θ_2	(-)	0.5			
ND compressor l_f	(-)	1.13			

<u>Engine Configurations</u>			<u>Property</u>	<u>Units</u>	<u>Values</u>
			TOC Fn	(kN)	17.3
			BPR	(-)	1.00
			IC effectiveness	(-)	0.55
			Cold IC dPqP	(-)	0.03
		SC-drive	SC Fuel W	(kg/s)	0.008
			SC dPqP	(-)	0.02
			SC LHV	(MJ/kg)	43
			<u>Off-design conditions</u>		
			CR Fn	(kN)	13.85
			EOR Fn	(kN)	78.95

An overview of the performance for all the engine configurations mentioned in Table 5-35, are shown in Table 5-36. It can be seen that the IP-drive configuration has the most competitive TSFC and mass, amongst all the configurations.

Comparatively, the IP-IC-SC configuration has the worst performance, however the compressor delivery temperature is markedly lower at EOR conditions in comparison to all the other engine configurations.

Despite, the significant reduction in compressor delivery temperature at EOR conditions the core exhaust velocity outperforms all other configurations considerably. This could potentially lead to a relatively noisier configuration, when compared to the other proposed engine variants. Another notable observations from Table 5-36 are that the IP-IC-drive compressor delivery temperature is lower than that of the IP-drive variant and the peak cycle temperature at TOC for the IP-SC-drive configuration is lesser than the IP-drive configuration. These figures show the relative benefit of using intercooling and secondary combustion, separately, in conjunction with the IP-drive configuration.

Table 5- 36: Performance overview of Y2050 IP-drive derivative configurations

<u>Property</u>	<u>Units</u>	<u>Y2050 GOR-ND IP- drive</u>	<u>Y2050 GOR- ND IP-IC- drive</u>	<u>Y2050 GOR- ND IP-SC- drive</u>	<u>Y2050 GOR- ND IP-IC-SC- drive</u>
<u>TOC</u>					
TSFC	(g/kNs)	12.38	15.63	12.43	16.27
Engine mass	(kg)	3598	4206	3758	4082
Peak cycle Temperature	(K)	1667	2133	1648	1955
<u>CR Conditions</u>					
TSFC	(g/kNs)	11.75	15.00	11.96	15.47
Peak cycle Temperature	(K)	1522	1959	1505	1782
<u>EOR Conditions</u>					
TSFC	(g/kNs)	6.25	6.96	7.07	8.56
Core nozzle exit velocity	(m/s)	325	406	340	575
CDT (T25)	(K)	1216	952	1241	761
Peak cycle Temperature	(K)	1952	2412	1986	2317

In addition to an overview of the performance of all four configurations, Figure 5-70, provides the relative fuel burn benefits of all four engine variants, with similar technology levels, when compared to a comparable year 2000 short range mission. It is apparent from, Figure 5-70, that the most competitive configuration in terms of fuel burn performance is the Y2050 GOR-ND IP-drive. However, in terms of compressor delivery temperature, the most competitive configuration is the Y2050 GOR-ND IP-IC-SC-drive despite its comparatively worse fuel burn performance.

In addition, to estimating the potential feasibility of the four ND engine system variants in terms of relative fuel burn and a qualitative NO_x and noise emissions it is necessary to assess the potential feasibility of the proposed configurations at higher TRL levels. Since the tools to quantitatively assess the feasibility of these configurations have not have not been developed as yet, a quasi-qualitative approach is presented. Variations of the proposed method, to rank the engine configurations, have been historically used on programs such as the B777 and joint strike fighter (JSF) programs to reach the most competitive design by the time the product is released[132].



Figure 5- 70: Overview of the relative fuel burn of all Y2050 GOR-ND IP configurations relative to a year 2000 short range mission

Initially, Table 5-37, quasi-quantitatively ranks the explored configurations at a TRL-1 level. Essentially the relative fuel burn score is assigned to each configuration from 0 to 10, which scales from 0 to 10 depending how close the configurations' relative fuel burn value is to the fuel burn target of -68%. Therefore, if one of the configurations yielded a fuel burn benefit of -68% a relative fuel burn score of 10 would be assigned to the configuration.

If any configuration, reached the target fuel burn value a score of 10 would be assigned as it meets a part of the SRIA target 3 requirement. Conversely if the configuration did not meet the SRIA target a score of zero is assigned.

The metric to determine the NO_x score is based on the relative change of the compressor delivery temperature and peak cycle temperature at EOR conditions to the reference GOR2050 engine cycle. Thus if the average deviation of the compressor delivery

temperature and the peak cycle temperature, relative to the reference GOR2050 engine, is -20% a score of 10 is assigned to the configuration. Likewise, if the average deviation of the compressor delivery temperature and peak cycle temperature is 20% higher than the reference GOR2050 engine a score of zero is assigned.

The choice of $\pm 20\%$ variation of CDT and TET at EOR conditions corresponds to the Trent-1000 series, where a 20% increase in the CDT for all the configurations in the series corresponds to a two fold increase in the Dp/FOO NO_x characteristic. Similarly, the unburned hydrocarbon (UHC) and the carbon-monoxide (CO) score is determined based on the deviation of the peak cycle temperature relative to the reference GOR2050 configuration.

Since the degree of UHC and CO emissions scale inversely with the firing temperature, as per [24], if the relative peak cycle temperature of any of the configurations deviate by -20% a score of zero is assigned, and a score of 10 for a +20% deviation. A $\pm 20\%$ variation of the TET is chosen in order for it to be comparable with the assumptions that determine the NO_x generation score due to increased TET.

Following a format similar to quasi-qualitatively ranking the possible emissions profile, if any of the configurations' relative core jet exit velocity at EOR conditions are 100% greater the score assigned for the noise metric is zero and vice versa for a -100% relative core jet velocity deviation. The choice of $\pm 100\%$ core jet velocity variation corresponds to the observations by Parthasarthy et al., where a 100% increase in the core jet velocity corresponds to a 35 fold increase in core noise intensity.

When the aggregate rank of all the configurations are considered, where each of the contributing scores bear equal significance, the Y2050 GOR-ND IP-IC-SC engine configuration seems to be the most competitive.

If the development, production and certification of the proposed engine configurations are considered past the TRL 1-2 levels a qualitative analysis should be carried out. Table 5-38, highlights the rank of the proposed engine configurations at TRL levels from 3-4, based on a series of criteria. Following which Table 5-39, ranks the proposed engine configurations from TRL levels 4 to production.

Table 5- 37: Y2050 GOR-ND IP-drive variants TRL-1 quasi-qualitative rank overview

<u>TRL level</u>	<u>Property</u>	<u>Y2050 GOR-ND IP-drive</u>	<u>Y2050 GOR-ND IP-IC-drive</u>	<u>Y2050 GOR-ND IP-SC-drive</u>	<u>Y2050 GOR-ND IP-IC-SC-drive</u>
TRL 1-2	Relative Y2000 fuel burn score	7.84	5.60	7.67	5.28
	NO _x score	1.22	2.01	0.68	5.21
	UHC & CO score	4.18	9.86	4.59	8.69
	Noise	2.25	0.33	1.91	0.00
	Aggregate Score	3.10	3.56	2.97	3.84

Within Table 5-38, ranks are associated with criteria that might potentially feature at a TRL 3-4 stage of configuration development. The scores are qualitatively provided based on a scale of 0 to 10, where the most suitable configuration in a particular category scores higher relative to the other configurations. Based on the peak cycle temperatures, of all the configurations, the IP-drive and IP-SC-drive are comparable.

Consequently, the wall temperatures of the combustion chamber and ND expander discs would be relatively less hot than the other two ND engine system variants. Therefore due to the relatively lower metal temperature of the ND-expander disc, in the IP-drive and IP-SC-drive, the configurations are ranked higher than the intercooled engine variants.

The product unit cost is generally estimated at a TRL of 3-4, and the rank of each engine configuration has been associated with the complexity of the technology being introduced to the engine configuration. For example, relative to the reference GOR2050 engine a discontinuous flow ND-core replaces the HP system in a IP-drive engine configuration, therefore a score of 5 was given. In the case of the IP-IC-drive due to the complexity involved in splitting the core flow and introduction of an axi-centrifugal compressor a score of 4 was given.

An IP-SC-drive engine is deemed to be relatively more expensive than the IP-drive due to the complexity of incorporating a recirculating-flow combustor and its associated control systems.

Finally, due to the incorporation of intercooling and secondary combustion technologies in the IP-IC-SC –drive configuration it has been assigned the least score. When engine component cooling is concerned, the complexity and power demands of the cooling temperature scale with the peak cycle temperature at EOR conditions, hence the scores assigned for the same. Typically the rapidness of transient responses of gas turbine engine components, primarily depends on the inertia of the components, which is affected by the volume and mass of the associated turbomachinery[32].

If the same argument were extended to the ND-disc engine systems of the engine configurations investigated, the IP-SC-drive would be relatively the most responsive to transient operation, as it relatively has the smallest core, followed by the IP-drive, IP-IC-drive and the IP-IC-SC-drive. The scores allocated for transient operational control reflect the relative difference between the configurations.

All the configurations have the same arrangement of gearboxes, however if we assume that the complexity of the lubricating system, and hence reliability, scales with the torque ratio of these gear trains investigated then it is possible to assign relative scores for each configurations. As a consequence of the innate complexity of having various torque transmission paths per configuration, the configuration with the lowest torque ratio was assigned a score of 5.

As the torque ratio increases, the configurations are ranked accordingly from 4 to 1. For the life limited part criteria, scores were assigned based on the peak cycle temperature at EOR and the number of potential parts added to the component. In this category, both IP-IC-drive and IP-IC-SC-drive variants scored poorly because of the high peak cycle temperature and the possibility of foreign object damage to the intercooler as well as ice accretion on the intercooler during altitude re-light conditions.

The IP-SC-drive scored the second best relatively as the added combustion temperature means that the IPT turbines would be subject to creep borne failures relatively more quickly than the IP-drive. The aggregate score for TRL 3-4 comparison of engines, assumes that all the categories are of equal importance.

Table 5- 38: Y2050 GOR-ND IP-drive variants TRL 3-4 quasi-qualitative rank overview

<u>TRL level</u>	<u>Property</u>	<u>Y2050 GOR-ND IP-drive</u>	<u>Y2050 GOR-ND IP-IC-drive</u>	<u>Y2050 GOR-ND IP-SC-drive</u>	<u>Y2050 GOR-ND IP-IC-SC-drive</u>
TRL 3-4	Material limitations	5	3	5	4
	Product unit cost	5	3	4	2
	Engine cooling	5	2	4	2
	transient control	6	5	7	4
	Gearbox reliability	2	5	3	4
	Life limited parts	5	2	4	2
	Aggregate Score	4.67	3.33	4.50	3.00

When the task of maturing the engine configurations, past TRL-4 and in to production is considered a qualitative ranking system has been applied to potential categories of interest, where the configurations are ranked from 0 to 10 based on the potential of each configuration. Table 5-39, outlines the categories that have been allocated for the quasi-qualitative rank of each of the investigated engine configurations. For most categories, most scores are uniform for all configurations as detailed knowledge of the potential engines operability is not known at this stage.

However, it is possible to qualitatively assume that the installation complexity, operational availability, mean time to failure, survivability of 120% over speed test, complexity of maintenance procedures and the degree of retooling required generally scales with the number of parts in an engine configuration. Therefore, the scores for these categories per engine configuration reflect the same. Besides, the aforementioned categories it is possible to hypothesize that the intercooled engine configurations will be relatively less susceptible to ingest birds and any other foreign objects in to the core turbomachinery, therefore they score

higher in that particular category. Once again the aggregate score, assumes that all the categories bear equal importance in the qualitative assessment.

Table 5- 39: Y2050 GOR-ND IP-drive variants TRL 4-production quasi-qualitative rank overview

<u>TRL level</u>	<u>Property</u>	<u>Y2050 GOR-ND IP-drive</u>	<u>Y2050 GOR-ND IP- IC-drive</u>	<u>Y2050 GOR-ND IP-SC-drive</u>	<u>Y2050 GOR-ND IP- IC-SC-drive</u>
TRL4- Production	Installation Complexity	4	3	2	1
	Operational Availability	4	3	3	2
	MTBF (mean time to failure)	4	2	3	2
	Degree of retooling for manufacturing	3	2.5	2	1
	Severity of new certification policies	3	3	3	3
	Complexity of maintenance procedures	3	2	2	1
	Fire Prevention	2	2	2	2
	Blade-Off containment	3	3	3	3
	Accessory reliability	4	4	4	4

<u>TRL level</u>	<u>Property</u>	<u>Y2050 GOR-ND IP-drive</u>	<u>Y2050 GOR-ND IP- IC-drive</u>	<u>Y2050 GOR-ND IP-SC-drive</u>	<u>Y2050 GOR-ND IP- IC-SC-drive</u>
	Survivability of 120% over speed test	4	3	3	2
	Control system reliability	5	5	5	5
	Bird/Hail ingestion	3	6	3	6
	Altitude relight	5	5	5	5
	Ice Ingestion	4	4	4	4
	Aggregate Score	3.64	3.39	3.14	2.93

Once a quasi-qualitative overview of the proposed engine configurations are performed, for TRL-1 to production, a weighted rank is presented in Figure 5-71 to show the relative competitiveness of each engine configuration. The weighting for TRL 1-2 is assigned at 50%, TRL 3-4 is assigned at 35% and the last category at 15%.

They weightings were chosen on the degree of quantitative certainty could be applied to each stage of concept development. In reality, the bias in the qualitative portion of the aforementioned study should be balanced by regularly updating the values amongst various members of the engineering, management and marketing teams of a potential engine concept development team.

In addition, quantitative scores and further categories should be updated and added to the analysis as and when they become available during the development of these engine concepts.

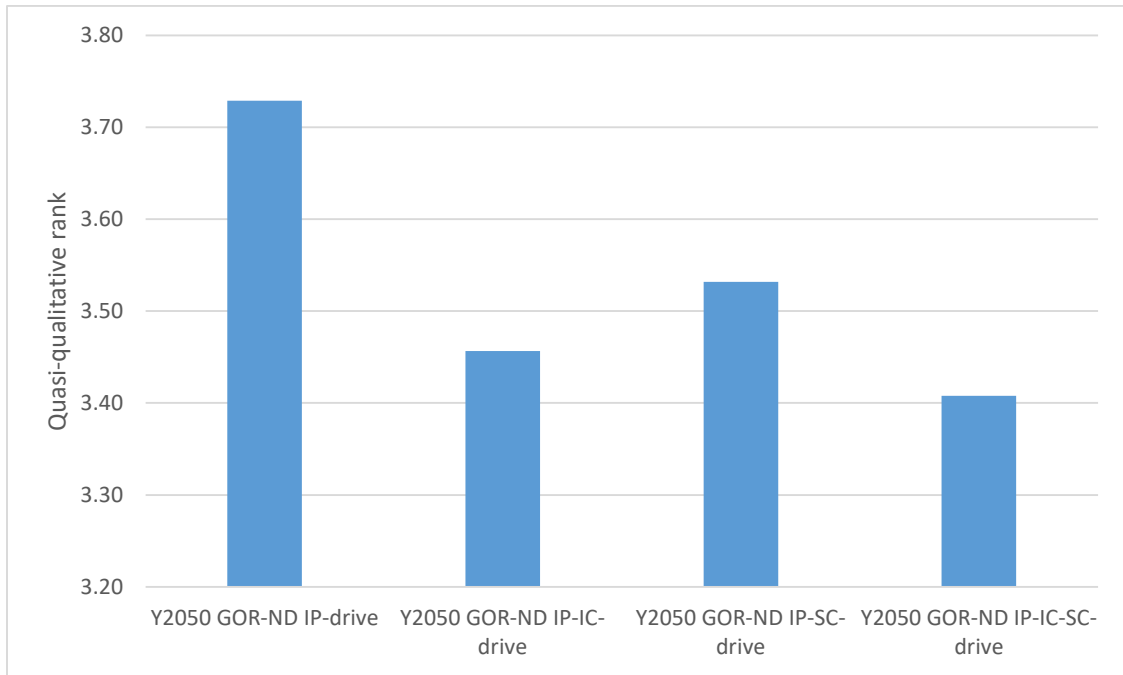


Figure 5- 71: Quasi-qualitative rank for all configurations

Based on a quasi-qualitative overview, it seems that the Y2050 GOR-ND IP-drive seems to be the most competitive in terms of the overall concept to production feasibility. This outlook, is subject to change depending on the degree of quantitative proof allowed for as the research and development of these engine configurations progresses.

6 Conclusions

Ever increasing environmental concern has provided a strong precedent to accelerate innovation, in all fields of the transportation sector, to stem the tide of increasing greenhouse gas emissions. In particular the aviation sector has set out strategic goals for the year 2050, to significantly curb harmful emissions. These goals are outlined in the strategic research and innovation agenda. One of these goals call for innovative technologies that will help reduce energy consumption, NO_x and noise emissions significantly by the year 2050.

Based on these goals, the work focused on addressing the reduction of energy consumption in the aviation sector by 75%, when compared to year 2000 levels. The reduction of energy consumption is analogous to reduction of the consumption of fuel during all phases of flight. In the aviation sector the prominent ways of reducing fuel consumption is to have more efficient flight path trajectories and air traffic control, lighter and low drag aircraft and more efficient propulsion systems. The impact of the benefits of flight path optimization are not considered within the scope of this work. Therefore, the fuel consumption reduction target attributed to advances in the aircraft and the engine development, for a fixed mission range, is 68%[7]. This work focused on deriving efficient civil aero-engines that would meet the 68% fuel burn reduction goal, while combusting Jet-A fuel.

In order to reduce fuel consumption it is necessary to increase the overall efficiency of an aero-engine. The overall efficiency is the product of the propulsive and thermal efficiency of an aero-engine configuration.

Historically, propulsive efficiency has been improved by increasing BPRs and reducing fan pressure ratios to reduce bypass exit velocities. However, the weight and drag penalty incurred by increasing BPRs of ducted turbofans cause diminishing returns in the case of fuel burn reduction. A technology that circumvents the associated drag and weight penalties is the geared open rotor. Therefore, it was chosen as the primary propulsive technology enabler to address the 68% fuel burn target.

The thermal efficiency has been improved by increasing OPRs and TETs of high bypass ratio turbofans within the civil aero-engine sector, which has largely been possible due to the advancement of durable high temperature materials. However, the scale effects of over tip leakage due to increased OPRs and current limitations of materials that enable higher TETs cause diminishing returns in terms of fuel burn reduction. Gleaning from the lessons learnt from the land based gas turbine power generation sector, it is beneficial to combine the Brayton cycle with other potential cycle variants in order to increase the overall thermal efficiency. A Brayton cycle coupled with an Otto type cycle theoretically offers the highest

relative thermal efficiency benefit, followed closely by intercooled and re-heated combinations of the Brayton cycle.

A technology enabler that allows for a Brayton-Otto combined cycle in aero-engine applications is the nutating disc engine system. The nutating disc engine system is a compact internal combustion engine that has a high working volume to overall volume ratio, when compared to 4-stroke or 2-stroke piston engines. As a consequence of its efficient spatial utility, and attractive power density, it was chosen as the primary technology enabler to improve thermal efficiency.

In the reviewed literature, to date, the performance of the nutating disc system has been described by Korakianitis et al. The methodology proposed, includes a thermodynamic model of the nutating disc engine system. However, this methodology does not provide a sizing methodology for the nutating disc engine system. It is critical to estimate the size of the nutating disc engine system as it has a direct impact on the allowed performance of the device. **Therefore, the primary contribution to knowledge of this work was to derive a preliminary sizing methodology for the nutating disc engine system.**

Primarily the performance of the nutating disc engine system was benchmarked against performance estimates, put forth by Korikianitis et al., and it was seen that the trends matched those produced in literature. Then, the validity of the proposed sizing methodology was demonstrated by calibrating the performance and size estimates against what was available in the public domain. The proposed methodology showed good confluence with public domain estimates. This method was further corroborated independently with a CAD study, which showed confidence in the method. The process of sizing the ND system is a computationally tedious process (as seen in section 4.3). Therefore, a curve fitted correlation was derived that predicts the size of a nutating disc engine system as a function of its defining design variables. This allows for robust preliminary design space exploration. The nutating disc engine system sizing methodology allowed for estimating the relative fuel burn benefits achieved when it is integrated within the core of a geared open rotor.

In order to meet the ambitious fuel burn target of 68% relative fuel burn by the year 2050 it was necessary to first determine whether an un-ducted geared open rotor would meet the fuel burn target by 2050. A final reference GOR 2050 engine configuration (presented in section 5.2) is integrated with a year 2050 short range aircraft and the relative fuel burn benefit from doing so indicated a 58.9% benefit compared to a year 2000 baseline engine, where the ratio of FB benefit attributed to the airframe and propulsor, respectively is roughly 1:1. The baseline engine was based on a typical high bypass turbofan engine for a conventional short/medium range aircraft (CFM56-5b).

In addition to presenting the 2050 reference engine design configuration, a parametric analysis with regards to the LP-system of the reference GOR2050 was conducted. This was done to identify the variables that had the greatest impact on fuel burn and whether it was possible to meet the 68% fuel burn target. The analysis indicated that the propeller operating speed and front propeller diameter had the strongest influence on fuel burn. Based on the outcome of the parametric study, it was opined that further improvements to the primary propulsive efficiency technology enabler are unlikely to bridge the gap to the 2050 fuel burn target (section 5.2.4). This therefore, led to the consideration and feasibility assessment of achieving this target through the integration of a nutating disc system within the core of the GOR2050 configuration.

In order to integrate the nutating disc engine system within the GOR2050 configuration, it was decided to remove the HP spool components (HPC, combustor and HPT). In lieu of the HP spool components a series of nutating disc engine systems were circumferentially distributed around the centre line of the engine. They were aerodynamically coupled with the IPC, fore of the ND engine system array, and the IPT which is located aft of the ND engine system array. An investigation was conducted on whether it would be beneficial to couple the excess shaft power generated by the ND engine system arrays with an IP shaft or a LP shaft. In terms of relative specific fuel consumption at top of climb and configuration complexity, it was determined that it was more beneficial to mechanically couple the ND arrays to the IP-shaft with a spur gear transmission (section 5.4). This configuration was coined as the IP-drive configuration.

In order to determine whether the IP-drive would outperform the reference GOR2050 configuration, in terms of fuel burn, a targeted optimization of the configuration was performed. It is termed as a targeted optimization because the design constraints in terms of acceptable technology limits for the nutating disc engine system and the associated turbomachinery are not defined at this stage. The design constraints (aerodynamic, mechanical and vibrational) are ideally derived from detailed design analyses of the nutating disc engine system and the coupled turbomachinery. Therefore, due to the uncertainty associated with these design constraints, a targeted optimization was undertaken to ascertain whether the IP-drive could outperform the GOR2050 in terms of fuel burn.

The IP-drive engine performance, as an outcome of a preliminary optimization, burnt 9.4% less fuel than the reference 2050 GOR engine. A sensitivity study with regards to the design variables of the ND engine system was subsequently conducted, in order to highlight the uncertainty the design choices had on the overall performance of the IP-drive engine. In terms of TSFC, the ND engine system design variables that had the most significant impact

on the TSFC are the accumulator expansion ratio, pre-combustor expansion ratio, heat loss through the combustion chamber wall and ratio of constant volume to constant pressure combustion. In terms of engine mass estimation, the ND engine system design variables that had the most significant impact is the tip radius of the nutating disc compressor. In terms of relative mission fuel burn, the heat loss factor and the ratio of constant volume combustion to constant pressure combustion had the most significant impact. To highlight the variance in possible relative fuel burn estimates, derived from the inclusion of an ND engine system, the relative fuel burn estimates of a pessimistic and optimistic IP-drive engine configuration were derived. It was seen that the possible variance in relative fuel burn, relative to the Y2000, varied from 37% benefit in the pessimistic design case and 74% in the optimistic design case (section 5.5). This clearly shows that there is still a lot of work to be done, when it comes to understanding the underlying design constraints of the ND engine system cycle. This will be discussed in the future work section (Chapter 7).

An interesting observation, from the nominal IP-drive configuration, indicates that compressor delivery temperature at EOR conditions are higher than the reference GOR2050 engine configuration, due to a higher relative OPR. Since high compressor delivery temperature could have an adverse impact on NO_x emissions the impact of including an intercooler in to the architecture of the IP-drive was then investigated. The quantification of the fuel burn benefit and subsequent uncertainty associated with an intercooled configuration of the IP-drive is one of the novelties of this work and is considered a further expansion to existing knowledge (section 5.6).

Similar to the IP-drive, a targeted optimization was conducted in order ensure that Y2050 IP-IC-drive configuration outperformed the reference GOR2050 relative mission fuel burn estimates. The nominal IP-IC-drive configuration burnt 11.6% less fuel than a reference GOR2050 engine, as a result of the targeted optimization. In addition, to providing the targeted performance estimates of the IP-IC-drive the sensitivity of varying the additional design variables, in terms of design point TSFC and engine mass, were investigated. It was seen that the BPR, inlet mass flow and magnitude of the booster and axi-centrifugal pressure ratio had the most significant impact on the TSFC and the overall engine mass. The EOR performance of the nominal IP-IC-drive indicated that the compressor delivery temperature reduced in comparison to the IP-drive variant. However, the peak cycle temperature increased significantly due to increased specific power demands imposed by splitting the core flow. Therefore, in order to alleviate the peak cycle temperature seen in the IP-IC-drive a secondary combustor was included within the architecture of the IP-drive, in the first instance. The quantification of the relative fuel burn benefit and subsequent uncertainty

associated with a re-heated configuration of the IP-drive is considered as an additional novelty of this work, and expands existing knowledge.

Similar to the nominal IP-drive, a preliminary design assessment was conducted on the IP-SC-drive configuration and optimized to ensure that it outperformed the reference GOR2050 fuel burn estimates. The IP-SC-drive configuration burnt 31.2% less fuel than a reference GOR2050 engine. In addition, to providing the preliminary performance of the IP-SC-drive the sensitivity of varying the additional design variables, in terms of design point TSFC and engine mass, were also investigated. It was seen that the inlet mass flow and secondary combustor fuel flow had the most significant impact on the TSFC and the engine mass. The EOR performance of the IP-SC-drive indicated that the peak cycle temperature reduced in comparison to the IP-IC drive variant. However it was seen that the compressor delivery temperature, increased relative to the IP-IC-drive configuration. Therefore, a GOR engine architecture consisting of a ND system, intercooling and secondary combustion technologies were investigated (see section 5.7). The quantification of the fuel burn benefit and subsequent uncertainty associated with an intercooled, re-heated, nutating disc system within a geared open rotor configuration is one of the novelties of this work and is considered a further contribution to existing knowledge.

The nominal IP-IC-SC-drive configuration burnt 14.2% less fuel than a reference GOR2050 engine, as a result of the targeted optimization. The effects of secondary combustor fuel flow and the intercooler bypass ratio on the TSFC and engine mass were demonstrated. An increasing BPR and secondary combustor fuel flow, for a fixed thrust level, favoured an increased relative design point TSFC. However, an increased BPR favoured a reduced relative overall engine mass and an increased secondary fuel flow resulted in an increased overall engine mass. At EOR conditions, it was seen that the compressor delivery temperature was reduced in comparison to the four other investigated engine variants (see section 5.8). In addition, the peak cycle temperature was lesser than the IP-IC drive configuration.

The primary purpose of the previous analyses for the IP-drive, IP-IC-drive, IP-SC drive and IP-IC-SC-drive engine configurations was to highlight a design that outperformed the reference GOR2050 engine. Additionally it was also used to demonstrate the relative influence of the core design variables and demonstrate the uncertainty associated with relative fuel burn estimates. In addition, a comparative study was performed to highlight the potential fuel-burn benefits that all the IP-drive configurations possessed with a common design thrust level and technology levels.

Relatively, the most fuel-burn efficient configuration was deemed to be the IP-drive configuration and the least fuel-burn efficient engine configuration was the IP-IC-SC-drive configuration. The lower fuel burn in the IP-drive is attributed to the relatively lower mass and the lower fuel to air ratio. However, the compressor delivery temperature, at EOR conditions, in the IP-IC-SC-drive configuration was reduced by ~40%, which helps reduce the relative NO_x emissions, life and potential cost.

In addition, to estimating the potential fuel-burn benefits a quasi-qualitative analysis was performed in order to determine which of the investigated configurations would be the most feasible to reach production. Based on the analyses, it was deemed that the most likely would be the IP-drive configuration.

The details of the work that should be done to extend this work beyond state of the art are described in the following section. The roadmap of the work that needs to be done to advance knowledge with regards to the nutating disc engine system is another novel aspect of this study.

7 Future Work

The further work involved in determining the feasibility of integrating nutating disc engine system topping cycles in aero engines, at a TRL 1-2 level, can be segmented in to two distinct sections, namely:

- Further work regarding the nutating disc engine system
- Further work regarding preliminary design assessment

7.1 Further work regarding the nutating disc core

The work done in estimating the performance and size of the nutating disc engine system, so far, entails a preliminary design approach. The multiplicative effect of uncertainty in the possible benefits that the ND engine system has in a Y2050 GOR engine, for short range aircraft, is illustrated most clearly in Figure 5-45. Where the possible relative fuel burn benefit for a Y2050 GOR-ND IP-drive-Y2050 short range aircraft configuration, just by varying the ND design parameters, results in a Y2000 relative fuel burn benefits ranging from -36% to 74%. The wide variance, in the relative fuel burn values, indicates that a better understanding of the interdependency of the key design parameters coupled with the limits of the core ND engine system design parameters is necessary.

The approach used in this dissertation, is one of a bottom-up approach in understanding the possible performance of the ND engine system. Where, sensitivity studies are performed on the low order proposed performance and sizing models and consequently claim relative potential fuel burn benefits for a fixed mission range, when incorporated in to the architecture of an aero-engine. However, if the concept is to be advanced to a higher TRL a top-down approach coupled with concurrent engineering principles must be applied.

Therefore, an outline will be provided to set-up an experimental rig, define higher order models which will be calibrated to the experimental set-up and finally define reduced order models that incorporate the performance limits of the ND engine system at a preliminary design stage.

Once, the realistic performance of the ND engine system can be accounted for at a preliminary design stage, optimizations can be carried out to determine the actual potential design space of a 2050 engine configuration. The following sub sections present the top-down research initiatives for the ND compressor module, accumulator module, pre-combustion chamber module and expander module respectively.

7.1.1 Compressor module

The design variables, as per the methodology showcased in Chapter 4, that directly influence the performance of the nutating disc compressor are the volumetric efficiency, isentropic compression efficiency and the volumetric compression ratio.

Figure 7-2, showcases a potential experimental arrangement that would assist in quantifying the range of the aforementioned values during operation. In addition, Figure 7-1, shows the equipment included in the potential experimental set-up.

Bill of materials									
Number	Item	Number	Item	Number	Item	Number	Item	Number	Item
1	Flow straightening hexagonal array	6	axially adjustable test stand rack	11	Oil scavenge tubes	16	oil feeder thermocouple	21	Data transmission lines
2	Inlet Pitot tube and total temperature probe rakes	7	Circumferential Scheleirn camera	12	Oil feeder tubes	17	oil scavenge thermocouple	22	ND inlet wedge
3	Clear case ND compressor housing	8	test stand	13	Bearing housing	18	oil flow meter	23	ND compressor delivery port and solenoid controlled valve
4	ND Z-shaft	9	oil tank	14	internal nuating disc structure	19	Roller and axial bearings	24	axial Schelirin camera
5	Outlet Pitot tube and total temperature probe rakes	10	oil scavenge pump	15	centrifugal oil pump	20	Power lines	25	Power management unit

Figure 7- 1: preliminary bill of materials for the ND compressor rig

Essentially, the ND compressor module (3) would be placed on the adjustable racks (6) and attached to an induction motor. The motor would drive the ND compressor disc to either volumetrically compress naturally aspirated air or pre-compressed air, coming through a hexagonal array flow straightener (1), and port the compressed air through solenoid controlled valves, located on the compressor deliver port (23).

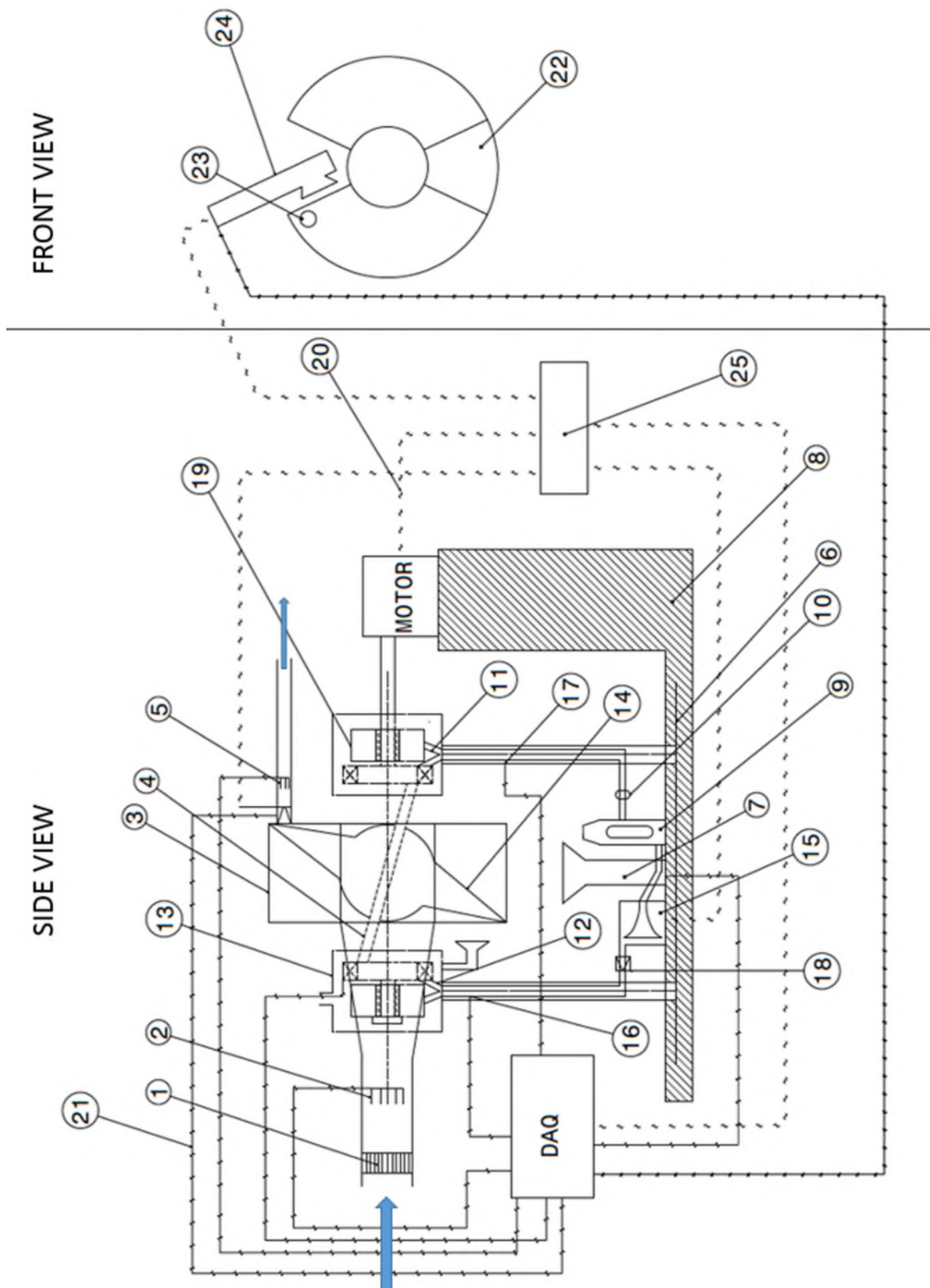


Figure 7- 2: Potential experimental arrangement for the ND compressor module

Based on the apparatus proposed in Figure 7-2 the experiments that could potentially be performed to determine the performance, mechanical limits and life limits of the ND engine systems are:

- Run the induction motor at a fixed speed, for a given start-up time, and allow the ND compressor module to naturally aspirate the air at speeds representative of operational conditions. Obtain time and cross-sectional area averaged total pressure and temperature measurements on both the inlet (2) and outlet (5) flow rakes. This experiment should provide an estimate of the volumetric and compression efficiency values expected of the compressor disc. The experiment can be repeated with pre-compressed air to provide a quantitative difference between naturally aspirated and boosted ND compressor discs.
- An experiment can be run where the, frequency and release pressure of the solenoid valve at the egress port can be varied during naturally aspirated or boosted operation at a fixed speed. This experiment will provide a relationship that between the effective volumetric compression ratio and compression efficiency.
- The aforementioned experiment can be furthered by operating the ND compressor at different operating speeds, in order to create a non-dimensional ND compressor map. Essentially the map would be a function of the non-dimensional volumetric flow and the volumetric compression ratio, which would be overlaid with efficiency and non-dimensional speed contours. This experiment can be repeated for ND compressors of different radii, angles of nutation, hub to tip radii and radii by adjusting the positioning of the vertical stands using the adjustable test stand rack. This would give a valuable insight as to how exactly does the geometry of the design dictate the efficiency of the module. In addition, this would provide valuable in determining the scale effects of the ND compressor module.
- A tool that is frequently used in gas-turbine experimental rigs for flow visualization, is the Schlieren camera [133]. The axial (24) and circumferential (7) cameras suggested in the experimental arrangement in Figure 7-2 can be used in measuring the scale of large scale eddies through the clear case housing (3) of the ND compressor. The coupled measurements of the flow velocities and frequency of discharge port operation can ultimately provide correlations between flow velocity and porting frequency and the magnitude of flow circulation vorticity and compression efficiency. A potential correlation, would provide useful design constraints at a preliminary design level.
- Attaching piezo –electric vibration sensors on the bearings (19) located in the housing (13) can provide useful data about the vibrational properties of the ND

compressor during operation. Particularly, using the aforementioned in conjunction with a data acquisition unit can provide details about the operational speeds that produce first mode and second mode of longitudinal and flexural vibration. Essentially, a potential Campbell diagram can be created for the ND compressor module.

- A dedicated experiment can be assigned to measuring the oil feed and scavenge temperatures during the operation of the ND compressor module. The temperature of the feed and scavenge oil temperatures can be measured by thermocouples as per [134]. An experiment of this nature can assist in ascertaining the oil-system operating limits in order to meet bearing life limits. Measuring the oil temperatures needs to be coupled with flow rate measurement. This will help in providing design guidelines for the fuel pump, scavenge pump and oil-air heat exchanger in addition to testing for failure cases.
- The series of experiments will involve constant usage of power drawn from the mains. However, if a power management unit interfaces between the mains and the proposed experimental arrangement a useful insight can be drawn with regards to the power demands of a potential oil-system and solenoid controlled release valve in operation. High level design objectives can then be proposed for the auxiliary electrical systems.

The proposed experiments would provide good insight with regards to the operation of ND compressor. However, bearing in mind that a concurrent design approach must be undertaken, high order models should be assembled and calibrated to experimental settings. This would provide rapid design space exploration without having to go through the rigor and cost of assembling additional experimental units. The proposed high-order models must be created in order to facilitate rapid design of ND compressors, namely:

- A scalable 3D URANS, LES or DNS CFD model of the nutating disc compressor. Luthfilaudri et al., conducted a study that set up a framework to estimate the volumetric efficiency of section of a ND compressor under idle conditions [84]. This work should be extended further in order to ensure that the static and dynamic meshes robustly morph as per parametric geometry changes made. This will ensure good convergence of results in the first instance. Secondly, the model should be calibrated to the potential experimental results. Finally, Reynolds correction correlations as well as seal clearance correction correlations can be ascertained.
- Using the boundary conditions of a calibrated CFD model, a fluid- structural interaction model an unsteady FEA model can be developed. This will provide an

insight in to possible regions of stress concentrations, fatigue patterns and vibrational signature of the ND compressor.

- A Simulink based control system model should be developed, to ascertain the PID or LQR controller tuning values needed to ensure timing consistency between the rotation of the shaft and the timing of the compressor delivery port. It can also be used to provide a look-up table of tuning values in the instance the PID or LQR controllers were to be used for variable compression ratio operation.

Concurrently to developing the experimental rig, high order models, the following low order mathematical expressions/models need to be ascertained:

- A methodology to mathematically describe the curvature of the surface of the ND wedge that meets the internal nutating disc structure. The shape is highly complex, and should be expressible as a function of the parametric design choices outlined in Chapter 5. Estimating the aforementioned will refine the swept volume estimation.
- A methodology to mathematically describe the volumes occupied by the seals should be developed, in order to refine the swept volume estimation.
- A methodology that explains the specific enthalpy rise of the ND compressor as a function of swirl addition needs to be developed, like Euler's turbomachinery law. Coupled with correlations derived from the high order models it can define feasible areas of the design space at an early stage of design.
- The internal oil flow path needs to be designed.
- A subcomponent design process for the ND compressor module should be developed, in order to design the component for ease of maintenance. Essentially, various design layouts need to be developed and down selected based on the ease of access and cost.

The next ND module that needs to be investigated further is the accumulator module, which is described in the following section.

7.1.2 Accumulator Module

The accumulator is connected to the ND compressor delivery ports and the pre-combustion chamber by a series of solenoid controlled valves. Its primary function is to prevent compressed air to flow back in to the ND compressor module and to provide uniform flow to the pre-combustion chamber. Similar to the ND compressor module a top-down approach coupled with a concurrent engineering approach is proposed in order to advance this sub component of the ND-engine to a higher TRL. Figure 7-3, highlights the potential experimental arrangement to investigate the performance and durability of the accumulator

module. Furthermore, Table 7-1 highlights the apparatus that would be potentially involved with the proposed rig. Essentially in the accumulator rig pressurized air would enter both entrances of the clear case accumulator (6), which is admitted in to the accumulation chamber by solenoid controlled valves (2). The air is subsequently released in to a plenum chamber (8) through another solenoid controlled valve (7).

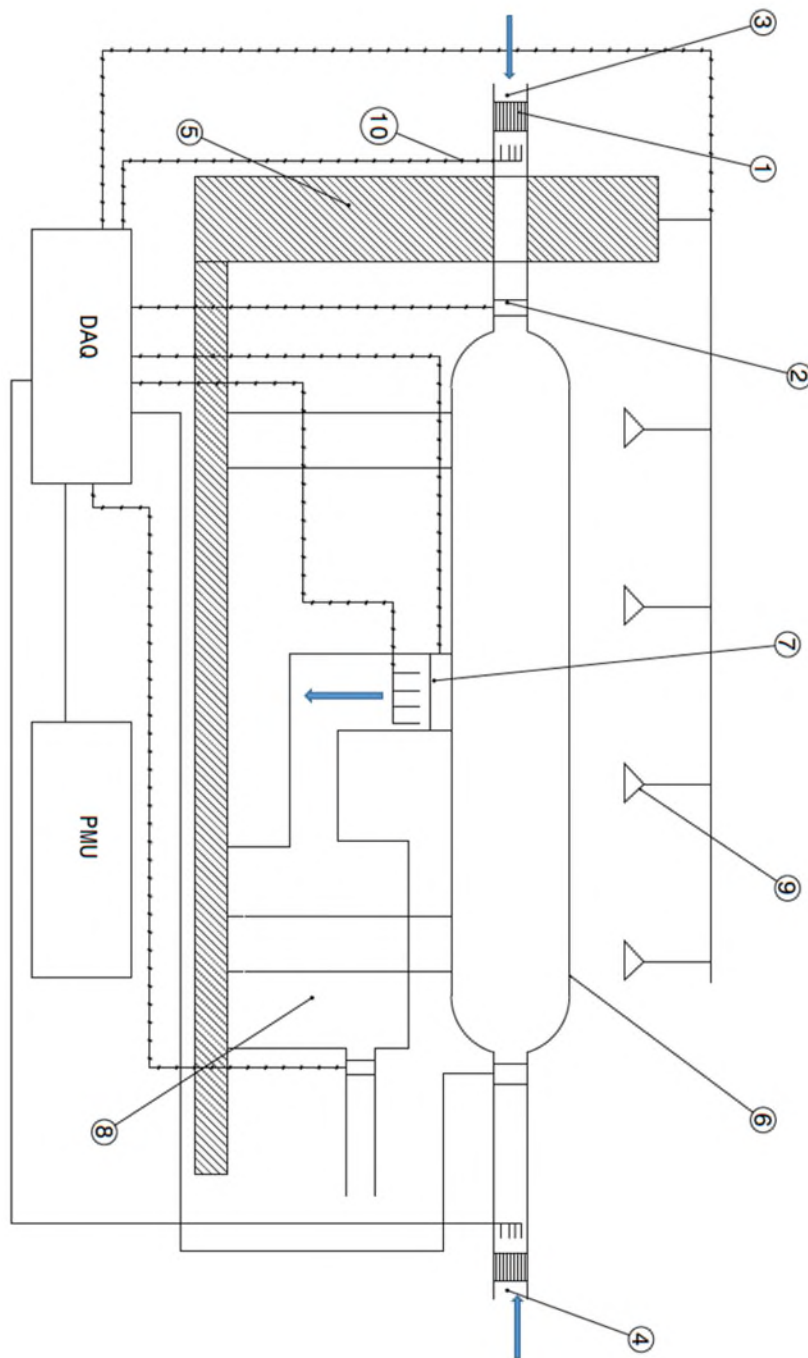


Figure 7- 3: Potential experimental arrangement of the accumulator test rig

Table 7- 1: Preliminary bill of materials for the accumulator rig

<u>Bill of materials</u>			
Number	Item	Number	Item
1	Flow straightening hexagonal array	6	Clear case accumulation chamber
2	Inlet Solenoid controlled valve	7	Outlet Solenoid controlled valve
3	Compressor delivery port 1	8	Plenum chamber
4	Compressor delivery port 2	9	Schilernen camera array
5	test stand	10	Data communication lines

The experiments that could be potentially conducted on the aforementioned rig are:

- Measuring the overall volumetric expansion ratio, of the process of porting air from the compressor outlet to the pre-combustion chamber. Using the pitot and total temperature rakes the expansion efficiency of the process can be measured.
- The pressure and temperature of the introduced air can be varied and inlet flow acceptance frequency can be varied, in order to produce a non-dimensional map that describes the performance of the accumulation chamber. Essentially, a consequence of this experiment should produce a map which depicts the expansion efficiency of the accumulator as a function of the volumetric flow rate and volumetric compression ratio amidst efficiency contours and non-dimensional frequency operating lines. This will help understand the limits of off-design operation and also provide relative frequency timing look-up tables for control system implementation in the future.
- Experiments to determine the scale effects of an accumulator as well as surface roughness effects on process efficiency should be assessed in order to derive lower order efficiency correction correlations for the same.

- A Schlieren camera can be used to determine how the size of the observable eddies scale as a function of the operating speed. This experiment can give insight in to the process efficiency loss mechanisms as well as assist in deriving a low-order expression that correlates operating speed with pressure loss.
- Since all experimental rig experimental needs pass through a power management unit (PMU). A design space of the potential operating electrical needs required by the solenoid controlled release valves can be determined.

Concurrently the high-order models that need to be developed to support rapid detailed design space exploration are:

- A scalable 3D URANS, LES or DNS CFD model of the nutating disc accumulator module. This work should entail static and dynamic meshes that robustly morph as per parametric geometry changes made. This will ensure good convergence of results in the first instance. Secondly, the model should be calibrated with the provided experimental results. Finally, relatively inexpensively, Reynolds correction correlations as well as seal clearance correction correlations can be ascertained.
- Using the boundary conditions of a calibrated CFD model, a fluid- structural interaction model an unsteady FEA model can be developed. This will provide an insight in to possible regions of stress concentrations, fatigue patterns and vibrational signature of the accumulator module.
- A Simulink based control system model should be developed, to ascertain the PID or LQR controller tuning values needed to ensure timing consistency between the series of solenoid controlled valves. It can also be used to provide a look-up table of tuning values in the instance the PID or LQR controllers were to be used for variable accumulator expansion ratio operation.

Concurrently to developing the experimental rig, high order models, the following low order mathematical expressions/models need to be ascertained for the accumulator module:

- Develop a methodology to size the accumulation chamber and overall volumetric expansion ratio, from when the compressed air is admitted to the accumulator to when the air is discharged in to the pre-combustion chamber. This methodology will help define the performance design values of volumetric expansion ratio as a function of the geometry of the accumulation chamber.
- A methodology that mathematically describes the velocity variation throughout the process of the air being transferred from the compressor delivery port to the pre-

combustion chamber. This provides design constraints at a preliminary design stage such that the flow does not choke in relatively continuous flow domains.

- A subcomponent design process for the ND compressor module should be developed, in order to design the component for ease of maintenance. Essentially, various design layouts need to be developed and down selected based on the ease of access and cost.

The following section describes the further work associated with the ND pre-combustor module.

7.1.3 Pre-combustor module

Prior to determining and understanding the combustion mechanism that occurs in the ND-pre combustor and expander module, it is critical to understand how fuel is atomized and sprayed in the pre-combustion chamber in addition to how the fuel and air is mixed within the pre-combustion module. Figure 7-4 shows the potential arrangement of an experiment that would allow inspection and fuel to air dispersion in the pre-combustion chamber. In addition, a prospective preliminary bill of materials that highlight the potential apparatus involved in the proposed experimental rig are presented in Figure 7-4.

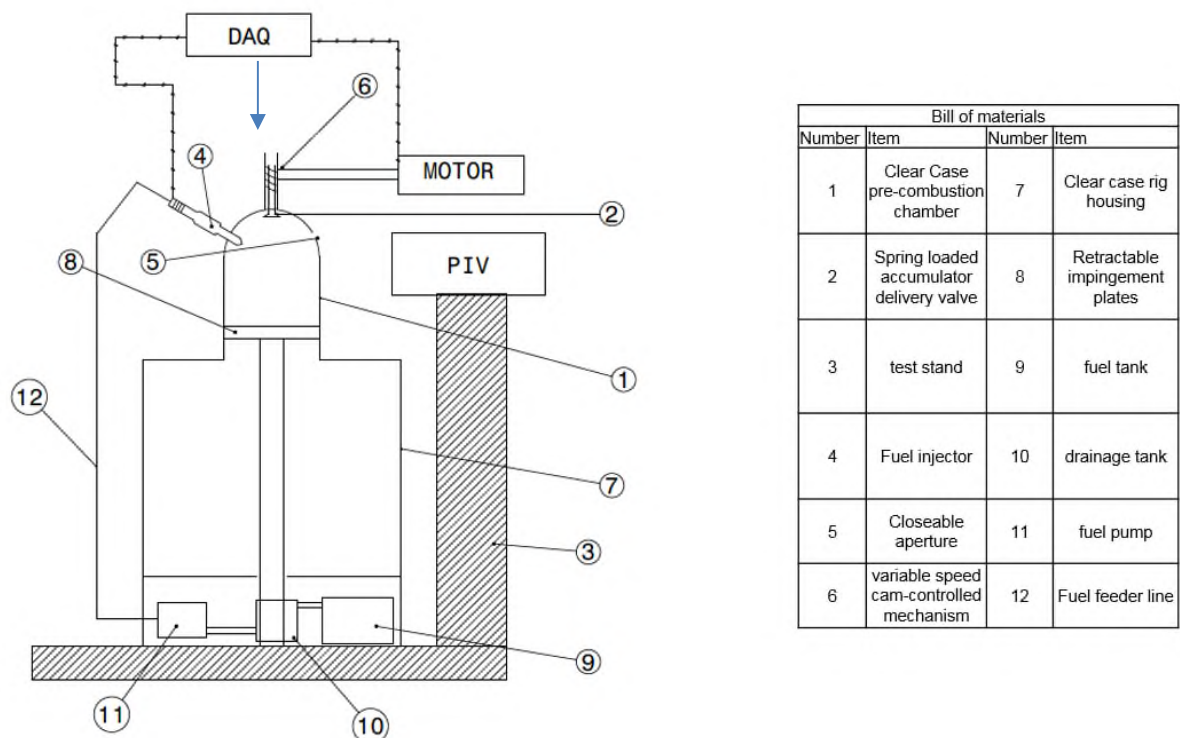


Figure 7- 4: ND pre-combustor module potential test rig and bill of materials

The operation of the proposed rig entails pressurized air being metered in to the clear case pre-combustion chamber (1), via a cam operated (6) spring loaded valve (2). In conjunction, fuel is periodically metered in to the pre-combustion chamber through the fuel injector (4), excess fuel drained past the impingement plates (8) and recycled using the drainage tank (10) and fuel pump (11). The following experiments can be performed within the proposed experimental arrangement:

- Pressurized air can be metered in to the pre-combustion chamber, while the periodic dispersion of air is tracked by particle image velocimetry (PIV)[135]. This assists in determining the cone angle of air dispersion as a function of the valve type. It can also provide a correlation that predicts air cone angle variation as a function of the valve lift profile. In addition, it can help define correlations that predict the swirl inducing characteristics inherent in a valve design with pre-swirler vanes located on the seat and those valves without [136]. Correlations that can quantify the aforementioned effects provide a robust preliminary design approach that can capture the effects of fuel-air mixing at a preliminary stage.
- Pressurized fuel can be intermittently sprayed in to the pre-combustion chamber at various locations, pressures, frequency and fuel injector designs to provide an idea of the fuel spray characteristics. Coupled with PIV techniques correlations can be derived for the spray cone angle as a function of the potential operating conditions. Furthermore, it can weed out any fuel injector locations that would cause fuel impingement on the pre-combustor wall in case of air valve delivery malfunction, which will lead to hotspots and reduced pre-combustor liner life.
- Intermittently spraying air and fuel, at different absolute and relative frequencies. Coupled with impingement plate area coverage analysis and PIV methods a probabilistic non-dimensional map can be created that showcases fuel to air ratio contours as a function of the non-dimensional volumetric flow and air and fuel admittance frequency. This would provide a useful design tool at a preliminary level to prevent hot spots caused by localized high fuel to air ratio regions.

All the aforementioned proposed experiments can be replicated for different types of fuel and help calibrate the control system tuning parameters for eventual operational use. Concurrently with the experimental rigs, the following high order models should be created:

- A 3D URANS/LES or DNS CFD model that predicts the distribution of the fuel to air ratio within a proposed pre-combustion chamber. This should include robust meshing algorithms that create suitable dynamic and static meshes that provide converged solutions for changes in geometry, valve lift profile and admittance frequency. Liberti et al. made a start with regards to this by assembling a representative 2D model [85].

- A Simulink based control system model should be developed, to ascertain the PID or LQR controller tuning values needed to ensure timing consistency between the fuel injector and air admittance valves. It can also be used to provide a look-up table of tuning values in the instance the PID or LQR controllers were to be used for variable valve timing operation.

The simple order models that can be concurrently developed are:

- Mathematical models that describe the air and fuel spray cone angles as function of the injector type and valve type. Lefebvre and Heywood have covered this topic in depth, and should be relatively less time consuming to implement [24,117]. Correlations developed at this rudimentary level would help designers at a preliminary stage determine the possible dispersion region of fuel and air respectively.

Once the future work entailed in the mixing characteristics of the pre-combustion chamber are defined, the details of the top-down approach to furthering work in the ND expander module are shown. Since part of the combustion process is expected to take place in the expander disc, it is essential to capture the combined effects that happen in the pre-combustor and expander chambers. Hence, the following section describes the work dedicated to the ND combustor-expander module.

Combustor-expander module

Bill of materials		
Number	Item	Number Item
1	Clear Case pre-combustion chamber module system	12 oil scavange pump
2	Data communication lines	13 test stand
3	PIV system	14 Power management unit
4	Clear case rotating disc expander chamber	15 Power transmission lines
5	Internal rotating disc structure	16 oil feeder lines
6	Pilot and total temperature probe rake	17 oil feedere thermocouple
7	Bearing housing containing vibratin sensors	18 oil feeder thermocouple
8	thermocouple data trasmission lines	19 oil flow meter
9	Schliermen camera system	20 axially adjustable track
10	oil pump	21 oil scavange thermocouple
11	oil tank	22 ND Z-shaft

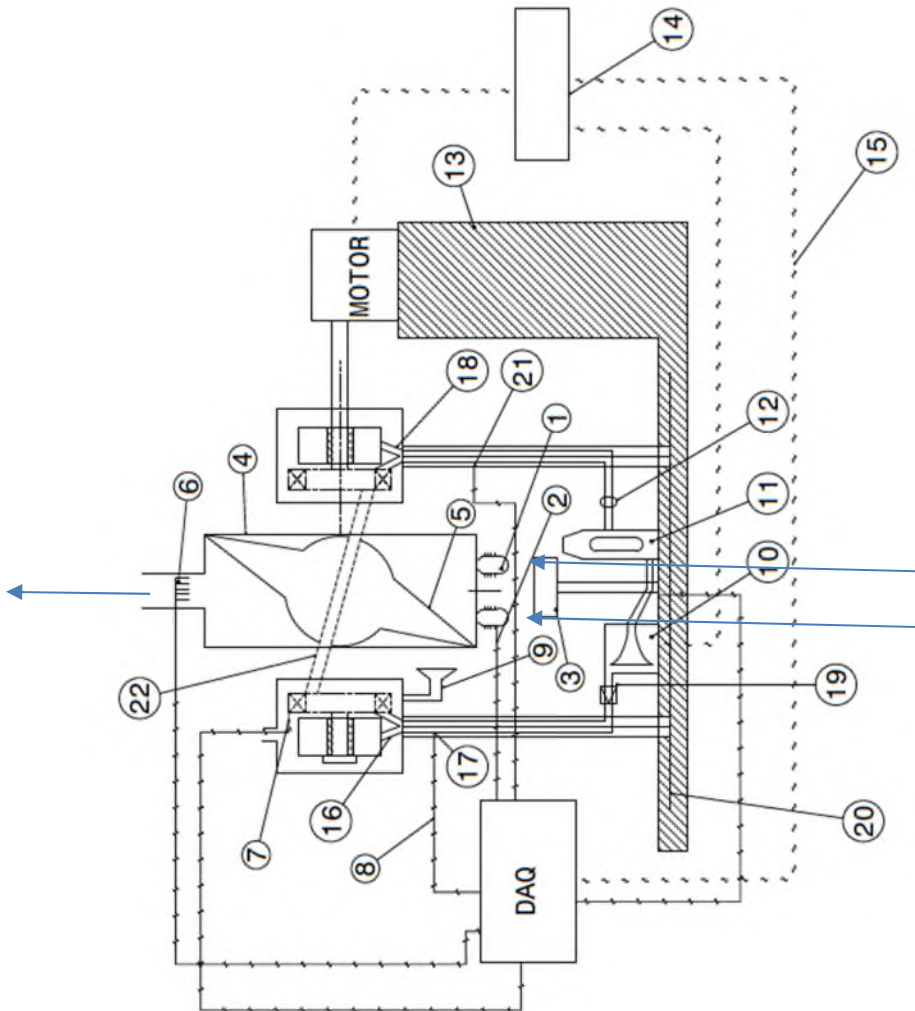


Figure 7- 5: Potential combustor-expander rig and bill of materials

Figure 7-5, shows the potential arrangement of an experimental rig for the combustor-expander module along with the associated expected bill of materials. The fundamental operation of the experimental rig begins by using a motor to spool up the internal structure of the ND expander (5) to a critical speed. Following which pressurized air and fuel is admitted in to the clear case pre-combustion system (1), a spark ignites the air-fuel mixture, the combusted flow is volumetrically expanded and the ported out of the nutating disc expander through an outlet port. The following experiments can be conducted to determine key design constraints:

- By varying the operating conditions of the pressurized flow, fuel admittance frequency, air admittance frequency and spark ignition frequency the following correlations / map can be obtained:
 - A heat release rate map which is a function of the operating conditions. This can potentially be determined by using a combination of the PIV techniques, Schlieren cameras and thermocouple measuring techniques. This will provide a useful tool in determining off-design performance at a preliminary analysis level as well as calibrate Wiebe correlations[117].
 - The boundary of the combustion process as a function of crank angle approximation per shaft revolution can be ascertained as a function of operational conditions and operating speed. The Schlieren camera apparatus can be used to track the periodic progression of the flame front. This would provide a useful map to be used in preliminary level design explorations.
 - A parametric analysis of the metering devices settings, involved in the aforementioned experimental campaign would essentially provide look-up values for eventual control systems.
 - If additional measuring equipment is incorporated in to the rig, the thermos-acoustic characteristics of the combustor can be determined.
- If the pre-combustion system is considered detachable, then representative combustor exit flow conditions could be periodically metered in to the expander module at varying operating conditions. Then by observing the data acquired from the combustion chamber delivery pitot probe and total temperature rakes and the outlet rake array an estimation of the volumetric expansion efficiency can be estimated. Essentially a map, similar to that described in section 7.1.1 can be created and utilized at the preliminary design level.
- The aforementioned experiments can provide valuable insights with regards to the scale effects and geometric variation effects of the detachable combustor and

expander modules with regards to their heat release rates and expansion efficiency respectively.

- Attaching piezo –electric vibration sensors on the bearings located in the housing (7) can provide useful data about the vibrational properties of the ND compressor during operation. Particularly, using the aforementioned in conjunction with a data acquisition unit can provide details about the operational speeds that produce first mode and second mode of longitudinal and flexural vibration. Essentially, a potential Campbell diagram can be created for the ND expander module.
- A dedicated experiment can be assigned to measuring the oil feed and scavenge temperatures during the operation of the ND expander module. The temperature of the feed and scavenge oil temperatures can be measured by thermocouples as per [134]. An experiment of this nature can assist in ascertaining the oil-system operating limits in order to meet bearing life limits. Measuring the oil temperatures needs to be coupled with flow rate measurement. This will help in providing design guidelines for the fuel pump, scavenge pump and oil-air heat exchanger in addition to testing for failure cases.
- The series of experiments will involve constant usage of power drawn from the mains. However, if a power management unit interfaces between the mains and the proposed experimental arrangement a useful insight can be drawn with regards to the power demands of a potential oil-system and solenoid controlled release valve in operation. High level design objectives can then be proposed for the auxiliary electrical systems.
- If infra-red cameras and operationally representative pre-combustor and expander housing cases were used for the experiments mentioned above. It would be possible to measure wall temperatures and consequently determine the amount of heat lost to the surroundings[137]. This would pave the way with regards to the design characteristics of the ND combustor-expander module cooling system.
- Additional experimental needs to be included within the framework of the rig to ascertain noise and NO_x emission profiles.

The high-order models that should be concurrently developed with the experimental apparatus are:

- A scalable 3D URANS, LES or DNS CFD model of the nutating disc combustor and expander. Liberti et al. made a start with regards to this by assembling a representative 2D model [85]. This work should be extended further in order to ensure that the static and dynamic meshes robustly morph as per parametric geometry changes made. This will ensure good convergence of results in the first

instance. Secondly, the model should be calibrated with the provided experimental results. Finally, relatively inexpensively, Reynolds correction correlations, heat loss correlations as well as seal clearance correction correlations can be ascertained.

- Using the results of the scalable 3D URANS, LES or DNS CFD model of the nutating disc combustor and expander model a transient thermal model should be created to address any cooling needs.
- Using the boundary conditions of a calibrated CFD model, a fluid- structural interaction model an unsteady FEA model can be developed. This will provide an insight in to possible regions of stress concentrations, creep-fatigue patterns and vibrational signature of the ND compressor.
- A Simulink based control system model should be developed, to ascertain the PID or LQR controller tuning values needed to ensure timing consistency between the series of solenoid controlled valves. It can also be used to provide a look-up table of tuning values in the instance the PID or LQR controllers were to be used for variable expansion ratio operation.

The simple order models that can and should be concurrently developed are:

- A methodology to mathematically describe the curvature of the surface of the ND wedge that meets the internal nutating disc structure. The shape is highly complex, and should be expressible as a function of the parametric design choices outlined in Chapter 4. Estimating the aforementioned will refine the swept volume estimation. In addition, a methodology should be developed to mathematically describe the pre-combustor exit area, which would assist in predicting the combustor exit conditions.
- A methodology to mathematically describe the volumes occupied by the seals should be developed, in order to refine the swept volume estimation.
- A methodology that explains the specific enthalpy drop of the ND expander as a function of swirl addition needs to be developed, like Euler's turbomachinery law. Coupled with correlations derived from the high order models it can define feasible areas of the design space at an early stage of design.
- The internal oil flow path needs to be designed.
- The pre-combustor and expander module cooling systems need to be designed as well.
- An important thermodynamic feature that affects the performance of a ND engine is the heat flux through the casing during the combustion process. Thus far under the scope of the methodology presented in Chapter 4 the heat flux is arbitrarily represented as a fraction of the potential heat release from the combustion process. However, the fraction of heat flux in the quasi 1-D performance model should indeed

be a function of the surface area, wall thickness, average wall temperature and the average Reynolds number of the flow. In essence, the magnitude of the heat flux through the casing should scale as with the size of the ND engine. Hence, a preliminary methodology is proposed to account for the heat flux through the combustor casing. This 1D methodology is used in the automotive industry to predict the heat release during the combustion process and the subsequent heat flux through the combustor casing [117,138]. The combustion model in this instance is a single zone combustion model, where the bulk temperature and pressure of the combustion process is predicted as a function of the absolute crank angle. The temperature and pressure variation during the combustion process is defined by means of the non-dimensionalized mass of fuel burned as a function of the combustion crank angle [138]. This representation of the non-dimensionalized mass of fuel consumed as a function of the crank angle is commonly referred to as a Wiebe function [139]. The non-dimensionalized curve that represents the rate of fuel consumed during the combustion process is dependent on a host of criteria such as the inlet temperature, pressure, operating speed, the rate of fuel evaporation, rate of fuel mixing and flame speed [140]. Hence the geometry of the combustion chamber and the subsequent placement of the spark plug/glow plug, the fuel injector and air injector valve play a fundamental role in defining the slope of the Wiebe curve [139]. Due to the extent of unknown variables involved in estimating the slope of the Wiebe function, usually experimental data derived from the proposed rig set-up can be used to determine the constants in the standard form of the Wiebe equation, represented in Equation 7-1. In Equation 8-1 a and m are the calibrated constants and θ represents the crank angle [138].

$$x(\theta_i) = 1 - e^{-a \left[\frac{\theta - \theta_{st}}{\Delta\theta} \right]^{m+1}} \quad \mathbf{7-1}$$

Once the fuel burn fraction is calculated for the combustion process, the total pressure and temperature variation as a function of crank angle can be calculated and is represented by Equation 7-2 and 7-3 [138]. In the following equations V is representative of the volume of the combustion chamber, FAR is the fuel-air ratio, LHV is the lower heating value of the fuel and Cv is the isochoric specific heat capacity.

$$T(\theta_i) = T(\theta_{i-1}) \left(\frac{V(\theta_{i-1})}{V(\theta_i)} \right)^{\gamma - 1} + \eta (FAR \cdot LHV (x(\theta_i) - x(\theta_{i-1}))) / Cv \quad \mathbf{7-2}$$

$$P(\theta_i) = P(\theta_{i-1}) \left(\frac{V(\theta_{i-1})}{V(\theta_i)} \right) (T(\theta_i) / T(\theta_{i-1})) \quad \mathbf{7-3}$$

It can be seen from the aforementioned equations that it is necessary to determine the estimated control volume as a function of the crank angle per shaft revolution in order for it to be applicable to the derived ND engines' performance models. Therefore mathematical derivations similar to the approaches explained in Chapter 4 are used to predict the change in volume of the combustion control volume as a function of the combustion crank angle, the derivation isn't explicitly reported here. If one refers to Chapter 4, it can be seen that the entire combustion crank angle, per shaft revolution, is defined by the tip radius, hub to tip ratio, angle of nutation and the height of the combustion chamber (defined by the dimension DE). If one were to extrapolate this assumption further, it is possible to define the boundary between constant volume combustion and constant pressure combustion by assuming that the combustion crank angle that corresponds to constant volume combustion is defined by the wedge angle occupied by the pre-combustion chamber. Consequently, the ratio of constant volume combustion to constant pressure combustion can be defined.

Finally, the correlations suggested by Woschni can be used to determine the heat flux through the combustor casing [141]. Equation 7-4 is a function of the bulk gas temperature, T , bulk gas pressure, P , the equivalent bore diameter, B , the average flow speed, w , the wetted surface area, A , average temperature of the chamber wall of the combustion chamber, T_w , and an experimentally calibrated constant, m .

$$Q = 3.26 B^{m-1} P^m w^m T^{0.95-1.62m} A (T - T_w) \quad \mathbf{7-4}$$

The aspects of the aforementioned model that needs defining, are the means of estimation of the average wetted surface area and the average speed of the mass flow mathematically. Developments with regards to this aspect of the combustor-expander would provide useful correlations and design guidelines during the preliminary design phase.

- A subcomponent design process for the ND compressor module should be developed, in order to design the component for ease of maintenance. Essentially, various design layouts need to be developed and down selected based on the ease of access and cost.

Once knowledge about the key operating parameters and design constraints of the ND engine system modules are derived, it is necessary to determine how the auxiliary systems that connect relatively continuous flow turbomachinery to the ND engine system affects the performance of the turbomachinery and ND engine system respectively. The following

subsection provides a generic overview of the approach that should be undertaken to estimate the same.

7.1.4 Auxiliary system module

The potential auxiliary systems that allow for coupling relatively continuous flow machines to discontinuous machines can either be plenums or tortuous manifolds/runners that account for mass flow fluctuations between the turbomachinery and the ND-core module. Figure 7-6, shows a meridional view of proposed inlet and exit plenum in a proposed Y2050 GOR-ND IP-drive core test section.

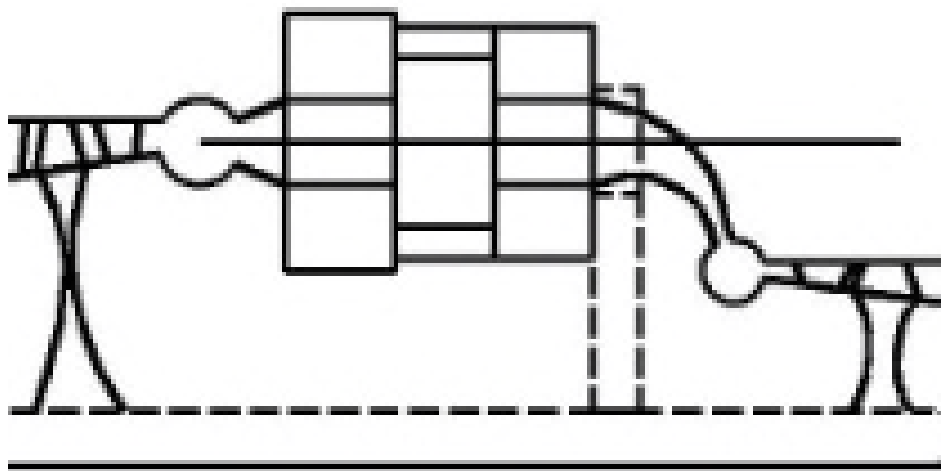


Figure 7- 6: Proposed meridional view of IP-drive core test section

Details of the possible experimental arrangement have been spared, instead experimental studies should be carried out to address the following gaps in knowledge:

- An axial compressor, axi-centrifugal performance and axial-turbine map corrections should be derived to account for possible backflow emanating from the ND engine compressor or expander modules in to the upstream compressor(s) and downstream turbines respectively.
- A map of the pressure loss and heat loss through the walls of the inlet and exhaust plenum should be created as a function of the non-dimensional volumetric flow at different operating speeds.
- A comparative performance and emissions study should be performed between a plenum or telescoping manifold arrangement to see which configuration is the most competitive[142].
- Derivation of a Campbell diagram for the vibrational response of the IP-drive core.

- IP-drive core gearbox integrity and life assessment. In addition, operational demand trends during failure case scenarios can be assessed. For example, if one of the nutating disc engine systems stopped producing useable work, what the impact on the performance would be.

Once the operational limits of the auxiliary components of the ND engine system are understood and adequately represented in a low-order model, the further work required to determine the operational limits of the additional technology enablers must be considered. The additional technologies, investigated in this study, are the intercooler and the re-circulating secondary burner.

Further work that should be considered for the intercooler component are:

- An experimental rig, for the intercooler must be created such that a map can be created that correlates the ratio of axi-centrifugal discharge pressure to the booster discharge pressure and the non-dimensional mass flow to the intercooler effectiveness and total pressure ratio. This map would assist in the prediction of the off-design performance of the intercooler component.
- From the aforementioned potential experimental rig, correlations should be derived to account for the effects of fouling and ice-accretion.
- A 3D-URANS CFD model, which will help derive correlations that correlate the dimensions and arrangement of the elliptical tube stacks to the thermal effectiveness and total pressure loss within a GOR type engine arrangement. This model will produce a calibrated representation of the experimental arrangement and will help in producing correlations for scale effects of the proposed intercooler arrangement.
- A low-order model, which correlates the dimensions and arrangement of the elliptical tube-stacks and operating conditions to the total pressure loss and intercooler effectiveness. This method would be similar to the method outlined in [143] and would assist explore the design space at a preliminary design stage.

Further work that should be accounted for the secondary combustor module are:

- An experimental rig should be assembled to estimate the total pressure loss across the combustion chamber in addition to determining the combustor outlet temperature pattern. Furthermore, the experimental arrangement should provide useful insight with regards to the possible areas of peak liner temperature.

- A scalable high-order 3D-URANS CFD model, should be created in order to derive correlations that account for scale effects. Bueno et al., has made considerable progress with regards to initiating this step [94].
- A correlation that accounts for the total pressure loss as a function of the operating conditions should be used in the low-order performance models in order to account for possible engine performance variations at a preliminary design stage.

In addition, to addressing the further work and gaps in knowledge with regards to the ND-engine system and it's auxiliary systems it is necessary to further develop the fidelity of the preliminary assessment platform for the rest of the engine. The following section details how this can potentially be done.

7.2 Further work for the design assessment platform

The preliminary design space of an aero-engine is defined by a series of constraints. These constraints include competitive fuel burn, integration constraints, noise constraints, NO_x constraints, life and financial constraints. Therefore, generally a multi-disciplinary design approach is considered which strives to be competitive and produce a preliminary engine design that meets the diversified design constraints. The theoretical platform that could be potentially used to achieve a feasible design is referred to as a techno-economic risk assessment platform (TERA)[144]. Figure 7-7 shows a modular representation of the modules required for a TERA process for a potential GOR engine.

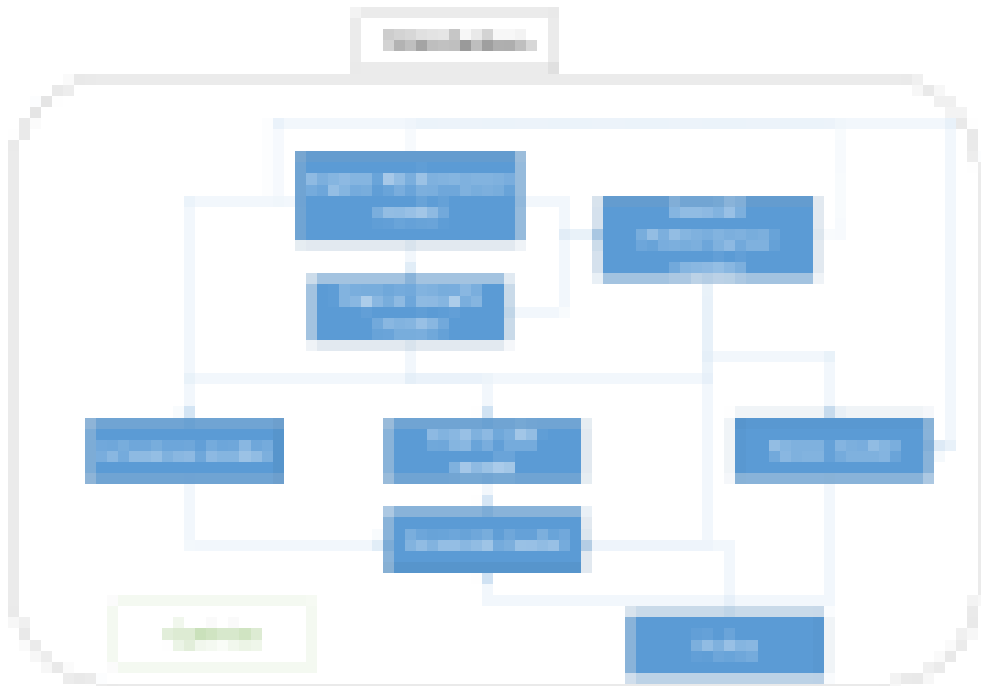


Figure 7- 7: Potential TERA platform for GOR engine

Within the scope of this thesis only the fuel burn competitiveness of the engine configurations have been investigated, and hence lacks some of the key modular components to provide a holistic view of the preliminary design space. Therefore in order to produce a more robust and representative TERA platform at a preliminary engine design level, the fidelity of the modular components should be improved. The future work required to improve the fidelity of the assessment platform is discussed in the following sections.

7.2.1 Engine performance, Mass and life module

Within the engine performance module, suggested in this thesis for all the potential engine configurations, entails assigning isentropic or polytropic efficiencies for the multi-stage compressors and turbines. However, once the designs progresses to a higher fidelity of analysis these efficiency assumptions are revised and the initial performance estimates are re-estimated, which can lead to time intensive process to find a realistic design. Therefore it would be beneficial if the efficiency of the multi-stage axial compressors and turbines could be accounted for as a function of their geometric and aerodynamic design considerations. Two methods are presented, that encompass geometric and aerodynamic design considerations for a multi stage axial compressor.

- A method (Method-I) that estimates the polytropic efficiencies of the compressor components based on the overall loading of the component (Pressure ratio), the Reynolds number effects (Re), sizing and Entry in to Service (EIS). The methods and assumptions that are employed to predict the polytropic efficiencies of the components are highlighted in [145]. Equation 7-5 indicates the how the efficiency of the component is calculated.

$$\eta_{pol} = \eta_{pol}^* + \Delta\eta_{pol,EIS} + \Delta\eta_{pol,Wc} + \Delta\eta_{pol,Re} \quad 7-5$$

η_{pol}^* is the nominal efficiency defined for a reference component with corrected mass flow $Wc=70$ kg/s, Reynolds number index $RNI=1.0$ and $EIS=1995$. This nominal efficiency is correlated on (outer) pressure ratio for fans and average stage loading ($\psi = \frac{2 \cdot \Delta h_0}{\sum_1^n U_i^2}$) for compressors and turbines. The nominal efficiency and the corrections for EIS, RNI and Wc are calculated using numerical expressions established from data presented by Grieb [145]. The correlation coefficients in these expressions are different for each type of turbomachinery component.

- Similar to the aforementioned method in predicting the polytropic efficiency of a multi-stage axial compressor component, the method (Method-II) outlined by Glassman

[146] can also be used. Essentially it estimates the polytropic efficiency of the component as a function of the stage pressure ratio (PR_{stg}), corrected mass flow (W_{corr}) and the blockage factor (K_{inp} [ranges from 0.01 to 0.05]). Equations 7-6 to 7-10 indicate how the polytropic efficiency of the component is calculated.

$$Pt_{2,i} = PR_{stg,i}(Pt_{1,i}) \quad 7-6$$

$$ETP_i = \left((0.047322)PR_{stg,i} \right)^2 - \left((0.21668)PR_{stg,i} \right) + 1.1241 \quad 7-7$$

$$ETP_i = \left((-0.027312)PR_{stg,i} \right)^1 + 0.93478 \quad 7-8$$

$$\Delta ETP_i = \left((0.00056826)W_{corr,i} \right)^1 - 0.00062224 + \left(\frac{0.050603}{W_{corr,i}} \right) \quad 7-9$$

$$\eta_{p,i} = (1 - K_{inp})^1 (1 - (ETP_i + \Delta ETP_i)) \quad 7-10$$

Using the aforementioned methods, it is possible to derive a more representative design point multi-stage compressor efficiency estimate. Similar to the multi-stage compressor a method is presented to account for the isentropic efficiency of a multi-stage turbine as a function of its aerodynamic and geometric design, namely;

- (Method-3) is suggested to predict the isentropic efficiency of uncooled multi-stage turbines is based on an empirical correlation of the Kacker-Okapuu efficiency chart [147,148]. The stage isentropic efficiency is derived as a function of the flow coefficient (ϕ) and work coefficient (ψ) respectively. Equations 7-11 to 7-19 indicate how the stage polytropic efficiency is calculated by Method-III. V_{in} , represents the axial velocity of the stage, ΔH_i , represents the total enthalpy drop across the stage. Kc_i , depends on the work loading of the multi-stage turbine [148]. TF (ranges from 1.0 to 1.05), represents the imposed technology factor to account for improvements in the detailed design phase, such as reducing surface roughness and improved materials [149], of the multi-stage turbines that yield increments in its polytropic efficiency.

$$U_{m,i} = \frac{\pi N_{mech} D M_i}{60} \quad 7-11$$

$$\Delta H_i = \Psi_i U_i^2 \quad 7-12$$

$$\Phi_i = V_{in} / U_i^1 \quad 7-13$$

$$\Phi_{i,optimum} = 0.375 + (0.25(\Psi_i)) \quad 7-14$$

$$\Psi_{i,optimum} = 1.35(\Phi_i)^{1.2} \quad 7-15$$

$$\eta_{p_{i,optimum}} = 0.913 + (0.103(\Psi_i)) - (0.0854(\Psi_i)^2) + (0.0154(\Psi_i)^3) \quad 7-16$$

$$Kc_i = 0.375 - 0.125\Psi_i \quad 7-17$$

$$Kc_i = 0.22/\Psi_i \quad 7-18$$

$$\eta_{p_i} = TF(\eta_{p_{i,optimum}} - Kc_i(\Phi_i - \Phi_{i,optimum})^2) \quad 7-19$$

Equation 7-20 is used in order to estimate the isentropic efficiency correction due to the introduction of cooling air, details of the efficiency correction are provided in [150]. δ , represents the efficiency penalty for the rotor and stator of the turbine stage. m , represents the mass fraction of the flow introduced before the rotor and stator blade rows.

$$\eta_{is,s,c_i} = \eta_{is,s,uc} (1 - \delta_r m_r - \delta_s m_s) \quad 7-20$$

It is envisaged that by the year 2050, blade cooling would still be necessary, despite the projected significant improvement in material operating temperatures [148]. Hence, a cooling methodology to estimate the blade metal temperature (BMT) must be employed. The current cooling methodology employed for multi-stage turbine components include only internal convection cooling, therefore a cooling model should account for the effects of film cooling as well. The proposed cooling model assumes that the multi stage turbine is an equivalent single stage turbine. The method used to predict the BMT of an equivalent rotor and stator is based in the work of Wilcock et al. [151]. The blade metal temperatures are derived by estimating the cooling flow factor (K_{cool}), the internal cooling efficiency (η_{int}), the film cooling effectiveness (ε_f), the metal and TBC Biot number (Bi_{met} and Bi_{TBC}). Equations 7-21 to 7-29 indicate how the blade metal temperature of the rotor and stator can be calculated. $\eta_{c,int}$, represents the internal convective cooling efficiency. $T_{0,c,x}$ and $T_{0,c,i}$, represent the exit coolant temperature and entry coolant temperature respectively. $T_{0,m,ext}$, represents the blade metal temperature. $T_{0,g}$, represents the total gas path temperature. m_c^+ , is a representation of the technology factor imposed on the blade row. ε_0 , Represents the overall blade cooling

effectiveness. T_{0aw} , represents the external temperature of the TBC. In order to account for radial temperature non-uniformity, T_g in Equations 7-22 and 7-26 are replaced by Equation 7-29. Equation 7-29 accounts for the maximum gas path temperature by accounting for the combustion factor (K_{comb}) and the total temperature rise across the combustion chamber (ΔH_i) as described in [151].

$$\eta_{c,int} = \frac{T_{0c,x} - T_{0c,i}}{T_{m,int} - T_{0c,i}} \quad 7-21$$

$$\varepsilon_f = \frac{T_{0g} - T_{0aw}}{T_{0g} - T_{0c,x}} \quad 7-22$$

$$m_c^+ = \frac{T_{0aw} - T_{0w}}{T_{0c,x} - T_{0c,i}} \quad 7-23$$

$$Bi_{TBC} = \frac{T_{0w} - T_{0m,ext}}{T_{0aw} - T_{0w}} \quad 7-24$$

$$Bi_m = \frac{T_{0m,ext} - T_{0m,int}}{T_{0aw} - T_{0w}} \quad 7-25$$

$$\varepsilon_0 = \frac{T_{0g} - T_{0m,ext}}{T_{0g} - T_{0c,i}} \quad 7-26$$

$$(1 + Bi_{TBC})m_c^+ = \frac{\varepsilon_0}{\eta_{c,ext}(1 - \varepsilon_0)} - \varepsilon_f \left[\frac{1}{\eta_{c,ext}(1 - \varepsilon_0)} - 1 \right] \quad 7-27$$

$$\eta_{c,ext} = \frac{\eta_{c,int}}{(1 + Bi_m \eta_{c,int} m_c^+)} \quad 7-28$$

$$\frac{m_c}{m_g} = K_{cool} m_c^+ \quad 7-29$$

In addition, to improving the fidelity of the modelling tools for the core turbomachinery of the GOR it is also necessary to improve the modelling fidelity of the LP-system of the GOR. The off-design performance of the LPT of the GOR is currently modelled using a representative LPT map of a turbofan.

However, the off-design performance should be predicted using a representative power turbine map. Also, the off-design performance of the LPT should be accounted for using variable LPT IGVs in order to account for different speed settings throughout the flight envelope.

Careful consideration should also be given to the air-oil heat exchangers system, for the planetary gearbox, performance on the overall engine performance of the engine throughout a potential flight envelope. Schnorhk et al., has described a potential low-order model to

account for the inclusion of the effects of the DPGB cooling system on the performance of the GOR[63].

The mechanical efficiency maps of the DPGB, should be derived from higher-order models or experimental data. Therefore more representative maps corresponding to the design conditions can be deciphered.

In addition, it is essential to investigate ND engine system based aero-engine architectures during abnormal modes of operation such as:

- Complete failure of one of the nutating disc engine modules during the operation of an IP-drive based configuration. In this case of abnormal operation the fuel burn must be observed.
- Abnormal operation caused due to severely fouled/ ice accreted involute-spiralled heat exchangers, the subsequent fuel burn variance from standard operation would be of great value.
- Abnormal operation during fuel system metering failure to a few injectors in the nutating disc systems. A fuel burn analysis during this mode of operation would be useful
- Abnormal operation during fuel injector failure of secondary combustor based engine configurations.

A key area of the GOR LP-system modelling that needs overhaul is the counter rotating propeller array. Current methods, include a 1D approach that resolves the performance of the CRP array at 75% blade span. A downside to this approach is that the performance of the CRP array is highly dependent on the airfoil profile span wise stacking, degree of blade sweep, blade lean, the number of blades and the aspect ratio of the blades. Therefore representative 2D and 3D approaches should be used to account for the aforementioned design options, which have been included in Section 2. In addition, a more representative methodology should be included to account for the performance of the CRP array located in the core stream. This is necessary because as per current models, it is assumed that the core section of the CRP does no work on the flow.

The mass of an engine is derived from correlations intended to estimate the mass of a VTOL (vertical take-off and landing) type engine[41]. In order to get a more accurate estimate of the engine mass a detailed sizing of the engine components should be conducted as proposed by [40]. Particular sub-components to the GOR engine configuration that need

detailed mass estimation methodologies developed are the DPGB, pitch change mechanism and the CRP propeller blades.

Finally, the life of life limited components within the structure of the GOR engine should be estimated. Therefore a methodology to estimate the life of the HPT, DPGB, PCM and the CRP array must be developed. A methodology to predict the HPT life throughout a potential flight envelope has been proposed by Elter et al. for robust implementation in to a low-order model [152]. In addition, the potential vibrational life limiting constraints should be accounted for in estimating the life of the turbomachinery and LP-system components of the GOR alike.

7.2.2 Aircraft performance, Emissions, Noise and Financial modules

The current state of the aircraft performance model, includes a point-mass based model. Where, through the non-linear fuel burn factor look-up table a series of individual aircraft designs are available for a particular mission. This arrangement is adequate to isolate the performance benefits derived by the engine for a fixed flight profile and mission. However, if the effects of the flight profile and mission range were to be investigated a more robust aircraft performance model should be developed. For instance a combination of OpenVSP and SUAVE can be used to create robust aircraft designs that can capture the snow-balling effect between aircraft and engine as well as intricacies of the flight profile and mission range[153,154].

In addition to improving the fidelity of the aircraft performance model, the emissions and noise modules need to be advanced. A NO_x prediction module should be developed for standard annular combustors, can combustors and can-annular combustors for constant pressure combustion. In addition, NO_x prediction modules should be developed for constant volume type combustion. Stirred reactor models and partially stirred reactor models could be potentially used as low-order physics based NO_x estimation models[155]. These low order models should be calibrated with higher order models or experimental data.

A noise estimation model, within the LTO envelope should also be developed for turbofans, GORs and GOR-ND engine variants. Ideally the low order model should be able to predict the noise dispersion within the LTO envelope emanating from the engine and aircraft respectively.

In order to get more reasonable estimates of the predicted outcomes of potential financial models for operators and OEMS, detailed estimates of the component masses of the engine and aircraft would correlate to better estimates of the engine and aircraft list prices, like in the work done by Goldberg et al [156]. In addition, better models to predict operator maintenance costs, aircraft and engine lease costs and regular calibration of personnel costs

and demand rates would lead to financial predictions with a lesser degree of standard deviation. In addition, the inclusion of random event union based strikes should be included for better credibility.

Once the future work regarding the ND engine systems and design assessment platform have been furthered, a more realistic depiction of the design space for GORs and GOR-ND engine system variants can be portrayed as well as a more realistic understanding as to how to surpass the SRIA targets.

REFERENCES

- [1] T. Korakianitis, L. Meyer, M. Boruta, H.E. McCormick, Introduction and Performance Prediction of a Nutating-Disk Engine, *J. Eng. Gas Turbines Power.* 126 (2004) 294. doi:10.1115/1.1635394.
- [2] T. Korakianitis, L. Meyer, M. Boruta, H.E. McCormick, Alternative Multinutating Disk Engine Configurations for Diverse Applications, *J. Eng. Gas Turbines Power.* 126 (2004) 482. doi:10.1115/1.1688770.
- [3] Airbus, Global Market Forecast Growing Horizons 2017/2036, 2017. doi:N/A.
- [4] V. Cox, N. LoBue, NextGen and the Environment, 2010. doi:10.1017/CBO9781107415324.004.
- [5] M. Darecki, C. Edelstenne, T. Enders, E. Fernandez, P. Hartman, J.-P. Herteman, M. Kerkloh, I. King, P. Ky, M. Mathieu, G. Orsi, G. Schotman, C. Smith, J.-D. Wörner, *Flightpath 2050*, 2011. doi:10.2777/50266.
- [6] P. Heinemann, Advanced tube and wing aircraft for year 2050 timeframe, in: *55th AIAA Aerosp. Sci. Meet.*, Grapevine, 2017: pp. 1–50. doi:N/a.
- [7] T. Grönstedt, A. Rolt, N. Tantot, C. Xisto, S. Donnerhack, O. Schmitz, A. Seitz, A. Lundblad, Ultra low emission technology innovations for mid-century Aircraftturbine engines, in: *ASME Press*, Seoul, 2016: pp. 1–13. doi:N/A.
- [8] R. Bucuroiu, Shorter routes possible with better planning, 2016. <https://www.eurocontrol.int/sites/default/files/content/documents/official-documents/skyway/articles/2016-winter-skyway-shorter-routes-better-flight-planning.pdf>.
- [9] A. Alexiou, B. Sethi, DEMOS Description of Action v1, H2020-Cs2-CFP01-2014-01, 2014.
- [10] L.L. Jensen, H. Tran, R.J. Hansman, Cruise Fuel Reduction Potential from Altitude and Speed Optimization in Global Airline Operations *, *11th USA/Europe Air Traffic Manag. Res. Dev. Semin.* (2015) 1–10. doi:N/A.
- [11] C.L. Nickol, Technologies and Concepts for Reducing the Fuel Burn of Subsonic Transport Aircraft, *Nato - Otan.* (2012) 1–21. doi:N/A.
- [12] A.L. Mohd Tobi, A.E. Ismail, Development in Geared Turbofan Aeroengine, *IOP Conf. Ser. Mater. Sci. Eng.* 131 (2016). doi:10.1088/1757-899X/131/1/012019.
- [13] C.E. Hughes, Aircraft Engine Technology for Green Aviation to Reduce Fuel Burn, 2011. doi:doi:10.2514/6.2011-3531.

- [14] A. Alexiou, V. Sethi, P. Cobas, DEMOS Description of action v2, H2020-Cs2-CFP01-2014-01, 2014.
- [15] A. Alexiou, K. Mathioudakis, Development of Gas Turbine Performance Models Using a Generic Simulation Tool, Vol. 1 Turbo Expo 2005. (2005) 185–194. doi:10.1115/GT2005-68678.
- [16] P. Bellocq, Multi-Disciplinary Preliminary Design Assessments of Pusher Counter-Rotating Open Rotors for Civil Aviation, PhD thesis, Cranfield University, 2012. doi:N/A.
- [17] A. Alexiou, C. Frantzis, N. Aretakis, Contra-rotating propeller modelling for open rotor engine performance simulations, in: Proceedings of ASME Turbo Expo 2016, 2016: pp. 1–12.
- [18] L. Larsson, T. Grönstedt, K.G. Kyrianiadis, Conceptual Design and Mission Analysis for a Geared Turbofan and an Open Rotor Configuration, Vol. 1 Aircr. Engine; Ceram. Coal, Biomass Altern. Fuels; Wind Turbine Technol. (2011) 359–370. doi:10.1115/GT2011-46451.
- [19] K.G. Kyrianiadis, A.M. Rolt, On the Optimization of a Geared Fan Intercooled Core Engine Design, J. Eng. Gas Turbines Power. 137 (2014) 041201. doi:10.1115/1.4028544.
- [20] A. Rolt, V. Sethi, F. Jacob, J. Sebastiampillai, C. Xisto, T. Grönstedt, L. Raffaelli, Scale effects on conventional and intercooled turbofan engine performance, Aeronaut. J. 121 (2017) 1–24. doi:10.1017/aer.2017.38.
- [21] A. Gamannossi, D. Bertini, D. Adolfo, C. Carcasci, Analysis of the GT26 single-shaft gas turbine performance and emissions, Energy Procedia. 126 (2017) 461–468. doi:10.1016/j.egypro.2017.08.219.
- [22] C.F. McDonald, D.G. Wilson, The utilization of recuperated and regenerated engine cycles for high-efficiency gas turbines in the 21st century, Appl. Therm. Eng. 16 (1996) 635–653. doi:10.1016/1359-4311(95)00078-X.
- [23] A. Rolt, J. Sebastiampillai, F. Jacob, V. Sethi, C. Xisto, Selecting Combinations of Advanced Aero Engine Technologies, ISABE 2017-22660, in: ISABE 2017-22660, Manchester, 2017.
- [24] A.H. Lefebvre, D.R. Ballal, Gas Turbine Combustion, 3rd Editio, CRC Press, 2010.
- [25] F. Jacob, A. Rolt, J. Sebastiampillai, V. Sethi, M. Belmonte, P. Cobas, Performance of a Supercritical CO₂ Bottoming Cycle for Aero Applications, Appl. Sci. 7 (2017) 255. doi:10.3390/app7030255.
- [26] T.G. Reichel, J.-S. Schäpel, B.C. Bobusch, R. Klein, R. King, C. Oliver Paschereit,

- Shockless Explosion Combustion: Experimental Investigation of a New Approximate Constant Volume Combustion Process, *J. Eng. Gas Turbines Power.* 139 (2016) 021504. doi:10.1115/1.4034214.
- [27] S.C. Gulen, Constant volume combustion the ultimate gas turbine cycle, 2013. doi:N/A.
- [28] C. Aero-engines, CIT SELECTS CFM56-5B FOR NEW A321 AIRCRAFT, (2015). <https://www.cfmaeroengines.com/press-articles/cit-selects-cfm56-5b-for-new-a321-aircraft/791/>.
- [29] VITAL Cordis webpage European commission, (n.d.).
- [30] NEWAC webpage, (n.d.). <http://www.newac.eu/>.
- [31] LEMCOTEC webpage, (2016). <http://www.lemcotec.eu>.
- [32] P. Walsh, P. Fletcher, *Gas Turbine Performance*, 4th editio, Blackwell Science, Oxford, 2008.
- [33] A. El-Syed, *Aircraft Propulsion & gas turbine engines*, CRC Press, 2015.
- [34] N. Tantot, M. Dubosc, S. Ghebali, innovative approaches to propellers off-design performance modelling, GT2015-42145, in: *Proc. ASME Turbo Expo 2015 Turbine Tech. Conf. Expo.*, ASME, Montreal, 2016: pp. 1–14.
- [35] J.H. Gao, Y.Y. Huang, Modeling and simulation of a aero turbojet engine with GasTurb, *Proc. - 2011 Int. Conf. Intell. Sci. Inf. Eng. ISIE 2011.* (2011) 295–298. doi:10.1109/ISIE.2011.149.
- [36] J. Lytle, G. Follen, C. Naiman, A. Evans, J.P. Veres, K. Owen, I. Lopez, Numerical Propulsion System Simulation (NPSS) 1999 Industry Review, *NASA Tech. Memo.* (2000) 1–96.
- [37] B. Nkoi, P. Pilidis, T. Nikolaidis, Performance assessment of simple and modified cycle turboshaft gas turbines, *Propuls. Power Res.* 2 (2013) 96–106. doi:10.1016/j.jprr.2013.04.009.
- [38] NASA, Weight Analysis of Turbine Engine - an Object-Oriented Version (WATE), (2018).
- [39] T. Gronstedt, *Weico 9.6*, (2015).
- [40] P. Lolis, development of a Preliminary Weight estimation method for Advanced Turbofan Engines, PhD thesis, Cranfield university, 2014.
- [41] S. D.A, L. S., Empirical expressions for estimating length and weight of axial-flow components of VTOL powerplants, *NASA TM X-2406*, Washington D.C, 1971. doi:N/A.

- [42] J.S. Vanderover, K.D. Visser, Analysis of a Contra-Rotating Propeller Driven Transport Aircraft, AIAA. (2000) 1–11.
- [43] S. D.A., D.B. Khazanov, Creation of the TV-2 (NK-12) turboprop engine, (n.d.). <http://www.airpages.ru/eng/ru/troph3.shtml>.
- [44] R.D. Hager, D. Vrabel, Advanced Turboprop Project, NASA SP-495f, 1988.
- [45] F. Metzger, Prop-Fan design and test experience, in: Adv. Propellers Their Install. Aircraft, Int. Conf. Proceedings, R. Aeronaut. Soc. 26th-27th Sept., 1988.
- [46] B.H. Little, D.T. Poland, Propfan test assessment (PTA): Final project report, NASA CR-185138, 1988.
- [47] R. Harris, R.. Cuthebertson, UDF TM/ 727 Flight Test Program, in: Proc. AIAA/SAE/ASME 23rd Jt. Propulsion Conf., AIAA-87/1733, San Diego, 1987.
- [48] C. Reid, Overview of flight testing of GE aircraft engines UDF engine, in: Proc. AIAA/SAE/ASME/ASEE 24th Jt. Propuls. Conf., AIAA-88-3082, Boston, 1988.
- [49] D.C. Chapman, G. J., D.E. Smith, Testing of the 578-DX propfan propulsion system, in: Proc. AIAA/SAE/ASME/ASEE 24th Jt. Propuls. Conf., AIAA-88-2804, Boston, 1988.
- [50] D.C. Chapman, R.E. Fleury, D.E. Smith, Testing of the 578-DX propfan propulsion system, in: Proc. AIAA/ASME/SAE/ASEE 25th Jt. Propuls. Conf., AIAA-89-2954, Monterey, 1989.
- [51] J.M. Bousquet, Etude de l'aerodynamique des helices pour avions rapides, in: AGARD 69th Symp. Propuls. Energ. Panel, Paris, 1987.
- [52] P. Gardarein, Calculs aerodynamiques des helices rapides transoniques, in: 28eme Colloq. d'Aerodynamique Appl., ISA, St. Louis, France, 1991.
- [53] T.J. Kirker, Procurement and testing of a 1/5 scale advanced counter rotating propfan model, in: Proc. AIAA 13th Aeroacoustics Conf., AIAA-90-3975, Tallahassee, 1990.
- [54] M. Daly, B. Gunston, Jane's Aero-engines, IHS Janes, 2002.
- [55] M.D. Guyn, J.J. Berton, initial Assesment of Open rotor Propulsion applied to an advanced single-aisle aircraft, in: Proc. 11th Aviat. Technol. Integr. Oper. Conf., AIAA 2011-7058, 2011.
- [56] S. Trimble, NASA concludes noise remains a challenge for open rotor, FlightGlobal. (2012).
- [57] A. Peters, Assessment of propfan propulsion systems for reduced environmental impact, Massachusetts Institue of Technology (MIT), 2010.

- [58] J.-F. Brouckaert, F. Mirville, K. Phuah, P. Taferner, Clean Sky research and demonstration programmes for next-generation aircraft engines, *Aeronaut. J.* 122 (2018) 1163–1175. doi:10.1017/aer.2018.37.
- [59] V. Gehlot, M. Attia, Multi-stage axial compressor with counter-rotation using accessory drive, US9353754B2, 2016.
- [60] P. Newton, N. Tantot, S. Donnerhack, A. Lundbladh, D1.1 – Establish common year 2050 technology level assumptions, 2015.
- [61] F. Jacob, J. Sebastiampillai, Deliverable 2.6- Year 2000 and initial year 2050 reference engine configurations, 2017.
- [62] J. Dominy, Transmission Efficiency in Advanced Aerospace Powerplant, 23rd Jt. Propuls. Conf. (1987).
- [63] Y. Schnorhk, Preliminary design of an air-oil heat exchanger system for a planetary gearbox for counter-rotating open rotor engines, MSc. thesis, Cranfield University, 2017.
- [64] C.A. Perullo, J.C.M. Tai, D.N. Mavris, Effects of Advanced Engine Technology on Open Rotor Cycle Selection and Performance, *J. Eng. Gas Turbines Power.* 135 (2013) 071204. doi:10.1115/1.4024019.
- [65] P. Bellocq, I. Garmendia, V. Sethi, A. Patin, S. Capodanno, F. Rodriguez Lucas, Multidisciplinary Assessment of the Control of the Propellers of a Pusher Geared Open Rotor—Part II: Impact on Fuel Consumption, Engine Weight, Certification Noise, and NO_x Emissions, *J. Eng. Gas Turbines Power.* 138 (2016) 072603. doi:10.1115/1.4032009.
- [66] G.A. Bobula, W.T. Wintucky, J.G. Castor, Compound cycle engine program, NASA-TM-88879, 1986. <http://hdl.handle.net/2060/19870002357>.
- [67] G. Smith, W.P. Afb, M. Boruta, Meyer Nutating Disk Engine, a New Concept in Internal Combustion Engine Technology, 43rd AIAA/ASME/SAE/ASEE Jt. Propuls. Conf. Exhib. 8-11 July. (2007) 1–8. doi:10.2514/6.2007-5122.
- [68] N. Nygen, A. Cutler, Pressure and Thrust Measurements of a High-Frequency Pulsed-Detonation Tube, in: 44th AIAA/ASME/SAE/ASEE Jt. Propuls. Conf. Exhib., 2008.
- [69] G. Lenoble, Performance Analysis of a Wave Rotor Topping Unit with Constant Volume Combustion, PhD thesis, Cranfield University, 2008.
- [70] N. Nguyen, a D. Cutler, I. Introduction, P.D. Engines, Pressure and Thrust Measurements of a High-Frequency Pulsed Detonation Tube, Combustion. (2008) 1–11.
- [71] C. Xisto, F. Ali, O. Petit, A. Lundbladh, A. Rolt, Analytical Model for the Performance

- Estimation of Pre-cooled pulse detonation turbofan engines, (2017) 1–14.
- [72] J. Sebastianpillai, F. Jacob, A. Rolt, Ultimate deliverable 1.3: Preferred nutating disc topping and bottoming cycle configurations. Confidential ULTIMATE report, 2017.
- [73] W.J. Anderson, Analysis of the Dynamics of a Nutating Body, NASA TN D-7569, 1974.
- [74] P. Wigful, The romping lion, the story of the Dakeyne engine, 3rd editio, Country books, 2011.
- [75] D.B. Day, Nutating Disc Internal Combustion Engine, 3102517, 1963.
- [76] L. Meyer, Nutating Internal Combustion engine, 5251594, 1993.
- [77] McMaster, Wobble Engine, 2002/0043238 A1, 2002.
- [78] T. Korakianitis, L. Meyer, M. Boruta, H.E. McCormick, One-Disk Nutating-Engine Performance for Unmanned Aerial Vehicles, J. Eng. Gas Turbines Power. 126 (2004) 475. doi:10.1115/1.1496770.
- [79] G. Smith, P. Meitner, J. Jerovsek, M. Boruta, Meyer Nutating Disc Engine: A New Concept in Internal Combustion Engine Technology, 43rd AIAA/ASME/SAE/ASEE Jt. Propuls. Conf. & Exhib. (2007) 1–8. doi:10.2514/6.2007-5122.
- [80] D. Wilson, T. Korakianitis, The design of High-efficiency Turbomachinery and Gas trubines, 2nd editio, The MIT Press, Cambridge, Massachussets, 2014.
- [81] B.R.D.S. Ribeiro, Thermodynamic Optimization of Spark Ignition Engines under Part Load Conditions, PhD thesis, Universidade Do Minho, 2006.
- [82] R. Mohanarangan, Development of a Performance Simulation Model for the Nutating Disk Engine, MSc thesis, Cranfield University, 2015.
- [83] D.A. Quintana, Implementation of the nutating disc engine in a high bypass turbofan engine, MSc thesis, Cranfield University, 2015.
- [84] N. L., 3D URANS CFD study of a nutating disc engine compressor, MSc thesis, Cranfield University, 2017. doi:N/A.
- [85] N. Liberti, 2D URANS CFD study of a nutating disc engine combustion chamber, MSc thesis, Cranfield University, 2017.
- [86] M. Kormann, R. Schaber, An intercooled recuperative aero engine for regional jets, in: Proc. ASME Turbo Expo 2014 Turbine Tech. Conferr. Expo., 2014.
- [87] X. Zhao, T. Grönstedt, Conceptual design of a two-pass cross-flow aeroengine intercooler,

- Proc. Inst. Mech. Eng. Part G J. Aerosp. Eng. 229 (2015) 2006–2023. doi:10.1177/0954410014563587.
- [88] X. Zhao, T. Gronstedt, K. Kyprianidis, Assessment of the performance potential for a two pass cross-flow intercooler for aero applications, in: ISABE, n.d.
- [89] A. Alexiou, T. Tsalavoutas, TURBO 3.2 Library Reference Manual, Emoresarios Agrupados Internacional S.A., 2013. doi:N/A.
- [90] K. Vogeler, The potential of sequential combustion for high bypass jet engine, in: Int. Gas Turbine Aeroengine Congr. Exhib., 1996.
- [91] A. Pellegrini, T. Nikolaidis, V. Pachidis, S. Köhler, On the performance simulation of inter-stage turbine reheat, Appl. Therm. Eng. 113 (2017) 544–553. doi:10.1016/j.applthermaleng.2016.10.034.
- [92] Y. Levy, V. Sherbaum, V. Erenburg, Flameless Oxidation Combustor development for a sequential combustion hybrid turbofan engine, in: Proc. ASME Turbo Expo 2016 Turbomach. Tech. Conf. Expo., 2016.
- [93] D. University, Ahead Project website, (2016). <http://www.ahead-euproject.eu>.
- [94] V.M. Bueno, 3D LES-RANS CFD Studies of a Novel Secondary Combustor concept for Low-NOx Emissions, MSc thesis, Cranfield university, 2018.
- [95] PROOSIS, (2016). doi:N/A.
- [96] P. Heinemann, S. Kaiser, MS2: Advanced tube and wing trade factors provided to WP1, (2016) 1–8. doi:N/A.
- [97] NEWAC, Specification Review Report of TERA2020 sub-modules, 2008. doi:no. R1.2.2K.
- [98] SAE, Engine Station Numbering and Nomenclature, SAE ARP755A, 1991.
- [99] Fan Rotor, J. Propuls. (1992) 200.
- [100] G. Accession, R. Date, Experimental Quiet engine program- summary report, NASA-CR-2519, 1975.
- [101] G.L. Converse, R.G. Giffin, Extended Parametric Representation of compressor Fans and turbines, 1984.
- [102] R.M. Plencer, Plotting component Maps in the Navy/NASA Engine Program (NNEP)-A Method and its usage, NASA TM 101433, 1989.
- [103] Diesinger, Linke, Systems of commercial turbofan engines: An introduction to systems

- functions, Springer, New York, 2008.
- [104] R.G. Stabe, W.J. Whitney, T.P. Moffit, Performance of High-Work Low Aspect Ratio turbine tested with a Realistic inlet Radial Temperature Profile, NASA TM 83655, 1984.
 - [105] G.K. Serovy, AGARD LS 83: Compressor and Turbine Prediction System Development - Lessons from Thirty Years of History, 1976.
 - [106] EASA, Type Certificate Data Sheet, 2012.
 - [107] Z. Heinemann, P., Panagiotou, P., Vratny, P., Kaiser, S., Vlahostergios, D2.1 Year 2000 reference aircraft and Year 2050 ATW models for intercontinental long-range and intra-european short-range configurations, 2017.
 - [108] W.. Nelson, Airplane propeller principles, J. Wiley & sons, Inc.; London, Chapman & Hall, Ltd, New York, 1944.
 - [109] S.C. Playle, K.D. Korkan, E. Von Lavantej, A Numerical Method for the Design and Analysis of Counter-Rotating Propellers, J. Propuls. 2 (1986).
 - [110] G.A. Mitchell, Experimental aerodynamic performance of advanced 40 deg-swept 10-blade propeller model at Mach 0.6 to 0.85, NASA TM-88969, 1988.
 - [111] D.C. Mikkelson, Summary of Recent NASA Propeller Research, NASA-TM-83733, n.d.
 - [112] T. Sinnige, THE EFFECT OF PYLON TRAILING EDGE BLOWING ON THE PERFORMANCE AND NOISE PRODUCTION OF A PROPELLER, in: 29th Congr. Int. Counc. Aeronaut. Sci., St. Petersburg, 2014.
 - [113] G. Gentry, E. Booth, M. Takallu, Effect of Pylon Wake With and Without Pylon Blowing on propeller Thrust, NASA-TM-4162, 1990.
 - [114] B. Chandrasekeran, Method for the prediction of the installation aerodynamics of a propfan at subsonic speeds, NASA CR-3887, 1985.
 - [115] D. Parzych, A. Shenkman, S. Cohen, Large Scale Advanced Prop-fan (LAP) Performance, Acoustic and weight estimation CR-174782, 1985.
 - [116] J.H. Horlock, Axial Flow Turbines: Fluid Mechanics and thermodynamics, Butterworths, London, 1966.
 - [117] H. J.B., Internal Combustion engine Fundamentals, 2nd ed., McGraw-Hill, 1988.
 - [118] R.J. Pearson, W. D.E., A Rapid Synthesis Technique for Intake Manifold Design, Int. J. Vehicle Des. (1989) 659–86. doi:N/A.

- [119] W.M. Kays, A.L. London, Compact Heat Exchangers, 3rd Editio, Krieger Pub Co, 1998.
- [120] P.M. Came, C.J. Robinson, Centrifugal compressor design, Proc. Inst. Mech. Eng. Part C J. Mech. Eng. Sci. 213 (1998) 139–155. doi:10.1243/0954406991522239.
- [121] E. Onat, G.W. Klees, A Method to estimate weight and dimensions of large and small gas turbines, NASA CR-199481, 1979.
- [122] P. Bellocq, I. Garmendia, V. Sethi, A. Patin, S. Capodanno, F. Rodriguez Lucas, Multidisciplinary Assessment of the Control of the Propellers of a Pusher Geared Open Rotor—Part I: Zero-Dimensional Performance Model for Counter-Rotating Propellers, J. Eng. Gas Turbines Power. 138 (2016) 072602. doi:10.1115/1.4032008.
- [123] Bansal R.K, Strength of Materials, 4th ed., Laxmi Publications, Mumbai, 2010. doi:N/A.
- [124] Haynes, HASTELLOY ® X alloy, Haynes International, 2017. <http://haynesintl.com/docs/default-source/pdfs/new-alloy-brochures/high-temperature-alloys/brochures/x-brochure.pdf?sfvrsn=12>.
- [125] T.V. Vu, Minimum weight design for toroidal pressure vessels using differential evolution and particle swarm optimization, Struct. Multidiscip. Optim. 42 (2010) 351–369.
- [126] H. Grieb, W. Klussman, Regenerative Helicopter Engine, American Helicopter Society, in: No. 302, AGARD-CP-302 57th Spec. Meet. AGARD Propuls. Energ. Panel, Toulouse, France, 1981.
- [127] M. Syed, Assesment of Conceptual, more efficienct and low emission Helicopter powerplant cycles, MSc. thesis, Cranfield university, 2012.
- [128] P. Koch, ISIGHT Reference Guide, 2010.
- [129] M. Pleguezuelos, P. Pedrero, M. Sanchez, Analytical Expressions of the Efficiency of Standard and High Contact Ratio Involute Spur Gears, Math. Probl. Eng. 2013 (2013).
- [130] W. Camilleri, E. Anselmi, V. Sethi, P. Laskaridis, T. Grönstedt, X. Zhao, A. Rolt, P. Cobas, Concept description and assessment of the main features of a geared intercooled reversed flow core engine, Proc. Inst. Mech. Eng. Part G J. Aerosp. Eng. 229 (2015) 1631–1639. doi:10.1177/0954410014557369.
- [131] N. Cumpsty, Compressor Aerodynamics, Longman Scientific & Technical, 1989.
- [132] Department of Defense, Integrated Product and Process Development Handbook, (1998).
- [133] P. Manovski, J. Wehrmeyer, K. Scott, B. Loxton, H. Quick, S. Lam, M. Giacobello, A Performance Comparison between Classical Schlieren and Background-Oriented

- Schlieren, (2016).
http://lces.dem.ist.utl.pt/lxllaser/lxllaser2016/finalworks2016/papers/02.1_2_293paper.pdf
 .
- [134] I. Mohammed, A.R.A. Talib, M.T.H. Sultan, S. Saadon, Temperature and heat flux measurement techniques for aeroengine fire test: a review, *IOP Conf. Ser. Mater. Sci. Eng.* 152 (2016) 012036. doi:10.1088/1757-899X/152/1/012036.
- [135] C.E. Willert, M. Gharib, Digital particle image velocimetry, *Exp. Fluids.* 10 (1991) 181–193. doi:10.1007/BF00190388.
- [136] H. Zhuang, D.L.S. Hung, Characterization of the effect of intake air swirl motion on time-resolved in-cylinder flow field using quadruple proper orthogonal decomposition, *Energy Convers. Manag.* 108 (2016) 366–376. doi:10.1016/j.enconman.2015.10.080.
- [137] J.F. Lafferty, A.S. Collier, Infrared surface temperature measurements in NAVSWC's hypervelocity wind tunnel No. 9, *ICIASF Rec. Int. Congr. Instrum. Aerosp. Simul. Facil.* (1991) 169–177. <https://www.scopus.com/inward/record.uri?eid=2-s2.0-0026399463&partnerID=40&md5=7b73ede716acd06ac9d9006312e43294>.
- [138] Xiaojian Yang, Guoming G. Zhu, A two-zone control oriented SI-HCCI hybrid combustion model for the HIL engine simulation, *2011 Am. Control Conf.* (2011) 973–978.
- [139] J.I. Ghojel, Review of the development and applications of the Wiebe function: A tribute to the contribution of Ivan Wiebe to engine research, *Int. J. Engine Res.* 11 (2010) 297–312. doi:10.1243/14680874JER06510.
- [140] D.A. Kouremenos, C.D. Rakopoulos, D. Hountalas, Thermodynamic Analysis of Indirect Injection Diesel Engines by Two-Zone Modeling of Combustion, *J. Eng. Gas Turbines Power.* 112 (1990) 138–149. doi:10.1115/1.2906468.
- [141] G.M. Shaver, M.J. Roelle, J.C. Gerdes, Modeling cycle-to-cycle dynamics and mode transition in HCCI engines with variable valve actuation, *Control Eng. Pract.* 14 (2006) 213–222. doi:10.1016/j.conengprac.2005.04.009.
- [142] M. Ganesan, S. Sendilvelan, Experimental Analysis of Telescopic Catalytic Converter in a Petrol Engine to Reduce Cold Start Emission, *Int. J. Eng. Res. Africa.* 25 (2016) 28–35. doi:10.4028/www.scientific.net/JERA.25.28.
- [143] C. Xisto, M1.1 – Intercooler and pulse detonation technology simulators, 2016.
- [144] S. Ogaji, P. Pilidis, R. Hales, TERA - a tool for aero-engine modelling and management, *Second World Congr. Eng. Asset Manag. Fourth Int. Conf. Cond. Monit.* (2007) 12.
- [145] S. Samuelsson, Gt2015-43331 Consistent Conceptual Design and Performance

- Modeling, (2017) 1–10.
- [146] A.J. Glassman, Users Manual for Updated Computer Code for Axial-Flow Compressor Conceptual Design, NASA-CR-189171, 1992.
 - [147] S.C. Kacker, U. Okapuu, A Mean Line Prediction Method for Axial Flow Turbine Efficiency, *J. Eng. Power.* 104 (1982) 111. doi:10.1115/1.3227240.
 - [148] R.H. Augnier, *Turbine aerodynamics: axial-flow and radial-inflow turbine design and analysis*, ASME Press, New York, 2006.
 - [149] Tong, Thurman, Guynn, Conceptual Design Study of an Advanced Technology Open Rotor Propulsion System, in: ISABE-2011-1311, ISABE, 2011.
 - [150] J.W. Gauntner, Algorithm for Calculating Turbine Cooling Flow and the Resulting Decrease in Turbine Efficiency, NASA TM-81453, 1980.
 - [151] R.C. Wilcock, J.B. Young, J.H. Horlock, The Effect of Turbine Blade Cooling on the Cycle Efficiency of Gas Turbine Power Cycles, *J. Eng. Gas Turbines Power.* 127 (2005) 109. doi:10.1115/1.1805549.
 - [152] M. Elter, J. Sebastiampillai, Development of an aero engine life prediction methodology for preliminary design multi-disciplinary optimisation assessments, in: ISABE, Manchester, 2017.
 - [153] NASA, OpenVSP, (2018).
 - [154] T. MacDonald, SUAVE, Stanford Aerospace Design Lab, (2017). <http://suave.stanford.edu/download/>.
 - [155] A. Prakash, Prediction of NOx emissions for an RQL combustor using a stirred reactor modelling approach, PhD thesis, Cranfield University, 2015.
 - [156] C. Goldberg, D. Nalianda, P. Pilidis, R. Singh, Economic Viability Assessment of NASA's Blended Wing Body N3-X Aircraft, 53rd AIAA/SAE/ASEE Jt. Propuls. Conf. (2017) 10–12. doi:10.2514/6.2017-4604.

APPENDIX-A

Table A1: Performance overview of the M-GOR2050 configuration

	Parameter	Units	CR			TOC	EOR
			SN	CU	Dev. (%)	CU	CU
General	Mach no	-	0.75	0.75	0.00	0.75	0.2
	Altitude	km	11.9	11.9	0.00	11.9	0.35
	dT ISA	K	0	0	0.00	10	28
	FHV	MJ/kg	42.8	42.8	0.00	42.8	42.8
	HP shaft power extraction	kW	77.5	77.5	0.00	77.5	322.7
	Total Thrust	N	16707	16707	0.00	18669	72321
	OPR	-	48.4	48.4	0.00	53.6	35.1
	TSFC	g/kNs	11.44	11.44	0.04	12.11	7.44
	W	kg/s		9.5		10.11	22.24
	Thermal Efficiency	-	0.465	0.468	0.58	0.453	0.310
	Propulsive Efficiency	-	0.948	0.961	1.39	0.957	0.736
Thermopropulsive Efficiency	-	0.441	0.450	1.94	0.434	0.228	
CRP array	Forward Propeller Diameter	m	4.27	4.27	0.00	4.27	0
	Rear Propeller Diameter	m	3.73	3.73	0.00	3.73	3.73
	Rear propeller pitch	deg.		30		30	57
	Forward Propeller loading	kW/m ²		188		221	413
	Rear Propeller loading	kW/m ²		208		244	457
	Forward propeller U at 0.75R	m/s		122		122	122
	Rear propeller U at 0.75R	m/s		107		107	107

	Parameter	Units	CR			TOC	EOR
			SN	CU	Dev. (%)	CU	CU
	Nacelle Diameter	m	1.6	1.6	0.00	1.6	1.6
	Percentage clipping	%	20	20	0.00	20	20
	H/T Propeller:nacelle	-	0.376	0.376	0.00	0.376	0.376
	relative spacing	-		0.29		0.29	0.29
	Forward Propeller C _p map	-		1.67		1.67	1.67
	Rear Propeller C _p map	-		1.67		1.67	1.67
	Forward Propeller J _{map}	-		2.30		2.30	2.30
	Rear Propeller J _{map}	-		2.30		2.30	2.30
	Forward and Rear PropellerTF	-		1.795		1.795	1.795
	BnBf	-		15		15	15
	BnBr	-		13		13	13
	Forward Propeller Eta	-		0.860		0.834	0.695
	Rear Propeller Eta	-		0.850		0.823	0.717
IPC	IPC PR (dP24qP20)	-	8.8	8.8	0.00	9.53	6.75
	IPC polytropic efficiency (EP23)	-	0.924	0.924	0.00	0.926	0.889
	IPC NcrDesMap	-		0.85		0.896	0.731
	IPC NcDes	-		0.9		0.949	0.774
	dP25qP24	%		1.43		1.43	1.43
	IPC W_bld			1.76		1.76	1.76
	HPC polytropic efficiency (EP27)	-	0.899	0.899	0.00	0.898	0.899

	Parameter	Units	CR			TOC	EOR
			SN	CU	Dev. (%)	CU	CU
	HPC MN_out	-				0.25	0.25
	HPC H/T ratio	-		0.895		0.895	0.895
	HPC LSBH	mm		12.25		12.25	12.25
	HPC W_bld 1	%		3.0		3.0	3.0
	dP30qP27	%		2.0		2.0	2.0
Burner	dP40qP30	%		4.0		4.0	4.0
	Burner efficiency (E3)	-		0.999995		0.999995	0.999995
HPT	COT (T40)	K		1660		1794	1939
	HPT TET* (T41)	K	1606	1606	0.00	1735	1877
	HPT isentropic efficiency (E4)	-	0.917	0.917	0.00	0.918	0.917
	HPT Tblade (Tm41)	K		1185		1278	1394
	HP Nmech	rpm		13850		14465	15000
	H/T	-		0.875		0.875	0.875
	MN	-					0.3
	AN2	rpm ^{2*} m ²		6 X 10 ⁶		6 X 10 ⁶	7 X 10 ⁶
	dP43qP42	%		2.5		2.5	2.5
	NcDes	-		0.85		0.86	0.85
	NcRdesMap	-		0.96		0.97	0.96
HPT cooling	WNGV (Fractional bleed in NGV)	%		0.45		0.45	0.45
	Wpump (Fractional bleed in rotor)	%		0.55		0.55	0.55
	Wtw/Wc (fractional bleed doing work)	-		0.8		0.8	0.8
	Cooling air constant	-		0.05		0.05	0.05
	Relative Temperature multiplier	-		0.9		0.9	0.9
IPT	IPT SIT (T43)	K		1268		1375	1491

	Parameter	Units	CR			TOC	EOR
			SN	CU	Dev. (%)	CU	CU
	IPT TET (T44)	K		1255		1360	1476
	IPT isentropic efficiency (E43)	-	0.948	0.948	0.00	0.951	0.940
	IPT Nmech	rpm		10145		10940	10000
	H/T	-		0.8		0.8	0.8
	MN	-					0.45
	AN2	rpm ^{2*} m ²		4E+06		5E+06	4E+06
	dP46qP45	%		2.4		2.4	2.4
	NcRDes	-		0.90		0.95	0.77
	NcRdesMap	-		0.89		0.92	0.81
IPT cooling	Fractional bleed in NGV (WNGV)	%		0.45		0.45	0.45
	Wpump (Fractional bleed in rotor)	%		0.50		0.50	0.50
	Wtw/Wc (fractional bleed doing work)	-		0.94		0.94	0.94
	Cooling air constant	-		0.05		0.05	0.05
	Relative Temperature multiplier	-		0.9		0.9	0.9
LPT	LPT SIT (T46)	K		1061		1152	1260
	LPT TET (T47)	K		1061		1152	1260
	LPT isentropic efficiency (E5)	-		0.945		0.932	0.943
	LPT Tblade (Tm47)	K		773		837	926
	EGT (T5)	K		650		706	891
	LPT Nmech	rpm		6760		6760	6760
	H/T	-		0.700		0.700	0.700
	MN	-					0.55
	AN2	rpm ^{2*} m ²		6E+06		6E+06	6E+06

	Parameter	Units	CR			TOC	EOR
			SN	CU	Dev. (%)	CU	CU
	dP50qP47	-		0.81		0.81	0.83
	NcRDes	-		0.90		0.86	0.83
	NcRdesMap	-		1.09		1.05	1.00
	DPGB torque ratio (TR)	-		1.242		1.242	1.242
	DPGB HeatLoss	W		54611		57822	68767
	DPGB Carrier Nmech	rpm		731		731	731
	DPGB Carrier trq	Nm		30019		35333	66090
	DPGB Ring Nmech	rpm		-731		-731	-731
	DPGB Ring trq	Nm		-24162		-28439	-53196
	DPGB Sun trq	Nm		5934		6975	12992
DPGB cooling system	Scoop Inlet W	kg/s		1.19		1.16	5.61
	Blower Power offtake	W		0		0	-245157
	Blower E	-		0.880		0.880	0.880
	HX Effectiveness	-		0.92		0.92	0.92
	HX dPqP	-		0.02		0.02	0.02
	Scoop Nozzle Aexit	m ²		0.019		0.019	0.019
	Net Thrust	N		22		23	1229
Nozzle	Cd	-		0.991		0.991	0.991
	Cx	-		0.994		0.994	0.994
	Alpha	deg.		9.5		9.5	9.5
	A _{exit}	m ²		0.395		0.395	0.395
	V out	m/s		218		250	145

Table A2: XX-GOR2050 performance

	<u>Parameter</u>	<u>Units</u>	<u>TOC</u>		
			<u>E1</u>	<u>E2</u>	<u>E3</u>
General	Mach no	-	0.73	0.73	0.73
	Altitude	m	10688	10688	10688
	dT ISA	K	10	10	10
	FHV	MJ/kg	42.8	42.8	42.8
	HP shaft power extraction	kW	0	0	0
	Total Thrust	N	18000	22200	25000
	OPR	-	52.78	55.82	59.22
	TSFC	g/kNs	10.85	10.61	10.35
	W	kg/s	8.23	10.04	11.19
CRP ARRAY	Forward Propeller Diameter	m	4.0	4.2	4.5
	Rear Propeller Diameter	m	3.5	3.7	3.9
	Forward propeller pitch	deg.	21	20	19
	Rear propeller pitch	deg.	26	26	25
	Forward Propeller loading	kW/m ²	221	221	221
	Rear Propeller loading	kW/m ²	245	266	261
	Forward propeller U at 0.75R	m/s	86	83	80
	Rear propeller U at 0.75R	m/s	75	73	70
	Percentage clipping	%	20	20	20
	H/T Propeller:nacelle	-	0.38	0.38	0.38
	relative spacing	-	0.29	0.29	0.29
	Forward Propeller C _p map	-	1.67	1.67	1.67

	<u>Parameter</u>	<u>Units</u>	<u>TOC</u>		
			<u>E1</u>	<u>E2</u>	<u>E3</u>
	Rear Propeller Cpmap	-	1.67	1.67	1.67
	Forward Propeller Jmap	-	2.30	2.30	2.30
	Rear Propeller Jmap	-	2.30	2.30	2.30
	Forward Propeller TF	-	1.80	1.80	1.80
	Rear PropellerTF	-	1.80	1.65	1.69
	BnBf	-	15	15	15
	BnBr	-	13	13	13
	Forward Propeller Eta	-	0.83	0.83	0.83
	Rear Propeller Eta	-	0.82	0.82	0.82
IPC	IPC PR (dP24qP20)	-	9.46	9.72	10.02
	IPC polytropic efficiency (EP23)	-	0.926	0.926	0.926
	IPC NcrDesMap	-	0.99	0.99	0.99
	IPC NcDes	-	0.95	0.95	0.95
	dP25qP24	%	1.43	1.43	1.43
	IPC W_bld	%	1.76	1.76	1.76
HPC	HPC PR (dP27qP25)	-	5.66	5.82	6.00
	HPC polytropic efficiency (EP27)	-	0.886	0.892	0.894
	HPC (EP27 deviation)	%	-1.36%	-0.72%	-0.49%
	HPC H/T ratio	-	0.895	0.895	0.895
	HPC LSBH	mm	10.29	11.10	11.44

	<u>Parameter</u>	<u>Units</u>	<u>TOC</u>		
			<u>E1</u>	<u>E2</u>	<u>E3</u>
	HPC W_bld 1	%	3	3	3
	HPC W_bld2	%	13.9	13.9	13.9
	dP30qP27	%	2	2	2
BURNER	dP40qP30	%	4	4	4
	Burner efficiency (E3)	-	0.99995	0.99995	0.99995
HPT	COT (T40)	K	1809	1808	1808
	HPT TET* (T41)	K	1750	1750	1750
	HPT polytropic efficiency (EP4)	-	0.903	0.906	0.907
	HPT polytropic efficiency deviation	%	-0.73%	-0.41%	-0.31%
	HPT Tblade (Tm41)	K	1289	1293	1298
	dP43qP42	%	2.5	2.5	2.5
	NcDes	-	0.85	0.85	0.85
	NcRdesMap	-	0.96	0.96	0.96
HPT COOLING	WNGV (Fractional bleed in NGV)	%	0.45	0.45	0.45
	Wpump (Fractional bleed in rotor)	%	0.55	0.55	0.55
	Wtw/Wc (fractional bleed doing work)	-	0.8	0.8	0.8
	Cooling air constant	-	0.05	0.05	0.05

	<u>Parameter</u>	<u>Units</u>	<u>TOC</u>		
			<u>E1</u>	<u>E2</u>	<u>E3</u>
	Relative Temperature multiplier	-	0.9	0.9	0.9
IPT	IPT SIT (T43)	K	1379	1387	1393
	IPT TET (T44)	K	1373	1380	1386
	IPTpoly efficiency (EP43)	-	0.926	0.926	0.926
	IPT Tblade (Tm44)	K	1227	1223	1217
	IPT Nmech	rpm	5359	5582	8325
	dP46qP45	%	2.4	2.4	2.4
	NcRDes	-	0.9	0.9	0.9
	NcRdesMap	-	0.888	0.888	0.888
IPT COOLING	Fractional bleed in NGV (WNGV)	%	0.45	0.45	0.45
	Wpump (Fractional bleed in rotor)	%	0.498	0.498	0.498
	Wtw/Wc (fractional bleed doing work)	-	0.94	0.94	0.94
	Cooling air constant	-	0.05	0.05	0.05
	Relative Temperature multiplier	-	0.9	0.9	0.9
LPT	LPT SIT (T46)	K	1149	1161	1170
	LPT TET (T47)	K	1149	1161	1170
	LPT isentropic efficiency (E5)	-	0.932	0.932	0.932

	<u>Parameter</u>	<u>Units</u>	<u>TOC</u>		
			<u>E1</u>	<u>E2</u>	<u>E3</u>
	LPT Tblade (Tm47)	K	847	843	839
	EGT (T5)	K	718	722	706
	LPT Nmech	rpm	5115	7516	6282
	dP50qP47	-	0.80	0.81	0.80
	NcRDes	-	0.86	0.86	0.86
	NcRdesMap	-	1.05	1.05	1.05
DPGB	DPGB (E_mech)	-	0.988	0.988	0.988
	DPGB torque ratio (TR)	-	1.241	1.143	1.156
	DPGB HeatLoss	W	50129	59270	66627
	DPGB Carrier Nmech	rpm	550	501	454
	DPGB Carrier trq	Nm	40689	50831	63371
	DPGB Ring Nmech	rpm	-550	-501	-454
	DPGB Ring trq	Nm	-32790	-44474	-54823
	DPGB Sun trq	Nm	7992	6432	8649
DPGB COOLING SYSTEM	Scoop Inlet W	kg/s	1.090	1.288	1.448
	HX Effectiveness	-	0.92	0.92	0.92
	HX dPqP	-	0.02	0.02	0.02
	Scoop Nozzle Aexit	m ²	0.015	0.018	0.020
	Net Thrust	N	19	23	25
NOZZLE	Cd	-	0.991	0.991	0.991
	Cx	-	0.994	0.994	0.994

	<u>Parameter</u>	<u>Units</u>	<u>TOC</u>		
			<u>E1</u>	<u>E2</u>	<u>E3</u>
	Alpha	deg.	9.5	9.5	9.5
	Aexit	m ²	0.298	0.284	0.353
	V out	m/s	239	300	266

Table A3: Reference GOR2050 performance

	<u>Parameter</u>	<u>Units</u>	<u>TOC</u>	<u>CR</u>	<u>EOR</u>
GENERAL	Mach no	-	0.73	0.71	0.2
	Altitude	m	10688	11277.6	0
	dT ISA	K	10	0	15
	FHV	MJ/kg	42.8	42.8	42.8
	HP shaft power extraction	kW	0	0	0
	Total Thrust	kN	17.34	13.85	78.95
	OPR	-	41.14	36.81	33.40
	W	Kg/s	7.08	6.17	17.43
	TSFC	g/(kN*s)	10.75	10.41	6.44
CRP ARRAY	Forward Propeller Diameter	m	4.0	4.0	4.0
	Rear Propeller Diameter	m	3.5	3.5	3.5
	Forward Propeller loading	kW/m ²	180	136	415
	Rear Propeller loading	kW/m ²	224	170	519
	Percentage clipping	%	20	20	20
	H/T Propeller:nacelle	-	0.38	0.38	0.38
	Forward Propeller Cpmap	-	1.67	1.67	1.67

	<u>Parameter</u>	<u>Units</u>	<u>TOC</u>	<u>CR</u>	<u>EOR</u>
	Rear Propeller Cpmap	-	1.67	1.67	1.67
	Forward Propeller Jmap	-	2.30	2.30	2.30
	Rear Propeller Jmap	-	2.30	2.30	2.30
	BnBf	-	15	15	15
	BnBr	-	13	13	13
	Forward Propeller Eta	-	0.83	0.87	0.58
	Rear Propeller Eta	-	0.82	0.85	0.58
IPC	IPC PR (dP24qP20)	-	8.35	8.22	7.47
	IPC polytropic efficiency (EP23)	-	0.926	0.939	0.933
	IPC NcrDesMap	-	0.99	0.93	0.89
	IPC Ncrdes	-	0.87	0.83	0.82
	dP25qP24	%	1.43	1.43	1.43
	IPC W_bld	%	1.76	1.76	1.76
HPC	HPC PR (dP27qP25)	-	5.00	4.54	4.54
	HPC polytropic efficiency (EP27)	-	0.890	0.892	0.891
	HPC H/T ratio	-	0.895	0.895	0.895
	HPC LSBH	mm	10.85	10.85	10.85
	HPC W_bld 1	%	3	3	3
	HPC W_bld2	%	13.9	13.9	13.9
	dP30qP27	%	2	2	2
BURNER	dP40qP30	%	4	4	4

	<u>Parameter</u>	<u>Units</u>	<u>TOC</u>	<u>CR</u>	<u>EOR</u>
	Burner efficiency (E3)	-	0.9999 5	0.9999 5	0.99995
HPT	COT (T40)	K	1812	1687	2019
	HPT TET* (T41)	K	1750	1628	1950
	HPT polytropic efficiency (EP4)	-	0.914	0.898	0.905
	HPT Tblade (Tm41)	K	1233	1139	1374
	dP43qP42	%	2.5	2.5	2.5
	NcRdes	-	0.86	0.81	0.83
	NcRdesMap	-	0.97	0.91	0.93
	HPT Nmech	rpm	8637	7869	8810
HPT COOLING	WNGV (Fractional bleed in NGV)	%	0.45	0.45	0.45
	Wpump (Fractional bleed in rotor)	%	0.55	0.55	0.55
	Wtw/Wc (fractional bleed doing work)	-	0.8	0.8	0.8
	Cooling air constant	-	0.05	0.05	0.05
	Relative Temperature multiplier	-	0.9	0.9	0.9
IPT	IPT SIT (T43)	K	1381	1276	1560
	IPT TET (T44)	K	1374	1269	1551
	IPTpoly efficiency (EP43)	-	0.951	0.946	0.945
	IPT Tblade (Tm44)	K	1216	1123	1373

	<u>Parameter</u>	<u>Units</u>	<u>TOC</u>	<u>CR</u>	<u>EOR</u>
	IPT Nmech	rpm	8392	7648	8289
	dP46qP45	%	2.4	2.4	2.4
	NcRDes	-	0.9	0.9	0.9
	NcRdesMap	-	0.888	0.888	0.888
IPT COOLING	Fractional bleed in NGV (WNGV)	%	0.45	0.45	0.45
	Wpump (Fractional bleed in rotor)	%	0.498	0.498	0.498
	Wtw/Wc (fractional bleed doing work)	-	0.94	0.94	0.94
	Cooling air constant	-	0.05	0.05	0.05
	Relative Temperature multiplier	-	0.9	0.9	0.9
LPT	LPT SIT (T46)	K	1161	1072	1320
	LPT TET (T47)	K	1161	1072	1320
	LPT isentropic efficiency (E5)	-	0.932	0.944	0.928
	LPT Tblade (Tm47)	K	840	776	960
	EGT (T5)	K	726	672	910
	LPT Nmech	rpm	9491	9491	9491
	dP50qP47	-	0.80	0.80	0.82
	NcRDes	-	0.86	0.90	0.81
	NcRdesMap	-	1.05	1.09	0.99
DPGB	DPGB (E_mech)	-	0.988	0.985	0.994
	DPGB torque ratio (TR)	-	1.23	1.23	1.23

	<u>Parameter</u>	<u>Units</u>	<u>TOC</u>	<u>CR</u>	<u>EOR</u>
	DPGB HeatLoss	W	43828	41731	54385
	DPGB Carrier Nmech	rpm	452	452	452
	DPGB Carrier trq	Nm	40941	31071	94624
	DPGB Ring Nmech	rpm	-452	-452	-452
	DPGB Ring trq	Nm	-37219	-28246	-86021
	DPGB Sun trq	Nm	3766	2867	8657
DPGB COOLING SYSTEM	Scoop Inlet W	kg/s	0.95	0.86	4.15
	HX Effectiveness	-	0.92	0.92	0.92
	HX dPqP	-	0.02	0.02	0.02
	Scoop Nozzle Aexit	m ²	0.013	0.013	0.013
	Net Thrust	N	17	16	895
NOZZLE	Cd	-	0.991	0.991	0.991
	Cx	-	0.994	0.994	0.994
	Alpha	deg.	9.5	9.5	9.5
	Aexit	m ²	0.243	0.243	0.243
	NPR	-	1.35	1.27	1.13
	V out	m/s	287	246	210

APPENDIX-B

Aspects of the research objectives have been addressed through publications in journals and conferences, namely:

Jacob F., Rolt A., Sebastampillai J., Sethi V., Belmonte M., Cobas P. ; “Performance of a Supercritical CO₂ Bottoming Cycle for Aero Applications”. Published online: March 2017 in the Journal of Applied Sciences

Rolt A., Sethi V., Jacob F., Sebastiampillai J., Xisto C., Gronstedt T., Raffaelli L. ; “Scale effects on conventional and intercooled turbofan engine performance”. Published online: 08 June 2017 in the RAeS Aeronautical Journal.

Rolt A., Sethi V., Jacob F., Sebastiampillai J., Xisto C., Gronstedt T., Raffaelli L.; “Selecting Combinations of Advanced Aero Engine Technologies”. Accepted manuscript for publishing October 2017 for the ISABE 2017 conference.

Elter M., Sebastiampillai J., Nalianda D., Chatzianagnostou D., Goldberg C., Sethi V., Staudacher S.; “Development of an aero engine life prediction methodology for preliminary design multi-disciplinary optimization assessments”. Accepted manuscript for publishing October 2017 for the ISABE 2017 conference.

Sebastiampillai J., Rolt A., Jacob F., Sethi V., Nalianda D., Cobas P. : “Performance of nutating disc topping cycles for short range aero applications”. **Submitted** to Journal of Energy , December 2018(under review)

Sebastiampillai J., Roumeioloitis I., Nalianda D., Sethi V.: “Performance of intercooled-nutating disc engine topping cycles in year 2050 short range applications”. **Submitted** to Journal of Applied Energy, January 2018

Sebastiampillai J., Jacob F., Mastropierro F., Tantot N., Whurr J., Seitz A.: “Modelling Geared Turbofan and open rotor performance for year-2050 long range and short range aircraft”. **Under review for Journal of Engineering for gas turbines and power .**

Sebastiampillai J., Nalianda D., Sethi V., Mastropierro F.: “Technical and economic viability of an installed 2050 geared open rotor engine”. **Accepted for** ASME turbo expo 2019, October 2018

APPENDIX-C

Throughout the course of the research, the author has technically supported many students across many research areas. A few notable pieces of work are:

Thomas Cheval: Technically supported the MSc student looking at the mission fuel burn benefits, when considering an open rotor mounted to a tube and wing aircraft.

Yuqing Li: Technically supported the MSc student looking at the preliminary design of an axi-centrifugal compressor using artificial neural networks.

Luthfilaudri Nadihra: Technically supported student looking at predicting the volumetric and isentropic compression efficiency of a nutating disc engine compressor using 3D URANS methods.

Marvin Elter: Technically supported research student looking at the life characteristics of HPT blades and discs.

Angelo Ugenti: Technically supported student looking at 2D methods to predict the performance of a counter rotating propeller array.

Alberto Sanchez: Technically supported student looking at intercooling using hydrogen and the dual fuel combustion in a direct drive turbofan.

Nicola Liberti: Technically supported student looking at 2D methods to predict the combustion characteristics of a nutating disc engine.

Yann Schnorok: Technically supported student looking at preliminary lubrication system design of a differential planetary gearbox for a geared open rotor.

Francesco Moro: Technically supported student looking at preliminary intercooler design and possible integration in to a ND-geared open rotor engine configuration.

APPENDIX-D

The following figure and excerpt indicate how the non-linear fuel burn trade factors were used within this work. Figure D-1, show the format of the non-linear trade factors for technologies that were investigated on the geared open rotor platform. Essentially, the tables provided allow the user to re-rate the design thrust of the engine as a consequence of significant engine weight and fuel burn reduction. The non-linear trade factors can account for variations in total engine mass from 0.9 to 2 times the reference GOR2050 engine weight (specified in section 5). Furthermore, it can also account for TSFC variation from 0.8 to 1.05 times the nominal TSFC of the GOR2050 engine[96].

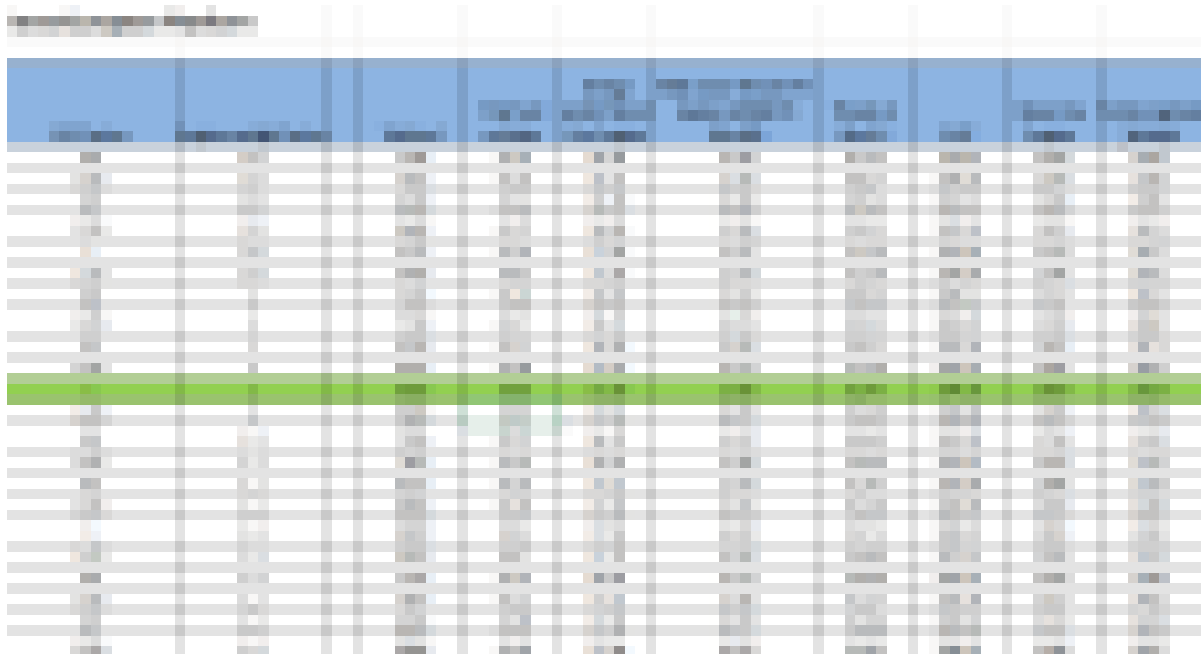


Figure D- 1: Snapshot of non-linear trade factors[96]

For instance, let us assume that by increasing the rotational speed of the contra rotating propellers in a particular design case, the mass of the engine increased by 10% and the TSFC at EOR,CR and TOC increased by 5%. Therefore, in the first instance we navigate to the row, in the non-linear trade factor, that has the same mass as the new engine design. This should produce a new TOC design thrust and subsequent CR and EOR thrust values. Once the engine performance model is re-run with the new thrust it will produce an engine mass and TSFC values at the three operating points. Consequently, the newly estimated TSFC must be compared against TSFC values in the table (with the new engine mass), this in turn should provide a new design thrust level. Once again the design thrust must be varied. Consequently, engine mass and thrust specific fuel consumption will vary and the iterative

procedure continues till the relative variation (from one iteration to another) in TSFC, thrust values and total engine weight becomes negligible (In all analyses the residual threshold was maintained at 0.02%). This condition generally occurs after four to 5 iterations. Once convergence has been achieved, the subsequent relative fuel burn value can be estimated.

APPENDIX-E

Table E-1, provides a comparative overview of the SRTF2000 engine model with the GOR2050 engine model.

Table E- 1: Comparison of SRTF2000 and GOR2050 key figures of merit

Parameter	SRTF2000	GOR 2050
Total engine weight (kg)	3086	3197
TOC TSFC (g/kN.s)	18.92	10.75
TOC Fn (kN)	30.08	17.34
OPR at TOC (-)	35.68	41.14
Maximum diameter (m)	2	4.2

Furthermore, Figure E-1 and Figure 5-19 (section 5) show the relative distribution of the mass for the SRTF2000 and GOR2050 respectively.

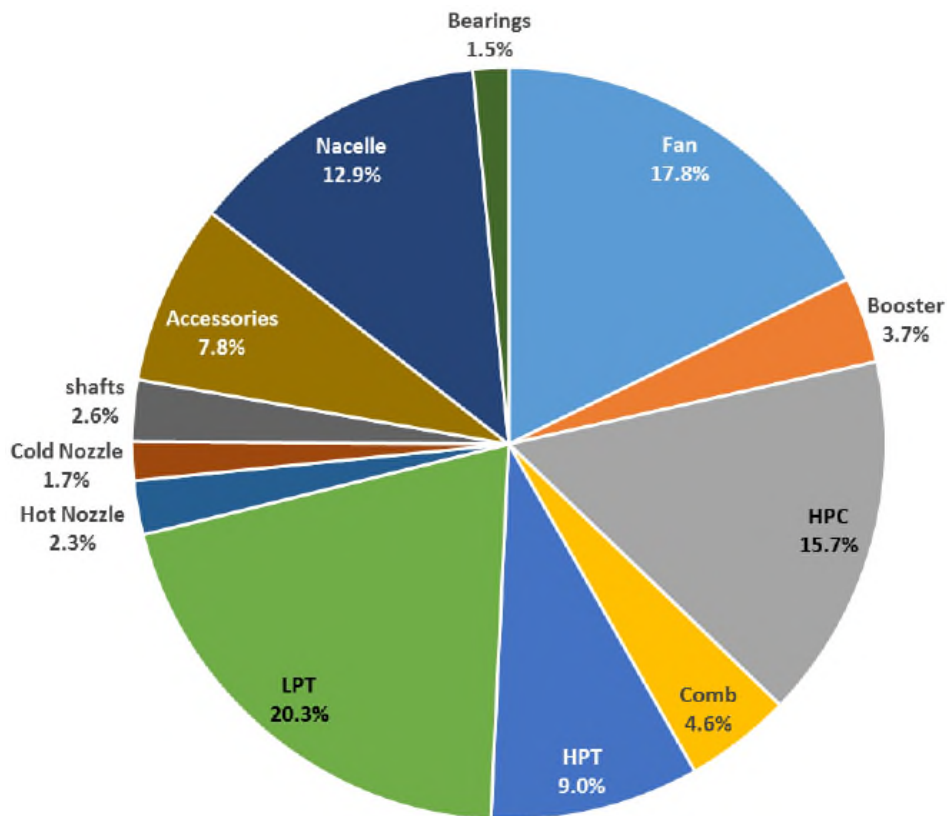


Figure E- 1:Normalized breakdown of engine weight SRTF2000[61]

In addition, to the normalized breakdown of the weight of the SRT2000 and the reference GOR2050 configuration Figures E-2 to E-7 shows the normalized weight distribution of the other engine configurations investigated in this thesis.

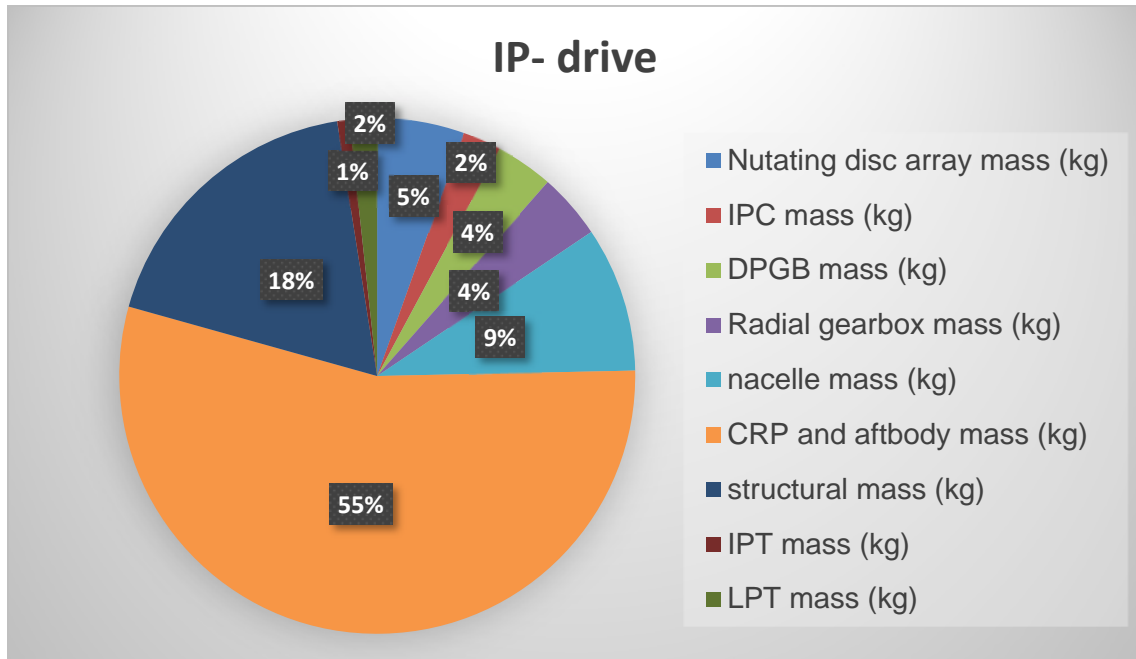


Figure E- 2: GOR2050 IP-drive configuration weight distribution

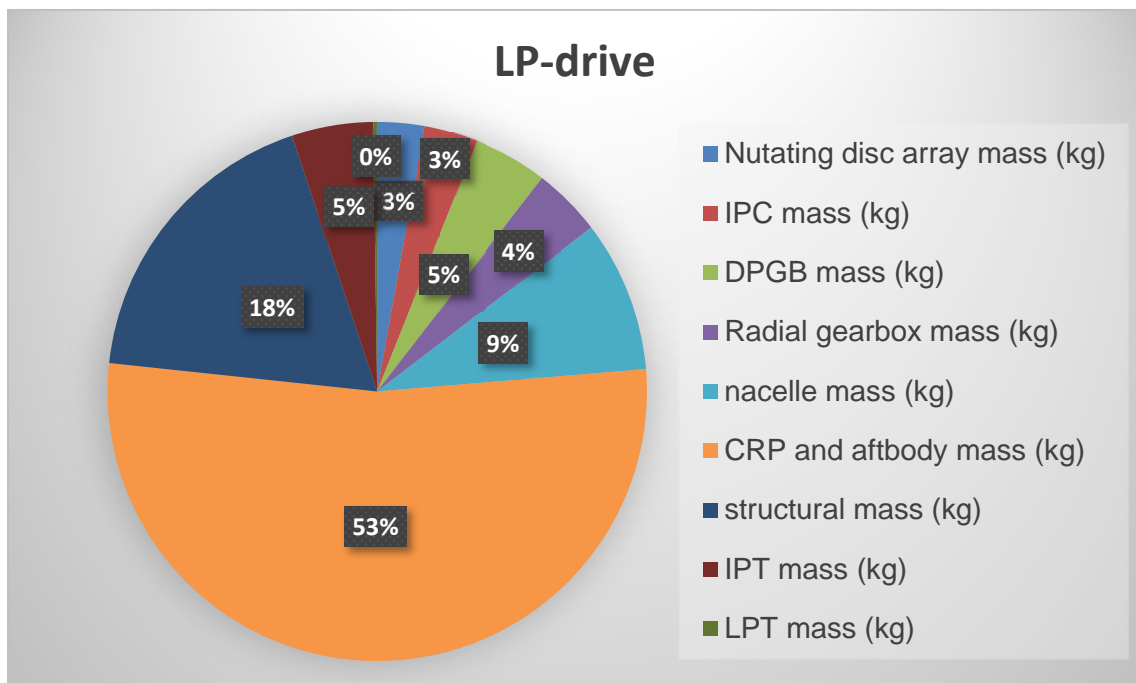


Figure E- 3: GOR2050 LP-drive configuration weight distribution

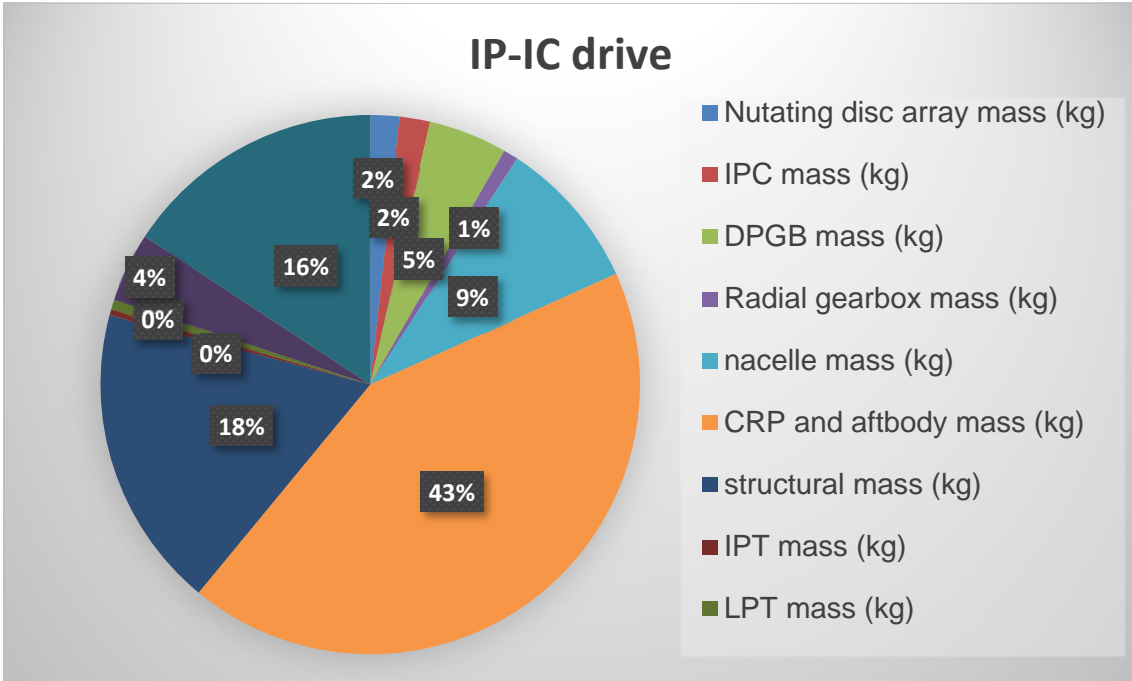


Figure E- 4: GOR2050 IP-IC drive weight distribution

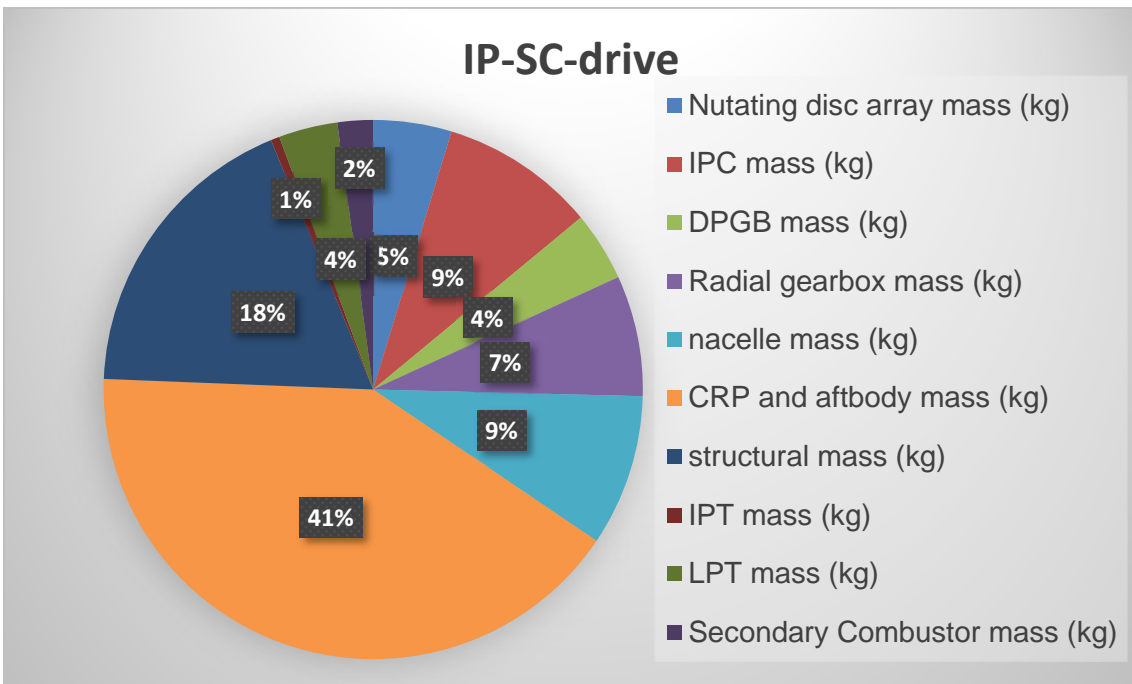


Figure E- 5: GOR2050 IP-SC drive weight distribution

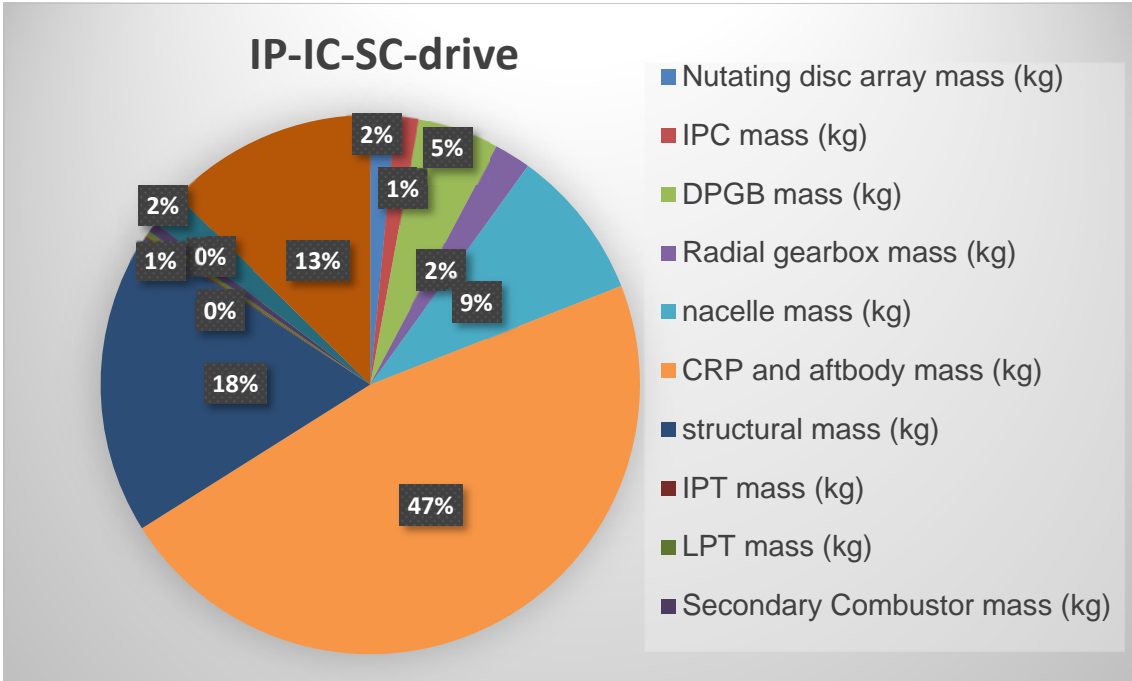


Figure E- 6: GOR2050 IP-IC-SC-drive weight distribution

APPENDIX-F

Figure F-1 shows the circumferential distribution of ND engine system modules in the Y2050-IP-drive and the Y2050-IP-SC drive concepts respectively. If one considers abnormal modes of operation, for instance if ND system module 5 fails for some reason ND system module 2 would have to also be shut down in order to achieve a balanced overall engine. This in turn would cause the rest of the nutating disc engine system modules to operate at a faster speed to maintain thrust.

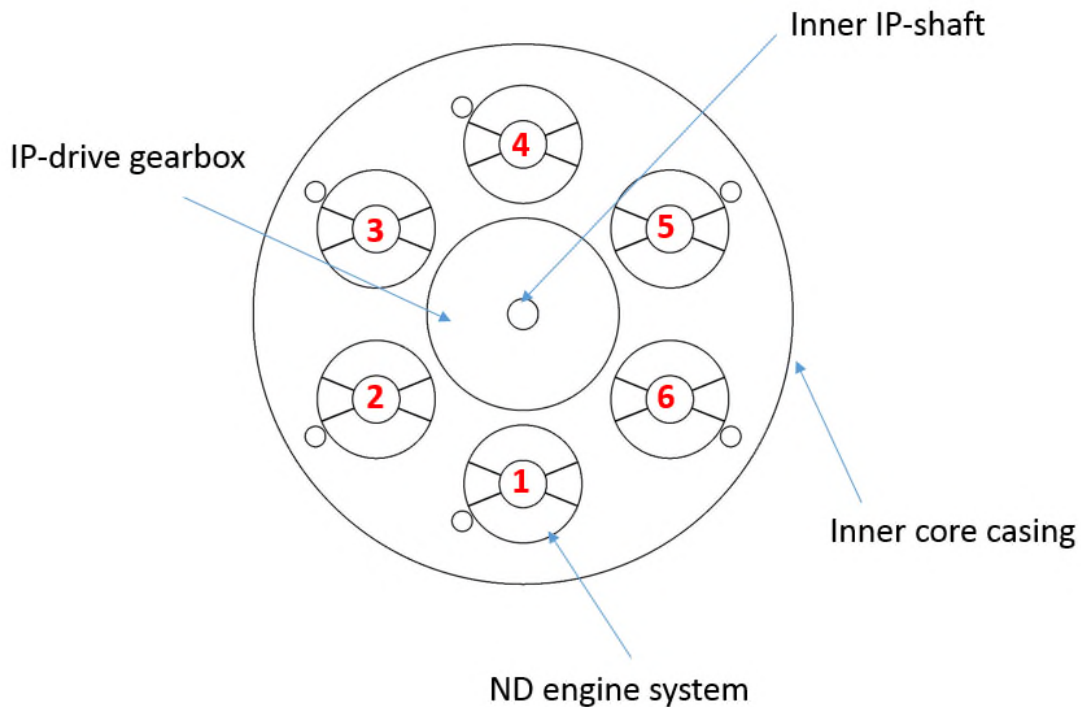


Figure F- 1: Circumferential distribution of ND engine modules for IP-drive and IP-SC-drive engines

Similar to Figure F-1, Figure F-2 shows the circumferential distribution of the ND engine modules for the Y2050 IP-IC-drive and Y2050 IP-IC-SC-drive engine configurations. To reiterate, the number of nutating disc modules for the aforementioned configurations is a consequence of having a reduced relative core flow rate compared to the other IP-drive configurations. Similar to the other IP-drive configurations, if one ND engine fails the mirror position of the ND engine module will shutdown in order to account for balancing the engine.

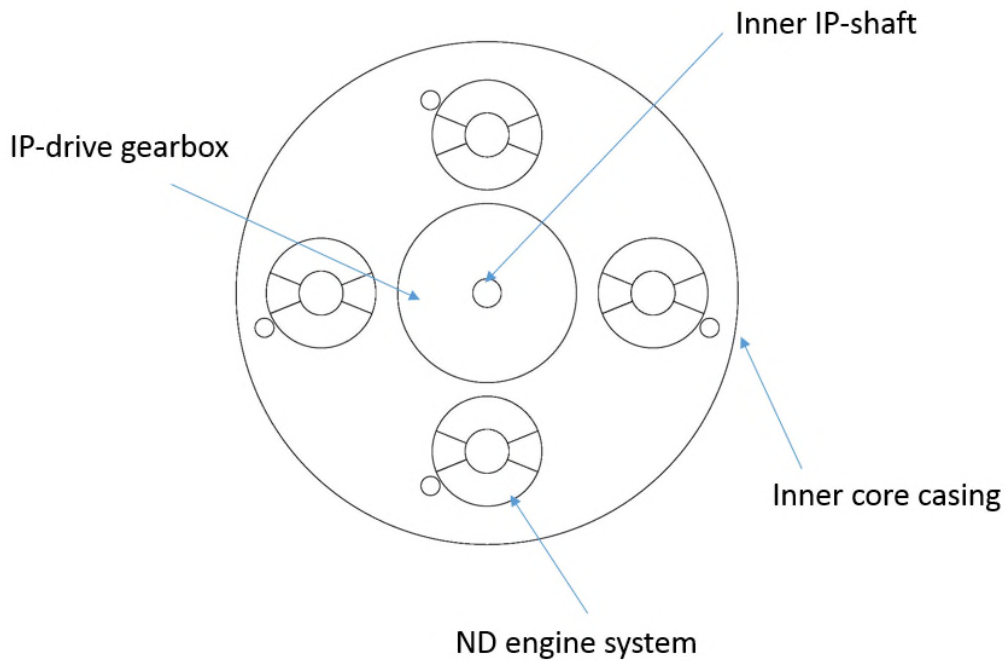


Figure F- 2: Circumferential distribution of ND engine modules for IP-IC-drive and IP-IC-SC-drive engines

Figure F-3 provide a preliminary free body diagram for pressure based forces as well as momments. Essentially, the forces and momments produced during the operation are assumed to be reacted b the anti-roll bar bearing and the bearing located on the z-shaft. The free-body diagram has to account for inertial and gyroscopic loads in future work on this subject as it would be pivotal in determining the mechanical constraints of the design.

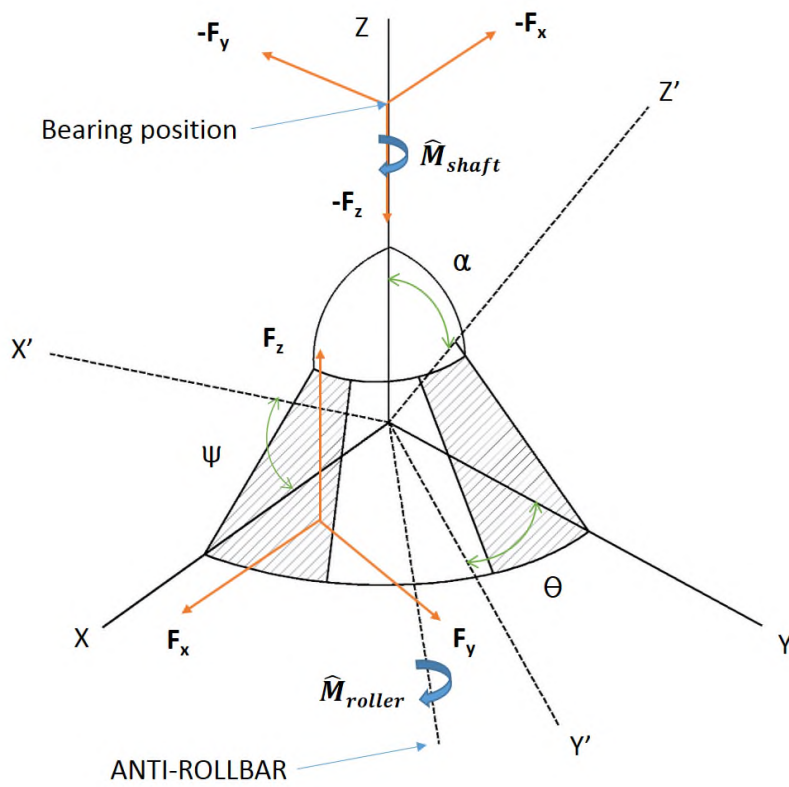


Figure F- 3: Preliminary free-body diagram of the nutating disc engine surface